SPECTROMETRY AND DOSIMETRY FOR ACCELERATOR BASED *IN-VIVO* MEASUREMENTS

By

Aslam, M.Sc., B.Sc.(Hons.)

A Thesis

Submitted to the School of Graduate Studies

in Partial Fulfilment of the Requirements

for the Degree

Doctor of Philosophy

McMaster University

SPECTROMETRY AND DOSIMETRY FOR ACCELERATOR BASED *IN-VIVO* MEASUREMENTS

DOCTOR OF PHILOSPHY (2003) McMaster University

(Medical Physics) Hamilton, Ontario

TITLE: Spectrometry and Dosimetry for Accelerator Based *In-Vivo* Measurements

AUTHOR: Aslam, M.Sc. (Quaid-e-Azam University)

SUPERVISORS: Drs. William V. Prestwich and Fiona E. McNeill

NUMBER OF PAGES: xvi, 180

Abstract

The neutron irradiation facility developed at the McMaster University 3 MV Van de Graaff accelerator will be employed to assess *in vivo* elemental content of aluminum and manganese in human hands. These measurements will be carried out to monitor the long-term exposure of these potentially toxic trace elements through hand bone levels. This thesis addresses two important issues regarding in-vivo neutron activation analysis (IVNAA) of the hand; the first relates to the optimization of operating conditions at the McMaster University 3 MV KN Van de Graaff accelerator to produce neutrons via the $^{7}Li(p, n)^{7}Be$ reaction for in-vivo neutron activation analysis and the second relates to the evaluation of the total dose equivalent delivered to the patient hand undergoing irradiation using a ½" diameter tissue equivalent proportional counter (TEPC).

The operating conditions at the 3 MV KN Van de Graaff accelerator have been optimized by employing a long counter designed for this study to monitor the neutron fluence and a NaI(Tl) detector to measure the ^{7}Be activity produced as a result of (p, n) interactions with ^{7}Li. It was observed that inefficient target cooling and the presence of oxide layers on the target surface resulted in lower measured yields than those calculated.

The computational method described in this work to estimate the average radiation dose equivalent delivered to a patient's hand during irradiation employs the neutron and gamma doses measured using a ½" diameter TEPC and the quality factor of the neutron beam calculated by using the Monte Carlo radiation transport code, MCNP4B. Based on the estimated doses delivered to a patient's hand, the proposed irradiation procedure for the IVNAA measurement of manganese in human hands (Med Phys 29(11) (2002) 2718) with normal (1 ppm) and elevated manganese content can be carried out with a reasonably low dose of 31 mSv to the hand which is less than the recommended maximum permissible dose equivalent limit (50 mSv) for such diagnostic procedures. 63% of the total dose equivalent is delivered by the non-useful fast neutron group (>10 keV); the filtration of this neutron group from the beam will further reduce the dose equivalent to the patient's hand.

Acknowledgements

I wish to express my sincere thanks to my supervisors Drs. W. V. Prestwich and F. E. McNeill. Their guidance and generous assistance were invaluable in the completion of this work. Their inspiring talks and stimulating discussions have contributed greatly to my understanding of the field. I thank Dr. McNeill who arranged funds for this research through Natural Sciences and Engineering Research Council of Canada (NSERC) and other funding institutions. I also thank Dr. McNeill for carrying out the added administrative work for me.

I am very appreciative of Dr. A. J. Waker, also a member of my supervisory committee, who acted as a consultant and collaborator for this research. Thanks to my other supervisory committee members, Drs. D. R. Chettle and J. C. Waddington, for their time commitment and suggestions as well.

I wish to recognize a number of individuals at the McMaster University accelerator laboratory. These include Jason Falladown, Jim Stark, John Cave, and Scot McMaster. I must thank them all for running the accelerator for my experiments, preparing the thick and thin lithium targets, constructing various pieces of equipment, and maintaining the computers I used, etc.

The financial assistance to me provided by the International Council for Canadian Studies (ICCS) is gratefully acknowledged. I thank Ms Diane Cyr at ICCS for carrying out the administrative work for me.

I am especially grateful to few of my friends, Rao Fawwad Husain Khan, Mir Mukkaram Ali, Dragana Stasic, Sean Carew, Sajid Bashir, and Siraj-ul-Islam Ahmad for their company and generous help at different occasions. I also acknowledge the help, advice, and encouragement of Drs. Nasir Ahmad, Tariq Majeed, Abdul Majeed during the course of this work.

I would also like to thank other friends and officemates Mahesh, Mehran, and Ryan. I am grateful to all the other medical physics graduate students as well, who have given McMaster an excellent research environment.

I wish to express my regards to my parents, sisters, brothers and parent in-laws for their encouragement during the course of this work. I acknowledge the moral assistance and

constant encouragement of Nadeem and his family members during the course of this work. I am also thankful to Uncle Ami and Aunt Bhano for so accommodating and looking after Erum while I was working in my office and also for remembering us on every important occasion.

Finally, I wish to thank my wife Erum for her moral support and understanding and I am grateful for her continued patience and encouragement. I appreciate her helping me in different ways. I dedicate this work to her and to my little, quite and calm girl Mash'al who was born in the last stages of graduation, my parents and sisters.

Table of Contents

List of Figures

Chapter II (*Paper I*)

Chapter III (*Paper II*)

Chapter IV (*Paper III*)

Chapter V (*Paper IV*)

Chapter VII (*Paper VI*)

List of Tables

Chapter II (*Paper I*)

CHAPTER I

Introduction

1.1 *In vivo* Neutron Activation Analysis (IVNAA)

In vivo neutron activation analysis (IVNAA) is a technique that has been in use for almost four decades for the measurement of various major, minor and trace elements in living subjects for purposes connected with medical research, clinical diagnosis and occupational health (Cohn, 1980; Chettle and Fremlin, 1984; Sutcliffe, 1996; Ellis, 2000). This technique is based on the measurement of characteristic γ-rays produced in the body by neutron interaction with the element of interest. *In vivo* elemental content of the body is assessed by employing the fast neutron interaction (for N and P), neutron inelastic scattering (for C and O) and thermal neutron capture reactions (for N, Ca, Cd, Al, Mn). The induced activity is measured either during the irradiation procedure (called prompt IVNAA) or after the irradiation (called delayed IVNAA). In cyclic activation, irradiations and activity measurements are carried out in alternate cycles.

IVNAA is widely used in body composition studies (Cohn, 1980; Chettle and Fremlin, 1984; Sutcliffe, 1996; Ellis, 2000). The measure of the body compartments such as fat, protein, intra- and extracellular water, and skeletal mass have been assessed variously by employing the major elemental contents of the body (Sutcliffe 1996). The major elements H, N, Cl, and Ca of the body can be measured *in vivo* by NAA in the whole body or in body organs of living subjects (Cohn, 1980; Chettle and Fremlin, 1984; Sutcliffe, 1996; Ellis, 2000). Practically, any departure from normal conditions in individuals may be judged by measuring these elements *in vivo*. This knowledge of elemental contents is of value in studying trends in disease processes and monitoring the response to treatment. For example, the measurement of nitrogen is a direct means of assessing a patient's protein status in many nutritional disorders and diseased states such as determining the efficacy of treatment in HIV-infected males for persistent involuntary weight loss (Ellis *et al.*, 1996). A large number of other elements are also measurable *in vivo* by IVNAA, including iodine, sodium, phosphorus, carbon, iron, aluminum, selenium, copper and silicon (Chettle and Fremlin, 1984). Body composition data may be useful in choosing the most appropriate treatment of wasting illness, sepsis, trauma, renal failure and nutritional disorders.

Several research groups around the world have been involved in the development and application of the technique of IVNAA for monitoring the uptake and distribution of potentially toxic elements found in trace amount in the human body. Neutron activation measurement of trace elements such as Cd, Al, and Mn in the liver, kidneys, and bones of both occupationally and environmentally exposed individuals has produced a significant volume of knowledge to provide a better understanding of the relationships between exposure, body burden, and health effects. Measurements of liver or kidney cadmium by IVNAA with the use of transportable facilities, have found application in occupational health studies.

The dose equivalents delivered to the subject for IVNAA purposes vary according to the sensitivity and precision required. The levels of dose equivalents delivered especially for major and minor elemental content of the body are comparable with, or in some cases slightly higher than, those in established diagnostic radiographic examinations. During the last four decades, facilities around the world have been designed and constructed in various centers specifically for use in medical research, and a large number of patients with various disease conditions have been measured.

The success of the IVNAA depends on the abundance and location of the element to be measured inside the body, the probability and type of neutron reactions that can take place with that particular element, and the characteristics of the decay products. Different factors related to the choice of neutron source, for IVNAA employing thermal neutron capture reactions, are discussed in the following sections.

1.2 Selection of Neutron Sources for Partial body (n, γ) IVNAA

The requirements of an ideal neutron source for installation in hospital settings to carry out clinical measurements using (n, γ) IVNAA include (a) precision (reproducibility), (b) an acceptable neutron dose equivalent, (c) uniformity of composite differential sensitivity throughout the organ of interest, (d) an irradiation procedure causing as little inconvenience and trauma as possible to the patient, (e) compactness, (f) transportability to other locations so that if needed can be used to monitor the population exposed to toxic elements at their work place, (g) easy to operate and (h) acceptable costs.

1.2.1 Patient dose

The dose equivalent received to a patient during an irradiation procedure is the limiting factor for IVNAA measurements. For use in clinical medicine, it is desirable to keep the dose

equivalent as small as possible, consistent with the requirements of the procedure. The absorbed dose includes contributions from both neutrons and accompanying external γ rays. The absorbed dose from incident γ-rays can be comparable in magnitude with that from neutrons (Bush, 1972; Aslam *et al.,* 2003), but, since a quality factor ranging from 5 to 20 depending upon the neutron spectrum is normally taken for neutrons and that for γ-rays is 1, neutrons still account for about 70-90% of the total dose equivalent. Neutron sources that have been in use in IVNAA produce energy spectra, which are continuous and have a wide range. The neutron dose is thus calculated as the convolution of the incident neutron fluence spectrum and the kerma coefficients. Kerma coefficients in tissue equivalent materials increase with increasing neutron energy (E_n>30 eV). Thus considering the radiation dose, neutrons with relatively low energies are most desirable for IVNAA. The International Commission on Radiological Protection (ICRP) have not recommended any dose limits specifically for patients undergoing IVNAA measurements, however, the patients doses are maintained well below the dose limits recommended by different regulatory boards. It should be noted that these figures alone cannot be used to compare techniques, since the precision and sensitivity varies considerably for various systems. There are significant ethical, practical and theoretical issues that need to be considered when carrying out IVNAA measurements. For example, whether the benefit derived from the measurements justifies the risk involved.

1.2.2 Neutron Fluence Spectrum

Calcium, nitrogen, sodium, chlorine, aluminum and manganese have been measured *in vivo* by the (n, γ) reaction (Chamberlain *et al.*, 1970; Nelp *et al.*, 1970; Cohn and Dombrowski, 1971). For this reaction, the (n, γ) activation cross-section is maximum at thermal neutron energy and decreases very rapidly with increase in neutron energy for the isotopes of interest. However, the exponential fall-off of the thermal neutron fluence in tissue (mean free path 2.6 cm) precludes the direct use of an incident beam of thermal neutrons for IVNAA measurements (Palmer *et al.,* 1968). Since the body itself provides some energy moderation, therefore an epithermal neutron beam having an incident energy spectrum on the order of a few keV improves the uniformity of activation of the isotope in question. Moreover, the mean free path of neutrons in a human subject or anthropomorphic phantom decreases with decreasing incident neutron energy because of the increase in scattering cross-section. Thus different neutron spectra are employed to measure the same element in different sites in the human body depending upon the depth of site of investigation in the body to maximize the

activation of the element of interest. For elements to be investigated in deep seated organs up to a depth of 10 cm in the human body, a predominantly epithermal neutron spectrum (4 eV-40 keV) is employed which is partially moderated in the body itself, whereas a considerably lower mean neutron energy is employed to activate an element of interest located in superficial tissues (Lewis *et al.,* 1997).

The reaction rate, R, of the γ rays produced by an element of interest having an (n, γ) activation cross-section, $\sigma(E)$, due to a neutron fluence spectrum, $\phi(E)$, is

$$R = n_T \int \sigma(E)\phi(E)dE \qquad (1)$$

where n_T is the number density of the isotope of the element of interest in the organ or tissue. The σ(E) is determined by the element of interest and n_T is determined by the organ, or body, so that the only variable under the experimenter's control is $\phi(E)$ which in turn determines the dose delivered to the tissue or organ. Thus the measurement of a trace element in a target organ having relatively low activation cross-section will be carried out using high neutron fluence. This will result in higher patient dose compared to those trace elements, which have higher activation cross-sections. Despite the fact that the thermal neutron capture cross-section of cadmium (σ_{th}~20,000b) is 10^5 times than that of aluminum (σ_{th}~0.23b), doses for cadmium measurements in liver or kidney vary from 0.5 to 8 mSv (Al-Hiti *et al.*, 1979; Krauel *et al.*, 1980; Morgan *et al.*, 1981; Cummins *et al.*, 1982; McNeill *et al.*, 1982; Scott *et al.*, 1983), which is not as different for aluminum measurements in hand (20 mSv) (Lewis *et al.,* 1997) as the differences in cross-sections. As pointed out by Chettle and Fremlin (1984) that there is a potential for cadmium measurement in liver or kidney with lower dose by further optimizing the incident neutron spectrum.

1.2.3 Neutron Sources

As discussed earlier, a neutron source and its spectrum are selected to maximize the activation of the element of the interest, minimize the dose equivalent per incident neutron, and to achieve the uniformity of activation throughout the site of investigation in the human body. The neutron sources that can be employed for IVNAA are accelerators of various types including portable neutron generators, nuclear reactors, radioactive sources (α, n) and spontaneous fission sources (^{252}Cf).

Many of the sufficiently intense neutron sources (with the exceptions of D-D and D-T neutron generators emitting 2.5 MeV and 14 MeV neutrons respectively) produce energy spectra, which are continuous and have a wide range. The majority of neutron sources that are used

for IVNAA have energies of a few MeV. For example, neutrons from nuclear fission have a mean energy, ~2 MeV, those from a ^{238}Pu-Be (or ^{241}Am-Be) radioisotope source have a mean energy of ~4.5 MeV whilst neutrons produced on a low energy accelerator using the D(T, n)^{4}He reaction are emitted at 14 MeV. Therefore, these fast neutrons are moderated in a manner dependent upon the application to have an incident energy spectrum on the order of a few keV to generate thermal neutrons at depth in tissue, with the tissue itself acting as an additional moderator. This external moderation of fast neutrons to epithermal energy range not only optimizes the activation of the intended isotope in the target organ but also reduces the dose significantly to the patient. Thus a careful selection of the neutron energy spectrum should be carried out to achieve an optimal sensitivity per unit subject dose equivalent.

1.2.3.1 Radio-Isotope Based Neutron Sources

The main advantage of using a radioisotope-based system for IVNAA over reactors or accelerators is that this type of device can be made sufficiently compact to be installed and operated in a clinical environment at relatively low cost (Cohn *et al.,* 1972; Mernagh *et al.,* 1977; Vartsky *et al.,* 1977; Evans *et al.,* 1979; Thomas *et al.,* 1979; Vartsky *et al.,* 1979; Krauel *et al.,* 1980; Beddoe *et al.,* 1984; Allen *et al.,* 1987; Ryde *et al.,* 1987). There is also the additional advantage arising from the ease of operation and high reproducibility inherent in the constant output of neutrons from (α, n) sources. Among the radio-isotope based neutron sources, the construction of a transportable system using ^{252}Cf is simpler than those of (α, n) sources because of the soft spectrum and lower average energy of the neutrons emitted by ^{252}Cf than those of (α, n) sources.

However, the relatively short half-life of ^{252}Cf (2.64 years) detracts from its widespread application as it must be replaced on a regular basis. Radioisotope based neutron sources constantly produce neutrons, whether required or not, and cannot be switched off like accelerators and reactors. Due to security issues, plutonium based neutron sources have rather stringent regulations on usage, storage and availability. Further, the low intensity of thermal neutrons may become a major limitation of the use of isotope based neutron sources in IVNAA measurements of trace elements having low thermal neutron capture cross-section (Wyatt *et al.,* 1993; Lewis *et al.,* 1997).

1.2.3.1 Accelerator Based Neutron Sources

Sufficiently intense fast neutrons for many clinical applications are produced by low-energy charged particle-induced reactions with low mass number targets using charged particles accelerators.

1.2.3.1.1 Large Accelerators

The use of an accelerator to generate the neutron fluence has other inherent advantages over the use of isotopes and reactor based neutron sources. A significantly softer neutron spectrum can be generated to improve the sensitivity per unit dose equivalent either by changing the incident charged particle beam energy or the target material. For example, 2.25 MeV protons on ^{7}Li results in an average neutron energy of 225 keV with no neutrons produced with energies greater than 520 keV. A relatively soft neutron energy spectrum of average energy 80 keV can be produced by changing the proton beam energy to 2.00 MeV. Low energy accelerators capable of producing moderate beam currents of less 200-300 μA can also be used to produce relatively soft neutron energy spectra of sufficient neutron yields by bombarding protons on ^{3}H, ^{9}Be and deuterons on ^{9}Be, ^{12}C and ^{13}C while operating with beam energies of 1–3 MeV (Colonna *et al.*, 1999). The incident neutron spectrum can further be optimized to reduce the average neutron energy either by changing the moderator material or thickness of the moderator material. The total neutron yield per unit incident beam charge (n/μC) incident on a thick target also changes with the change in the incident beam energy. The total neutron yield at a given beam energy is a continuous variable that can be set through the beam current on target. This allows the operator to establish the appropriate tradeoff between the dose equivalent, acquisition time and electronics throughput rate for an individual patient (O'Meara *et al.*, 2001). Thus a combination of various operating parameters of an accelerator-based neutron source provides a significant inherent flexibility to produce an optimum incident neutron fluence required for different IVNAA applications.

One disadvantage associated with the charged particle accelerators is that the high incident particle energies of a few MeV are required to generate a significant neutron yield, because the reactions employed in accelerators have high threshold energies. Thus large accelerator facilities are needed to produce the incident charged particle beam. However, such a device has a wide range of additional biological and clinical applications in boron neutron capture therapy (BNCT), boron neutron capture synovectomy (BNCS), and neutron brachytherapy. Furthermore, the availability of transportable accelerators in the near future will outweigh

the disadvantage due to large size compared to transportable radioisotope based neutron sources.

1.2.3.1.2 Sealed Tube Neutron Generators

The neutron-production cross sections of the D-D and D-T reactions are high at relatively low energies, and an acceleration voltage between 100 and 200 kV is enough to produce high neutron yields. The low acceleration voltage requirement makes these reactions viable candidates for compact, portable neutron generators. All the neutrons produced using D-D reaction have approximately the same energy of 2.5 MeV. Similarly neutrons all of 14 MeV are produced in the D-T reaction. This is because the incident particle energy is small compared with the Q-value of either reaction. The reproducibility obtained with sealed tube neutron generators, in practice, is as good as that obtained with radioactive neutron sources.

Given the need of a compact installation for clinical applications, small, sealed, commercially available D–T neutron generators have been implemented in the clinical measurements of total body nitrogen employing IVNAA using fast neutron interactions (Kehayias *et al.,* 2000; Williams *et al.,* 1978; Leach *et al.,* 1977; Cohn and Dombrowski, 1971).

The neutron fluxes obtainable from commercial generators are 4×10^{9} n/s for the D-D and 4×10^{11} n/s for D-T reactions (Yanch *et al.,* 1999). The energy of the neutrons produced by the D-D reaction is similar to the average energy of the neutrons emitted by ^{252}Cf and the neutron flux is ~2 times higher than the 1 mg ^{252}Cf source used in IVNAA applications. Thus there is a possibility to construct a similar compact moderator and reflector assembly as optimized for ^{252}Cf (Lewis *et al.,* 1997). Such a system will have the added benefits of compactness; it will be safer to use because the target does not use radioactive tritium, simpler to transport, a less costly irradiation facility, easy to install, easier to operate, and able to operate in pulsed mode compared with the large accelerator facilities. Moreover, D-D neutron generators have a constant neutron output over the lifetime of the tube which suggests the reproducibility obtained with D-D generators will be as good as obtained with other sources.

The other sealed tube generator which employs the D-T reaction produces approximately 100 times higher neutron flux than that of D-D reaction with neutron of 14 MeV energy. Although there is a possibility to construct a moderator and reflector assembly to produce a thermal-epithermal source of neutrons, the assembly would be larger than those of other compact sources like D-D neutron generator and radioisotope based sources. The targets in

D-T generators contain tritium which is radioactive, however, the activity is much lower than contained by Pu/Be sources. Moreover, for generators using D-T generators, it is necessary to replace the target sealed tube generator from time to time, which is a potential disadvantage. However, in practice, the patient irradiation times are so short compared with the expected tube lifetime that such replacements are infrequent.

When sealed tube neutron generators are used, it is not economically prohibitive to utilize two generators to achieve a simultaneous bilateral irradiation. This avoids manipulation of the patient by rotating him at about the mid-time of irradiation as is common with some major facilities (Chamberlain *et al.* 1968; Palmer *et al.,* 1968; Cohn *et al.,* 1970).

1.2.4 Uniformity of Sensitivity

Although neutron activation has proved very useful in a wide range of important studies, its accuracy in absolute as well as sequential measurements of body elements is limited because of the large variation in differential composite sensitivity over the organ of interest. This is both because of the distribution of the thermal-neutron flux that activates the element in question within the body depending on the body's shape and dimensions and the variation of efficiency of γ-detection system employed to measure the activation signal.

Over the years, various measures have been taken to alleviate this problem of non-uniformity of composite sensitivity through the human subject to a degree of uniformity up to 25-35%:

- Improving the uniformity of the thermal flux throughout the body by surrounding the patient with pre-moderating and neutron-reflecting material or irradiating the patient bilaterally — that is, irradiating the patient from different directions, or moving him from prone to supine position in mid-irradiation.
- Using an internal standard to normalize the *in-vivo* measurement. For example, determining total body nitrogen using hydrogen as an internal standard in determining.
- Using calibration phantoms of various sizes to match patients' shapes and sizes.

1.3 Dosimetry for (n, γ) IVNAA

A number of individuals including the patient and the technicians are exposed to low doses of low energy neutron beams employed for IVNAA measurements. The neutron energy spectrum to which such individuals will be exposed varies widely, depending on the beam

parameters, the degree of moderation in *in-vivo* setup and shielding. The photons arising within the neutron source and in the *in-vivo* setup also contribute towards the total dose delivered to the patient. For purposes of radiation protection, the relative risk associated with exposure to low doses of various ionizing radiations are compared quantitatively by multiplying the absorbed dose with the effective quality factor. The product of absorbed dose and the quality factor is defined as the dose equivalent (ICRP, 1977, 1991). A quality factor ranging from 5 to 20 depending upon the neutron spectrum is normally taken for neutrons and that for γ-rays is 1. Thus the estimation of dose equivalent delivered to patients and technicians involved in IVNAA measurements would not only involve the determination of neutron dose equivalent but also the photon dose equivalent. It is important to determine the total dose equivalent due to both neutrons and photons as MDL for IVNAA measurements is determined following the maximum permissible dose equivalent limit defined for such clinical diagnostic procedures.

1.3.1 Absorbed Dose

Ionizing radiation interacting with matter results in a field of charged particles within the material involved. The energy imparted, ε, in the volume of a material by ionizing radiation is

$$\varepsilon[J] = R_{in} - R_{out} + \sum Q \tag{2}$$

R_{in} is the sum of energies of all charged and uncharged particles entering the volume, R_{out} is the sum of energies of all charged and uncharged particles leaving the volume and ΣQ is the sum of all rest mass changes that occur in the volume.

The specific energy, z, imparted in the mass m is defined as

$$z[Gy] = \frac{\varepsilon}{m} \tag{3}$$

The energy, $d\varepsilon$, imparted by a given ionizing radiation in an infinitesimal volume of mass, dm, is defined as the absorbed dose, D, as

$$D\ [Gy] = \frac{d\varepsilon}{dm} \tag{4}$$

The absorbed dose D is related to the mean specific energy,

$$\bar{z}\,[Gy] = \int_0^\infty z f(z) dz \tag{5}$$

by

$$D = \lim_{m \to 0} \bar{z} \tag{6}$$

where $f(z)$ is the frequency distribution of z. The absorbed dose is defined as the energy imparted in an infinitesimal volume at a point and dm is the mass of this volume. The absorbed dose is therefore the expectation value of the specific energy z. A measurement of absorbed dose is really a measurement of the absorbed dose averaged over that volume with mass Δm.

Kerma, K, is the amount of kinetic energy, dE_{tr}, given to charged particles by indirectly ionizing radiation per unit mass.

$$K\ [Gy] = \frac{dE_{tr}}{dm} \tag{7}$$

The absorbed dose refers to the absorption of energy in matter whereas kerma refers to the transfer of energy to charged particles in the matter. Under charged particle equilibrium (CPE) conditions, kerma is numerically equal to absorbed dose.

1.3.2 Neutron and Photon Dosimetry Using TEPC

The low pressure tissue equivalent plastic walled proportional counters have proved to be quite useful particularly for the simultaneous measurement of neutron and photon dose equivalents in mixed n-γ fields. The TEPC provides four distinct technical advantages as compared with other neutron-measuring instruments. These are (1) the similarity of wall material and fill gas atomic composition to tissue simplifies the direct evaluation of dose to tissue from the measured dose, (2) the simultaneous evaluation of neutron and photon dose equivalents in a single measurement, (3) self contained calibration source, and (4) small size provides better spatial resolution compared to other large size detectors.

1.3.2.1 Low Pressure Tissue Equivalent Proportional Counter

A Rossi counter is one of the most common microdosimetric counters and is available commercially in a number of different sizes. The wall of the counter is made up of A150 tissue equivalent plastic (a mixture of nylon, polyethylene, graphite), which is black in color

due to the presence of carbon in the plastic. The thickness of the wall is chosen to be greater than the range of charged particles generated in the wall to provide charged particle equilibrium. The 3 mm thick wall of the TEPC provides charged particle equilibrium for the neutron energies up to 14 MeV but because of the larger range of electrons, a build up cap would be required for the photon energies greater than 600 keV.

These counters are spherical in shape and have an anode wire which traverses a diameter of the detector. The anode is surrounded by a helix (diameter ~ 1.8 mm) which serves to produce a strong uniform electric field in the vicinity of the anode. This establishes a proportional counting region between the helix and anode wire. The detector is therefore a cylindrical proportional counter coupled to a spherical volume. The counter produces pulses with amplitudes that are proportional to the energy deposition of secondary charged particles generated in the tissue-equivalent plastic counter wall and tissue equivalent-gas. The typical tissue volumes simulated with these detectors are ½ - 2 μm, with 2 μm appearing most frequently in the literature.

All the measurements described in this thesis were carried out using a spherical ½″ diameter Rossi counter (manufactured by Far West Technology, Goleta, California, USA) filled with propane based tissue equivalent gas (a mixture of propane, CO_2 and N_2) to simulate a 2 μm tissue equivalent.

1.3.2.2 Microscopic Tissue Site-Size Simulation

The principle of microscopic tissue site-size simulation is based on using a macroscopic detector under conditions which will result in the same energy deposition as that in a microscopic tissue volume. This is generally achieved by filling a tissue equivalent walled detector with a tissue equivalent gas, at a very low pressure. The molecules in the gas will then undergo similar reactions with ionizing radiation to a tissue volume which is much smaller, but much more dense. There are two main types of tissue equivalent gases - methane based and propane based. These consist of the gas mixed with CO_2 and N_2 (ICRU, 1983). The methane based TE gas matches more closely the elemental composition of tissue, however propane based TE gas is usually used because of the higher gas gain.

To simulate a tissue volume of diameter Δx_{tissue} using a detector of a larger volume of tissue equivalent gas of diameter of Δx_g, the required density of TE gas would be

$$\rho_g = \frac{\rho_{tissue} \times \Delta x_{tissue}}{\Delta x_g} \tag{8}$$

This relationship implies that the ratio of the mass stopping powers of the charged particles in the tissue equivalent gas and in the tissue is 1 for all the energies involved.

Employing the above equation, the density of the TE gas required to simulate a 2 μm tissue equivalent diameter using a ½" counter would be

$$\rho_g = \frac{1\times10^3 kg/m^3 \times 2\times10^{-6} m}{1.27\times10^{-2} m} = 0.157 kg/m^3 \tag{9}$$

This required density can further be used to calculate the required pressure of TE gas by employing the general gas equation as

$$P = P_o \frac{\rho}{\rho_o} \times \frac{T}{T_o} \tag{10}$$

$$P = 750\tau \times \frac{0.157}{1.798} \times \frac{293}{293} = 65 torr \tag{11}$$

Detectors of different sizes are available commercially to simulate the same tissue volume by choosing an appropriate gas pressure for each detector size. For instance, a 2 μm tissue equivalent diameter can be simulated using a TEPC filled with a propane based TE gas either by employing a ½" counter at a pressure of 65 torr or a 5" counter with a pressure of 6.5 torr. In a radiation field which is fairly uniform over the volumes of two counters of different sizes simulating the same tissue volume would result in the same dose equivalent within the experimental uncertainty. However, this would not be the case for accelerator based neutron sources where neutron fields are quite non-uniform. Although the sensitivity of large size counters is higher than small size counters, small size counters are preferred for dosimetry of IVNNA systems compared to other radiation protection problems because of the high flux of neutrons available for activation which would otherwise contribute towards a high detector dead time and pulse pile-up.

1.3.2.3 Equipment Setup

The pulse height spectra of single energy-deposition events due to secondary charged particles produced in the wall and the gas of Tissue Equivalent Proportional Counter (TEPC) were measured using a low-noise preamplifier connected directly to the anode of the counter.

Analog pulses from the preamplifier are fed through dual SPEC amplifier with high and low gain settings into two 16 k analog-to-digital converters (ADCs) and stored in ORTEC memory units. Lineal energy measurements of mixed n-γ fields are conducted with two overlapping blocks of amplifier settings because of the wide range of at least three to four decades of lineal energy involved in these measurements. The processing of the raw data was carried out employing the computer programs written in KMAX version 4.1 developed at AECL, Chalk River, Canada (Waker, 1995; Khaloo and Waker, 1995).

1.3.2.4 Gas Gain Calibration

The gas gain represents the gas multiplication which depends on the Townsend coefficient. This coefficient depends on the gas pressure and electric field established, and thus the voltage applied to the detector. The variation of gas gain of propane based TE gas with the applied voltage to the anode wire of ½" Rossi type counter was investigated by varying the applied voltage between 300 and 580 V (step size of 40 V) as this is the typical operational range of the detector. It is not recommended that voltages greater than 600 V be used as this can cause breakdown of the gas and can damage the detector. The helix voltage was adjusted to be 15% of that on the anode. For each measurement the amplifier gain and position of the α-peak from the internal source were recorded. It was noted that the relationship between log(gas gain) and applied voltage is linear, indicating proper operation of the detector. The maximum resolution was observed between 450V and 500V.

In commercial detectors there is a voltage divider which delivers 20% of the anode voltage to the helix. However, for all the measurements described in this thesis, this voltage divider was removed and separate voltages were delivered to the anode and helix independently in order to reduce the capacitance in the electronics and therefore reduced system noise. A 15% of the anode voltage applied to helix resulted in an increased gas gain, compared to the standard 20% case (Arnold, 2000).

1.3.2.5 Counter Calibration

The pulse height spectra of single energy-deposition events are converted into the lineal energy distributions *f(y)* and *d(y)* by applying the appropriate calibration factors. The lineal energy dose distribution, *d(y)*, is then either directly used to evaluate the effective quality factor, $\overline{Q}$, which is defined as a function of linear energy transfer (LET) by assuming $L = y$ or by transforming the *d(y)* into an LET dose distribution, *d(L)*, using an algorithm suggested by Rossi (Rossi, 1968). The dose rates in a mixed radiation field of neutrons and photons are

directly evaluated using the *d(y)* distribution and counter's physical and simulated diameters as discussed in the Section 3.2.5.

The system is calibrated by irradiating the counter with a finely collimated internal ^{244}Cm alpha source. The mean lineal energy, y_α, of the α particles emitted by ^{244}Cm is calculated as the quotient the energy deposited in the cavity to the average chord length of the cavity. The ^{244}Cm emits α particles with an average energy of 5.80 MeV (Srdoc and Marino 1996) which deposit an energy of 170 keV (ICRU 1983) in a 2 μm diameter TE gas and correspond to a lineal energy of y_α= 127 keV/μm. The mean pulse height, h_α, corresponding to the mean energy imparted in the cavity is evaluated at an amplifier gain setting, A_α, by fitting a Gaussian curve to the measured peak. Using y_α and h_α, the calibration factors are calculated to convert the pulse height measurements, h, conducted with two overlapping blocks of amplifier gain settings (A_1 and A_2) into a single spectrum of lineal energy as (Waker, 1995; Arnold 2000; Aslam *et al.*, 2003)

$$y = \frac{y_\alpha}{h_\alpha} G \times h \tag{12}$$

where G is the gain ratio for the two different amplifier settings (A_α/A_1 and A_α/A_2). Since the LET of neutrons is greater than that of photons the amplifier gain for neutron measurements is set lower than that for gamma measurements. To determine the gain ratio G accurately, a pulser is used to perform an electronic calibration for the amplifier gains. The calibration is checked before and after each measurement and the average h_α is used for the purpose of calibration. Sources of uncertainties associated with this method of calibration have been discussed elsewhere (ICRU, 1983).

This calibration assumes a constant W value for all ionizing events caused by different LET particles. Different correction factors are applied to different regions of *d(y)* for the events caused by different LET particles. However, the various W values given in ICRU (1983) for different LET particles in propane based TE gas only vary by a few percent between particles. In common radiation protection studies, no corrections are generally made to account for this difference.

1.3.2.6 Neutron and Photon Dose Separation

The spectra of single energy-deposition events measured using a TEPC simulating a unit density sphere of a few micrometers diameter are used to estimate the neutron and photon absorbed doses and neutron quality factors in mixed n-γ fields.

Low energy neutrons (E_n < 1 MeV) mainly interact with the TEPC wall and gas via the elastic scattering of protons. The energy distribution of recoil protons ranges from *0* to E_n. The energy deposition of these protons in the gas cavity depends upon their stopping power and track length. Among these recoil protons, the protons corresponding to the Bragg peak have the maximum stopping power. The tracks of recoil protons also follow a distribution of tracks in the gas cavity which range from *0* to *d*. The recoil protons of Bragg peak energy traversing through the diameter *d* (maximum track length) of the gas sphere deposit the maximum energy, $\varepsilon_{max}=S_{max}\times d$. The proton edge (or y_{max}) for neutrons depositing energy via protons inside the TEPC gas can thus be obtained by $y_{\max} = \frac{\varepsilon_{\max}}{\frac{2}{3}d}$, where $\frac{2}{3}d$ is the mean chord length of a sphere of simulated diameter *d*. The proton edge is a sharp edge in the *d(y)* distribution and appears approximately at 136 keV/μm. This proton edge is independent of the neutron energy above 300 keV showing that the mean track length of the recoil protons does not depend on the neutron energy. This defines the lower limit for a TEPC simulating 2 μm TE diameter to meet the necessary assumptions for correlating lineal energy to LET. Below 300 keV neutron energy, almost all the recoil protons produced by these neutron energies have insufficient ranges to cross the cavity diameter and thus deposit the entire energy in the cavity. However, the neutron beams containing a large fraction of thermal neutrons which cause ^{14}N(n, p) interactions in the counter wall and gas and produce 580 keV protons. These capture protons have a range larger than the 2 μm simulated diameter while at the same time recoil protons have ranges smaller than the simulated diameter. Charged particles other than protons (^{2}H, ^{14}C) produced via neutron interactions deposit energies greater than that of proton because of the higher LET of these charged particles and appear beyond the proton edge resulting in the lineal spectrum (Stinchcomb and Borak, 1983; Srdoc and Marino 1996; Aslam *et al.*, 2003).

The γ–ray contamination of the neutron field and ^{1}H(*n*, γ)^{2}H interactions in the wall and cavity of TEPC also give rise to an 'electron peak' due to low energy deposition events in the lineal energy spectrum (Waker, 1995). In a mixed field spectrum, the gamma information is contained solely in the lower portion of the spectrum resulting from electron events whereas the neutron information is restricted to much higher parts of the spectrum. This happens because of the lower LET of the electrons compared to those of protons. The gamma ray contribution extends below 10 keV/μm and is separated from the n-γ overlapping region between 1 and 10 keV/μm by subtracting a measured and scaled ^{60}Co gamma spectrum using

the same simulated tissue site size (Waker, 1995; Arnold 2000; Aslam *et al.*, 2003). Thus measuring the energy deposited in simulated microscopic tissue volumes in a mixed n-γ field enables the separation of the contribution of different LET radiations; the quality factors of different LET radiations can be estimated and hence the dose equivalent can be determined. The assumption made in separating the neutron and photon dose contributions is that the spectrum obtained from ^{60}Co roughly matches the gammas from a neutron source. This assumption is valid for a wide range of photon energies as the lineal energy spectrum varies slowly with changes in gamma ray energy (ICRU, 1983).

Analysis of the pulse height distribution produced by the TEPC demonstrated that the portions of the distribution produced by the electrons and photons could be distinguished, so that a single measurement with the TEPC would yield a measurement of both the photon and the neutron dose.

1.3.2.7 Dose Calculations

The energy absorbed in the gas cavity of TEPC may be calculated using the lineal energy distribution $d(y)$ and the mean chord length, $\bar{\ell}$. The total energy imparted in a volume during the exposure may be obtained E [keV] $=\Sigma yf(y)$ [keV/μm]$\times \bar{\ell}$ [μm]. For a right cylinder, the mean chord length, $\bar{\ell}$, is equal to 2/3 the diameter of the cylinder. The mass in the cavity may be calculated as the density of the gas times the volume of the cavity. This yields the following expression for the calculation of absorbed dose from the measured lineal energy dose distribution

$$D_g\,[Gy] = \frac{E[J]}{m[kg]} = \frac{\sum_i y_i f(y_i) \times \bar{\ell}}{\rho \times V} \times 1.602 \times 10^{-16}\,[Gy] \qquad (13)$$

The absorbed dose to the gas of TEPC using a ½" counter is thus calculated by using the lineal energy dose distribution as

$$D_g\,[mGy] = 1.26 \times 10^{-6} \sum_i y_i f(y_i) \qquad (14)$$

Due to the similarity in hydrogen and nitrogen concentration in A-150 plastic and in propane-based TE gas as these are the only two elements which contribute in the energy deposition in this range of neutron energies, the absorbed doses in the wall and gas are taken equal by applying Fano's theorem to assess the dose to tissue and the error in dose

assessment is not of practical importance. Unlike the neutron quality factors measured using a TEPC with different simulated site sizes at low neutron energies; measured neutron doses are independent of simulated site size (Pszona and Makarewicz, 1982).

1.3.2.8 Neutron Quality Factor Evaluation

The effective quality factor, $\overline{Q}$, can be determined from the LET dose distribution, *d(L)*, and the quality factor function, *Q(L)*, as (ICRU, 1983)

$$\overline{Q} = \frac{\int Q(L)d(L)dL}{\int d(L)dL} \tag{15}$$

To evaluate the quality factor, $\overline{Q}$, the lineal energy dose distribution, *d(y)*, measured with a TEPC is transformed into an LET dose distribution, *d(L)*, using an algorithm suggested by Rossi (1968). This algorithm is based on the assumptions that the tracks of the charged particles generated by neutron interactions in the counter wall are long compared to the simulated diameter and the energy loss of the charged particles is negligible compared with their energy upon entering the cavity. To avoid transformation of *d(y)* into *d(L)*, based on the same assumptions as made by Rossi (1968), Ricourt *et al.* (1981) suggested substituting *Q(8/9y)* instead of *Q(L)* and *d(y)* instead of *d(L)* in Eq (15). However, in most of radiation protection studies instead of using *L=8/9y*, the evaluation of $\overline{Q}$ is further simplified by directly substituting $L = y$ (Pihet *et al.*, 1989; ICRP, 1991; Gerdung *et al.*, 1994; Waker, 1995; Khaloo and Waker, 1995; Taylor, 1995; Nunomiya *et al.*, 2002). This substitution would result in slightly larger $\overline{Q}$ value as compared to $\overline{Q}$ calculated by substituting *L=8/9y* (Stinchcomb and Borak, 1983).

Various forms of *Q(L)* have been defined in the past (ICRU, 1983) but the standard adopted by the ICRU and ICRP is the definition of *Q(L)* presented in ICRP publication 60 (1991),

$$Q(L) = \begin{cases} 1, & L < 10 keV/\mu m \\ 0.32L - 2.2, & 10 keV/\mu m < L < 100 keV/\mu m \\ \dfrac{300}{\sqrt{L}}, & L \geq 100 keV/\mu m \end{cases} \tag{16}$$

The functional relationship assumed between the lineal energies measured by using a TEPC simulating 2 μm TE diameter and the LET of the recoiling protons is known to be improper for the neutron energies below 300 keV (Eisen, *et al.*, 1986; Aslam *et al.*, 2003); the neutron energies which are employed here at MAL for IVNAA (Aslam *et al.*, 2003). Various approaches have been followed in the past to improve the response of TEPCs either by physical modification (Pihet *et al.*, 1989; Gerdung *et al.*, 1994; Khaloo and Waker, 1995) of the counter or analytical approaches (ICRU, 1983; Taylor, 1995) for quality factor (hence dose equivalent) evaluation at low neutron energies.

1.3.2.9 TEPC Dose Equivalent Response

The response of a TEPC simulating a 2 μm TE diameter to estimate the neutron dose equivalent is energy dependent and deteriorates with the neutron energy especially below 200 keV neutron energy (Pihet *et al.*, 1989; Gerdung *et al.*, 1994; Khaloo and Waker, 1995; Taylor, 1995). This under-response is largely because of the average range of the recoil protons created by the neutrons, which contribute most to the absorbed dose in the counter in this neutron energy region, becomes less than the simulated diameter (2 μm). These resultant lineal energies are no more a good approximation of the LET of the protons (Pihet *et al.*, 1989; Gerdung *et al.*, 1994; Khaloo and Waker, 1995; Waker, 1995; Taylor, 1995). This leads to an underestimation of the quality factor assigned to such events. This underestimation besides other factors also contributes to the low neutron dose equivalent response of TEPCs in the neutron energy range 0.1-200 keV (Pihet *et al.*, 1989; Gerdung *et al.*, 1994; Khaloo and Waker, 1995; Waker, 1995; Taylor, 1995). Dietze *et al.* (1988) has estimated that this incorrect evaluation of the mean quality factor at these low neutron energies contributes to about half of the deviation of measured dose equivalent from the ambient dose equivalent *H*(10).* Thus it is necessary to make corrections in the dose equivalent measured by a TEPC simulating a 2 μm diameter tissue for neutron energies below 200 keV.

1.4 IVNAA at McMaster University Accelerator Laboratory — Research Proposal

The 3 MV Van de Graaff accelerator at the McMaster University accelerator laboratory (MAL) is primarily dedicated to *in-vivo* neutron activation measurements of various toxic trace elements. Fast neutrons at the facility are produced by bombarding protons on a thick lithium metal target using the $^{7}Li(p, n)^{7}Be$ reaction. A neutron irradiation facility for *in-vivo*

neutron activation measurement of aluminum and manganese found in trace amounts in human hands has been developed at the McMaster University 3 MV Van de Graaff accelerator (Pejović-Milić, 1998, 2001; Arnold, 2000). These publications considered various issues of system design and evaluation, including determining moderator and reflector material type and thicknesses, optimizing system design to minimize the measurement dose, verifying reproducibility of the activation and counting processes, considering various shapes and positioning of the hand, and lastly the use of the calcium activation signal from the bone was determined to be an accurate means of normalizing the measurement to the amount of bone.

The reports of the *in-vivo* measurements of aluminum and manganese in human hand bones by activation analysis at MAL have dealt primarily with the technique and demonstrated its clinical feasibility. However, there are various other important issues regarding the neutron producing targets and the radiation dosimetry which need to be addressed for example, (a) non-uniformity of activation along the transverse and longitudinal directions in the hand phantom, (b) estimation of the neutron quality factors for the neutron beams used for IVNAA of hand, (c) estimation of average dose equivalent received to the patient hand undergoing irradiation, (d) optimization of neutron fluence spectrum for proton beam energies other than 2.00 MeV to take advantage of higher neutron yields at higher beam energies, (e) problems associated with target preparation of the lithium targets used to produce neutrons for IVNAA of hand.

These issues have been investigated to improve the measurements made at the *in-vivo* neutron activation facility at McMaster University and these investigations are presented in this thesis. The dosimetric measurements reported in this thesis were also carried out to get the necessary ethical approval from the McMaster University Human Ethics Board which restricts the maximum local dose to the irradiated hand to less than 50 mSv for an *in-vivo* measurement of toxic trace elements. Moreover, the investigations of filtering the non-useful fast neutron energy group from the beam producing an increase of dose to the patient's hands would help to reduce the dose equivalent.

An outline of the thesis contents, including the author's contributions is listed here:

Chapter (ii) (Paper I) This chapter describes the optimization of operating conditions at the McMaster University 3 MV KN Van de Graaf accelerator to produce neutrons via the $^{7}Li(p, n)^{7}Be$ reaction for IVNAA. The need for optimization arose after a number of earlier studies (Arnold, 2000; Pejović-Milić *et al.*, 2000; Pejović-Milić, 2001) pointed out a

significant discrepancy between the experimental and the calculated neutron doses. To resolve the discrepancy, first it was shown that the neutron yields calculated by using a method which employs the differential cross-section and the thick target yield formula which employs the total cross-sections for (p, n) interaction agree with each other within 5% above E_p = 2.00 MeV. Second, it was observed that inefficient target cooling and the presence of oxides layer on the target surface resulted in lower measured yields than those calculated yields. The calculated neutron yields were achieved experimentally at MAL by an appropriate choice of parameters affecting the target performance.

Chapter (*iii*) (*Paper II*) Although the performance of lithium target for neutron production had been optimized by measuring the ^{7}Be activity produced as a result of (p, n) interaction (*Paper I*), the online measurement of inelastic γ ray yields resulting from the ^{7}Li(p, $p'\gamma$)^{7}Li interaction below the (p, n) threshold could provide a much simpler method of optimization. To accomplish the objective, a preliminary study of the measurement of thin target angular distributions of inelastic gamma ray yields resulting from ^{7}Li(p, $p'\gamma$)^{7}Li interaction for incident proton energies below the threshold of the ^{7}Li(p, n)^{7}Be reaction is described in this chapter.

Chapter (*iv*) (*Paper III*) The spectra of secondary charged particles measured by a tissue equivalent proportional counter (TEPC) simulating a unit density sphere of a few micrometers tissue equivalent (TE) diameter can be used to estimate the absorbed doses and neutron quality factors in mixed n-γ fields. The counter response to measure the neutron quality for low energy neutrons employed here at MAL deviated very significantly from the calculated quality factors at these energies. Thus we report the development of an algorithm to evaluate the quality factors using measured *dose-mean lineal energy*, $\overline{y_D}$, and compare the algorithm with other reported algorithms and analytical methods developed for the improvement in TEPC dose equivalent response in the low neutron energy region.

Chapter (*v*) (*Paper IV*) A method based on the Monte Carlo simulation of the irradiation facility was described to calculate the quality factors of the neutron beams encountered in IVNAA of the hand at MAL. Calculated quality factors were compared with the measured quality factors using the algorithm described in the earlier paper. The non-uniformity of the incident neutron spectrum resulted in a non-uniformity of activation in

the transverse and longitudinal directions as well as the dose to the hand. It is essential to determine the average radiation dose received to the patient's hand because the dose heterogeneity defined as D_{max}/D_{min} is 3 for E_p = 2.25 MeV and 5 for E_p = 2.00 MeV on the phantom surface. Using the measured quality factors and dose rates as a function of position on the phantom surface, the dose equivalent averaged over the phantom surface was estimated. Based on the estimated doses received to the patient hand, the proposed irradiation procedure for the IVNAA measurement of manganese in human hands (Arnold, 2000; Arnold *et al.*, 2002) with normal (1 ppm) and elevated manganese content can be carried out without violating the prescribed maximum dose limits for such diagnostic procedures.

Chapter (vi) (Paper V) The method described in our earlier work (*Paper IV*) to estimate the average dose delivered to the patient's hand undergoing irradiation for IVNAA measurements, employed dose rates measured using TEPC at two points, one in the center and the other one on the phantom edge. The method described in this work employs only one measured dose rate in the center of the irradiation facility. Further, a computational method is also discussed in this paper to calculate the differential composite sensitivity along the phantom surface and along the depth of the phantom. It is shown that the bilateral irradiation of the hand i.e., irradiating the hand from the palm side and then from the other side, the variation of differential composite sensitivity along the phantom depth will be improved to < 10%. To alleviate the problem of achieving uniform composite sensitivity on the phantom surface which is approximately 70-80%, use is made of the calcium activation signal from the bone to normalize the measurement to the amount of bone.

Chapter (vii) (Paper VI) In order to extend the use of facility for those applications in radiobiological and radiochemical research where moderate neutron dose rates are needed, the feasibility of producing monoenergetic neutron beams of energy less than 1 MeV at the McMaster University 3 MV KN Van de Graff accelerator are described in this chapter. The calculated dose rates of the monoenergetic neutrons produced using thin lithium targets as functions of beam energy, target thickness, lab angle, and the solid angle subtended by the sample with the target, are reported in tabular form.

Chapter (*vii*) (*Conclusions*) The thesis results are summarized and, based on them, suggestions are made for the possible directions of future work.

CHAPTER II

Paper I

The following paper examines the optimum operating conditions at the McMaster University KN Van de Graaf accelerator to produce neutrons using thick lithium target via the $^{7}Li(p, n)^{7}Be$ reaction for *in-vivo* neutron activation analysis. After determining the optimum target conditions, the loss in neutron yield either because of inefficient target cooling and / or due to presence of oxides layer on target surface, can be avoided and higher fluence rates may be achieved. This could be useful especially for IVNAA of those trace elements which have relatively low neutron capture cross-sections.

The work presented in this paper was performed by me under the supervision of Drs. Prestwich and McNeill. Dr. McNeill had many good suggestions for experimental set-up and data analysis. The manuscript was written by me and edited by Drs. Prestwich and McNeill.

(Reprinted from Appl. Radiat. Isot. 58(3), Aslam, W. V. Prestwich, F. E. McNeill, Lithium target performance evaluation for low energy accelerator-based in vivo measurements using gamma spectroscopy, 321-331, Copyright (2003), with permission from Elsevier)

PERGAMON

Applied Radiation and Isotopes 58 (2003) 321–331

Applied Radiation and Isotopes

www.elsevier.com/locate/apradiso

Lithium target performance evaluation for low-energy accelerator-based in vivo measurements using gamma spectroscopy

Aslam*, W.V. Prestwich, F.E. McNeill

Medical Physics and Applied Radiation Sciences Unit, McMaster University, Nuclear Research Building, Hamilton, ON, Canada L8S 4M1

Received 29 August 2002; received in revised form 21 October 2002; accepted 26 November 2002

Abstract

The operating conditions at McMaster KN Van de Graaf accelerator have been optimized to produce neutrons via the ^{7}Li(p, n)^{7}Be reaction for in vivo neutron activation analysis. In a number of earlier studies (development of an accelerator based system for in vivo neutron activation analysis measurements of manganese in humans, Ph.D. Thesis, McMaster University, Hamilton, ON, Canada; Appl. Radiat. Isot. 53 (2000) 657; in vivo measurement of some trace elements in human Bone, Ph.D. Thesis. McMaster University, Hamilton, ON, Canada), a significant discrepancy between the experimental and the calculated neutron doses has been pointed out. The hypotheses formulated in the above references to explain the deviation of the experimental results from analytical calculations, have been tested experimentally. The performance of the lithium target for neutron production has been evaluated by measuring the ^{7}Be activity produced as a result of (p, n) interaction with ^{7}Li. In contradiction to the formulated hypotheses, lithium target performance was found to be mainly affected by inefficient target cooling and the presence of oxides layer on target surface. An appropriate choice of these parameters resulted in neutron yields same as predicated by analytical calculations.

Keywords: Charged particle accelerator; Lithium target; Total neutron yield; Target thickness

1. Introduction

In vivo neutron activation analysis is a well-established clinical research technique used to measure the trace and major element content of the human body (Cohn, 1980, 1981; Sharafi et al., 1983; Chettle and Fremlin, 1984; Cohn and Parr, 1985; Beddoe and Hill, 1985; Scott and Chettle, 1986; Heymsfield et al., 1989; Pierson et al., 1990; Hill, 1990; Chettle et al., 1990; Heymsfield and Waki, 1991; Heymsfield et al., 1993; Sutcliffe, 1996; Morgan, 2000; Ellis, 2000). In order to develop a facility for such analyses at the McMaster KN Van de Graaf Accelerator, several projects were initiated during the last 10 years (Palerme, 1993; Pejović-Milić, 1998, 2001; Pejović-Milić et al., 1998, 2000; Arnold et al., 1999, 2000, 2002; Arnold, 2000). Low-energy fast neutrons at the facility are produced by bombarding protons on a thick lithium target using the ^{7}Li(p, n)^{7}Be reaction. Extensive modeling, simulation and experimental investigations have been performed for this purpose. However, it was found that the measured doses were significantly different from the calculated doses (Arnold, 2000; Pejović-Milić et al., 2000; Pejović-Milić, 2001). Such a deviation for lithium targets has also been reported at other research facilities, for instance, Yu et al. (1998) reported the measured neutron yields at $E_p = 1.885$ MeV lower by a factor of 2 in

*Corresponding autho
E-mail addresses:

comparison to calculated yields (C/E = 2) and Bleuel et al. (1999) reported a deviation of 1.6 (C/E = 1.6). In this paper, C/E refers to the ratio of the calculated to the experimental neutron yields.

Arnold (2000) has suggested a number of reasons to explain the discrepancy, for example, partial loss of proton beam current due to misalignment of the beam with the target, loss of target due to target melting at higher beam currents, error in theoretical cross-sections and stopping powers, or non-availability of charged particle cross-sections at the energies of interest. This situation motivated us to investigate the performance of the lithium targets used for neutron production. The investigation was also motivated by the possible further improvements in the use of the facility when running at higher beam currents than those currently in use.

This paper describes a simple method to evaluate thick lithium target performance. Section 2 describes the materials and methods used for testing the hypotheses formulated to explain the differences between the experimental and theoretical results in earlier studies. Methods of target preparation, the description of target holders and the method used for neutron yield measurement using the ^{7}Be activity produced as a result of (p, n) interaction are presented there. To compare the measured neutron yields with analytical calculations, two methods for the total neutron yield calculation using the differential and total (p, n) cross-sections are also described and compared with each other in this section. Section 3 presents the results of the comparison of calculated neutron yields at the corresponding proton energies with the measured total neutron yields under different operating conditions and target configurations.

2. Materials and methods

2.1. Neutron source

The 3 MV Van de Graaff accelerator at the McMaster University Accelerator Laboratory is used to produce low-energy fast neutrons of mean neutron energy less than 500 keV by bombarding protons on a thick lithium target. This facility can be operated at proton beam currents as low as a few nA (Aslam et al., 2001, 2002) up to 100 μA (Pejović-Milić, 2001).

2.1.1. Target preparation

Targets were prepared from solid 99.9% ^{7}Li metal or amorphous powder of ^{7}LiF salt. Targets of thickness down to 1 mm were prepared by putting a weighed amount of the target material into the target holder and then pressed to a pressure of 6895 kPa for ^{7}Li and 34474 kPa for ^{7}LiF. Targets of thickness less than 0.1 mm were prepared by vacuum deposition of target materials onto copper discs.

2.1.2. Target holders

Three different target holders were used for experimentation. One had a copper backing of 10 mm between the 2.5 mm diameter water coolant tubes and the target. In another, the target was placed in an aluminum cup providing a target backing of approximately 3 mm between the 12.5 mm wide (7.5 mm deep) water channel and target. The third target holder was designed to place the target at an angle of 45° to the beam direction. Effective target thickness in these cases was $\sqrt{2}$ times the actual physical target thickness. Targets prepared by vapor deposition were placed in these target holders. The targets were mounted on the end of a beam duct and were cooled with water to prevent heating by proton beam currents. The coolant average flow rate was 6.3×10^{-3} m^{3}. Coolant entrance temperature was approximately 10°C.

2.2. Thick target neutron yield calculations

Low-energy neutrons for many clinical applications are produced by low-energy charged particle-induced reactions with low mass number targets using charged particles accelerators. Lithium targets using the ^{7}Li(p, n)^{7}Be reaction are widely used as a low-energy neutron source for clinical applications in BNCT (Wang et al., 1985; Yanch et al., 1992; Allen and Benyon, 1995, Zhou and Lee, 1997a, b; Magagula and Watterson, 1998; Bayanov et al., 1998; Powell et al., 1999; Lee and Zhou, 1999), BNCEFNT (Pignol et al., 1998), BNCS (Gierga et al., 2000a, b), in vivo neutron activation measurements (Palerme, 1993; Pejović-Milić, 1998; Arnold, 2000; Arnold et al., 1999, 2000, Pejović-Milić et al., 2000) and in radiobiological experiments (Endo et al., 1995; Schmid et al., 2000, 2002). The total neutron yield of lithium and its compounds for (p, n) interaction at a given beam energy was calculated first by integrating the neutron energy spectrum and the angular distribution of the neutrons obtained through the reported differential (p, n) cross-sections and second through thick target formula using the reported total (p, n) cross-sections. These calculations were aimed at the investigation of the hypotheses and further to provide a comparison of the measured yields with those analytical calculations.

The neutron energy spectrum and angular distribution of the neutrons in the near threshold region of 1.88–1.93 MeV were calculated using the Breit–Wigner approximation to avoid singularities (Ritchie, 1976; Meadows, 1977; Kononov et al., 1977; Lee and Zhou, 1999) and the reported measured cross-sections (Liskien and Paulsen, 1975) were employed above this region. Our calculations are briefly summarized here.

The number of neutrons produced from an element of target of thickness dx (corresponding to an energy loss of dE_p in thickness dx) emitted at angle θ into

an element of solid angle $d\Omega$ per incident proton is given by

$$\frac{d^2 Y(E_n,\theta)}{d\Omega\, dE_n} = \frac{n_T}{e}\frac{d\sigma}{d\Omega'}\frac{d\Omega'}{d\Omega}\frac{1}{S(E_p)}\frac{dE_p}{dE_n}, \quad (1)$$

where n_T is the lithium target atomic density, dE_n refers to the width of the neutron spectrum because of the thickness dx (or dE_p), and dE_p/dE_n was calculated from the Q-value equation (Ritchie, 1976; Lee and Zhou, 1999; Arnold, 2000). The differential cross-section in the c.m., $d\sigma/d\Omega'$, were taken from the compilations of (p, n) cross-section data for ^{7}Li (Liskien and Paulsen, 1975) and the stopping powers, $S(E_p)$, for ^{7}Li and ^{7}LiF were taken from Janni (1982) compilations.

The spectrum of the neutrons produced as a result of bombardment of a unidirectional proton beam on a thick lithium target was calculated by assuming the thick target to consist of several thin targets each of thickness dx, with decreasing incident proton energies, ranging from the incident beam energy, E_p, down to the E_{th}. The generated spectrum was finally integrated over the solid angle and the neutron energy range to get the total neutron yield.

However, the thick target total neutron yield was also calculated by another approach using the well-known thick target yield formula which could be obtained from Eq. (1) as

$$Y(E_p) = \int_{E_n}\int_{\Omega}\frac{d^2 Y(E_n,\theta)}{d\Omega\, dE_n}d\Omega\, dE_n = \frac{n_T}{e}\int_{E_p}\frac{1}{S(E_{p'})}\left[\int_{\Omega}\frac{d\sigma}{d\Omega'}\frac{d\Omega'}{d\Omega}d\Omega\right]dE_{p'}, \quad (2)$$

$$Y(E_p) = \frac{n_T}{e}\int_{E_{th}}^{E_p}\frac{\sigma(E_{p'})}{S(E_{p'})}dE_{p'}. \quad (3)$$

To estimate the total neutron yield as a function of incident proton beam energy, E_p, the total (p, n) cross-section, $\sigma(E_p)$, for ^{7}Li was taken from the charged particle cross-sections compiled by Kim et al. (1966). The integral in (3) was evaluated by cubic spline integration (Press et al., 1992).

2.3. *Li target performance evaluation*

Target performance was evaluated using proton activation. The neutrons at the activation facility are produced via the ^{7}Li(p, n)^{7}Be reaction. Thus, the activity of the ^{7}Be ($T_{1/2}$ = 53.4 day and E_γ = 478 keV) in the target determined using calibrated NaI(Tl) and HPGe detectors provides a direct and absolute measurement of the number of neutrons produced. Using the observed rate of emitted gamma rays corrected for detector efficiency, absorption in the target holder and the known branching ratio for 478 keV gamma rays (10.52%), the total number of neutrons produced in a run was determined. The measured neutron yields were corrected for background by measuring the ^{7}Be activity prior to the irradiation of the target in the same target-geometry conditions.

2.3.1. *Distribution of ^{7}Be activity*

The target diameter of the pellets formed by pressing was approximately 1.6 cm, while the diameter of the typical target formed by vapor deposition was approximately 2.5 cm. The distribution of the ^{7}Be activity in the target produced as a result of (p, n) interaction depends upon the shape of proton beam. Although no direct effort was made to measure the diameter of the proton beam, a slight change in the color of the target material was observed as a result of beam exposure. Thus, the exposed area of the target determined from the change in color was taken as the area in which ^{7}Be activity was distributed. This area appeared approximately circular in shape with a diameter of $\sim$1 cm. However, the maximum depth of ^{7}Be in the target should be limited to the range of the protons for (p, n) interaction. This range as shown in the next section is limited to $\sim$50 μm for E_p = 2.25 MeV and $\sim$100 μm for E_p = 2.5 MeV. These ranges are much smaller for ^{7}LiF targets. Thus, the ratio of the radial to lateral dimensions of the ^{7}Be gamma source was greater than 100 for the range of proton energies we are interested in. Hence for the practical purposes of the activity measurements, the source was assumed to be a plane circular disk source instead of a volumetric disk source. The amount of activity produced depended upon the beam energy and the amount of proton charge bombarded on the target. The ^{7}Be activity varied from a fraction of a μCi to tens of μCi depending upon the nature of the experiment.

2.3.2. *Detector efficiency*

In order to measure the ^{7}Be activity prior knowledge of the full energy peak efficiency of the detector was required.

2.3.3. *NaI(Tl) detector*

The calculated absolute efficiency of the 76.2 mm × 76.2 mm NaI(Tl) detector was used to determine the ^{7}Be activity. The efficiency of the detector as a function of distance in the range of 10–50 cm was calculated by generating the response function for E_γ = 478 keV using the photon mode of the Monte Carlo radiation transport code MCNP4B (Briesmeister, 1997). This was obtained by modeling the detector as a bare cylinder of NaI with a circular disk source at some distance along the cylinder's axis emitting monoenergetic gamma rays isotropically inside a solid angle with its vertex on the source and its base on the detector's front side. The Gaussian energy broadening parameter for the MCNP pulse height tally (F8) was used to represent the experimentally measured resolution of the

form FWHM (MeV) = 0.075 $E_\gamma^{1/2}$, with the pulse height tallied according to a Gaussian distribution about the energy E_γ.

The generated response of the NaI detector for a disk source emitting 478 keV γ-rays isotropically is shown in Fig. 1. The calculated absolute efficiencies shown in Fig. 2 agree fairly well, within 1%, with those of analytical calculations available for an idealized bare detector at 3 and 10 cms in Crouthamel (1970). However, when the efficiency was measured for the closest energy source available ^{137}Cs (E_γ = 662 keV), the measured efficiency at source–detector distances ranging from 10 to 50 cm was found to be approximately 30% lower than those calculated at the same energy for a bare NaI detector. When the aluminum cladding of 2 mm was included in the model, the results improved by ~11% but still a difference of around 20% persisted. The modeling of detectors using Monte Carlo method encounters problems due to the insufficiency of accurate detector parameters available from the manufacturer (Rogers, 1982; Ewa et al., 2001).

2.3.4. HPGE detector

In a few cases, the ^{7}Be activity was also measured using a calibrated HPGe detector. Because of the wide range of gamma-ray energies produced in the decay scheme of National Bureau of Standards reference source, ^{152}Eu was used to calculate the efficiency of the detector (Knoll, 1989).

2.4. Sources of uncertainty

The overall uncertainty of the measured yields was estimated by analyzing the propagation of uncertainty through the various steps of the measurement. There were three sources of error in our measurements: the uncertainty in proton beam current, the inherent counting statistics, and the detector efficiency. The proton beam was used as a reference to compare the performance of targets under different conditions. In those cases where targets were exposed to low beam currents, long exposure times to beams were chosen in order to measure the ^{7}Be activity in a reasonable time with sufficient counting precision (~1%). The measured detector efficiency of NaI(Tl) closest to the energy of interest was found to be ~20% lower than the calculated one. Such a discrepancy has also been reported in literature for lower energies (Steyne et al., 1971; Berger and Seltzer, 1972; Nardi, 1970; Rogers, 1982).

Consequently, we estimate the experimental error conservatively at ±25–30%.

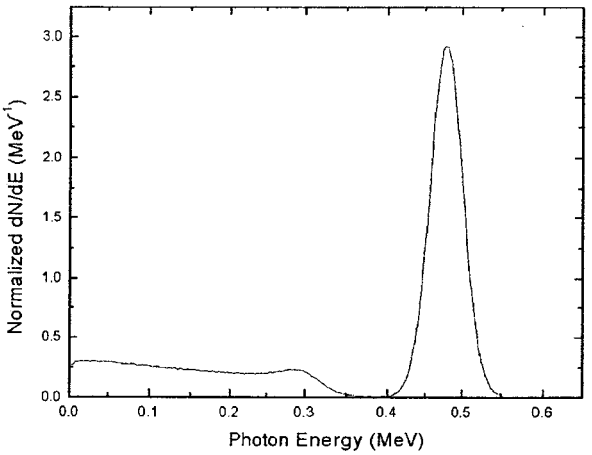

Fig. 1. Monte Carlo calculated response function of 3″ × 3″ NaI(Tl) detector.

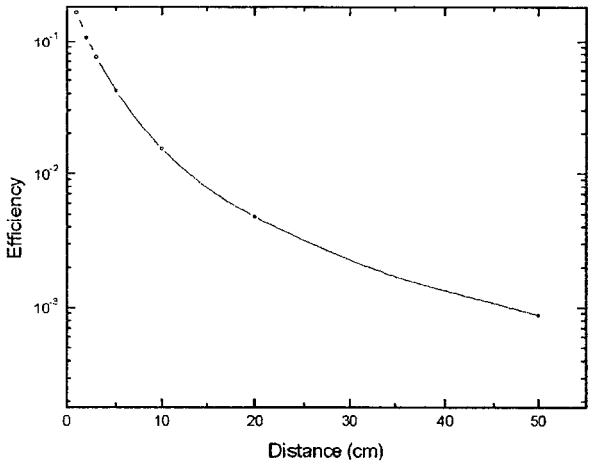

Fig. 2. Calculated NaI(Tl) detector efficiency as a function of distance.

3. Results and discussion

3.1. Target thickness

The smallest proton beam energy at which the ^{7}Li(p, n)^{7}Be interaction can take place is E_{th} = 1.88 MeV, i.e., no neutrons are produced in lithium or its compounds for $E_p < E_{th}$. Thus a lithium target thick enough to slow the proton beam energy, E_p, down to E_{th}, can be used to produce neutrons without any loss of yield, however, the remaining beam energy instead would be deposited in the target backing material. The target thickness, $T_{th}(E_p)$, required to slow the proton beam of incident energy E_p to below E_{th} was calculated by using the definition of stopping power as

$$T_{th}(E_p) = \int_{E_{th}}^{E_p} \frac{dE}{S(E)} \quad (4)$$

which was simplified to

$$T_{th}(E_p) = \int_0^{E_p} \frac{dE}{S(E)} - \int_0^{E_{th}} \frac{dE}{S(E)} = R(E_p) - R(E_{th}), \quad (5)$$

where $R(E_p)$and $R(E_{th})$ are the ranges of proton at the incident and threshold proton energies in the target material. The ranges of protons for ^{7}Li and ^{7}LiF target materials have been taken from Janni (1982) and cubic spline interpolation was used to get the intermediate values. The calculated target thickness for ^{7}Li metal and its compound ^{7}LiF target are given in Table 1. Because of the larger stopping power in ^{7}LiF, the proton range in ^{7}LiF is smaller than in the ^{7}Li target.

3.2. Total neutron yield

The yields calculated by the two approaches discussed in Section 2.2 have been presented in Table 2. These calculations. for $E_p \geq 2.00$ MeV agree fairly well, as the difference ($\leq 5\%$) lies within the overall uncertainty involved in these calculations. However, at $E_p = 1.95$ MeV, the difference is around 13%. Although the total cross-sections for the (p, n) interaction below 1.95 MeV are available (Kim et al., 1966), the differential cross-sections for (p, n) are available only for $E_p \geq 1.95$ MeV (Liskien and Paulsen, 1975). Moreover, the Jacobians based on measured cross-sections data, produce infinities close to the reaction threshold to calculate thick target neutron yields (Lee and Zhou, 1999). This is the region, $1.88 \leq E_p \leq 1.95$ MeV, where the Breit–Wigner approximation was used to represent the differential cross-section for the calculation of total neutron yield (Ritchie, 1976; Lee and Zhou, 1999).

Table 1
Target thickness for natural lithium metal and ^{7}LiF targets

Proton energy (MeV)	Thickness of target (μm)	
	^{7}Li Metal	^{7}LiF
1.89	1.33	0.30
1.95	9.43	2.13
2.00	16.32	3.69
2.05	23.35	5.27
2.10	30.52	6.89
2.15	37.81	8.53
2.20	45.24	10.20
2.25	52.79	11.89
2.30	60.48	13.62
2.35	68.30	15.37
2.40	76.25	17.15
2.45	84.33	18.96
2.50	92.53	20.79

These thicknesses are sufficient to reduce the incident beam energy to E_{th}. ^{7}LiF and other lithium compounds reduce the beam energy much faster than ^{7}Li.

Table 2
Total neutron yields for ^{7}Li metal and ^{7}LiF targets

Proton energy (MeV)	Total neutron yield (n/μC) × 10^7		
	^{7}Li Metal		^{7}LiF
	(Eq. (3))	(Eq. (1))	(Eq. (3))
1.89	0.41		0.12
1.95	5.99	6.8	1.77
2.00	11.0	11.6	3.23
2.05	16.1	16.7	4.74
2.10	21.7	22.0	6.39
2.15	28.4	28.6	8.34
2.20	36.8	37.1	10.8
2.25	47.7	47.7	14.0
2.30	59.1	58.8	17.4
2.35	69.1	68.0	20.3
2.40	77.6	75.8	22.7
2.45	85.1	82.6	24.9
2.50	92.3	89.0	27.0

The total neutron yields for ^{7}Li metal calculated by using differential (Eq. (1)) and total (p, n) cross-sections (Eq. (3)) are in fairly good agreement within 5% above $E_p = 2.00$ MeV. Total neutron yields for ^{7}LiF targets at all beam energies are smaller than that of ^{7}Li. Proton ranges and the neutron yields for ^{7}LiF and other lithium compounds are lower than those of ^{7}Li. The loss in neutron yield because of the presence of oxides layer on a ^{7}Li target depends on the composition (LiH, LiOH, Li_2O) and the thickness of the layer. Maximum loss in neutron yield would be observed when the thickness of oxides layer develops to the proton range at a given energy.

However, Lee and Zhou is in much better agreement with the approach based on total cross-section (5%). Our values agree within 1–2% with those of Lee and Zhou above $E_p \geq 2.10$ MeV and 3–4% above $E_p \geq 1.95$ MeV. At 1.95 MeV, our value agrees with that of Lee and Zhou within 9%, although we have followed the same approach as discussed by Lee and Zhou (1999).

The total neutron yields calculated for ^{7}LiF have also been presented in Table 2 for comparison. These neutron yields are lower than for a lithium metal target at the same beam energies. This is due to the larger stopping powers and also the lower lithium atomic density (n_T) for ^{7}LiF that appear in denominator and numerator respectively of Eqs. (1) and (3). This also happens for other lithium compounds. Thus when a lithium target that has oxides layer (Li_2O, LiH and LiOH) on the surface, formed during the exposure to air, is used for neutron production, lower neutron yields are obtained in comparison to a pure lithium target having no oxides layer on the surface. The loss in neutron yield depends upon the thickness of the oxides layer formed on the target surface, which in turn depends upon the exposure time as shown in Section 3.5.3.

3.3. Target melting or evaporation

3.3.1. Below (p, n) threshold energy

The linearity of the reaction rate occurring in the target with the measured proton current at a given proton energy was verified by measuring the inelastic gamma ray yield (Aslam et al., 2002) with the same target as used by other investigators (Pejović-Milić et al., 2000; Arnold, 2000; Arnold et al., 2002; Pejović-Milić, 2001). Before exposure, a calibrated NaI(Tl) spectrometer was used to measure the background which is mainly due the ^{7}Be activity which also emits the 478 keV line. The background was subtracted from the collected online spectrum to find the area under the 478 keV peak. At $E_p = 1.6$ MeV, the beam current was varied ranging from 1.5 to 25 μA and the resulting gamma spectrum was collected. The distance between the counter and the target was chosen to keep the detector dead time well below 5% in the entire range of beam current. We have observed a linear increase in count rate with the beam current as shown in Fig. 3, thus confirming the insignificant evaporation of target for beam currents less than 25 μA. This is in contradiction to that hypothesized (Arnold, 2000) as an explanation of the difference between the calculated and the measured neutron doses and for the reduced neutron yields from lithium targets.

3.3.2. Above (p, n) threshold energy

A locally designed long counter was used to confirm the linearity of the (p, n) reaction rate with the beam current.

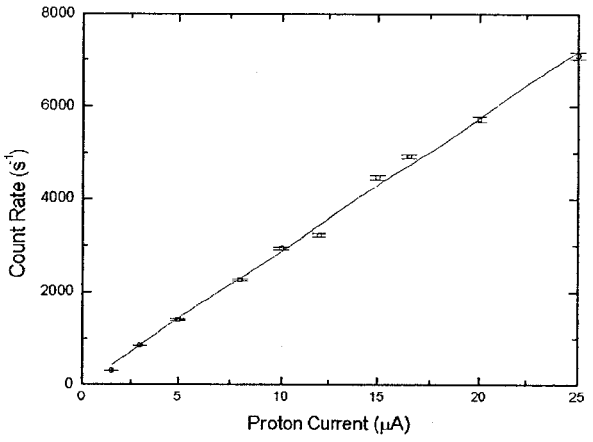

Fig. 3. Linearity of reaction rate of inelastically scattered gamma rays with the measured proton current at a beam energy of 1.6 MeV. The gamma yield was measured in the beam direction. Error bars show only the statistical uncertainty in measured counts and not the overall uncertainty in measured counts.

Table 3
Effect of electron suppression by using ~2 mm thick ^{7}Li metal target

	Count rate (CPS)
Cage	7452
Magnet	7181
No electron supp.	7696

The background was measured as 8.33 CPS at a distance of 50 cm. Proton energy was chosen to be 1.7 MeV and the beam current was 2 μA.

3.4. Effect of electron suppression

This set of experiments was aimed at studying the effect of electron suppression by first putting the target in a cage, which was connected to −300 V and second by putting a magnet around the beam. No significant variation in γ-ray yield was observed within 10%. Either neither of the two techniques was able to suppress electrons in the target or electron suppression does not have significant impact on current measurement in the energy range we studied. Results have been given in Table 3.

3.5. Neutron yield measurements

3.5.1. Effect of target thickness

This set of experiments was performed to study the effect of ^{7}Li target thickness on the neutron yields. Each target was exposed to a beam energy of 2.25 MeV. Fluence rates during the course of exposure were monitored using a locally designed long counter. No appreciable change in fluence rate was observed (~1%).

The results of this set of experiments presented in Table 4 shows an increasing trend in neutron yield with the decrease in target thickness and the measured neutron yield of target thickness less than 100 μm was found to be in good agreement within experimental uncertainty of that from analytical calculations (see Table 2). The improvement in the neutron yield as a result of reduction in target thickness, target backing thickness and the use of wider coolant channels is attributed to the improvement in the removal of heat from the target that is deposited by the proton beam. Targets of thickness ~0.5 mm were also tested but no appreciable change in the C/E was observed (results have not been included in Table 4). However, when we tested the target of thickness 100 μm prepared by vapor deposition, we observed an improvement in neutron yield. This further improvement in neutron yield was attributed to the absence of oxides layer on the target surface as the target material was evaporated on the target backing using vacuum deposition. This could be justified as oxides have a higher melting point than

lithium and any oxides present in the target material were left in the evaporating dish because of the higher melting point and only lithium metal was deposited on the backing material.

The first result in Table 4 refers to the same old target as used by other investigators (Pejović-Milić et al., 2000; Arnold, 2000; Pejović-Milić, 2001). Using this target, Arnold (2000) reported the dose equivalents as a function of incident proton energy in the energy range $2.00 \leqslant E_p \leqslant 2.25$ MeV with a $1/2''$ diameter spherical tissue-equivalent proportional counter simulating 2 μm diameter tissue at a distance of 50 cm from target in bare beam conditions. Taking into account the energy dependence of the counter's response and the corrections made in MCNP model used for dose calculations, the C/E for the reported measurements at $E_p = 2.25$ MeV was estimated as 8.7. This C/E is in close agreement within the experimental uncertainty with that reported in this work (C/E = 7.01). This gives us a confidence in the methodology adopted to evaluate the target performance.

3.5.2. Effect of target cooling

The results of the study of inefficient target cooling on neutron yields are presented in Table 5. Targets placed in aluminum target holders were exposed to beam with and without turning the target cooling on. To avoid any possible target evaporation in the absence of target cooling, the targets were exposed to very low beam currents. The target physically appeared to be the same as it was before exposure even in the absence of a cooling system. The measured neutron yield with this target without cooling the target is comparable to 1 cm thick target (presented in 1st row of Table 4), which was water-cooled. The results for the 1 cm thick target presented in Table 4 have also been provided in Table 5 for the sake of comparison. It can be inferred from this Table that the target cooling in the case of a 1 cm thick target with a 1 cm target backing was as inefficient as in the case of a 3 mm thick target with a 3 mm target backing without target cooling. The conclusion was further validated when the same target with aluminum backing was exposed to beam with target cooling on and an improved C/E was observed (see last row Table 5). The results presented in Table 5 are also in confirmation with the conclusion drawn from Table 4 that an increasing trend in neutron yield with the reduction in target and backing thickness (thus an improved heat removal from the target) was observed.

3.5.3. Effect of oxides layer

The effect of the presence of oxides layer on the target surface was studied using the same 3 mm thick ^{7}Li metal target whose measured neutron yield is given in Table 4 (second row). The target was placed in open air for 24 h and the neutron yield was then measured. These

Table 4
Comparison of neutron yields for different Li metal target thicknesses at $E_p = 2.25$ MeV

Beam current (μA)	Thickness (mm)		TT/MT	Neutron yield (n/μC) × 10^7	C/E
	Target	Backing			
28	10	10 mm Cu	200	6.8	7.0
25	3	10 mm Cu	60	18.0	2.7
0.1	1	3 mm Al	20	31.6	1.5
2 (for 2 h) & 10 (for 1 h)	~0.1	1 mm Cu		65.4	0.7

Background corrected counts under 478 keV peak were used to calculate the total neutron yields. C/E refers to the ratio of calculated to the measured neutron yields and TT/MT refers to the ratio of target thickness to minimum target thickness.

Table 5
Effect of target cooling studied at $E_p = 2.25$ MeV

Beam current (μA)	Thickness (mm)		TT/MT	Neutron yield (n/μC) × 10^7	C/E	Parameter
	Target	Backing				
28	10	10	200	6.8	7.0	With cooling
2	3	3	60	6.0	7.9	Without cooling
25	3	3	60	18.0	2.7	With cooling

C/E refers to the ratio of calculated to the measured neutron yields and TT/MT refers to the ratio of target thickness to minimum target thickness.

measurements have been summarized in Table 6. The neutron yield as expected dropped from 18×10^7 n/μC (Table 6; first row third column) to 7×10^7 n/μC (Table 6; second row third column) as a result of the formation of oxides layer on the target surface. However, when the target surface was scratched to remove the oxides layer, the measured neutron yield was the same as before the exposure (within the experimental uncertainty). Thus, the loss in neutron yield as expected was dependent on the thickness of oxides layer as well as on the exposure time to air. Longer exposure to air resulted in a larger thickness of the oxides layer on the target surface. Thus a careful handing of ^{7}Li metal target is always needed; precautionary measures should always be taken if the target needs to be exposed to open atmosphere.

3.5.4. Neutron yield measurements using ^{7}Li compounds

This set of experiments was performed to examine the compounds of lithium for neutron production. Table 7 summarizes the effect of ^{7}LiF target thickness on neutron yields. We observed a similar increasing trend in the neutron yield with the decrease in target thickness and the increase in coolant channel widths as in the case of lithium metal targets (see Table 4). The improved agreement (smaller C/E) in results could be because of the higher melting point of ^{7}LiF as compared to ^{7}Li metal target. The conclusions drawn through a series of experiments presented in Tables 4, 5 and 7 were further enhanced by results presented in Table 8 which again clearly emphasize the need of improvement of the cooling system and the use of an optimized target thickness.

Table 6
Effect of oxides layer on neutron yields studied at $E_p = 2.25$ MeV

Beam current (μA)	Neutron yield (n/μC) × 10^7	C/E	Parameter
25	7.4	6.4	Exposed to open air
25	17.4	2.7	Scratched to remove oxides layer

C/E refers to the ratio of calculated to the measured neutron yields.

3.5.5. Neutron yield measurements at different clinical facilities

A comparison of ^{7}Li metal target neutron yield measurements at different facilities developed for clinical applications is presented in Table 9.

First row in Table 9 lists the deviation (C/E) of the measured neutron yield reported by Yu et al. (1998) for a lithium metal target of thickness 1.2 mm at $E_p = 1.885$ MeV. Although the deviation could be different at different beam energies because of the change in the range with proton energy (larger yield loss at lower proton energies as compared to higher proton energies); C/E in this work (see third row in Table 4) at $E_p = 2.25$ MeV with a target thickness of 1 mm matches that of Yu et al. within 25%. Yu et al. have not provided any explanation for the loss in yield; however, it could be attributed to the presence of oxides layer if the cooling system was sufficient to remove the deposited heat from the target.

In another study at the LBNL cyclotron, Bleuel et al. (1999) reported the total number of neutrons produced during operation as 1.87×10^{13} neutrons from irradiation of a 100 μm thick ^{7}Li metal target for more than an hour with 9.6 μA proton beam at $E_p = 2.5$ MeV. This results in the total neutron yield per unit charge onto lithium as 54×10^7 n/μC, whereas the calculated neutron yield energy at the same energy is 89×10^7 n/μC (see Table 2), the ratio came out to be 1.65 (see second row in Table 9). Possible reason for the deviation may be inefficient cooling as the target was prepared by vapor deposition (so no oxides layer existed on the target surface).

The third row in the Table 9 lists the same results presented in Table 4 (see fourth row). This optimum yield was achieved by optimizing target thickness, target backing, target cooling and by avoiding the formation of oxides layer on the target surface.

Table 7
Effect of target thickness for ^{7}LiF targets observed at $E_p = 2.25$ MeV

Beam current (μA)	Thickness (mm)		TT/MT	Neutron yield (n/μC) × 10^7	C/E
	Target	Backing			
30	10	10 mm Cu	1000	6.3	2.2
0.1	0.6	10 mm Al	60	11.3	1.2

Background corrected counts under 478 keV peak were used to calculate the total neutron yields. C/E refers to the ratio of calculated to the measured neutron yields and TT/MT refers to the ratio of target thickness to minimum target thickness.

Table 8
Effect of target cooling on ^{7}LiF targets studied at $E_p = 2.25$ MeV

Beam current (μA)	Target thickness (mm)	TT/MT	Neutron yield (n/μC) × 10^7	C/E	Parameter
0.1	0.6	60	11.3	1.2	With cooling
2	1.7	170	2.2	6.4	Without cooling

C/E refers to the ratio of calculated to the measured neutron yields and TT/MT refers to the ratio of target thickness to minimum target thickness.

Table 9
Comparison of ^{7}Li metal target neutron yield measurements at different facilities

Facility	Year reported	Energy (MeV)	Current (μA)	Thickness (mm)		Measurement	C/E
				Target	Backing	Method	
Peking University	1998	1.885	—	1.2	—	Long counter	2
LBNL	1999	2.5	10	0.1	6.3	HPGe	~1.6
McMaster University	2000–2001	2.25	10	~0.1	1	HPGe	0.7

Peking University result refers to that reported by Yu et al. (1998) and LBNL refers to that reported by Bluel et al. (1999). In the case of Yu et al., no mention was made about the uncertainty in experimental results. Although target cooling is mandatory in case of ^{7}Li metal targets, no information is available about the target cooling and also about the beam diameter for Peking University beam. However, in the case of LBNL (Bluel et al., 1999), the target diameter was 7.62 cm. In this work the target diameter was ~3 cm and beam diameter was around 1 cm.

4. Conclusions

The main aim of the study was to improve the lithium target performance for neutron production via the ^{7}Li(p, n)^{7}Be reaction used frequently in the in vivo neutron activation facility at McMaster University. The target performance was monitored using a simple method based on gamma spectroscopy.

The following conclusions can be drawn from this work:

- The lithium target performance was found to be affected mainly by inefficient target cooling and the presence of oxides layer on the target surface.
- Improvements in target cooling were achieved by using reduced target thickness, a reduction in target backing thickness and wider coolant channel widths.
- The formation of oxides layer on the target surface was avoided by preparing targets using vapor deposition.
- Using the reported differential and total cross-sections for the (p, n) interaction and stopping powers in lithium, close agreement was found in calculated neutron yields to within 5% above $E_p = 2.00$ MeV. It was also shown through a series of experiments that the theoretically predicted neutron yields could be achieved by an appropriate choice of parameters affecting the target performance.
- We have not observed any non-linear variation of reaction rate with the measured proton current signal either below the (p, n) threshold energy or above the (p, n) threshold. A locally designed long counter was used to monitor the time dependent variations in neutron fluence rate. In the beam current ranging from few nA to 30 μA, no appreciable drop in fluence rate was observed confirming the insignificant evaporation of the lithium as a result of exposure.
- The integrated proton beam current on the target was used as a reference rather than the beam current directly readable from the ammeter. This improved the precision of current measurement. However, at least within experimental limits, we could not observe any appreciable effect of electron suppression in our measurements of current, which limits the accuracy of current measurement.

Future work includes the upgrading of the facility to run at higher beam currents (a few hundred μA) than those currently in use. This will extend the use of facility for those applications of in vivo neutron activation where the use of higher beam currents has been proposed (Pejović-Milić, 2001). Targets prepared by vapor deposition will be tested for higher beam currents. This will need an enhanced heat removal rate from the target using an increased coolant flow rate and the wider beam area.

References

Allen, D.A., Benyon, T.D., 1995. A design study for an accelerator-based epithermal neutron beam for BNCT. Phys. Med. Biol. 40, 807–821.

Arnold, M.L., 2000. Development of an accelerator based system for in-vivo neutron activation analysis measurements of manganese in humans, Ph.D. Thesis, McMaster University, Hamilton, ON, Canada.

Arnold, M.L., McNeill, F.E., Chettle, D.R., 1999. The feasibility of measuring manganese concentrations in human liver using neutron activation analysis. NeuroToxicology 20 (2-3), 407–412.

Arnold, M.L., McNeill, F.E., Prestwich, W.V., Chettle, D.R., 2000. System design for in-vivo neutron activation analysis measurements of manganese in the human brain: based on Monte Carlo Modeling. Appl. Radiat. Isot. 53, 651–656.

Arnold, M.L., McNeill, F.E., Stronach, I.M, Pejović-Milić, A., Chettle, D.R., Waker, A.J., 2002. An accelerator based system for in-vivo neutron activation analysis measurements of manganese in human hand bones. Med. Phys. 29 (11), 2718–2724.

Aslam, Prestwich, W.V., McNeill, F.E., Waker, A.J., 2001. Spectrometry and dosimetry for low energy accelerator based in-vivo measurements, Annual Report McMaster Accelerator Laboratory, McMaster University, Hamilton, ON, Canada.

Aslam, Prestwich, W.V., McNeill, F.E., 2002. Thin target $^{7}Li(p,p'\gamma)^{7}Li$ inelastic gamma ray yield measurements, J. Radioanal. Nucl. Chem. 254(3), 533–544.

Bayanov, B.F., Belov, V.P., Bender, E.D., Bokhovko, M.V., Dimov, G.I., Kononov, V.N., Kononov, O.E., Kuksanov, N.K., Palchikov, V.E., Pivovarov, V.A., Salimov, R.A., Silvestrov, G.I., Skrinsky, A.N., Soloviov, N.A., Taskaev, S.Yu, 1998. Accelerator-based neutron source for the neutron-capture and fast neutron therapy at hospital. Nucl. Inst. Meth. Phys. Res. A 413 (2-3), 397–426.

Beddoe, A.H., Hill, G.L., 1985. Clinical measurement of body composition using in-vivo neutron activation analysis. JPEN J. Parenter. Enteral. Nutr. 9 (4), 504–520.

Berger, M.J., Seltzer, S.M., 1972. Response function for sodium iodide scintillation detectors. Nucl. Inst. Meth. 104, 317–332.

Bleuel, D.L., Chu, W.T., Donahue, R.J., Ludewigt, B.A., McDonald, R.J., Smith, A.R., Stone, N.A., Vujic, J., 1999. Initial Experimental verification of the neutron beam modeling for the LBNL BNCT facility, in: Application of Accelerators in Research and Industry, Proceedings of the Fifteenth International Conference, November 4–7, 1998, Denton, Texas; AIP Conf. Proc. 475 (Part 21) 1050–1055.

Briesmeister, J.F. (Ed.), 1997. MCNP: A General Monte Carlo N-Particle Transport Code, Version 4B, LA-12625-M, Los Alamos, USA.

Chettle, D.R., Fremlin, J.H., 1984. Techniques of in vivo neutron activation analysis. Phys. Med. Biol. 29 (9), 1011–1043.

Chettle, D.R., Armstrong, R., Todd, A.C., Franklin, D.M., Scott, M.C., Somervaille, L.J., 1990. Measurements of trace elements in-vivo. Basic Life Sci. 55, 247–257.

Cohn, S.H., 1980. The present state of in-vivo neutron activation analysis in clinical diagnosis, and therapy. At. Energy Rev. 18 (3), 599–660.

Cohn, S.H., 1981. In-vivo neutron activation analysis: state of the art and future prospects. Med. Phys. 8 (2), 145–154.

Cohn, S.H., Parr, R.M., 1985. Nuclear-based techniques for the in-vivo study of human body composition. Report of an advisory group of the international atomic energy agency. Clin. Phys. Physiol. Meas. 6 (4), 275–301.

Crouthamel, C.E., 1970. In: Adams, F., Dams, R. (Eds.), Applied Gamma-ray Spectrometry, 2nd Edition. Pergamon Press, Oxford, New York.

Endo, S., Hoshi, M., Tauchi, H., Takeoka, S., Kitagawa, K., Suga, S., Meada, N., Komatsu, K., Sawada, S., Iwamoto, E., Sakamoto, S., Takeyama, K., Omura, M., 1995. Neutron generator at Hiroshima University for use in radiobiology study. J. Radiat. Res. 36, 91–102.

Ellis, K.J., 2000. Human body composition: in vivo methods. Physiol. Rev. 80 (2), 649–680.

Ewa, I.O.B., Bodizs, D., Czifrus, S., Molnar, Z., 2001. Monte carlo determination of full energy peak efficiency for a HPGE detector. Appl. Radiat. Isot. 55 (1), 103–108.

Gierga, D.P., Yanch, J.C., Shefer, R.E., 2000a. An investigation of the feasibility of gadolinium for neutron capture synovectomy. Med. Phys. 27 (7), 1685–1692.

Gierga, D.P., Yanch, J.C., Shefer, R.E., 2000b. Development and construction of a neutron beam line for accelerator-based boron neutron capture synovectomy. Med. Phys. 27 (1), 203–214.

Heymsfield, S.B., Waki, M., 1991. Body composition in humans: advances in the development of multicompartment chemical models. Nutr. Rev. 49 (4), 97–108.

Heymsfield, S.B., Wang, J., Lichtman, S., Kamen, Y., Kehayias, J., Pierson Jr., R.N., 1989. Body composition in elderly subjects: a critical appraisal of clinical methodology. Am. J. Clin. Nutr. 50 (Suppl. 5) 1167–75, 1231–1235.

Heymsfield, S.B., Wang, Z., Baumgartner, R.N., Dilmanian, F.A., Ma, R., Yasumura, .S., 1993. Body composition and aging: a study by in-vivo neutron activation analysis. J. Nutr. 123 (Suppl. 2), 432–437.

Hill, G.L., 1990. Clinical body composition using in-vivo neutron activation analysis. Infusionstherapie. 17 (Suppl. 3), 18–20.

Janni, J.F., 1982. Proton range-energy tables, 1 keV–10 GeV. At. Data Nucl. Data Tables 27, 147.

Kim, H.J., Milner, W.T., McGowan, F.K., 1966. Nuclear Cross-Sections for Charged-Particle Induced Reactions, Section A, Nucl. Data Tables Vol. 1, No. 3&4, Academic Press, New York & London.

Knoll, G.F., 1989. Radiation Detection and Measurement. Wiley, New York.

Kononov, V.N., Poletaev, E.D., Yurlov, B.D., 1977. Absolute yield and spectrum of neutrons from the $^{7}Li(p, n)^{7}Be$. At. Energy 43, 947–949.

Lee, C.L., Zhou, X.L., 1999. Thick target neutron yields for the $^{7}Li(p, n)^{7}Be$ reaction near threshold. Nucl. Inst. Meth. Phys. Res. B 152, 1–11.

Liskien, H., Paulsen, A., 1975. Neutron production cross-sections and energies for the reactions $^{7}Li(p, n)^{7}Be$ and $^{7}Li(p, n)^{7}Be^{*}$. At. Data Nucl. Data Tables 15, 57–84.

Magagula, T.K., Watterson, J.W., 1998. The excitation of isomeric states by accelerator neutrons from the $^{7}Li(p, n)^{7}Be$ reaction and their application in selective activation analysis. Nucl. Inst. Meth. Phys. Res. B 139, 293–297.

Meadows, J.W., 1977. Determination of the Energy Scale for Neutron Cross-section Measurements Employing a Monoenergetic Accelerator, ANL/TDM-25.

Morgan, W.D., 2000. Of mermaids and mountains. Three decades of prompt activation in-vivo. Ann. N. Y. Acad. Sci. 904, 128–133.

Nardi, E., 1970. A note on Monte Carlo calculations in NaI crystals. Nucl. Inst. Meth. 83, 331–332.

Pejović-Milić, A., 1998. An accelerator-based in-vivo measurement of aluminum in human bone by neutron activation analysis, M.Sc. Thesis. McMaster University, Hamilton, ON, Canada.

Pejović-Milić, A., 2001. in-vivo measurement of some trace elements in human bone, Ph.D. Thesis. McMaster University, Hamilton, ON, Canada.

Pejović-Milić, A., McNeill, F.E., Prestwitch, W.V., Waker, A.J., Chettle, D.R., 1998. Development of an accelerator-based determination of aluminum burden in peripheral bone by neutron activation analysis. Appl. Radiat. Isot. 49 (5/6), 717–719.

Pejović-Milić, A., Arnold, M.L., McNeill, F.E., Chettle, D.R., 2000. Monte Carlo design study for in-vivo bone aluminum measurement using a low energy accelerator beam. Appl. Radiat. Isot. 53, 657–664.

Pierson Jr., R.N., Wang, J., Heymsfield, S.B., Dilmanian, F.A., Weber, D.A., 1990. High precision in-vivo neutron activation analysis: a new era for compartmental analysis in body composition. Basic Life Sci. 55, 317–325.

Pignol, J.P., Cuendet, P., Brassart, N., Fares, G., Colomb, F., M'Bake Diop, C., Sabattier, R., Hachem, A., Prevot, G., 1998. Combined use of FLUKA and MCNP-4A for Monte Carlo simulation of the dosimetry of ^{10}B neutron capture enhancement of fast neutron irradiations. Med. Phys. 25 (60), 885–891.

Powell, J.A., Ludewig, H., Todosow, M., Reich, M., 1999. Target and filter concepts for accelerator-driven boron neutron capture therapy applications. Nucl. Tech. 125, 104–115.

Press, W.H., Teukolsky, S.A., Vetterling, W.T., Flannery, B.P., 1992. Numerical Recipes in Fortran 77: The Art of Scientific Computing, 2nd Edition, Fortran Numerical Recipes, Vol. 1. Cambridge University Press, Cambridge.

Ritchie, A.I.M., 1976. Neutron yields and energy spectra from thick target Li(p, n) source. J Phys. D 9, 15–26.

Rogers, D.W.O., 1982. More realistic Monte-Carlo calculations of photon detector response functions. Nucl. Inst. Meth. Phys. Res. 199 (3), 531–548.

Schmid, E., Regulla, D., Guldbakke, S., Schlegel, D., Bauchinger, M., 2000. The effectiveness of monoenergetic neutrons at 565 keV in producing dicentric chromosomes in human lymphocytes at low doses. Radiat Res. 154 (3), 307–312.

Schmid, E., Regulla, D., Guldbakke, S., Schlegel, D., Roos, M., 2002. Relative biological effectiveness of 144 keV neutrons in producing dicentric chromosomes in human lymphocytes compared with ^{60}Co gamma rays under head-to-head conditions. Radiat Res. 157 (4), 453–460.

Scott, M.C., Chettle, D.R., 1986. In-vivo elemental analysis in occupational medicine. Scand. J. Work Environ. Health 12 (2), 81–89.

Sharafi, A., Pearson, D., Oxby, C.B., Oldroyd, B., Krupowicz, D.W., Brooks, K., Ellis, R.E., 1983. Multi-element analysis of the human body using neutron activation. Phys. Med. Biol. 28, 203–214.

Palerme, S., 1993. Pilot studies for in-vivo bone aluminum measurements, M.Sc. Thesis. McMaster University, Hamilton, ON, Canada.

Steyne, J.J., Huang, R., Harris, D.W., Nardi, E., 1971. Numerical simulation of NaI(Tl) experimental response functions. Trans. Am. Nucl. Soc. 14, 125.

Sutcliffe, J.F., 1996. A review of in vivo experimental methods to determine the composition of human body. Phys. Med. Biol. 41, 791–833.

Wang, C.K.C., Blue, T.E., Gahbauer, R., 1985. A neutronic study of an accelerator-based neutron irradiation facility for boron neutron capture therapy. Nucl. Tech. 84 (1), 93–107.

Yanch, J.C., Zhou, X.L., Shefer, R.E., Klinkowstein, R.E., 1992. Accelerator-based epithermal neutron beam design for neutron capture therapy. Med. Phys. 19 (3), 709–721.

Yu, W., Yue, G., Han, X., Chen, J., Tian, B., 1998. Measurement of the neutron yields from $^{7}Li(p, n)^{7}Be$ reaction (thick target) with incident energies from to 1.885 to 2.0 MeV. Med. Phys. 25 (7), 1222–1224.

Zhou, X.L., Lee, C., 1997a. Analysis of epithermal neutron production by near-threshold (p, n) reactions. Appl. Radiat. Isot. 48, 1571–1575.

Zhou, X.L., Lee, C., 1997b. Lithium compounds as targets for (p, n) reactions. Appl. Radiat. Isot. 48, 1493–1496.

CHAPTER III

Paper II

In our earlier paper, it was shown that an appropriate choice of those parameters affecting the target performance would result in neutron yields same as predicated by analytical calculations. However, any change in target operating conditions may affect the target neutron yield. The method used to measure neutron yield in Paper I was tedious, it was hoped that an alternative competitive reaction, ^{7}Li(p, $p'\gamma$)^{7}Li, which occurs alongside ^{7}Li(p, n)^{7}Be, could be employed to monitor the target conditions. This was the motivation for the work presented in Paper II.

The work in this paper was performed by me under the supervision of Drs. Prestwich and McNeill. Both Drs. Prestwich and McNeill had many good suggestions for the experimental set-up and data analysis. The manuscript was written by me and edited by Drs. Prestwich and McNeill.

(Reprinted from J. Radioanal. Nucl. Chem., 254(3), Aslam, W. V. Prestwich, F. E. McNeill, Thin target ^{7}Li(p, $p'\gamma$)^{7}Li inelastic gamma-ray yield measurements, 533-544, Copyright (2003), with permission from Kluwer Academic Publishers and Akadémiai Kiadó)

Journal of Radioanalytical and Nuclear Chemistry, Vol. 254, No. 3 (2002) 533–544

Thin target ^{7}Li(p, p'γ)^{7}Li inelastic gamma-ray yield measurements

Aslam, W. V. Prestwich, F. E. McNeill

Medical Physics and Applied Radiation Sciences Unit, McMaster University, Hamilton, ON, Canada, L8S 4K1

(Received February 26, 2002)

Abstract

Thin target angular distributions of inelastic gamma-ray yields resulting from ^{7}Li(p, p'γ)^{7}Li interaction have been measured for incident proton energies between 1.0 and 1.8 MeV. McMaster 3 MV KN Van de Graaff accelerator facility primarily dedicated to in-vivo neutron activation measurements has been used to perform experiments using a thin lithium metal target and 7.62 cm × 7.62 cm, 12.7 cm × 12.7 cm NaI(Tl) scintillation detectors and HPGe detectors. The uncertainty in the relative yield determination is based on the statistics of the data, uncertainty in the 478 keV peak area determination due to other interfering reactions, and the uncertainty in the recording of the proton charge. The results for the angular distribution provide an evidence for anisotropic nature of the radiation as compared to the presumed isotropic nature. The total relative yield was determined from the angular distributions and then compared with the published total cross sections for the reaction. Thick target yields calculated from thin target yields were also found to be in good agreement with other studies.

Introduction

Proton induced γ-ray emission spectrometry (PIGE) is based on the detection of gamma-rays emitted as a result of (p, γ), (p, p'γ), and (p, αγ) interactions.[1–6] The application of the technique for the determination of light elements in a variety of materials has been used in the past.[6] In particular, the inelastic scattering of protons on ^{7}Li has been explored for application to the quantitative microanalysis of lithium concentration profiles in the near-surface regions of materials.[3,4]

Lithium targets using ^{7}Li(p, n)^{7}Be are also widely used for neutron production for applications in boron neutron capture therapy (BNCT),[7–9] boron neutron capture enhanced fast neutron therapy (BNCEFNT), boron neutron capture synovectomy (BNCS),[10,11] in-vivo neutron activation measurements[12–18] and in radiobiological experiments.[19,20] Neutron production is also accompanied by 478 keV inelastic gamma-rays resulting from (p, p'γ) with other low and high-energy gammas, namely (p, n'γ) and (p, γ) interactions. The accurate calculation of neutron and gamma doses to a subject is possible only when thick target angular distributions or differential cross sections are available for these interactions. The neutron production cross sections are well documented,[21] however, differential cross sections for inelastic scattering of protons are available only at $\theta_{lab} = 90°$ and 120°.[22–26] Thick target yields for the interaction have also been reported at $\theta_{lab} = 55°$[1,2] and 90°.[6]

Despite its importance, relatively few measurements either of differential cross section or thick target yields have been performed, and these are largely inconsistent. The present measurements were undertaken to provide the relative total cross section and angular distributions for the ^{7}Li(p, p'γ)^{7}Li inelastic gamma-reaction. However, these preliminary measurements were limited to below the threshold of the (p, n) reaction. The data is still of importance to provide evidence for the anisotropic nature of gamma yields and may be useful for applications in PIGE because such low energies can be reached even by small accelerators and the γ-ray yields are still measurable.

Experimental

The experiments were performed at the McMaster Accelerator Laboratory at McMaster University, Hamilton, Canada, using the 3 MV KN Van de Graaff accelerator of the laboratory. The target was placed at an angle of 45° with respect to the beam. The beam intensity was kept constant at around 1 nA. In order to ensure accurate measurement of such a low beam current, no target cooling was used. As no electron suppression technique was used to measure the beam current, it may have introduced a small uncertainty not beyond 1–2% in the current measurement. The target was placed in a target holder at the end of the beam tube. This holder was electrically isolated from the beam tube and it served as a Faraday cup for the beam current integration.

Thin targets were made by vacuum evaporation of target material onto a tantalum disc. The thickness of the targets was controlled by the evaporated weight of each target material. A lithium metal target was prepared from a solid 99.9% ^{7}Li metal piece. The tantalum disc was mounted in the target holder such that the angle between the beam and target was 45°. The target holder had a 10 mm copper backing.

The detector used was a $7.62 \times 7.62\ cm^2$ NaI(Tl) scintillator detector, with a resolution of 7% at the $E_\gamma = 662$ keV γ-ray. Photon intensity at selected angles was measured by moving the detector in that particular direction while keeping the distance between the target center and detector as 50 cm. Normalization between runs involving various proton energies at a fixed angle was done on the basis of current integration. Finally, the yield curves at each fixed angle were normalized by the corresponding resonance peak yields observed at an incident proton energy of 1.12 MeV. The target thickness was checked several times during the irradiations by measuring the gamma-yield in the same target-detector geometry.

A further detector used was an intrinsic germanium γ-ray detector, with a resolution of 1.5% at the $E_\gamma = 662$ keV γ-ray. Detailed spectra were taken at energies $E_p = 1.0$–1.8 MeV. The accumulated charge for each spectrum was varied so that the spectra were characterized by good statistics and the peaks were well shaped. Excitation functions were taken at the energy range 1.0–1.80 MeV in steps of 50 keV. Computer based APTEC MCA was used to acquire and analyze the data. The detectors were calibrated using ^{137}Cs and ^{22}Na gamma-lines.

Data analysis

Spectrum analysis: Data were acquired using three detectors $12.7 \times 12.7\ cm^2$ shielded NaI(Tl), $7.62 \times 7.62\ cm^2$ NaI(Tl) and HPGe detectors. Typical spectra collected by using these detectors are shown in Figs 1 to 3. In the case of NaI(Tl) detectors, there was no peak beyond 478 keV, however when the same spectra were collected using HPGe detector, because of better resolution, two hidden peaks corresponding to 442 and 511 keV were resolvable. The peak intensity of these additional peaks in our region of interest was found to be the function of proton energy. The maximum intensity of 442 keV peak was around 2–3% of the 478 keV peak at 1.8 MeV while 511 keV peak was much less than the 442 keV. Below $E_p = 1.5$ MeV, 442 keV also became insignificant. The origin of 442 keV peak is not known. The excitation functions at an angle of 90° relative to the beam measured by NaI(Tl) and HPGe detectors under the same target–detector geometry conditions, have been compared in Fig. 4. Because of the difference in cross-sectional areas of two detectors, to keep the solid angle constant in two measurements, the distance between the target face and detector was changed. The two excitation functions match within the overall experimental uncertainty. Tantalum also has an excited state of about 482 keV. Again, in the energy range over which we measured excitation function, the 482 keV peak's contribution was significantly lower than our overall uncertainty of experiments, i.e., 2–3%. Thus the data acquired by using the $7.62 \times 7.62\ cm^2$ NaI(Tl), was used in further analysis without making any correction.

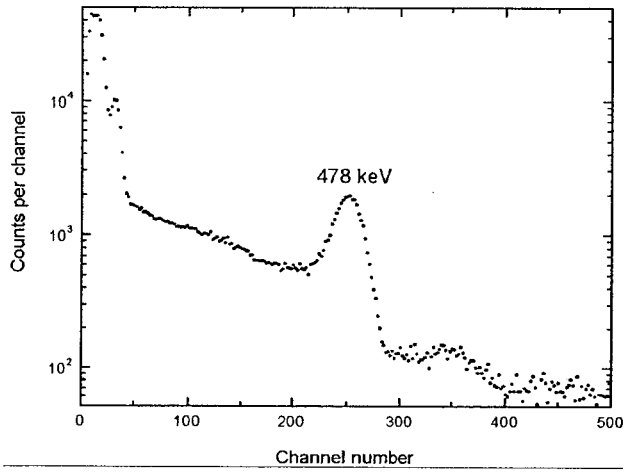

Fig. 1. Typical gamma-ray spectrum for thin lithium metal target on tantalum disc in beam direction using $12.7 \times 12.7\ cm^2$ shielded NaI(Tl) detector at $E_p = 1.8$ MeV

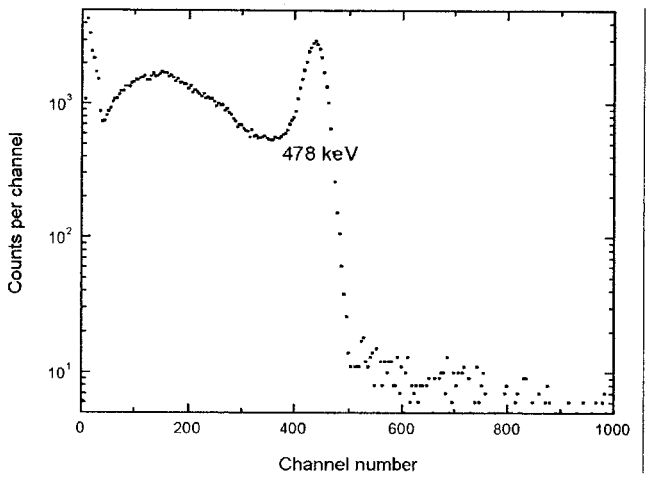

Fig. 2. Typical gamma-ray spectrum for thin lithium metal target on tantalum disc in beam direction using 7.62 × 7.62 cm^2 NaI(Tl) detector at E_p = 1.8 MeV

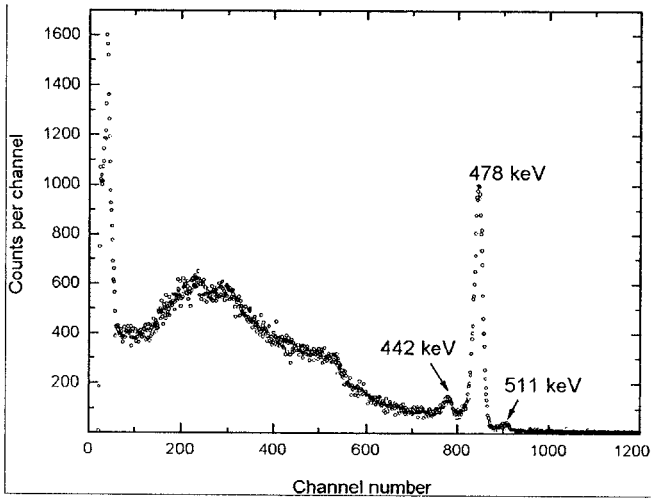

Fig. 3. Typical gamma-ray spectrum for thin lithium metal target on tantalum disc in θ_{lab} = 90° to beam using HPGe detector at E_p = 1.8 MeV

Transformation of yield into CM system: The measured γ-yields in lab coordinate system, $n_l(E_p, \vartheta)$, at incident proton energy, E_p, and angle relative to beam direction, ϑ, for a thin target per incident proton can be written as:

$$n_l(E_p,\vartheta) = n\frac{d\sigma(E_p,\vartheta)}{d\Omega} \tag{1}$$

where n is the target thickness in atoms/barn and ϑ is the angle with respect to the beam in lab coordinate system. The term $d\sigma(E_p, \vartheta)/d\Omega$ represents the differential cross section in lab coordinate system.

The relative γ-yields may be transformed into center of mass (cm) system:

$$n_l(E_p,\vartheta) = n\frac{d\sigma(E,\vartheta_{cm})}{d\Omega_{cm}}\frac{d\Omega_{cm}}{d\Omega_l} = \\ = n_c(E,\vartheta_c)\frac{d\Omega_{cm}}{d\Omega_l} \tag{2}$$

where the quantity $n_c(E, \vartheta_c)$ represents the yield in center of mass coordinate system and

$$\frac{d\Omega_{cm}}{d\Omega_l} = \frac{(1+\gamma^2+2\gamma\cos\vartheta_c)^{3/2}}{1+\gamma\cos\vartheta_c} \tag{3}$$

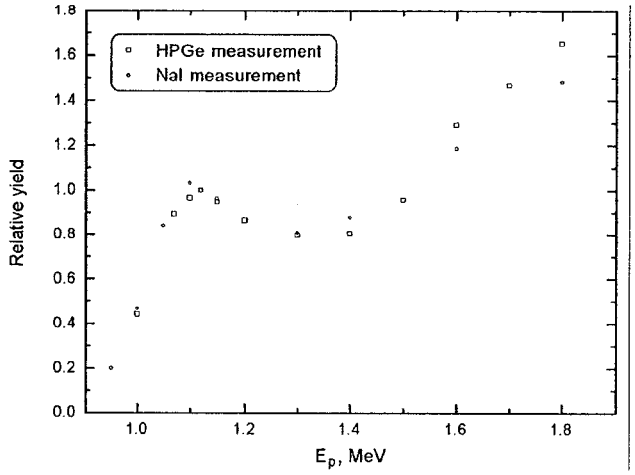

Fig. 4. Comparison of the excitation functions measured by using NaI(Tl) and HPGe detectors at 90° to beam. The difference between the two functions is always around 10%, which is within the overall uncertainty in the experimental results

The cm angle, ϑ_c, must be determined from inversion of:

$$\tan\vartheta = \frac{\sin\vartheta_c}{\gamma + \cos\vartheta_c} \tag{4}$$

where

$$\gamma^2 = \left(\frac{m_p}{m_{Li}}\right)^2 \frac{E_p}{E_p - E_{th}} \tag{5}$$

E_{th} = 0.55 MeV represents the threshold proton energy for the interaction ^{7}Li(p, p'γ)^{7}Li.

Total relative yield and cross section: Relative angular gamma-ray yields in laboratory angle, ϑ, were expressed as the Legendre polynomial expansion:

$$\frac{dY}{d\Omega}(E_p,\vartheta) = \sum_{i=1}^{4} A_i(E_p) P_i(\cos\vartheta) \tag{6}$$

where

$$\begin{aligned} P_0(\cos\vartheta) &= 1 \\ P_1(\cos\vartheta) &= \cos\vartheta \\ P_2(\cos\vartheta) &= 1/2(3\cos^2\vartheta - 1) \\ P_3(\cos\vartheta) &= 1/2(5\cos^3\vartheta - 3\cos\vartheta) \end{aligned} \tag{7}$$

while higher order Legendre polynomials have been evaluated using the recurrence relation:

$$\begin{aligned} &(n+1)P_{n+1}(\cos\vartheta) = \\ &= (2n+1)\cos\vartheta P_n(\cos\vartheta) - nP_{n-1}(\cos\vartheta) \end{aligned} \tag{8}$$

The coefficients of these fitted polynomials are given in Table 3.

In order to obtain the total cross section, the angular yield was integrated over the solid angle as:

$$\begin{aligned} &\int_{\Omega} \frac{dY}{d\Omega}(E_p,\vartheta)d\Omega = \\ &= 2\pi \sum_{i=1}^{4} A_i(E_p) \int_{\vartheta=0}^{\pi} P_i(\cos\vartheta)\sin\vartheta d\vartheta \end{aligned} \tag{9}$$

and using orthogonality of the Legendre polynomials yields:

$$Y(E_p) = 4\pi A_0 \tag{10}$$

Thus the relative total cross section, assuming to be proportional to the total yield, was derived from the relative yield curve.

Calculation of the thick target yields using thin target yields

In order to integrate thin target differential yields to get the thick target yields, thin target yields were divided by target energy thickness. Cubic spline integration[27] was used to get the thick target yields.

Results and discussion

Total cross section

The yield curves at each fixed angle were normalized by corresponding resonance peak yields by assuming that there is no appreciable departure from isotropy at 1030 keV resonance peak.[22,23,25,28] Values for normalized angular distributions in lab and cm coordinate systems in the proton energy range 1.0–1.8 MeV measured using 7.62 × 7.62 cm^2 NaI(Tl) at a distance of 50 cm from the target face, are given in Tables 1 and 2. However, we have not observed any significant change while converting the yields in lab system to cm system (maximum ~1%).

Table 1. Thin target normalized angular distribution of gamma-ray yields in lab coordinate system

	Laboratory angle, ϑ, degrees					
E_p, MeV	0	15	45	75	90	120
1.80	1.548	0.690	0.951	1.756	1.482	2.415
1.70	1.147	–	0.934	1.358	–	2.029
1.60	1.038	0.611	0.814	1.193	1.186	1.277
1.50	–	0.685	0.765	1.040	–	0.589
1.40	0.725	0.655	0.745	0.898	0.878	0.475
1.30	0.709	0.693	0.755	0.804	0.808	0.556
1.20	0.825	0.856	0.853	0.867	–	0.543
1.15	0.941	0.938	0.935	0.964	0.963	0.656
1.12	1.000	1.000	1.000	1.000	1.000	1.000
1.10	0.990	1.016	1.028	0.974	1.031	–
1.05	0.784	0.834	0.885	0.795	0.841	0.933
1.00	0.441	0.441	0.500	0.444	0.466	0.384
0.95	0.197	0.186	0.212	0.184	0.200	–

Table 2. Thin target normalized angular distribution of gamma-ray yields in cm coordinate system

	Laboratory angle, ϑ, degrees					
E_p, MeV	0	15	45	75	90	120
1.80	1.588	0.707	0.966	1.763	1.488	2.379
1.70	1.177	–	0.948	1.364	–	2.001
1.60	1.055	0.622	0.828	1.200	1.191	1.261
1.50	–	0.697	0.778	1.046	–	0.583
1.40	0.737	0.662	0.752	0.904	0.883	0.470
1.30	0.715	0.699	0.761	0.801	0.813	0.552
1.20	0.832	0.857	0.861	0.866	–	0.542
1.15	0.941	0.938	0.935	0.963	0.972	0.656
1.12	1.000	1.000	1.000	1.000	1.000	1.000
1.10	0.990	1.016	1.028	0.975	1.031	–
1.05	0.778	0.828	0.885	0.794	0.842	0.938
1.00	0.437	0.437	0.496	0.441	0.468	0.387
0.95	0.194	0.183	0.209	0.183	0.201	–

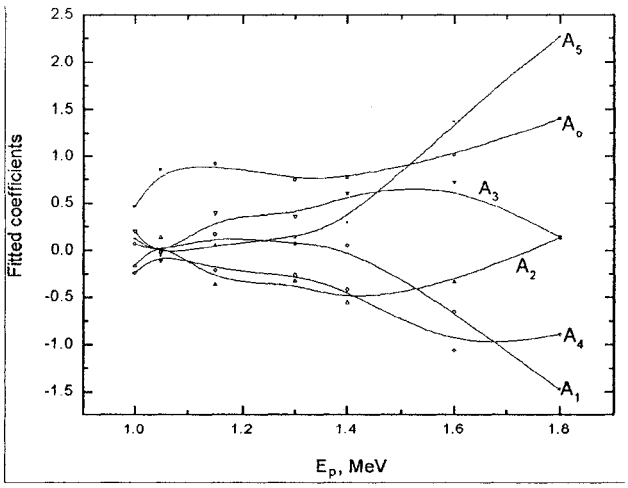

Fig. 5. Fitted Legendre coefficients

Table 3. Fitted 4th order Legendre coefficients using MATLAB function fitlegen()

	E_p, MeV						
	1.8	1.6	1.4	1.3	1.15	1.05	1.00
A_0	1.3955 ± 0.2105	1.0018 ± 0.1303	0.7631 ± 0.0269	0.7459 ± 0.0116	0.9151 ± 0.0046	0.8556 ± 0.0046	0.4603 ± 0.0105
A_1	–1.4361 ± 0.6158	–0.6108 ± 0.3354	0.0578 ± 0.0594	0.0721 ± 0.0267	0.1676 ± 0.0106	–0.0271 ± 0.0119	0.072 ± 0.025
A_2	1.1776 ± 1.0253	0.2958 ± 0.4978	–0.4202 ± 0.0718	–0.2688 ± 0.0324	–0.3455 ± 0.0125	0.1068 ± 0.0154	–0.1063 ± 0.03
A_3	–1.9402 ± 1.1954	–0.5097 ± 0.6588	0.3528 ± 0.111	0.249 ± 0.0472	0.3472 ± 0.0183	–0.0701 ± 0.0199	0.1022 ± 0.0411
A_4	1.955 ± 1.2039	0.6581 ± 0.721	–0.059 ± 0.1391	–0.1024 ± 0.0574	–0.1486 ± 0.0225	–0.0773 ± 0.0217	–0.0993 ± 0.0486
χ_ν^2	1.1057	1.0627	1.0157	1.0494	0.9617	1.0484	1.0313
σ_{total}, %	32	27	7	3.1	1	1.1	4.5

Total experimental uncertainty in results was estimated to be 20%.

In order to calculate the total cross section for the reaction, 4th order Legendre polynomials were fitted. Least square Legendre polynomial fitting[29] MATLAB™ function fitlegen() was used for this purpose. The function returns the Legendre coefficients, the uncertainty in coefficients, χ^2, and the covariance matrix. The calculated coefficients as a function of proton energy have been reported in Table 3 and shown graphically in Fig. 5. Because of the orthogonality of Legendre polynomials, fitting of lower order Legendre polynomials also resulted in the identical values of A_0 with higher χ^2.[29] The independence of our fitted coefficient, A_0, on higher-order terms is a result of fact that the experiment samples uniformly the entire range of the Legendre polynomial, so the orthogonality relation is satisfied by a finite set of data.[29] In Table 3, we also report the χ^2 per degree freedom for the fitted function. On the basis of χ^2 per degree of freedom, the estimated uncertainty in the experimental results below 1.4 MeV proton energy, was 1–7% and 25–30% above 1.4 MeV. The estimated increase of uncertainty in the data is because of the availability of fewer experimental data points and it emphasizes the increase in experimental data points because at higher energies well above the resonance, the anisotropy increases and more experimental data points are needed. Even with this estimated uncertainty in data based on χ^2, the data points do not overlap signifying the anisotropy of the angular distribution.

The total yield was calculated by using the zeroth order Legendre coefficient, A_0, as shown in Eq. (10). The total yield as a function of energy is listed in Table 3, which after proper normalization can be compared with the published total inelastic cross section.[22–26] All these authors reported their results in graphical form rather than in tabular form, which made the comparison of our results difficult with these earlier studies. However, above 1.5 MeV, the reported data for one of these references[26] were retrieved using the NNDC facility (http://www.nndc.bnl.gov/nndc/endf/) for data retrieval. Below 1.5 MeV, KRAUS et al.[23] data for relative yields were directly read from the graph. Digitization of the yield curve besides the experimental uncertainty in data, also introduced some more uncertainty in data.

Although no mention has been made in the reference cited about the measurement angle, according to authors, the results matched that of BROWN et al.,[22] where measurements were made at an angle of 90°. On the basis of close match in results with those of measurements made at 90°, it was assumed that KRAUS et al.,[23] also measured at 90° same as opted by PRESSER et al.[26] Thus KRAUS data were normalized to those of PRESSER et al.[26] to obtain the complete set of inelastic cross sections for proton energies ranging from 0.7–1.8 MeV.

Table 4. Comparison of the measured total cross section with the published results. The difference in results is around 10% and may be attributed to the target thickness

E_p, MeV	Relative ($4\pi A_0$)	Cross section, mb		
		Normalized	This work	Published
1.80	17.60	1.47	60.02	68.61
1.60	12.76	1.07	43.50	45.16
1.40	9.63	0.81	32.83	37.77
1.30	9.39	0.79	32.03	34.47
1.15	11.51	0.96	39.23	37.77
1.12	11.95	1.00	40.76	40.76
1.05	10.74	0.90	36.64	42.53
1.00	5.81	0.49	19.80	23.10

Table 5. Comparison of the measured total cross section with the published results. Average proton energy was estimated by using the target thickness and stopping power

E_p	Average E_p	Cross section, mb				
		Relative	Normalized	This work	Published	Ratio
1.80	1.78	17.60	1.47	62.64	65.52	1.05
1.60	1.58	12.76	1.07	45.41	44.60	0.98
1.40	1.38	9.63	0.81	34.27	36.55	1.07
1.30	1.28	9.39	0.79	33.42	34.07	1.02
1.15	1.13	11.51	0.96	40.96	39.72	0.97
1.12	1.10	11.95	1.00	42.53	42.53	1.00
1.05	1.03	10.74	0.90	38.22	36.33	0.95
1.00	0.98	5.81	0.49	20.68	16.36	0.79

E_p, MeV = E_p–$S(E_p)$×Δx/2.

Table 6. Thick target relative angular distribution of gamma-ray yields obtained by integrating the yields given in Table 1

E_p, MeV	Laboratory angle, θ, degrees 0	15	45	75	90	120
1.80	19.89	14.89	17.78	22.52	22.17	21.93
1.70	15.73	12.98	14.88	17.72	17.77	15.09
1.60	12.52	11.28	12.30	13.96	14.04	10.20
1.50	9.82	9.46	10.09	10.82	10.94	7.56
1.40	7.68	7.67	8.07	8.23	8.40	6.14
1.30	5.87	5.97	6.17	6.07	6.26	4.83
1.20	4.03	4.12	4.25	4.07	4.22	3.52
1.15	3.02	3.09	3.22	3.02	3.15	2.83
1.12	2.37	2.44	2.57	2.36	2.49	2.27
1.10	1.93	1.99	2.13	1.93	2.04	1.81

Cubic spline interpolation was used to calculate the relative yield at 1.12 MeV as 11.95. The curve was finally normalized to those of published value at the same energy and results are shown in Table 4.

The target thickness was taken into account by correcting the energy scale; E_p was replaced by $E_p - \Delta E_p/2$, for each value of the incidence energy E_p. The energy loss, ΔE_p, in target can be estimated from the product of target thickness and stopping power. The proton's stopping power in lithium target was estimated by using Bethe's stopping power as:

$$\frac{1}{\rho}S(E) = 4\pi N_a z^2 \left(\frac{Z}{A}\right)\frac{m_e c^2}{\beta^2} r_0^2 \ln\left(\frac{2m_e v^2}{I}\right) \qquad (11)$$

where N_a is the Avogadro's number, $\beta = v/c$, and r_0 is the classical electron radius.

Using $Z=3$, $A=6.941$ for Li target, with $I=57.20$ eV:[30]

$$\frac{1}{\rho}S(E) = \frac{62.26462}{E_p}\ln(38.085E_p) \qquad (12)$$

Target thickness has been estimated from the difference in peak energies as:

$$E_{peak\,pub} - E_{peak} = S(E_p = 1.12\ \text{MeV})\,\Delta x$$
$$45\ \text{keV} = 1.10 \cdot 10^5\ \text{keV/cm} \cdot \Delta x$$

which gives the target thickness as 4 μm.

The calculated cross section has been plotted in Fig. 6. The two sets of data are in close agreement within the experimental error. However, when the target energy thickness was taken into account, the difference was further reduced to less than 5%. The results have been summarized in Table 5. Interestingly, our measurements which support the anisotropic nature of angular distribution, match the results which were obtained by assuming the isotropicity of γ-radiations as the transition take place from $J=½$ levels. In the earlier study, the total inelastic cross section was obtained by measuring the gamma-yield at an angle of 90° relative to the beam.

NEWSON et al.[24] measured the excitation function for inelastically scattered 478 keV gamma-rays at an angle of 120° to beam in the proton energy range 1.2–3.5 MeV. They also measured the angular distribution at proton energies of 1.7, 2.0, 2.6, and 3.0 MeV and in contrast to our study, they found the angular distribution to be isotropic.

All the earlier reported measurements were made at either 90° or 120° with the assumption of isotropy because of transition from $J=½$ levels. However, our extended measurement in the energy range of 1–1.8 MeV with the assumption of isotropy at resonant peak at 1.030 MeV showed that the differential cross sections well above this resonance peak at a given energy decreases with the decreasing angle in the range $15° < \vartheta_{lab} < 120°$ and also showed a minima at 15° (Tables 1 and 2).

Thin and thick target yields

12.7×12.7 cm^2 NaI(Tl) was used to measure the excitation function with very large solid angle. At $\theta_{lab} = 90°$ and 0° to beam, the target–detector distance was 5 cm while $\theta_{lab} = 45°$, distance was around 1 cm. While changing the distance from 5 cm to 1 cm, the solid angle was increased by 1.45.

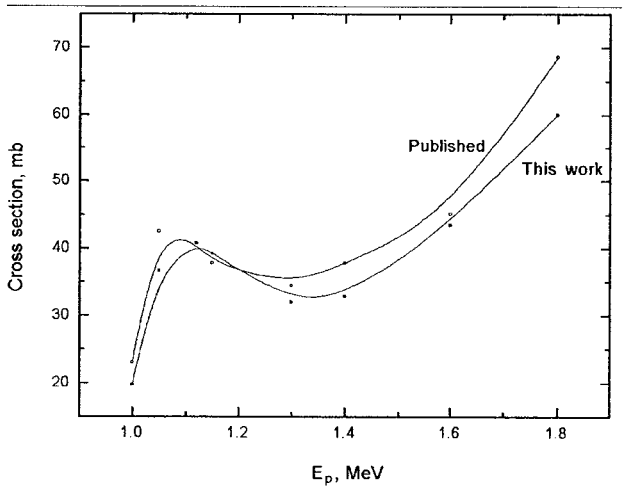

Fig. 6. Comparison of measured and published cross sections. A peak shift in two studies is evident. In the case of earlier studies, the resonance peak was observed at $E_p = 1.030$ MeV proton energy while in the present study, it is at 1.12 MeV. The difference between the two peaks is because of finite target thickness

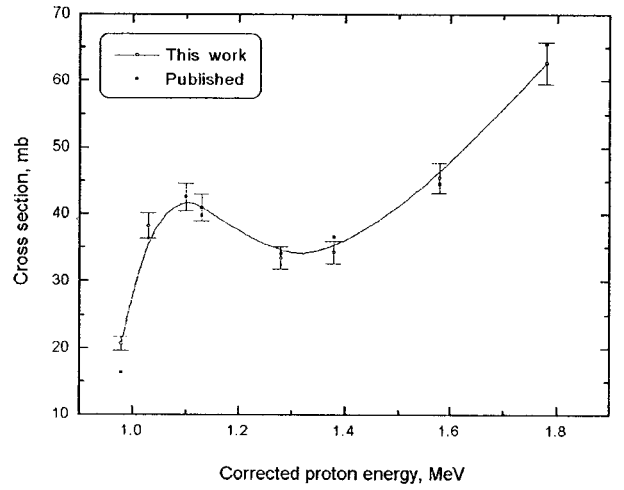

Fig. 7. Comparison of the measured cross sections with published results after thickness energy correction

Comparing the solid angle with small NaI(Tl) where the target–detector distance was around 50 cm, the ratio of solid angle for large NaI(Tl) at 5 cm was around 50 while at 1 cm it was around 80.

Again, the comparison of our calculated thick target yields (Table 6) with previously reported values is difficult since graphs are given in these references rather than numerical values.

ANTILLA et al.,[1] KISS et al.,[2] and SAVIDOU et al.[6] report data for thick targets in tabular form. ANTILLA et al.[1] tabulated the values at $E_p = 1.0$, 1.7 and 2.4 MeV while SAVIDOU et al.[6] tabulated values at $E_p = 1.77$ and 4.0. However, SAVIDOU et al.[6] also provided a graph covering a range of energy $E_p = 1.0$–1.8 MeV. Unfortunately the results were given only as a plot, which is difficult to read. Thus the values were extracted from the plot. In order to compare the two measurements, cubic spline interpolation was used to get the intermediate values (Fig. 7). Two data sets have been listed in Table 7.

Table 7. Comparison of thick target $^{7}Li(p,p'\gamma)^{7}Li$ yields measured at an angle of 55° (ANTTILA et al.) with those of measured at 90° (SAVIDOU et al.)

E_p, MeV	γ/μC Sr		Ratio
	ANTTILA et al.	SAVIDOU et al.	
1.0	$6.5 \cdot 10^5$	$3.0 \cdot 10^5$	2.17
1.1	$1.2 \cdot 10^6$	$5.0 \cdot 10^5$	2.40
1.2	$1.9 \cdot 10^6$	$9.0 \cdot 10^5$	2.11
1.3	$2.9 \cdot 10^6$	–	–
1.4	$4.0 \cdot 10^6$	$2.0 \cdot 10^6$	2.00
1.5	$5.4 \cdot 10^6$	$2.7 \cdot 10^6$	2.00
1.6	$6.9 \cdot 10^6$	$3.0 \cdot 10^6$	2.30
1.7	$8.6 \cdot 10^6$	$4.0 \cdot 10^6$	2.15
1.8	$1.1 \cdot 10^7$	$5.8 \cdot 10^6$	1.90
2.5	$2.9 \cdot 10^7$	$2.0 \cdot 10^7$	1.45

Although the two measurements support our argument about the anisotropic nature of the radiation, the results are in contradiction with our study in the sense that our 90° yield curve above the resonance peak is more intense than that of the closest angle measured to 55° i.e., 45°. In the case of ANTILLA et al.,[1] a large solid angle was used for measurements while SAVIDOU et al.[6] has not mentioned the solid angle used in their measurements. Since the angular distribution of the observed gamma-rays is not isotropic, the yield or cross section measured using a large solid angle, should be taken as average value. In another measurement, where the larger 12.7×12.7 cm^2 NaI(Tl) scintillator detector at a distance of around of around 5 cm from target face was used to measure the yields. In this case the detector subtended a large solid angle, again the 90° yields above the resonance were also found to be larger than that of 45° as found in the case of small solid angle. However, the shape of the curves was different than those of measured with small solid angle. This also supports our argument about the anisotropic nature of the emitted radiation, which would otherwise be independent of the solid angle (Fig. 8).

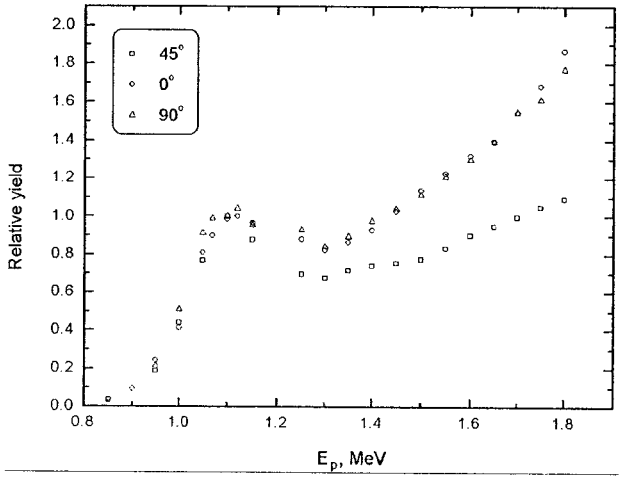

Fig. 8. Effect of using large solid angle on excitation function. A 12.7×12.7 cm^2 NaI(Tl) was used to measure the excitation function with very large solid angle. At $\theta_{lab} = 90°$ and 0° to beam, the target–detector distance was 5 cm while at $\theta_{lab} = 45°$, distance was around 1 cm. While changing the distance from 5 cm to 1 cm, the solid angle was increased by 1.45. Comparing the solid angle with the small NaI(Tl) where the target–detector distance was around 50 cm, the ratio of solid angle for large NaI(Tl) at 5 cm was around 50 while at 1 cm it was around 80

Table 8. Comparison of normalized thick target $^{7}Li(p,p'\gamma)^{7}Li$ yields measured at an angle of 55° (ANTTILA et al.) and 90° (SAVIDOU et al.) with this work

E_p, MeV	ANTTILA et al. at θ=55°	This work at θ=45°	SAVIDOU et al. at θ=90°	This work at θ=90°
1.1	1.00	1.00	1.00	1.00
1.2	1.58	2.00	1.80	2.07
1.3	2.42	2.90	–	3.07
1.4	3.33	3.80	4.00	4.12
1.5	4.50	4.75	5.40	5.36
1.6	5.75	5.79	6.00	6.88
1.7	7.17	7.00	8.00	8.71
1.8	9.17	8.36	11.60	10.87

In order to compare our thin target measurements with those of thick target measurements given by ANTILLA et al.,[1] KISS et al.[2] and SAVIDOU et al.,[6] thin target yields were integrated over the target thickness. Calculated relative thick target yields are given in Table 8. For the sake of comparison, the relative yields (this work) and absolute yields were normalized against the $E_p = 1.1$ MeV. Our 45° measurements surprisingly match the measurements by ANTILLA et al.[1] within the experimental uncertainty, i.e., 5%, which were measured at 55°. Our 90° normalized measurements were also found to be in close agreement with those of SAVIDOU et al.[6] The comparison of our measurements with those of thick target measurements are given in Table 8. However, either on the basis of our measurements, which support anisotropic angular distribution, suggests that the 90° yield curve should be more intense than that of 55° or on basis of isotropic angular distribution, the two yields curves should be the same instead of consistently higher than that of 55°. Thus we noticed a discrepancy in the absolute values of the two published measurements. Our normalized yield comparison points out that there is some systematic error in either of the two measurements and the data needs to be corrected for absolute values prior to the use in PIGE applications.

Excitation functions have been measured with thin targets by BONI et al.[4,5] above 2.2 MeV proton energy, and RIO et al.[5] above 1.2 MeV. RIO et al. have also measured thin target yields at 120° to proton beam with large solid angle. In the case of RIO et al.,[5] yield at 1.8 MeV normalized to yield at 1.2 MeV is 2.25 which is about a factor of two lower than ours. This difference may be attributed to the difference in the target thickness.

Conclusions

Relative photon yields for the ^{7}Li(p, p'γ)^{7}Li reaction have been measured in the energy range between 1.0 and 1.8 MeV incident proton energy with uncertainties of about 5–10%. Thin target measurements of the angular distribution of photons show that they are not emitted isotropically. The relative angular photon yield shows a resonance at all the selected angles. No appreciable change in FWHM of the resonance peak in the forward direction was observed while it was found to be a bit larger in backward direction. Above resonance, in the angular range $15° < \theta_{lab} < 120°$, the yield was found to be increasing with increasing angle. However, a minima was found at 15° and the yield again starts increasing with decreasing angle. The maximum observed photon yield was obtained at proton energy of 1.8 MeV at angle of 120°. The total cross section calculated from the angular distributions matches the published cross section within 5%. Our normalized thick target yields were found to be in close agreement with the earlier studies. However, on the basis of our measurements, we found a discrepancy in the absolute values of these measurements.

*

One of the authors, ASLAM, acknowledges the International Council for Canadian Studies (ICCS) for awarding a postgraduate scholarship. We are also thankful to Natural Sciences and Engineering Research Council of Canada (NSERC) who helped fund this research in the form of a Research Grant for F. E. McNeill. The authors also wish to recognize a number of individuals at the McMaster accelerator, including Jason FALLADOWN, Jim STARK, John CAVE and Scot MCMASTER.

References

1. A. ANTTILA, R. HANNINEN, J. RAISANEN, J. Radioanal. Chem., 62 (1981) 293.
2. A. Z. KISS, E. KOLTAY, B. NYAKO, I. S. SOMORIAL, A. ANTTILA, J. RAISANEN, J. Radioanal. Nucl. Chem., 89 (1985) 123.
3. C. BONI, E. CEREDA, G. M. B. MARCAZZAN, Nucl. Instr. Meth. Phys. Res., B35 (1988) 80.
4. C. BONI, A. CARIDI, E. CEREDA, G. M. B. MARCAZZAN, Nucl. Instr. Meth. Phys. Res., B35 (1990) 133.
5. S. RIO, M. METRICH, M. MOSBAH, P. MOSSIOT, Nucl. Instr. Meth. Phys. Res., B100 (1995) 141.
6. A. SAVIDOU, X. ASLANOGLOU, T. PARADELLISC, M. PILAKOUTAC, Nucl. Instr. Meth. Phys. Res., B152 (1999) 12.
7. J. C. YANCH, X. L. ZHOU, R. E. SHEFER, R. E. KLINKOWSTEIN, Med. Phys., 19 (1992) 709.
8. X. L. ZHOU, C. LEE, Appl. Radiation Isotopes, 48 (1997) 1571.
9. X. L. ZHOU, C. LEE, Appl. Radiation Isotopes, 48 (1997) 1493.
10. D. P. GIERGA, J. C. YANCH, R. E. SHEFER, Med. Phys., 27 (2000) 1685.
11. D. P. GIERGA, J. C. YANCH, R. E. SHEFER, Med. Phys., 27 (2000) 203.
12. M. ARNOLD, Development of an Accelerator Based System for In-Vivo Neutron Activation Analysis Measurements of Manganese in Humans, PhD Thesis, McMaster University, 2000.
13. M. ARNOLD, F. E. MCNEILL, W. V. PRESTWICH, D. R. CHETTLE, Appl. Radiation Isotopes, 53 (2000) 651.
14. M. ARNOLD, F. E. MCNEILL, D. R. CHETTLE, NeuroToxicology, 20 (1999) 407.
15. A. PEJOVIĆ-MILIĆ, An Accelerator Based in Vivo Measurement of Aluminum in Human Bone by Neutron Activation Analysis, MSc Thesis, McMaster University, 1998.
16. A. PEJOVIĆ-MILIĆ, F. E. MCNEILL, W. V. PRESTWITCH, A. J. WAKER, D. R. CHETTLE, Appl. Radiation Isotopes, 49 (1998) 717.
17. A. PEJOVIĆ-MILIĆ, M. L. ARNOLD, F. E. MCNEILL, D. R. CHETTLE, Appl. Radiation Isotopes. 53 (2000) 657.
18. S. PALERME, Pilot Studies for In-Vivo Bone Aluminum Measurements, MSc Thesis, McMaster University, 1998.
19. S. ENDO, M. HOSHI, H. TAUCHI, S. TAKEOKA, K. KITAGAWA, S. SUGA, N. MEADA, K. KOMATSU, S. SAWADA, E. IWAMOTO, S. SAKAMOTO, K. TAKEYAMA, M. OMURA, J. Radiat. Res., 36 (1995) 91.
20. E. SCHMID, D. REGULLA, S. GULDBAKKE, D. SCHLEGEL, M. BAUCHINGER, Radiat. Res. 154 (2000) 307.
21. H. LISKIEN, A. PAULSEN, At. Data Nucl. Data Tables, 15 (1975) 57.

22. A. B. BROWN, C. W. SNYDER, W. A. FOWLER, C. C. LAURITSEN, Phys. Rev., 82 (1951) 159.
23. A. A. KRAUS Jr., Phys. Rev., 93 (1954) 1308.
24. H. W. NEWSON, R. M. WILLIAMSON, K. W. JONES, J. H. GIBBONS, H. MARSHAK, Phys. Rev., 108 (1957) 1294.
25. S. CAVALLARO, R. POTENZA, A. RUBBINO, Nucl. Phys., 39 (1962) 597.
26. G. PRESSER, R. BASS, Nucl. Phys., A182 (1972) 321.
27. W. H. PRESS, S. A. TEUKOLSKY, W. T. VETTERLING, B. P. FLANNERY, Numerical Recipes in Fortran 77: The Art of Scientific Computing, 2nd ed., Volume 1 of Fortran Numerical Recipes, Cambridge University Press, 1992.
28. F. MOZER, W. A. FOWLER, C. C. LAURITSEN, Phys. Rev., 93 (1954) 829.
29. P. R. BEVINGTON, Data Reduction and Error Analysis for the Physical Sciences, D. K. ROBINSON (Ed.), 2nd ed., McGraw-Hill, New York, 1992, p. 133.
30. J. F. JANNI, At. Data Nucl. Data Tables, 27 (1982) 147.

CHAPTER IV

Paper III

The following paper examines the feasibility of using a tissue equivalent proportional counter (TEPC) filled with propane based tissue equivalent (TE) gas simulating a 2 μm diameter to determine the neutron quality factor for the neutron fields used in *in-vivo* neutron activation measurements at the McMaster University 3 MV Van de Graaff accelerator. Knowing the quality factors in low energy neutron fields used for IVNAA, the dose equivalent received to the patients undergoing hand irradiation can be estimated.

The work presented in this paper was performed by me under the supervision of Drs. Prestwich and McNeill. The TEPC based microdosimetric system and the computer programs employed for data acquisition and analysis of the raw data that was used in the experiments at MAL had been previously developed and characterized at AECL, Chalk River, Canada by Dr. Waker. Dr. Waker acted as a consultant and collaborator for the research presented in this paper. The manuscript was written by me and edited by Drs. Prestwich, McNeill and Waker.

(Reprinted from Radiat. Prot. Dosim., 103(4), Aslam, W. V. Prestwich, F. E. McNeill, A. J. Waker, Investigating the TEPC radiation quality factor response for radiation protection in low energy accelerator based clinical applications, 311-322, Copyright (2003), with permission from Nuclear Technology Publishing)

Radiation Protection Dosimetry
Vol. 103, No. 4, pp. 311–322 (2003)
Nuclear Technology Publishing

INVESTIGATING THE TEPC RADIATION QUALITY FACTOR RESPONSE FOR LOW ENERGY ACCELERATOR BASED CLINICAL APPLICATIONS

Aslam†, W. V. Prestwich†, F. E. McNeill† and A. J. Waker‡
†Medical Physics and Applied Radiation Sciences Unit, McMaster University
Hamilton, ON, Canada, L8S 4K1

Received August 8 2002, in final revised form January 6 2003, accepted January 20 2003

Abstract — The use of a tissue equivalent proportional counter (TEPC) filled with propane based tissue equivalent gas simulating a 2 μm diameter tissue sphere has been investigated to estimate the radiation quality factor of the neutron fields used in *in vivo* neutron activation measurements at the McMaster University 3 MV Van de Graaff accelerator. The counter response to estimate the effective quality factor based on the definitions of $Q(L)$ provided in ICRP 26 and 60 as a function of neutron energy has been examined experimentally using monoenergetic and continuous neutron spectra in the energy range of 35 to 600 keV. In agreement with other studies, the counter failed to provide a flat R_Q response and showed a sharp drop below 200 keV neutron energy. Development of an algorithm to evaluate the quality factors using measured dose-mean lineal energy, $\bar{y}_D$, and comparison of the algorithm with other reported algorithms and analytical methods developed for the improvement in TEPC dose equivalent response has been reported.

INTRODUCTION

In vivo neutron activation analysis is a clinical technique used to measure various major and trace elements in the human body by measuring the induced radioactivity as a result of neutron irradiation of the human body[1–10]. A neutron source and its spectrum are selected to obtain the best compromise between achieving the uniformity of activation and minimising the dose per incident neutron[9]. Since the elements of interest have differing activation cross sections and are located in different sites in the human body, a variety of neutron sources and spectra are employed[9]. The 3 MV Van de Graaff accelerator at the McMaster University accelerator laboratory (MAL) is primarily dedicated to *in vivo* neutron activation measurements. Fast neutrons at the facility are produced by bombarding protons on a thick lithium target using the ^{7}Li(p,n)^{7}Be reaction. The resulting neutron energy spectrum as well as the angular distribution of the neutrons produced depends upon the energy of incident protons. Theoretical neutron yield and energy spectrum calculations prompted by low energy accelerator applications in boron neutron capture therapy (BNCT), boron neutron capture enhanced fast neutron therapy (BNCEFNT), boron neutron capture synovectomy (BNCS), and in *in vivo* measurements have been reported[11–25]. Based on these calculations, various irradiation facilities have been developed at MAL for *in vivo* neutron activation measurements of different trace elements found in humans[24–32]. In order to optimise the activation of the intended isotope while minimising dose, the direct neutron beam may be moderated in a manner dependent upon the application. Extensive modelling, simulation and experimental arrangements have been reported[24–32].

The proton energies investigated for *in vivo* measurements at MAL range from 2.00 to 2.25 MeV while the neutrons produced in the beam direction as a result have mean neutron energies from 100 to 280 keV[33]. At 2.00 MeV incident proton energy, the mean neutron energy in the beam direction is around 100 keV which drops to 35 keV at $\theta_{lab} = 90°$[33]. Thus the neutron energies investigated in bare beam conditions (without any neutron moderation) under different irradiation conditions range from 35 to 280 keV. However, for an arrangement consisting of a neutron moderator and reflector, developed for *in vivo* measurements of aluminium[26–32] and manganese[25,32] in the hand, the neutron energy spectrum softens further to ~10–20 keV with an increased thermal neutron contribution as compared to a bare beam for $E_p = 2.00$ MeV[33]. For $E_p = 2.25$ MeV, the mean neutron energy softens to ~40–80 keV[33]. During measurements of a patient's aluminium and manganese content, a number of individuals including the patient and the technicians will be exposed to low doses of these low energy neutron beams. The neutron energy spectrum to which individuals will be exposed varies widely, depending on the beam parameters, the degree of moderation and shielding.

These neutron fields have been routinely monitored using a 12.7 mm (½″) diameter spherical TEPC simulating a 2 μm diameter tissue[25,28,30]. These studies were conducted with the assumption of a flat response of TEPC (R_Q = measured quality factor/calculated quality factor and R_K = measured kerma/calculated kerma)

Contact author E-mail:

within the entire range of neutron energies investigated. However, the detector quality factor response, R_Q, is energy dependent, deteriorating significantly below 200 keV[34–42]. This under-response is largely because the average range of the recoil protons created by the neutrons, which contribute most to the absorbed dose in the counter in this neutron energy region, becomes less than the simulated diameter (2 μm). In this case the resultant lineal energies are not a good approximation to the LET of the protons[34–42]. This leads to an underestimation of the quality factor assigned to such events[34–42]. This underestimation as well as other factors also contributes to the low neutron dose equivalent response of TEPCs in the neutron energy range 0.1–200 keV[34–42]. Dietze *et al*[35] has estimated that this incorrect evaluation of the mean quality factor at these low neutron energies contributes to about half of the deviation of measured dose equivalent from the ambient dose equivalent $H^*(10)$. Therefore it was decided to investigate the feasibility of using a TEPC to measure the quality factors of the neutron beams encountered in *in vivo* neutron activation measurements.

This study describes the use of a TEPC to estimate the effective quality factors of the neutron fields used in *in vivo* neutron activation measurements at the McMaster University 3 MV Van de Graaff accelerator. The variation of R_Q with neutron energy was examined experimentally using monoenergetic and continuous neutron energy spectra in the energy range of 35 to 600 keV. In agreement with other studies, the counter failed to provide a flat R_Q response based on the definitions of $Q(L)$ provided in ICRP 26[43] and 60[44] and showed a sharp drop below 200 keV neutron energy. A modified algorithm[45,49] based on calculated dose-mean lineal energy[45,49], $\overline{y_D}$, from the measured lineal energy spectrum and the calculated quality factor in an ICRU tissue sphere, has been implemented to provide an improved estimate of the quality factors for the beams encountered in *in vivo* activation measurements. The objective was achieved by calculating $\overline{y_D}$ and the effective quality factors, $\bar{Q}$, using the measured lineal energy spectra with monoenergetic neutrons of energy ranging from 150 to 600 keV. Below 150 keV neutron energy, the reported measurements of $\overline{y_D}$ and $\bar{Q}$ performed with a similar TEPC using neutrons with continuous energy spectra having corresponding calculated mean neutron energies were used. The modified algorithm developed was used to calculate the dose equivalent response and compared with other reported algorithms and analytical methods developed for the improvement in TEPC response in the low energy region.

MATERIALS AND METHODS

Neutron source

A thin ^{7}Li target was designed to produce monoenergetic neutrons of energy ranging from 150–600 keV using the 3 MV KN Van De Graaff accelerator. The target was prepared by vacuum evaporation onto a 1 mm thick tantalum disc. The thickness of the target was controlled by the evaporated weight of the target material. The tantalum disc was mounted at the end of a beam duct and was cooled with water to prevent heating by proton beam currents.

Neutron energy measurements

Neutron energy was measured using a ^{3}He filled gridded ionisation chamber (FNS-1, Seforad Applied Radiation Ltd. of Emek Hayarden, Israel). The active volume of the chamber is 5 cm in diameter and 15 cm in length and is filled with a gas containing ^{3}He gas at a pressure of 10 atm (1.013 kPa). The dimensions exceed the range of the low energy charged particles produced by the ^{3}He(n,p)T reaction in the active volume of the counter at the energies used here. Thus the neutron energy measured was proportional to the energy deposited inside the active volume by the resulting protons and tritons. All the energy measurements were performed in such a way that the detector axis always coincided with the beam axis.

The ^{3}He detector anode was maintained at a constant +3000V by a Power Designs AEC1000 power supply. A voltage divider within the preamp (SR-101) kept the grid at +850 V, thus alleviating the need for a separate power supply[46]. Preamplifier output signals were processed by an ORTEC 572 spectroscopy amplifier with a 3 μs shaping time constant. The pulse height spectra were analysed by a personal computer using an APTEC data acquisition system. A Model PB-3, Berkley Electronics pulser was used together with the peak corresponding to thermal neutrons to establish a linear relationship between the pulse height and the energy deposited.

Microdosimetric measurements

A Rossi-type spherical proportional counter (model LET ½″, Far West Technology, Goleta, USA), with 2.5 mm thick walls made of A-150 tissue-equivalent plastic (TEPC), filled with propane based TE gas at a pressure of 8.8 kPa to simulate a tissue sphere of 2 μm diameter was used to measure the lineal energy distributions of the monoenergetic neutron fields.

The experimental technique generally followed that described in the literature[25,39,40]. The proportional counter and a low-noise preamplifier connected directly to the anode of the counter were located in the irradiation room. Analogue pulses from the preamplifier were fed through an ORTEC 855 dual SPEC amplifier into two 16 k analogue-to-digital converters (ADCs) and stored in an ORTEC HM 413 HISTO memory unit. The low and high gain histograms obtained were finally transferred to a Macintosh Power PC book. The processing of the raw data was carried out by using the

computer programs written in KMAX version 4.1 developed at AECL, Chalk River, Canada[25,39,40].

The pulse height spectra were converted into the lineal energy distributions $f(y)$ and $d(y)$ by applying the appropriate calibration factors, taking into account the mean chord length of the sensitive volume simulated. The system was calibrated by irradiating the counter with a finely collimated internal ^{244}Cm alpha source which deposits 170 keV[48] in a 2 μm diameter TE gas corresponding to a lineal energy of $y_\alpha = 127$ keV μm^{-1}. The mean pulse height, h_α, corresponding to the mean energy imparted in the cavity was evaluated by fitting a Gaussian curve to the measured peak. Using y_α and h_α, the calibration factors were calculated to convert the pulse height measurements conducted with two overlapping blocks of amplifier settings into a single spectrum of lineal energy as[25,39,40]

$$CF = y_\alpha / h_\alpha \, G \tag{1}$$

where G is the gain ratio for the two different amplifier settings. Sources of uncertainties associated with this method of calibration have been discussed elsewhere[49].

Data analysis

The frequency-mean lineal energy, $\overline{y_F}$, and the dose-mean lineal energy, $\overline{y_D}$, are defined as[49]

$$\overline{y_F} = \frac{\int_0^\infty y f(y)\mathrm{d}y}{\int_0^\infty f(y)\mathrm{d}y} \cong \frac{\sum_i y_i f(y_i)}{\sum_i f(y_i)}, \tag{2}$$

$$\overline{y_D} = \frac{\int_0^\infty y d(y)\mathrm{d}y}{\int_0^\infty d(y)\mathrm{d}y} \cong \frac{\sum_i y_i d(y_i)}{\sum_i d(y_i)}, \tag{3}$$

where i is the log bin number[25]. The statistical uncertainty estimated in $\overline{y_F}$ using the error propagation formula[50] is given as

$$\frac{\sigma_{\overline{y_F}}}{\overline{y_F}} = \sqrt{\frac{\sum_i y_i^2 f(y_i)}{\left(\sum_i y_i f(y_i)\right)^2} + \frac{\sum_i f(y_i)}{\left(\sum_i f(y_i)\right)^2}}. \tag{4}$$

A similar expression results for $\overline{y_D}$. Like $\overline{y_F}$, the associated statistical uncertainty, $\sigma_{\overline{y_F}}$, was also smaller than $\sigma_{\overline{y_D}}$.

In radiation protection dosimetry, TEPC based instruments provide information on radiation quality and are also used to obtain a mean quality factor, $\bar{Q}$, in a mixed photon–neutron radiation field[42,51]. For a TEPC, $\bar{Q}$ is given by[43–45]

$$\overline{Q} = \frac{\int Q(L)d(L)\mathrm{d}L}{\int d(L)\mathrm{d}L}, \tag{5}$$

where $Q(L)$ is the quality factor function and $d(L)$ is the dose distribution. Assuming that the linear energy transfer L is equal to lineal energy y[43,51–53], the effective quality factor, $\bar{Q}$, was determined using the lineal energy distribution, $d(y)$ as[39,40]

$$\overline{Q} = \frac{\int Q(y)d(y)\mathrm{d}y}{\int d(y)\mathrm{d}y} = \frac{\sum_i Q(y_i)d(y_i)}{\sum_i d(y_i)}. \tag{6}$$

Various forms of $Q(L)$ have been defined in the past[54–56] but the standard adopted by the ICRU and ICRP is the definition of $Q(L)$ presented in ICRP 60[44],

$$Q(L) = \begin{cases} 1, & L < 10 \text{ keV } \mu\text{m}^{-1} \\ 0.32L - 2.2, & 10 \text{ keV/}\mu\text{m} < L < 100 \text{ keV } \mu\text{m}^{-1} \\ \dfrac{300}{\sqrt{L}}, & L \geq 100 \text{ keV } \mu\text{m}^{-1}. \end{cases} \tag{7}$$

However, the $Q(L)$ relationship defined in ICRP 26[43], is still in use

$$Q(L) = \tag{8}$$
$$\begin{cases} 1, & L \leq 3.5 \text{ keV } \mu\text{m}^{-1} \\ 8.368 \times \log\left(\dfrac{L}{16.05}\right) + 13.75 & \\ \quad \exp[-0.142\exp(0.88\mathrm{Log}(\mathrm{L}-3.5))], & L > 3.5 \text{ keV } \mu\text{m}^{-1} \end{cases}$$

The statistical uncertainty in $\bar{Q}$ was estimated as

$$\frac{\sigma_{\overline{Q}}}{\overline{Q}} = \sqrt{\frac{\sum_i Q(y_i)d(y_i)}{\left(\sum_i Q(y_i)y_i d(y_i)\right)^2} + \frac{\sum_i d(y_i)}{\left(\sum_i d(y_i)\right)^2}}. \tag{9}$$

Sources of uncertainty

There were four sources of uncertainty that contributed to the total uncertainty in the measured data: inherent counting statistics (maximum 3%), drift in the gain of the counter during the measurements (±2–3%)[25], uncertainty in the estimation of energy deposition of alpha particles for the purpose of calibration (±4%)[49], and merging of two spectra collected at two different amplifier gains (3–4%)[25]. These uncertainties were added in quadrature to yield a 6–7% overall experimental uncertainty.

RESULTS AND DISCUSSION

Neutron energy measurements

The neutron energy spectra at proton energies of 2.00–2.40 MeV in steps of 50 keV using a thin ^{7}Li target were measured by the ^{3}He gas filled ionisation chamber as shown in Figure 1. The results have also been summarised in Table 1. The full energy peaks are clearly seen in all spectra, but below 150 keV neutron energy the spectrometer does not resolve the peak, which merges with the tail of the intense thermal neutron peak. In the energy region 150–600 keV, the FWHM was almost energy independent and was about 25 keV. Measured neutron energies were found to be lower than the neutron energies calculated from kinematics[57] for the corresponding proton energies using an infinitely thin target. In an earlier study for beam characterisation, Endo *et al*[58,59] used the same approach to measure the neutron energy spectrum with a thin lithium target. Endo *et al*[58,59] reported the measured neutron energies as 110, 370, 570 and 990 keV corresponding to incident proton energies of 2.0, 2.2, 2.4 and 2.8 MeV, respectively. Our measured neutron energies were found to be higher than those reported by Endo *et al*[58,59]. This difference is attributed to the different target thicknesses used in these experiments. The fluence weighted mean neutron energies show a decreasing trend with increase in target thickness at the same incident proton energy and target–detector geometry[33]. This happens because the neutron energy spectrum broadens and softens with increase in target thickness.

Microdosimetric measurements

Microdosimetric averages of monoenergetic neutrons

Lineal energies in this study were measured in the range of 0.2 to 1000 keV μm^{-1}. The gamma ray contribution extending below 10 keV μm^{-1} was eliminated from the n-γ overlapping region between 1 and 10 keV μm^{-1} by subtracting a measured and scaled ^{60}Co gamma spectrum using the same simulated tissue site size[25,39,40,42]. The complete set of measured lineal energy spectra ranging in neutron energies from 150 to 600 keV corresponding to E_p = 2.00–2.40 MeV, has been presented in Figure 2. The first six spectra ranging in neutron energies $320 < E_n < 600$ keV, have a sharp proton edge at approximately 136 keV μm^{-1} for the higher energies. This decreases to about 110 keV μm^{-1} for 150 keV neutrons. At these neutron energies the range of the recoil protons becomes less than 2 µm.

The values of $\overline{y_F}$ and $\overline{y_D}$ obtained after the subtraction of the gamma ray contribution, for the entire range of measured neutron energies have been listed in Table 2. Srdoc and Marino[47] reported $\overline{y_F}$ and $\overline{y_D}$ values for monoenergetic neutrons of energies 0.44, 1.5 and 6 MeV measured with a simulated site size of 2 µm. The ratio of our calculated $\overline{y_D}$ value to that of Srdoc and Marino[47] is 1.065 while that for $\overline{y_F}$, the ratio is 1.1 at a neutron energy of 448 keV. This provides a fairly good agreement within the experimental uncertainty.

Microdosimetric averages of continuous neutron energy spectra

Microdosimetric measurements performed with monoenergetic neutrons produced using accelerator based thin targets can be compared with those produced using thick targets with continuous spectra with corresponding mean neutron energies. Arnold[25] has reported $\overline{y_D}$ and $\bar{Q}$ using the same counter under similar conditions for a thick ^{7}Li target. The fluence weighted mean neutron energies, $\langle E_n \rangle_\theta$, for a proton beam energy, E_p, and lab angle between the target and detector with the proton beam, θ, were calculated using the thick target neutron energy spectrum as

$$\langle E_n \rangle_\theta = \frac{\int E_n \frac{d^2Y(E_n,\theta)}{d\Omega dE_n} dE_n}{\int \frac{d^2Y(E_n,\theta)}{d\Omega dE_n} dE_n}, \quad (10)$$

where the neutron energy spectrum was calculated by[11–25]

$$\frac{d^2Y(E_n, \theta)}{d\Omega dE_n} = \frac{n_T}{e} \frac{d\sigma}{d\Omega'} \frac{d\Omega'}{d\Omega} \frac{1}{S(E_p)} \frac{dE_p}{dE_n}. \quad (11)$$

The differential cross section, $d\sigma/d\Omega'$, was taken from the compilations of the (p,n) cross-section for ^{7}Li[60] while the stopping power was calculated by using the Bethe formula[61]:

$$\frac{1}{\rho} S(E) = 4\pi N_a z^2 \left(\frac{Z}{A}\right) \frac{m_e c^2}{\beta^2} r_o^2 \ln\left(\frac{2m_e v^2}{I}\right), \quad (12)$$

where N_a is Avogadro's number, $\beta = v/c$, and r_o is the classical electron radius. The integrals in Equation 10 were evaluated by cubic spline integration[62]. Keeping in mind the detector size and the distance between the target and the detector, the solid angle subtended by the detector was very small and hence only the yield at the mean angle, θ, was taken into consideration. These microdosimetric measurements performed with thick targets encompassed the neutron energy range from 35 to 280 keV. The $\overline{y_D}$ measurements performed with monoenergetic neutrons and neutrons with continuous spectra are compared in Table 3. Our results agree fairly well, within 10%, with those of the thick target measurements. An additional source of uncertainty comes from the calculation of mean neutron energies, where uncertainty results from the uncertainty in the ^{7}Li(p,n)^{7}Be differential cross section and the stopping power of protons in the lithium target. However, the difficulty in making and handling thin lithium targets,

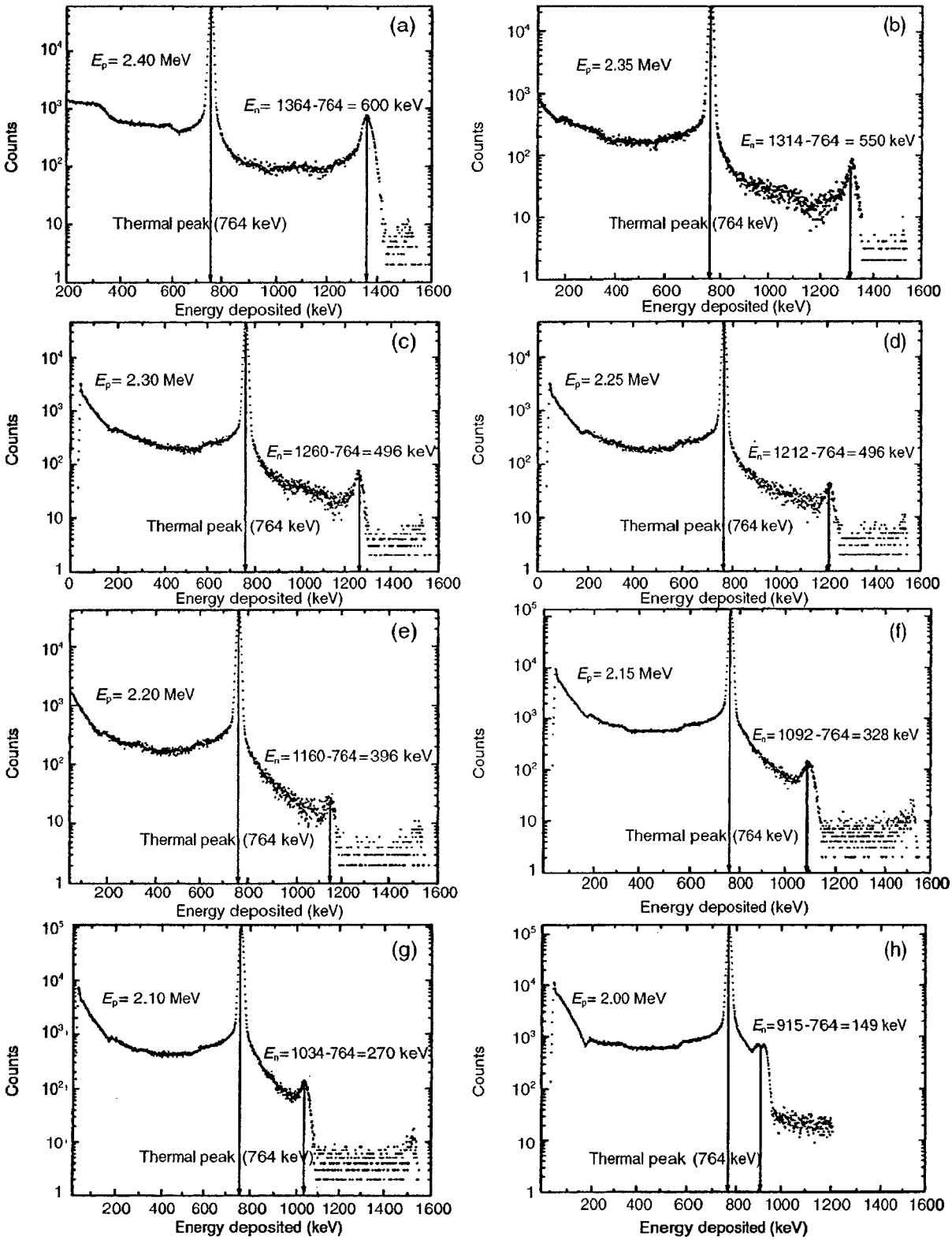

Figure 1. Measured neutron energy spectra (150–600 keV) using a ^{3}He ionisation chamber for E_p = 2.40, 2.35, 2.30, 2.25, 2.20, 2.15, 2.10 and 2.00 MeV.

and more importantly the need for prolonged measurements for thin targets to reduce inherent statistical uncertainty because of lower neutron yield, suggests that the detector performance can be evaluated more conveniently in this neutron energy range using thick lithium targets. The measurements reported in this work encompass the range of neutron energies, which are generally encountered in the field of *in vivo* neutron activation analysis at McMaster University. Measured $\overline{y_D}$ values in the energy range $35 < E_n < 600$ keV using accelerator based thick and thin targets are shown Figure 3. The decrease in the average energy deposited in the simulated site with decreasing neutron energy is both because of the decreasing LET for recoil protons with energies below 70 keV and the decreasing range of the recoil protons in general[47,49].

Radiation quality factor of monoenergetic neutrons

For radiation protection studies, $\bar{Q}$ can be evaluated using the microdosimetric measurements without characterising the complete neutron energy spectrum[49]. The effective quality factors calculated using the measured lineal energy spectra and the definitions of $Q(L)$ given in ICRP 26[43] and 60[44] for the entire range of measured neutron energies have been listed in Table 2.

In the case of $\bar{Q}$ calculated by using the definition of $Q(L)$ given in ICRP 26, $\bar{Q}$ does not change as significantly as $\bar{Q}$ based on ICRP 60. Above 150 keV neutron energy, the quality factor is approximately constant within 15%. These values are in good agreement with the measured published values[35]. For example, Dietze *et al*[35] have reported a value of 12 at a neutron energy of 570 keV measured with a TEPC filled with propane gas simulating a site of 2 μm (wall thickness 2.5 mm). The effective quality factor, $\bar{Q}$, based on our measurements does not change significantly in the energy range of 550 keV to 600 keV (see Table 2). Thus our measured $\bar{Q}$ value at 570 keV is in good agreement with the one reported in the literature[35]. Our measured $\bar{Q}$ value at 150 keV is also in good agreement within the statistical uncertainty with the reported values at 144 keV[35].

Table 1. Measured neutron energies in beam direction using a ^{3}He ionisation chamber.

Proton energy (MeV)	Neutron energy (keV)		
	This work	Endo *et al*[58,59]	Calculated
2.00	149	110	231
2.10	270	—	351
2.15	328	—	408
2.20	396	370	464
2.25	448	—	519
2.30	496	—	573
2.35	550	—	627
2.40	600	570	681

— No measurements reported at those proton energies.

Radiation quality factor of continuous neutron energy spectra

The same procedure was adopted for comparison of our measured $\bar{Q}$ values with those performed with thick targets[25] as discussed in the earlier section. The comparison of measured $\bar{Q}$ based on ICRP 26 and 60, using monoenergetic neutrons with continuous neutron spectra, characterised by the mean neutron energy, has been summarised in Table 4. Our results agree fairly well with thick target results except at one energy point where the agreement is within 12%. One interesting point is that the deviation in effective quality factor from the earlier reported results at any given energy point is of the same order in both cases, i.e. ICRP 26 and 60. It is noteworthy that the measured effective quality factor at the mean neutron energy of 65 keV reported by Arnold[25] was also found to be in good agreement with that of Dietze *et al*[35] at 73 keV (monoenergetic) neutron energy. As the two measurements performed with thick and thin targets not only show good agreement with each other but are also found to be in agreement with those Dietze *et al*[35], this justifies combining the two different data sets shown in Figures 3 and 4.

Quality factor response

Although the measured effective quality factors are in good agreement with the measurements reported earlier, the counter quality factor response, R_Q, defined as the ratio of the measured quality factor, $\bar{Q}$, to the calculated quality factor, Q, in an ICRU tissue sphere at a 10 mm depth, was also examined. Calculated effective quality factors based on ICRP 26 and 60 for monoenergetic neutrons in an ICRU tissue sphere phantom have been reported in the literature. The values for the effective quality factors based on ICRP 26 have been calculated using the algorithm described by Wagner *et al*[63] while the values based on ICRP 60 have been directly read from the graph provided by Dietze *et al*[64]. The detector response, R_Q, calculated from the corresponding measured and calculated Q values in the energy range $35 < E_n < 600$ keV has been plotted in Figure 4. In both cases, whether ICRP 26 or 60, the detector response deteriorates with decreasing mean neutron energy. The maximum underestimate was observed at 65 keV and the situation improved as the neutron energy increased. The counter response based on ICRP 26 is ~0.7 at 150 keV which deteriorates further to ~0.6 at 65 keV. The counter response in the case of ICRP 60 was ~0.65 at 150 keV which dropped to ~0.4 at 65 keV. The decline in counter response in the case of ICRP 60 was found to be much sharper in the case of ICRP 26. This underestimation of the quality factor in the low energy

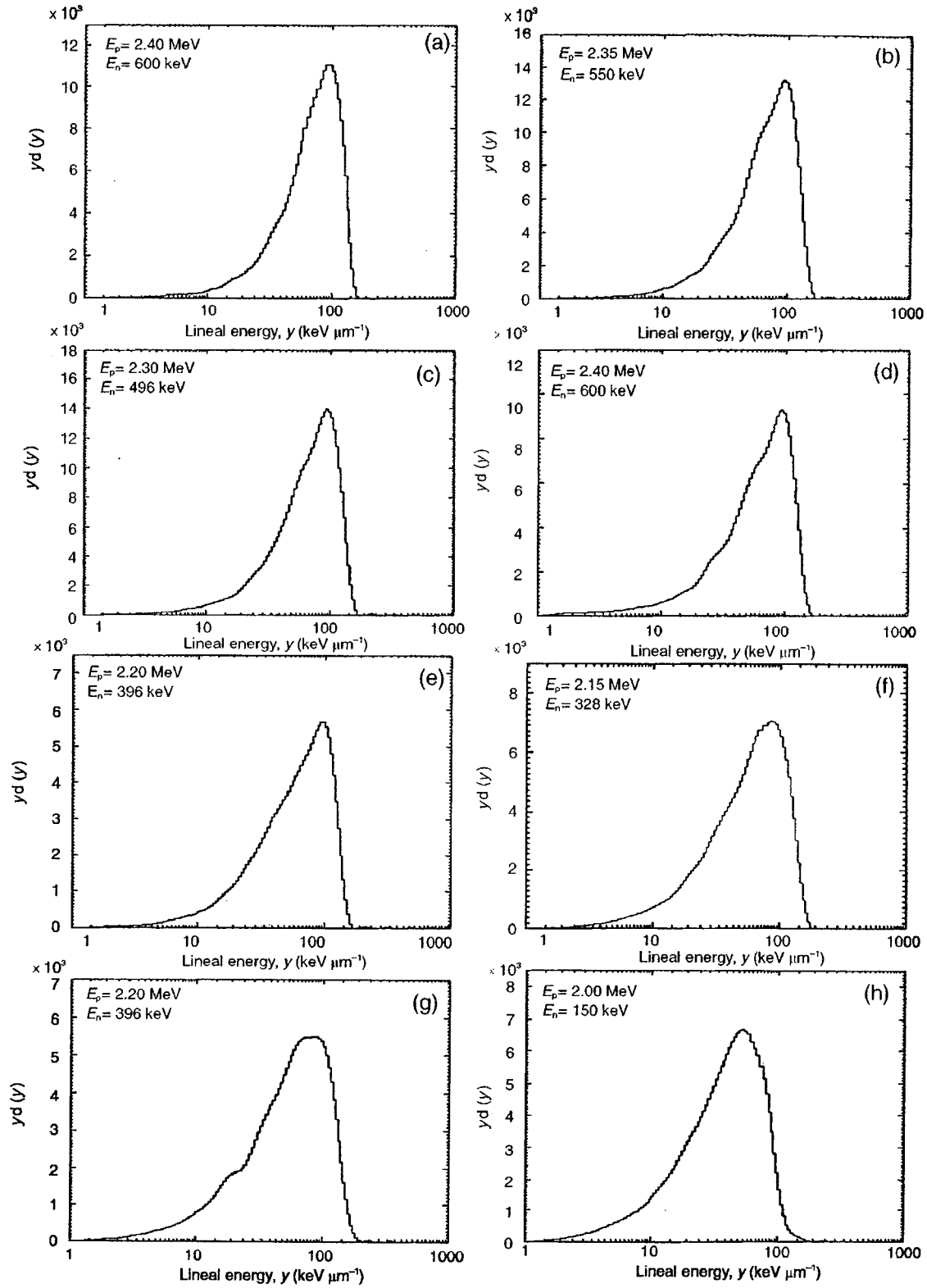

Figure 2. Measured lineal energy distributions of monoenergetic neutrons (150–600 keV) using a 2 μm diameter simulated size for E_p = 2.40, 2.35, 2.30, 2.25, 2.20, 2.15, 2.10 and 2.00 MeV.

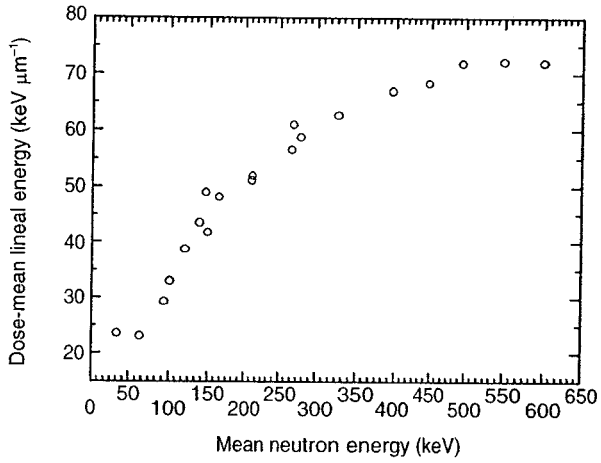

Figure 3. Measured $\overline{y_D}$ values as a function of mean neutron energy using monoenergetic (150–600 keV) and continuous spectra neutrons (35–280 keV).

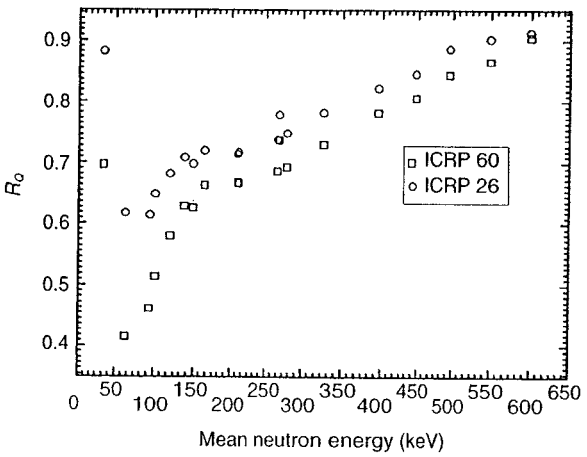

Figure 4. Measured quality factor response, $R_Q(E_n)$, of TEPC simulating a 2 μm diameter simulated tissue sphere. R_Q has been calculated using the measured $\bar{Q}$ values using monoenergetic (150–600 keV) and continuous spectra neutrons (35–280 keV)[25].

region has been estimated to contribute about a half to the deviation of dose equivalent measurement from the ambient dose equivalent[35,36].

An increasing trend in the measured quality factor values with the decrease in sensitive site size at low neutron energies has been reported[35,36,38,53]. The small physical size of the detector is needed to simulate the small tissue site sizes in order improve the operational stability[47]. Although the use of the counters simulating the smaller diameters will improve the counter response, it does not present a feasible solution to the problem as the neutron energies in the fields range from 10 to 200 keV. For 10 keV neutron energy, the average initial recoil proton energy is 5 keV which has a range of ~0.2 μm in propane based TE gas. Moreover, the reduced simulated site size with a small physical diameter will also reduce the sensitivity of the counter. Thus the selection of a site diameter is a compromise between optimal counter operation and the smallest possible site size with a reasonable sensitivity. Other approaches to improve the response of TEPCs have also been discussed in the literature, either by altering the gas composition[37,38,40] or changing the detector wall thickness[38]. Various other approaches have also been discussed elsewhere[49].

Table 3. Comparison of measured $\overline{y_D}$ of monoenergetic and continuous neutron spectra at the corresponding mean neutron energies.

Proton energy (MeV)	Mean neutron energy (keV)	$\overline{y_D}$ (keV μm⁻¹)		
		This work	Arnold[25]	Ratio
2.10	139	41.73*	43.44	0.96
2.15	165	46.90	48.03	0.98
2.20	212	56.94	51.86	1.10
2.25	280	61.22	57.43	1.07

*Value at 149 keV neutron energy.

Table 2. Measured $\overline{y_D}$ and $\bar{Q}$ using accelerator based thin ^{7}Li target in the energy range of 150 to 600 keV.

Neutron energy (keV)	$\bar{Q}$		$\overline{y_D}$ (keV μm⁻¹)	$\overline{y_F}$ (keV μm⁻¹)
	ICRP 60	ICRP 26		
149	11.73 ± 0.25	8.19 ± 0.15	41.73 ± 0.84	22.52 ± 0.31
270	16.23 ± 0.39	10.36 ± 0.24	60.97 ± 1.90	31.29 ± 0.67
328	16.51 ± 0.38	10.57 ± 0.22	62.62 ± 1.80	34.20 ± 0.70
396	17.64 ± 0.46	11.13 ± 0.27	66.86 ± 2.22	39.18 ± 0.97
448	18.17 ± 0.38	11.36 ± 0.22	68.28 ± 1.83	41.51 ± 0.85
496	18.99 ± 0.33	11.79 ± 0.20	71.84 ± 1.63	44.94 ± 0.79
550	19.14 ± 0.34	11.86 ± 0.20	72.19 ± 1.68	46.78 ± 0.86

Derivation of quality factor algorithm

Any physical modification of the counter restricts the experimental conditions under which it can be operated[40,41]. Thus we have followed an analytical approach discussed in the literature[49] to improve the detector response for quality factor evaluation at low energies.

In order to improve the detector response to estimate the effective quality factor and hence the dose equivalent, a modified algorithm suggested in ICRU 36, based on the measured $\overline{y_D}$, and the calculated $Q^{(63,64)}$ in an ICRU tissue sphere at 10 mm depth has been implemented. The modified expression for the effective quality factor based on ICRP 26 and 60 suggested is

$$Q = a + b\overline{y_D}, \tag{13}$$

where a and b are the parameters calculated by fitting a straight line between calculated $Q^{(63,64)}$ and the measured $\overline{y_D}$ values. The expressions for ICRP 26 and 60 were found to be

$$Q_{ICRP60}(\overline{y_D}) = 10.02 + 0.20\,\overline{y_D}, \quad \text{ICRP 60}$$
$$Q_{ICRP26}(\overline{y_D}) = 6.29 + 0.12\overline{y_D}, \quad \text{ICRP 26} \tag{14}$$

with $24 \leq \overline{y_D} \leq 63$ keV μm^{-1}, or in terms of neutron energy, $35 \leq E_n \leq 400$ keV. The fitting procedure has been demonstrated in Figures 5 and 6. Above $\overline{y_D} > 63$ keV μm^{-1} or $E_n = 400$ keV, the underestimation in $\bar{Q}$ is around 10% which is of the same order as the uncertainties generally involved in these measurements.

Implications for ambient dose equivalent, H

The dose equivalent response, R_H, has been calculated as the product of the quality factor response, R_Q, (shown in Figure 4) and the kerma response, R_K. The comparison of dose equivalent response for a TEPC simulating a 2 μm diameter tissue sphere using different reported quality factor algorithms[43,44,49] and other analytical approaches[34] has been presented in Figure 7. In order to calculate R_H, the reported kerma response, R_K, for a 2 μm diameter simulated tissue using a 12.7 mm ($\frac{1}{2}$ inch) diameter counter with 3 mm wall thickness has been taken from Dietze *et al*[35]. Below 50 keV, all algorithms including the adjusted response algorithm developed by Eisen *et al*[34] showed a sharp drop in R_H. The algorithm developed in this work resulted in much

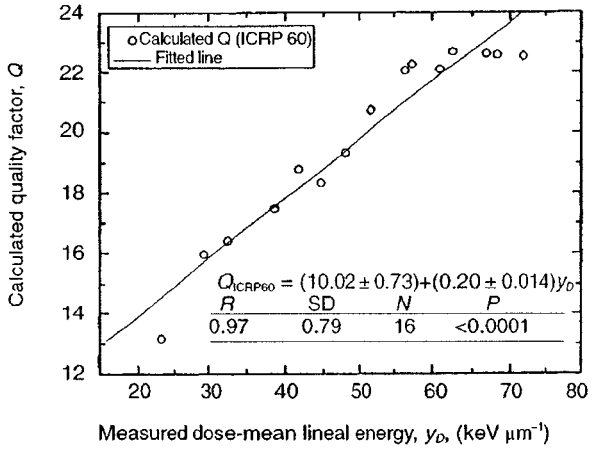

Figure 5. $\bar{Q}$–$\overline{y_D}$ relationship for ICRP 60 in the neutron energy range of $35 \leq E_n \leq 600$ keV.

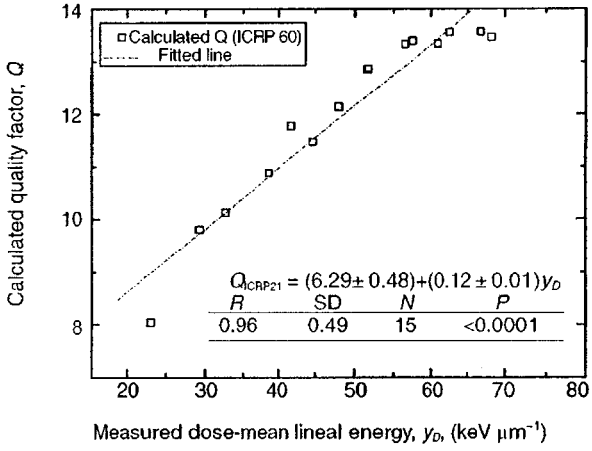

Figure 6. $\bar{Q}$–$\overline{y_D}$ relationship for ICRP 26 in the neutron energy range of $35 \leq E_n \leq 600$ keV.

Table 4. Comparison of measured $\bar{Q}$ of monoenergetic and continuous neutron spectra at the corresponding mean neutron energies.

Proton energy (MeV)	Mean neutron energy (keV)	$\bar{Q}$					
		ICRP 60			ICRP 26		
		This work	Arnold[25]	Ratio	This work	Arnold[25]	Ratio
2.10	139	10.6	11.5	0.92	7.7	8.10	0.95
2.15	165	13.0	12.80	1.02	8.8	8.70	1.01
2.20	212	15.4	13.80	1.12	9.9	9.20	1.08
2.25	280	16.3	15.10	1.08	10.4	9.80	1.06

improved dose equivalent response as compared to other reported algorithms and depends only on the counter's kerma response.

Although the algorithm developed can be used to determine $\bar{Q}$ in neutron fields of unknown specification in the energy range of 35 to 600 keV with a TEPC more accurately than other algorithms[43,44,49], the dose equivalent response is underestimated because of the counter's kerma response at these neutron energies. This was taken into account by defining a new quantity, Q_M, called 'adjusted quality factor' as the quotient of calculated quality factor in an ICRU tissue sphere at a depth of 10 mm to the measured TEPC kerma response. A similar procedure was adopted as discussed in the last section to define

$$Q_M(\overline{y_D}) = -2 \times 10^{-4}(\overline{y_D})^3 + 0.26(\overline{y_D})^2 - 0.87(\overline{y_D}) + 27.31, \text{ ICRP 60}$$
$$Q_M(\overline{y_D}) = -2 \times 10^{-4}(\overline{y_D})^3 + 0.23(\overline{y_D})^2 - 0.76(\overline{y_D}) + 19.17, \text{ ICRP 26} \quad (15)$$

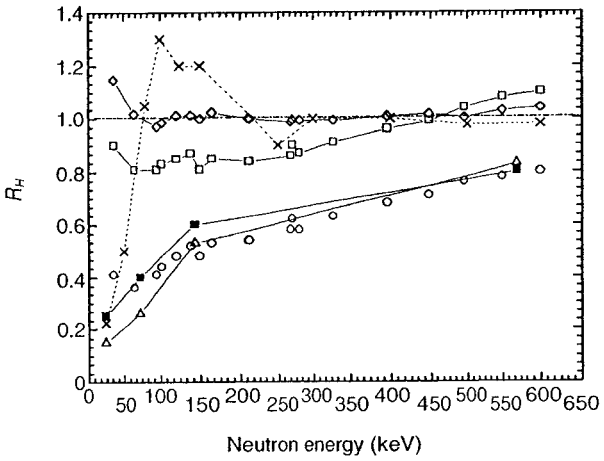

Figure 7. Comparison of dose equivalent responses in the neutron energy range of $35 \leq E_n \leq 600$ keV for 2 μm simulated diameter using different algorithms for the quality factor evaluation and other reported analytical approaches. □ This work using ICRP 60 $Q(y_D)$; ◇ This work using ICRP 60 $Q_m(y_D)$; ○ ICRU 36: $Q(y_D) = 0.8 + 0.14\ y_D$; ■ Using ICRP 26 $Q(L)$, Dietze *et al* (1989); △ Using ICRP 60 $Q(L)$; ..X.. Eisen *et al* (1986): adjusted response.

with $R^2 = 0.97$. The dose equivalent response calculated using the adjusted quality factor as $R_H = R_K R_{QM}$ has also been shown in Figure 7. This resulted in a smoother response curve as compared to the adjusted response reported by Eisen *et al*[34].

CONCLUSIONS

The main aim of this study was to investigate the response of a TEPC to estimate the quality factors and to improve the understanding of the underlying physical processes in order to obtain information on further improvements for dosimetry at the *in vivo* neutron activation facility at McMaster University. The objective was achieved by combining the two different measured data sets using the same counter under similar conditions. The following conclusions can be drawn from this work.

(1) The counter failed to provide a flat R_Q response based on the definitions of $Q(L)$ provided in ICRP 26[43], ICRP 60[44] and $Q(\overline{y_D})$ in ICRU 36[49] in the energy range of 35 to 600 keV and showed a sharp drop below 200 keV neutron energy. This decreasing trend was much more pronounced in the case of ICRP 60 than ICRP 26.

(2) A modified algorithm based on $\overline{y_D}$ values measured using monoenergetic and continuous spectra neutron sources and the calculated Q in an ICRU tissue sphere has been implemented to provide a better estimate of the effective quality factors in the energy range of 35 to 600 keV for low energy accelerator based *in vivo* neutron activation measurements.

(3) Comparing the quality factor algorithm developed here in this work, below 50 keV neutron energy, different algorithms for quality factor evaluation and the adjusted response algorithm developed by Eisen *et al*[34] showed a sharp drop in R_H.

(4) Further improvement in the counter's R_H response was made by taking the counter's kerma response into account and defining $Q_M(\overline{y_D})$, a relatively flat dose equivalent response curve was obtained in the energy range of 35 to 600 keV neutron energy as compared to other algorithms and approaches.

REFERENCES

1. Palmer, H. E., Nelp, W. B., Murano, R. and Rich, C. *The feasibility of* in vivo *neutron activation analysis of total body calcium and other elements of body composition.* Phys. Med. Biol. **13**(2), 269–279 (1968).
2. Chamberlain, M. J., Fremlin, J. H., Holloway, I. and Peters, D. K. *Use of the cyclotron for whole body neutron activation analysis: theoretical and practical considerations.* Int. J. Appl. Radiat. Isot. **21**, 725–734 (1970).
3. Boddy, K., Dennis, J. A. and Lawson, R. C. *Neutron dosimetry in the* in vivo *measurement of intrathyroidal iodine in man by activation analysis.* Phys. Med. Biol. **14**(3), 471–480 (1969).
4. Boddy, K., Elliott, A., Robertson, I., Mahaffy, M. E. and Holloway, I. *A high sensitivity dual-detector shadow-shield whole-body counter with an 'invariant' response for total body* in vivo *neutron activation analysis.* Phys. Med. Biol. **20**(2), 296–304 (1975).

5. Evans, H. J., Leblanc, A. D. and Johnson, P. C. *Facility for regional* in vivo *neutron activation analysis of skeletal calcium.* Phys. Med. Biol. **24**, 181–187 (1979).
6. Cohn, S. H. *The present state of* in-vivo *neutron activation analysis in clinical diagnosis, and therapy.* At. Energ. Rev. **18**(3), 599–660 (1980).
7. Beddoe, A. H., Zudmeer, H. and Hill, G. L. *A prompt gamma* in vivo *neutron activation analysis facility for measurement of total body nitrogen in the critically ill.* Phys. Med. Biol. **29**, 371–383 (1984).
8. Heymsfield, S. B., Wang, J., Lichtman, S., Kamen, Y., Kehayias. J. and Pierson, R. N. Jr. *Body composition in elderly subjects: A critical appraisal of clinical methodology.* Am. J. Clin. Nutr. **50**(5 Suppl), 1167–1175; 1231–1235 (1989).
9. Chettle, D. R. and Fremlin, J. H. *Techniques of* in vivo *neutron activation analysis.* Phys. Med. Biol. **29**(9), 1011–1043 (1984).
10. Ellis, K. J. *Human body composition:* in vivo *methods.* Physiol Rev. **80**(2), 649–80 (2000).
11. Ritchie, A. I. M. *Neutron yields and energy spectra from thick target Li(p,n) source.* J. Phys. D: Appl. Phys. **9**, 15–26 (1976).
12. Meadows, J. W. *Determination of the energy scale for neutron cross-section measurements employing a monoenergetic accelerator.* ANL/TDM-25 (1977).
13. Kononov, V. N., Poletaev, E. D. and Yurlov, B. D. *Absolute yield and spectrum of neutrons from the $^{7}Li(p,n)^{7}Be$.* At. Energ. **43**, 947–949 (1977).
14. Clayton, C. G. and Spackman, S. *Neutron intensity and energy distributions from protons in the energy range 1.95 MeV to 5.5 MeV incident on thick targets of lithium.* Int. J. Appl. Radiat. Isot. **36**(1), 13–50 (1985).
15. Yanch, J. C., Zhou, X. L., Shefer, R. E. and Klinkowstein, R. E. *Accelerator-based epithermal neutron beam design for neutron capture therapy.* Med. Phys. **19**(3), 709–721 (1992).
16. Allen, D. A. and Benyon, T. D. *A design study for an accelerator-based epithermal neutron beam for BNCT.* Phys. Med. Biol. **40**, 807–821 (1995).
17. Zhou, X. L. and Lee, C. *Analysis of epithermal neutron production by near-threshold (p,n) reactions.* Appl. Radiat. Isot. **48**, 1571–1575 (1997).
18. Zhou, X. L. and Lee, C. *Lithium compounds as targets for (p,n) reactions.* Appl. Radiat. Isot. **48**, 1493–1496 (1997).
19. Pignol, J. P., Cuendet, P., Brassart, N., Fares, G., Colomb, F., M'Bake Diop, C., Sabattier, R., Hachem, A. and Prevot, G. *Combined use of FLUKA and MCNP-4A for Monte Carlo simulation of the dosimetry of ^{10}B neutron capture enhancement of fast neutron irradiations.* Med. Phys. **25**(60), 885–891 (1998).
20. Magagula, T. K. and Watterson, J. W. *The excitation of isomeric states by accelerator neutrons from the $^{7}Li(p,n)^{7}Be$ reaction and their application in selective activation analysis.* Nucl. Instrum. Methods Phys. Res. B **139**, 293–297 (1998).
21. Bayanov, B. F. and 14 others. *Accelerator-based neutron source for the neutron-capture and fast neutron therapy at hospital.* Nucl. Instrum. Methods Phys. Res. A **413**(2–3), 397–426 (1998).
22. Powell, J. A., Ludewig, H., Todosow, M. and Reich, M. *Target and filter concepts for accelerator-driven boron neutron capture therapy applications.* Nucl. Tech. **125**, 104–115 (1999).
23. Lee, C. L. and Zhou, X. L. *Thick target neutron yields for the $^{7}Li(p,n)^{7}Be$ reaction near threshold.* Nucl. Instrum. Methods Phys. Res. B **152**, 1–11 (1999).
24. Arnold, M. L., McNeill F. E., Prestwich, W. V. and Chettle D. R. *System design for in-vivo neutron activation analysis measurements of manganese in the human brain: based on Monte Carlo modeling.* Appl. Radiat. Isot. **53**, 651–656 (2000).
25. Arnold, M. L. *Development of an accelerator based system for* in vivo *neutron activation analysis measurements of manganese in humans.* PhD Thesis, McMaster University, Hamilton, ON, Canada (2000).
26. Palerme, S. *Pilot studies for* in-vivo *bone aluminum measurements.* MSc Thesis, McMaster University, Hamilton, ON, Canada (1993).
27. Pejovic-Milic, A. *An accelerator-based* in-vivo *measurement of aluminum in human bone by neutron activation analysis.* MSc Thesis, McMaster University, Hamilton, ON, Canada (1998).
28. Pejovic-Milic, A. In-vivo *measurement of some trace elements in human bone.* PhD Thesis, McMaster University, Hamilton, ON, Canada (2001).
29. Pejovic-Milic, A., McNeill, F. E., Prestwitch, W. V., Waker, A. J. and Chettle, D. R. *Development of an accelerator-based determination of aluminum burden in peripheral bone by neutron activation analysis.* Appl. Radiat. Isot. **49**(5/6), 717–719 (1998).
30. Pejovic-Milic, A., Arnold, M. L., McNeill, F. E. and Chettle, D. R. *Monte Carlo design study for* in-vivo *bone aluminum measurement using a low energy accelerator beam.* Appl. Radiat. Isot. **53**, 657–664 (2000).
31. Arnold, M. L., McNeill, F. E. and Chettle, D. R. *The feasibility of measuring manganese concentrations in human liver using neutron activation analysis.* NeuroToxicol. **20**(2–3), 407–412 (1999).
32. Arnold, M. L., McNeill, F. E., Stronach, I. M., Waker, A. J., Pejovic-Milic, A. and Chettle D. R. *An accelerator based system for* in vivo *neutron activation analysis measurements of manganese in human hand bones.* Med. Phys. **29**(11), 2718–2724 (2002).
33. Aslam, Prestwich, W. V., McNeill, F. E. and Waker, A. J. *Spectrometry and dosimetry for low energy accelerator based in-vivo measurements.* Annual Report McMaster Accelerator Laboratory, McMaster University, Hamilton, ON, Canada (2001).

34. Eisen, Y., Brake, R. J., Vasilik, D. G., Erkkila, B. H. and Littlejohn, G. J. *The performance of low pressure tissue-equivalent chambers and a new method for parameterising the dose equivalent.* Radiat. Prot. Dosim. **15**(2), 117–130 (1986).
35. Dietze, G. and 10 others. *Intercomparison of dose equivalent meters based on microdosimetric techniques.* Radiat. Prot. Dosim. **23**(1/4), 227–234 (1988).
36. Alberts, W. G., Dietze, E., Guldbakke, S., Kluge, H. and Schuhmacher, H. *International intercomparison of TEPC systems used for radiation protection.* Radiat. Prot. Dosim. **29**, 47–53 (1989).
37. Pihet, P., Menzel, H. G. Alberts, W. G. and Kluge, H. *Response of tissue-equivalent proportional counters to low and intermediate energy neutrons using modified TE-^{3}He gas mixtures.* Radiat. Prot. Dosim. **29**(1–2), 113–118 (1989).
38. Gerdung, S., Grillmaier, R. E., Lim, T., Pihet, P., Schuhmacher, H. and Ségur, P. *Performance of TEPCs at low pressures: some attempts to improve their dose equivalent response in the neutron energy range from 10 keV to 1 MeV.* Radiat. Prot. Dosim. **52**(1–4), 57–59 (1994).
39. Waker, A. J. *Principles of experimental microdosimetry.* Radiat. Prot. Dosim. **61**(4), 297–308 (1995).
40. Khaloo, R. and Waker, A. J. *An evaluation of hydrogen as a TEPC counting gas in radiation protection microdosimetry.* Radiat. Prot. Dosim. **58**(3), 185–191 (1995).
41. Taylor, G. C. *An analytical correction for the TEPC dose equivalent response problem.* Radiat. Prot. Dosim. **61**(1–3), 67–70 (1995).
42. Nunomiya, T., Kim, E., Kurosawa, T., Taniguchi, S., Yonai, S., Nakamura, T., Nakane, Y., Sakamoto, Y. and Tanaka, S. *Measurement of lineal-energy distributions for neutrons of 8 keV to 65 MeV by using a tissue-equivalent proportional counter.* Radiat. Prot. Dosim. **102**(1), 49–59 (2002).
43. ICRP. *Recommendations of the ICRP.* Ann. ICRP **1**(3). ICRP Publication 26 (Oxford: Pergamon Press) (1977).
44. ICRP. *Radiation protection recommendation of the International Commission on Radiological Protection.* ICRP Publication 60 (Oxford: Pergamon Press) (1991).
45. ICRU. *The quality factor in radiation protection.* ICRU Report 40 (Bethesda, MD: ICRU Publications) (1986).
46. Cousins, T. *The application of monochromatic photoneutron spectroscopy in an examination of nuclear levels of ^{180}Ta, ^{202}Tl and ^{204}Tl.* PhD Thesis, McMaster University, Hamilton, ON, Canada (1982).
47. Srdoc, D. and Marino, S. A. *Microdosimetry of monoenergetic neutrons.* Radiat. Res. **146**(4), 466–474 (1996).
48. ICRU. *Stopping powers and ranges for protons and alpha particles.* ICRU Report 49 (Bethesda, MD: ICRU Publications) (1983).
49. ICRU. *Microdosimetry.* ICRU Report 36 (Bethesda, MD: ICRU Publications) (1983).
50. Knoll, G. F. *Radiation detection and measurement.* 2nd Edn (New York: Wiley) (1989).
51. Folkerts, K. H., Menzel, H. G., Schuhmacher H. and Arend, E. *TEPC radiation protection dosimetry in the environment of accelerators and at nuclear facilities.* Radiat. Prot. Dosim. **23**(1–4), 261–264 (1988).
52. Kawecka, B., Morstin, K. and Booz, J. *Optimization of the design of microdosimetric dose equivalent meters.* Radiat. Prot. Dosim. **9**(3), 203–206 (1984).
53. Kadachi, A., Waheed, A., Al-Eshaikh, M. and Obeid, M. *Use of photodiode in microdosimetry and evaluation of effective quality factor.* Nucl. Instrum. Methods Res. A **404**(2–3), 400–406 (1998).
54. Baum, J., Kuehner, V. and Chase, R. *Dose equivalent meter designs based on tissue equivalent proportional counters.* Health Phys. **19**, 813–824 (1970).
55. Stinchcomb, T. G. and Borak, T. B. *Neutron quality parameters versus energy below 4 MeV from microdosimetric calculations.* Radiat. Res. **93**(1), 1–18 (1983).
56. Townsend, W., Wilson, J. and Cucinotta, F. *Simple parameterization for quality factors as a function of linear energy transfer.* Health Phys. **53**(5), 531–532 (1987).
57. Evans, R. D. *The atomic nucleus* (New York: McGraw-Hill) (1955).
58. Endo, S. and 12 others. *Neutron generator at Hiroshima university for use in radiobiology study.* J. Radiat. Res. (Tokyo) **36**(2), 91–102 (1995).
59. Endo, S., Hoshi, M., Takada, J., Tauchi, H., Matsuura, S., Takeoka, S., Kitagawa, K., Suga, S. and Komatsu, K. *Neutron generator (HIRRAC) and dosimetry study.* J. Radiat. Res. (Tokyo) **40**(Suppl.) 14–20 (1999).
60. Liskien, H. and Paulsen, A. *Neutron production cross-sections and energies for the reactions ^{7}Li(p,n)^{7}Be and ^{7}Li(p,n)^{7}Be*.* At. Data Nucl. Data Tables **15**, 57–84 (1975).
61. Attix, F. H. *Introduction to radiological physics and radiation dosimetry.* (New York: Wiley) (1986).
62. Press, W. H., Teukolsky, S. A., Vetterling, W. T. and Flannery, B. P. *Numerical recipes in FORTRAN 77: the art of scientific computing.* 2nd edn, Vol. 1. In: FORTRAN numerical recipes (Cambridge University Press) (1992).
63. Wagner, S. R., Grosswendt, B., Harvey, J. R., Mill, A. J., Selbach, H. J. and Siebert, B. R. L. *Unified conversion functions for the ICRU operational radiation protection quantities.* Radiat. Prot. Dosim. **12**(2), 231–235 (1985).
64. Dietze, G. and Siebert, B. R. *Photon and neutron dose contributions and mean quality factors phantoms of different size irradiated by monoenergetic neutrons.* Radiat. Res. **140**(1), 130–133 (1994).

CHAPTER V

Paper IV

This article describes a method used to measure and control the radiation dose equivalent received to the patient's hand undergoing the irradiation of hand in the facility developed at the McMaster University 3 MV Van de Graaff accelerator for the IVNAA measurement of toxic elements in human hand bones.

The work presented in this paper was performed by me under the supervision of Drs. Prestwich and McNeill. The TEPC based microdosimetric system and the computer programs employed for data acquisition and analysis of the raw data that was used in the experiments at MAL had been previously developed and characterized at AECL, Chalk River, Canada by Dr. Waker. Dr. Waker acted as a consultant and collaborator for the research presented in this paper. The manuscript was written by me and edited by Drs. Prestwich, McNeill and Waker.

Estimation of Dose Equivalents to Patients Undergoing Hand Irradiation at the Facility Developed for Accelerator Based *In-Vivo* Neutron Activation Measurements in Human Hand Bones

Aslam[1], W.V. Prestwich[1], F.E. McNeill[1] and A.J. Waker[2]

[1]Medical Physics and Applied Radiation Sciences Unit, McMaster University, Hamilton, ON, Canada, L8S 4K1.

[2]AECL, Chalk River Laboratories, Chalk River, ON, Canada K0J 1J0

ABSTRACT

The measurement of long-term exposure of many potentially toxic trace elements is monitored through bone levels. *In-vivo* neutron activation analysis provides a practical and feasible technique for non-invasive measurements of various trace elements in bones. A neutron irradiation facility for *in-vivo* neutron activation (IVNAA) measurement of aluminum and manganese in human hands has been developed at the McMaster University 3 MV Van de Graaff accelerator. Before implementing these modalities into clinical practice, prior knowledge of subject dose is always required in order to implement the proposed dose limits for diagnostic procedures (ICRP 26 & 60). Absorbed doses to the irradiated hand phantom are estimated using a tissue equivalent proportional counter (TEPC) filled with propane based tissue equivalent gas simulating 2 μm tissue equivalent (TE) diameter. These counters do not provide LET information for the neutron energies employed here at McMaster University accelerator laboratory (MAL) for IVNAA. Thus we have investigated experimentally the counter response (R_Q) to estimate the effective quality factor based on the definitions of *Q(L)* provided in ICRP 60 as a function of neutron energy using monoenergetic and continuous neutron spectra in the energy range of 35 to 600 keV. The counter failed to provide a flat R_Q response and showed a sharp drop below 200 keV neutron energy. We have developed a neutron quality factor algorithm of the form, $Q(\overline{y_D}) = a + b\,\overline{y_D}$, to evaluate the quality factors that utilizes measured *dose-mean lineal energy*, $\overline{y_D}$, but does not attempt to correlate lineal energy with LET. Measured quality factors in the hand irradiation facility using this algorithm have been compared with those calculated by using MCNP. The algorithm overestimates the quality factors in the center of the irradiation facility at beam energies 2.00 and 2.25 MeV by 30 and 8% respectively. Using the measured quality factors and dose rates as a function of position on the phantom surface, the dose equivalent averaged over the phantom surface was estimated. Based on the estimated doses received to the patient hand, the proposed irradiation procedure for the IVNAA measurement of manganese in human hands (Med Phys 29(11) (2002) 2718) with normal (1 ppm) and elevated manganese content can be carried out without violating the prescribed dose limits for such diagnostic procedures.

I. INTRODUCTION

The measurement of long-term exposure of many trace elements is monitored through bone levels.[1] A neutron irradiation facility for *in-vivo* neutron activation (IVNAA) measurement of aluminum and manganese found in trace amounts in human hands has been developed at the McMaster University 3 MV Van de Graaff accelerator.[2-11] The reports of the *in-vivo* measurements of aluminum and manganese in human hand bones by activation analysis at the McMaster University 3 MV Van de Graaff accelerator have dealt primarily with the technique and demonstrated its clinical feasibility. Because of the radiation risk involved in such diagnostic procedures, the dosimetry has been considered separately and is discussed in this paper.

This article describes a method used to measure and control the radiation dose equivalent received to the patient's hand during irradiation in the facility developed at the McMaster University 3 MV Van de Graaff accelerator for the IVNAA measurement of potentially toxic elements in human hand bones. We further discuss the development of a neutron quality factor algorithm for a TEPC simulating 2 μm TE diameter to estimate the effective quality factors in the hand irradiation facility. Using the measured dose rates reported earlier as a function of position[7, 11] in the hand irradiation facility and the quality factors measured at the corresponding positions in this work we report a methodology to estimate the average radiation dose equivalent received to the patient's hand as a result of *in-vivo* measurement. It is essential to determine the average radiation dose equivalent received to the patient's hand because of the dose heterogeneity defined as D_{max}/D_{min} is 3 for E_p = 2.25 MeV and 5 for E_p = 2.00 MeV on the phantom surface. **Section II** describes the materials and methods used for the neutron quality factor evaluation using a TEPC in the neutron irradiation facility. The measurement technique for lineal energy distributions is also discussed in this section. To compare the measured quality factors with the calculations performed using MCNP4B, the computational procedure to calculate the probability density functions (PDFs) for energy and angular distributions of neutrons produced using thick lithium target via ^{7}Li(p, n)^{7}Be reaction is outlined in this section. **Section III** presents the results of comparison of measured quality factors using the quality factor algorithm (developed in this work) in the irradiation facility with the MCNP calculations. The objective of this study was achieved by first describing the variation of measured quality factor response (R_Q) of TEPC as a function of neutron energy in the energy range $35 \leq E_n \leq 600$ keV by equating the LET (L) to lineal energy (y). In agreement with earlier studies for determining R_Q using the definition of

quality factor function, *Q(L)*, given in ICRP 26[12] and the approximation $L = y$ used commonly in radiation protection studies,[13-20] the TEPC also fails to provide a flat R_Q response based on the definitions of *Q(L)* provided in ICRP 60[21] and shows a similar but a sharper drop below 200 keV neutron energy because of the invalidity of the underlying assumption $L = y$ for 2 μm TE simulated diameter. The approximation $L = y$ which arises from Rossi's algorithm[22] for transformation of the measured lineal energy dose distribution, *d(y)*, into an LET dose distribution, *d(L)*, the underlying assumptions for the transformation algorithm also become invalid in this energy region. Thus the development of a neutron quality factor algorithm of the form, $Q(\overline{y_D}) = a + b\,\overline{y_D}$, utilizing the average of measured lineal energy dose distribution is also reported in this section. Finally we report a methodology to calculate the average dose equivalent received to a patient's hand by taking into account the spatial distribution of dose equivalent on the hand surface. **Section IV** concludes the study that the proposed irradiation procedure for the IVNAA measurement of manganese in human hands[7, 11] with normal (1 ppm) and elevated manganese content can be carried out without violating the prescribed dose limits for such diagnostic procedures.

II. MATERIALS AND METHODS

A. Neutron Source

The 3 MV Van de Graaff accelerator at the McMaster University Accelerator Laboratory (MAL) was used to produce low energy fast neutrons of mean neutron energy less than 1 MeV by bombarding protons on thick and thin lithium (^{7}Li) metal targets. Monoenergetic neutrons at MAL were produced using thin lithium metal targets prepared by vacuum deposition of lithium onto 1-mm-thick tantalum disks. The energy and yield of these monoenergetic neutrons in a given direction depend upon the incident proton beam energy, E_p. Monoenergetic neutrons of energy down to 150 keV were obtained by varying the proton beam energy above the threshold of the ^{7}Li(p, n)^{7}Be interaction (E_{th} = 1.88 MeV). Unlike thin targets, thick lithium targets produce energy spectra, which are continuous and have a wide range. Thick targets at the facility were prepared by simply putting a weighed amount of the target material into the target holder and then pressing to a pressure of 6895 kPa (1000 PSI). These thin and thick targets were mounted at the end of a beam duct and cooled with water to prevent heating by proton beam currents. This facility can be operated at proton beam currents as low as a few nA[23] up to 100 μA.[10] The total neutron yield (n/μC) of a thick lithium target increase with the increase in the incident proton beam energy. This increase

in total neutron yield of a thick lithium target with the increase in beam energy[24] is accompanied by an increase in mean neutron energy (80 and 225 keV at E_p = 2.00 and 2.25 MeV respectively, averaged in the forward direction).[25] Kerma coefficients in tissue equivalent materials also increase with the increase in neutron energy (E_n > 30 eV).[26] To reduce the patient dose, lower beam energies (E_p = 2.00 MeV) are preferred for IVNAA using higher beam currents to compensate for lower neutron yield at these beam energies.[2-11] The neutron activation (n, γ) cross-sections at these neutron energies are very low for the isotopes of interest (Al and Mn).[2-11] Thus in order to maximize the activation of the isotope in question and also to minimize the dose at the same time, the direct neutron beams are moderated in a manner dependent upon the application. The beam current and the irradiation time depending upon the half-life of the radioisotope produced as a result of activation are also chosen to be optimal.[2-11]

B. Hand Irradiation Facility for IVNAA

The hand irradiation facility designed for IVNAA of aluminum[2-5, 9, 10] and manganese[7, 11] is illustrated in **Figure 1**. This irradiation facility has the inner dimensions of 30×30×4.5 cm^3 and consists of 2.4 cm thick polyethylene walls on five of the six sides. These walls are used to moderate and reflect the neutrons entering the irradiation facility. The open side of the irradiation facility is used to insert hand phantoms inside the facility for IVNAA.

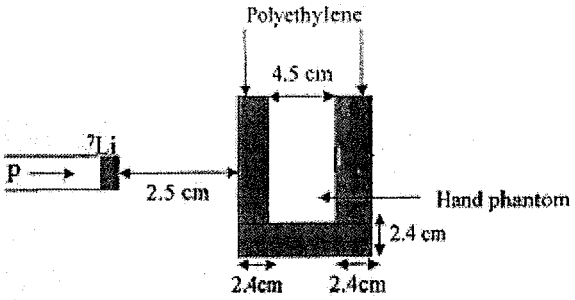

FIG. 1: Schematic diagram of the hand irradiation facility used IVNAA at MAL.

C. Estimation of Dose Equivalent to the Patient Hand

The McMaster University Human Ethics Board restricts the maximum local dose equivalent to the irradiated hand to less than 50 mSv for an *in-vivo* measurement of toxic trace elements.[10, 11] The procedure to estimate the dose equivalent to the patient's irradiated hand using a TEPC simulating 2 μm TE diameter has been outlined earlier.[7, 9, 10, 11] The neutron field inside the irradiation facility is non-uniform[5, 7, 10, 11] i.e., the ratio of the maximum (at the

center) to the minimum dose on the phantom surface (which occurs on the extreme edges of the phantom) is greater than 1.30. However, a conservative dose estimate is made by measuring the neutron and gamma dose rates in the center of the hand irradiation facility (where the maximum dose rate occurs at all beam energies) using a TEPC at the selected beam energy. The total dose equivalent to the patient's irradiated hand is estimated by multiplying the measured dose rates with appropriate quality factors, and with the period of irradiation and the beam current.

D. Microdosimetric Measurements

The spectra of single energy-deposition events due to secondary charged particles produced in the cavity wall and the gas of the TEPC simulating a unit density sphere of a few micrometers diameter is used to estimate the absorbed doses and neutron quality factors in mixed n-γ fields. A lineal energy spectrum of low energy neutrons contains mainly a 'proton peak' due to the energy deposition by elastically recoiled protons with hydrogen ($^{1}H(n, n)^{1}H$) and capture protons produced by thermal neutrons ($^{14}N(n, p)^{14}C$).[17, 20, 27, 28] The maximum deposited energy is from protons with energies in the region of maximum stopping power (Bragg peak) and longest path length across the cavity. is characterized by a sharp cut-off known as the 'proton edge'. The mid point of the edge is designated as the proton edge. The γ–ray contamination of the neutron field and $^{1}H(n, \gamma)^{2}H$ interactions in the wall and cavity of TEPC also give rise to an 'electron peak' due to low energy deposition events in the lineal energy spectrum. [17, 20, 27, 28] The partial overlap of the two peaks is separated by a fitting procedure.[7, 17, 20, 27, 28] Thus measuring the energy deposited in simulated microscopic tissue volumes in a mixed n-γ field enables the separation of the contribution of different LET radiations; the quality factors of different LET radiations can be estimated and hence the dose equivalent can be determined.

A Rossi-type spherical proportional counter (model LET ½″, Far West Technology, Goleta, USA), with 2.5 mm thick walls made of A-150 tissue-equivalent plastic (TEPC), filled with propane based TE gas at a pressure of 8.8 kPa to simulate a tissue sphere of 2 μm diameter was used to measure the lineal energy distributions of the monoenergetic and continuous energy neutron fields.

Lineal energy measurements of monoenergetic and continuous energy neutrons in the energy range $35 \leq E_n \leq 600$ keV were made in-air to evaluate the counter's quality factor response and further to derive a quality factor algorithm utilizing the average of the measured lineal

energy dose distributions (afterward referred as *dose-mean lineal energy*), $\overline{y_D}$. The maximum monoenergetic neutron energy for the development of the neutron quality factor algorithm was chosen as the thick target neutron energy spectrum at E_p = 2.25 MeV which extends to approximately 520 keV neutron energy while the maximum energy neutrons emitted in the forward direction at E_p = 2.00 MeV are 230 keV.[7, 28, 29]

Dose-mean lineal energies estimated from the lineal energy measurements made in the center and at horizontal distances of ±7 cm in the irradiation facility for beam energies of 2.00 and 2.25 MeV were used to evaluate the neutron quality factors using the derived algorithm. The measured quality factors were then used to estimate the radiation dose equivalent received to the patient hand as a result of IVNAA measurement of Mn at MAL.[7, 11]

1. Measurement Technique

The experimental technique generally followed that described in the literature.[7, 17, 20, 27, 28] The proportional counter and a low-noise preamplifier connected directly to the anode of the counter were located in the irradiation room. Analogue pulses from the preamplifier were fed through an ORTEC 855 dual SPEC amplifier into two 16 k analogue-to-digital converters (ADCs) and stored in an ORTEC HM 413 HISTO memory unit. The low and high gain histograms obtained were finally transferred to a Macintosh Power PC book. The processing of the raw data was carried out employing the computer programs written in **KMAX** version 4.1 developed at AECL, Chalk River, Canada.[7, 17, 28]

2. Counter Calibration

The pulse height spectra measured with the TEPC were converted into the lineal energy distributions *f(y)* and *d(y)* by applying the appropriate calibration factors. The system was calibrated by irradiating the counter with a finely collimated internal ^{244}Cm alpha source which deposits 170 keV[30] in a 2 μm diameter TE gas corresponding to a lineal energy of y_α= 127 keV/μm. The mean pulse height, h_α, corresponding to the mean energy imparted in the cavity was evaluated at an amplifier gain setting, A_α, by fitting a Gaussian curve to the measured peak. Using y_α and h_α, the calibration factors were calculated to convert the pulse height measurements, h, conducted with two overlapping blocks of amplifier gain settings (A_1 and A_2) into a single spectrum of lineal energy as[7, 17, 20, 28]

$$y = \frac{y_\alpha}{h_\alpha} G \times h \qquad (1)$$

where G is the gain ratio for the two different amplifier settings (A_α/A_1 and A_α/A_2). Sources of uncertainties associated with this method of calibration have been discussed elsewhere.[31] The calibration was checked before and after each measurement and the average h_α was used for the purpose of calibration.

3. Data Analysis

The effective quality factor, $\overline{Q}$, can be determined from the LET dose distribution, *d(L)*, and the quality factor function, *Q(L)*, as[32]

$$\overline{Q} = \frac{\int Q(L)d(L)dL}{\int d(L)dL} \tag{2}$$

To evaluate the quality factor, $\overline{Q}$, the lineal energy dose distribution, *d(y)*, measured with a TEPC is transformed into an LET dose distribution, *d(L)*, using an algorithm suggested by Rossi.[22] This algorithm is based on the assumptions that the tracks of the charged particles generated by neutron interactions in the counter wall are long compared to the simulated diameter and the energy loss of the charged particles is negligible compared with their energy upon entering the cavity. To avoid transformation of *d(y)* into *d(L)*, based on the same assumptions as made by Rossi[22], Ricourt *et al.*[33] suggested substituting *Q(8/9y)* instead of *Q(L)* and *d(y)* instead of *d(L)* in Eq (2). However, in most of radiation protection studies instead of using *L=8/9y*, the evaluation of $\overline{Q}$ is further simplified by directly substituting $L = y$. [15-21] This substitution would result in slightly larger $\overline{Q}$ value as compared to $\overline{Q}$ calculated by substituting *L=8/9y*.[34]

Various forms of *Q(L)* have been defined in the past[31] but the standard adopted by the ICRU and ICRP is the definition of *Q(L)* presented in ICRP publication 60,[21]

$$Q(L) = \begin{cases} 1, & L < 10 keV/\mu m \\ 0.32L - 2.2, & 10 keV/\mu m < L < 100 keV/\mu m \\ \dfrac{300}{\sqrt{L}}, & L \geq 100 keV/\mu m \end{cases} \tag{3}$$

The functional relationship assumed between the lineal energies measured by using a TEPC simulating 2 μm TE diameter and the LET of the recoiling protons is known to be improper

for the neutron energies below 300 keV[28, 35]; the neutron energies which are employed here at MAL for IVNAA[25, 28]. Various approaches have been followed in the past to improve the response of TEPCs either by physical modification[15, 16, 18, 31] of the counter or analytical approaches[19, 31] for quality factor (hence dose equivalent) evaluation at low neutron energies.

In this work we have developed an algorithm which permits a more direct method of measuring neutron quality factor based on ICRP 60[13] by developing a quality factor algorithm of the form, $Q(\overline{y_D}) = a + b\,\overline{y_D}$, which utilizes the average of measured lineal energy dose distribution. No effort has been made to correlate the lineal energy with LET. The development of this algorithm will eliminate any necessity for transforming the measured lineal energy dose distribution, *d(y)*, into an LET dose distribution, *d(L)*.

4. Sources of Uncertainty

There were four sources of uncertainty that contributed to the total uncertainty in the measured lineal energy distributions: inherent counting statistics (maximum 3%), drift in the gain of the counter during the measurements (±2-3%)[7], uncertainty in the estimation of energy deposition of α particles for the purpose of calibration (±4%)[7], and merging of two spectra collected at two different amplifier gains (3-4%)[7]. The overall uncertainty in the measured mean quality factor was conservatively estimated to be less than 10%. Further sources of uncertainty for the lineal energy measurements made in the irradiation facility were detector positioning inside the irradiation facility (2-3%), and the uncertainty in proton beam energy (2%). The overall uncertainty in the effective quality factor measurements made in the irradiation facility was estimated to be approximately 11-12%.

E. MCNP Modeling of Hand Irradiation Facility

These calculations were aimed at providing a comparison of the calculated effective quality factors with the measured quality factors at the corresponding proton energies and positions inside the hand irradiation facility. The quality factor was averaged only over the neutron component of the total dose. No account was taken of the contribution to quality factor from any external or internal γ radiation which may be present.

Time independent simulation was used as the accelerator is normally run under constant operating conditions for any given measurement. The target cooling systems and other aspects of the beam line were not included in the modeling. The target backing was made of high Z material to minimize neutron scattering.

1. Thick Target Energy Spectrum and Angular Distribution of Neutrons Produced via ^{7}Li(p, n)^{7}Be Reaction

Low energy neutrons for many clinical applications are produced by low energy charged particle induced reactions with low mass number targets using charged particle accelerators. Lithium targets using the ^{7}Li(p, n)^{7}Be reaction are widely used as a low energy neutron source for clinical applications in BNCT[36-42], BNCEFNT,[43] BNCS,[44, 45] *in-vivo* neutron activation measurements[2-11] and in radiobiological experiments.[46-50]. The neutron energy spectrum and angular distribution of the neutrons in the near threshold region of 1.88 – 1.93 MeV were calculated using the Breit-Wigner approximation to avoid singularities[29, 51-53] and the reported measured cross-sections[54] were employed above this region. Our calculations are briefly summarized here.

The number of neutrons produced from an element of target of thickness dx (corresponding to an energy loss of dE_p in thickness dx) emitted at angle θ into an element of solid angle dΩ per unit incident proton charge is given by

$$\frac{d^2Y(E_n,\theta)}{d\Omega dE_n} = \frac{n_T}{e}\frac{d\sigma}{d\Omega'}\frac{d\Omega'}{d\Omega}\frac{1}{S(E_p)}\frac{dE_p}{dE_n} \tag{4}$$

where n_T is the lithium target atomic density, dE_n refers to the width of the neutron spectrum because of the thickness dx (or dE_p), and dE_p/dE_n was calculated from the Q-value of the nuclear reaction.[7, 29, 51] The differential cross-section in the c.m., dσ/dΩ′, was taken from the compilations of (p, n) cross-section data for ^{7}Li[54] and the stopping powers, $S(E_p)$, of protons in ^{7}Li were taken from Janni[55].

The spectrum of the neutrons produced as a result of bombardment by a unidirectional proton beam on a thick lithium target was calculated by assuming the thick target to consist of several thin targets each of thickness dx, with decreasing incident proton energies, ranging from the incident beam energy, E_p, down to the E_{th}. The generated spectrum was used to define the energy and angular distributions of neutrons for Monte Carlo simulation of hand irradiation facility.

2. MCNP Source Card

The energy and angular distributions of neutrons produced via the ^{7}Li(p, n)^{7}Be were used to characterize the neutron source using the MCNP[56] source cards. A realistic model of thick target ^{7}Li(p, n)^{7}Be interaction was provided to quantify the energy, angular, and positional,

distributions of neutrons entering the irradiation facility. The lithium target source was represented by a point source geometry. The angular and energy distribution of the neutrons produced as a result of (p, n) interaction with the thick lithium target depend upon the incident proton beam energy. The probability density functions (PDFs) for the resulting neutron energy spectrum as a function of cosine of angle, μ ($=\cos\theta$), corresponding to particular proton beam energy were provided in the MCNP[56] input file. The lab angle, θ, was defined relative to the proton beam axis.

Step 1: The PDF for initial direction cosines, $p(\mu)$, was calculated using the angular neutron yield. This PDF was used by MCNP to assign randomly the initial direction cosine, μ, to each source neutron. Azimuth angle, φ, was selected uniformly between 0° and 360° to produce a neutron beam symmetric along the beam axis. The differential angular neutron yield, $\frac{dY(6)}{d\Omega}$, was calculated by using the double differential neutron energy spectrum, $\frac{d^2Y(E_n,\theta)}{d\Omega dE_n}$, as

$$\frac{dY(\theta)}{d\Omega} = \int \frac{d^2Y(E_n,\theta)}{d\Omega dE_n} dE_n \tag{5}$$

The differential angular neutron yield in units of neutrons/degree μC was calculated by multiplying (5) by solid angle differential element $2\pi\sin\theta$, as

$$\frac{dY}{d\theta} = 2\pi \sin\theta \int \frac{d^2Y(E_n,\theta)}{d\Omega dE_n} dE_n \tag{6}$$

The PDF $p(\theta)$ was then calculated using the angular neutron yield calculated in (6) as follows:

$$p(\theta) = \frac{\frac{dY}{d\theta}}{\int_{\theta=0}^{\theta=\pi/2} \frac{dY}{d\theta} d\theta}. \tag{7}$$

The denominator in (7) represents the total neutron yield at a given proton beam energy. The PDF $p(\theta)$ was defined as a 19 bin histogram in the forward direction only ($0 \le \theta \le \pi/2$). The bin boundaries were transformed from θ into μ using the relationship $\mu = \cos\theta$, to transform the pdf $p(\theta)$ into $p(\mu)$. The PDFs $p(\mu)$ for beam energies of 2.00 and 2.25 MeV have been

illustrated in **Figure 2**. This figure demonstrates that the neutron field is more forward directed for lower beam energies and broadens as the proton beam energy is increased.

Step 2: The PDF for the initial neutron energy, $p(E_n|\mu)$, corresponding to a pre-selected direction μ was calculated using the double differential neutron energy spectrum, $\frac{d^2Y(E_n,\theta)}{d\Omega dE_n}$, as

$$p(E_n|\mu) = \frac{\left|\frac{d^2Y}{d\mu dE_n}\right|}{\int\left|\frac{d^2Y}{d\mu dE_n}\right|dE_n} = \frac{\frac{d^2Y}{d\Omega dE_n}\left|\frac{d\Omega}{d\mu}\right|}{\int\frac{d^2Y}{d\Omega dE_n}\left|\frac{d\Omega}{d\mu}\right|dE_n} = \frac{\frac{d^2Y}{d\Omega dE_n}}{\int\frac{d^2Y}{d\Omega dE_n}dE_n}. \quad (8)$$

For each bin in the histogram of μ, a corresponding histogram for neutron energy distribution calculated by using the PDF $p(E_n|\mu)$ was provided in the MCNP input file. Each energy distribution was represented by a 40 bin histogram. The PDFs $p(E_n|\mu)$ for beam energies of 2.00 and 2.25 MeV have been illustrated in **Figure 3** and **Figure 4**. These figures demonstrate that with the increase in beam energy, the spectrum hardens and the mean neutron energy increases in the given direction. At any particular beam energy, the maximum mean neutron energy is obtained along the beam axis and the minimum in the direction orthogonal to beam. These spectra contain very small fractions of thermal and epithermal neutrons. The neutron activation (n, γ) cross-sections above these neutron energies are very low for the isotopes of interest (Al and Mn). This fraction of neutron energies decreases with the increase in beam energy. The direct neutron beams are thus moderated to increase the fraction of thermal and epithermal neutrons.

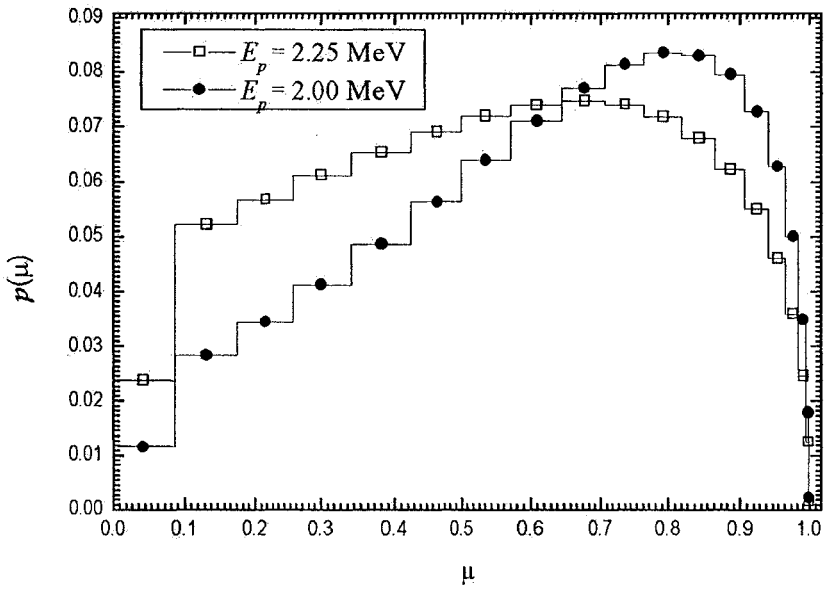

FIG. 2: PDFs for the angular distribution of the neutrons produced as a result of (p, n) interaction with thick lithium target for proton beam energies E_p = 2.00 and 2.25 MeV.

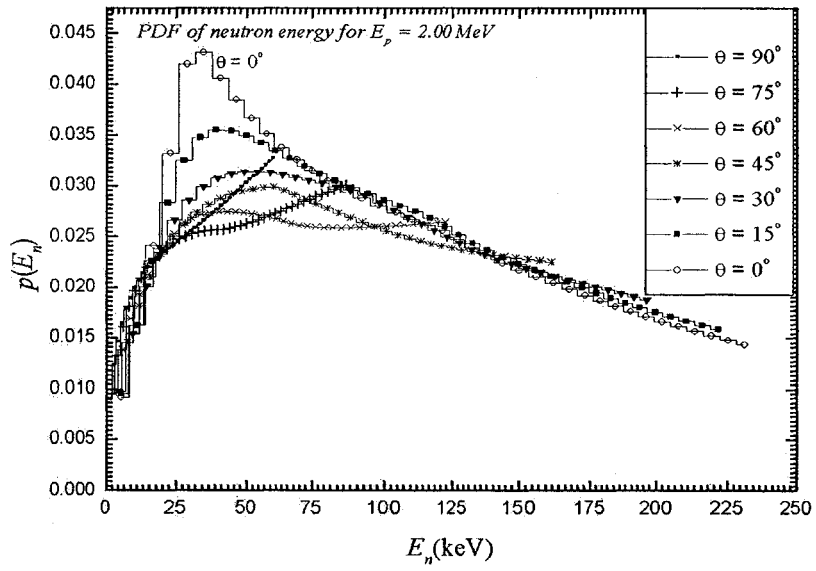

FIG. 3: PDFs for the direction-dependent energy distribution of the neutrons produced as a result of (p, n) interaction with thick lithium target for proton beam energy E_p = 2.00 MeV.

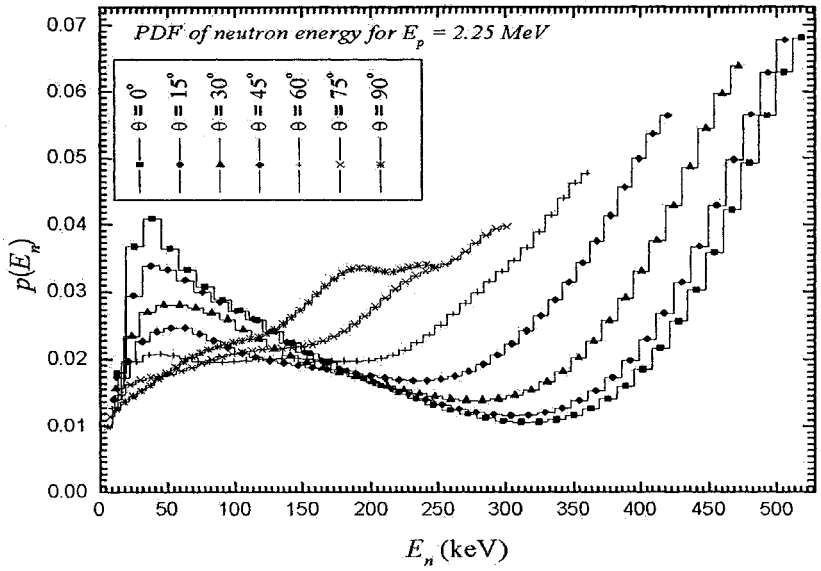

FIG. 4: PDFs for the direction-dependent energy distribution of the neutrons produced as a result of (p, n) interaction with thick lithium target for proton beam energy E_p = 2.25 MeV.

3. Neutron Quality Factor

As we discussed earlier, changing the proton beam energy from E_p = 2.00 MeV to 2.25 MeV also change the neutron energy spectrum. Dose averaged quality factors for the neutrons of varying neutron energies at any position, $\vec{r}$=(x,y,z), inside the irradiation facility were calculated as follows

$$\overline{Q}(\vec{r}) = \frac{\int_0^{E_n} Q(E_n)\, D(E_n, \vec{r})\, dE_n}{\int_0^{E_n} D(E_n, \vec{r})\, dE_n} = \frac{\int Q(E_n) k(E_n) \Phi(E_n, \vec{r})\, dE_n}{\int k(E_n) \Phi(E_n, \vec{r})\, dE_n} \qquad (9)$$

Here the numerator represents the dose equivalent as defined in ICRP 60[13] while the denominator represents the absorbed dose. The neutron fluence spectrum, $\Phi(E_n, \vec{r})$, at the particular location where measurements were performed, was calculated by using the neutron tally **F5**.[56] The calculated neutron fluence spectrum was modified using the dose function **DF5**[56] defined in MCNP. The function **DF5**[56] in the case of the numerator in (9) was defined as fluence-to-dose equivalent conversion factors while in the case of the denominator it was defined as fluence-to-dose conversion factors as a function of energy. This modified tally also provides the integral over energy bins defined using the tally E5.[56] An appropriate number of energy bins was used in MCNP[56] to get the integrals used in the denominator and

the numerator of (9). The fluence-to-Kerma conversion factors for neutrons in soft tissue, ***D(E)***, were taken from ICRU 46[26] while the quality factor, ***Q(E)***, were taken from the values reported in literature.[62]

III. ANALYSIS AND RESULTS

A. Lineal Energy Distributions of Monoenergetic and Continuous Energy Spectra Neutrons

Lineal energies in this study were measured in the range of 0.2 to 1000 keV/μm. The γ–ray contribution extending below 10 keV/μm was eliminated from the n-γ overlapping region between 1 and 10 keV/μm by subtracting a measured and scaled ^{60}Co (1.25 MeV) gamma spectrum using the same simulated tissue site size.[7, 11, 17, 25, 31, 50, 57, 58] The γ–ray events were mainly contributed by the 478 keV inelastic gamma rays resulting from the ^{7}Li(p, p′γ)^{7}Li[23] with other low intensity gamma rays produced via (p, n′γ) and (p, γ) interactions. The (gamma ray) contamination decreases with the increase in proton beam energy.[50] The lineal energy spectrum varies slowly with changes in gamma ray energy,[31, 57, 58] therefore there is only a slight difference between 1256 and 478 keV spectra.

The complete set of measured lineal energy spectra of monoenergetic neutrons of energy ranging from 150 to 600 keV corresponding to E_p = 2.00 – 2.40 MeV, is presented in **Figure 5**. The energies of the monoenergetic neutrons were measured using a ^{3}He-filled gridded ionization chamber (FNS-1, Seforad Applied Radiation Ltd. of Emek Hayarden, Israel).[28, 50, 59, 60] The first six spectra ranging in neutron energies 320 < E_n < 600 keV, have a sharp proton edge at approximately 136 keV/μm which decreases to about 110 keV/μm for 150 keV neutrons. Thus below 320 keV neutron energy, almost all the recoil protons produced by these neutron energies have insufficient ranges to cross the cavity diameter and thus deposit the entire energy in the cavity. This does not conform to the basic assumption made by Rossi to extract LET information from the lineal energy distribution that the energy loss of the recoil particles is negligible compared with their energy upon entering the gas. This was investigated further by studying the variation of proton edge with neutrons of varying energies using continuous energy spectra.

Neutrons of mean neutron energy ranging from 35≤E_n≤280 keV were obtained at MAL using a thick ^{7}Li metal target with proton beam energies ranging from 2.00 to 2.25 MeV. Lineal energy distribution measurements were performed in the beam direction as well as in other directions, 0° ≤ θ ≤ 90°, to obtain neutrons of varying energies. The complete set of measured

microdosimetric spectra ranging in mean neutron energies from 35 to 280 keV is presented in **Figure 6**. The proton edge is marked there.

In contrast to lineal energy distributions for neutron energies greater than 270 keV where the proton edge was fixed (see **Figure 5** and **6**), we observed a decreasing trend in the proton edge for a decrease in neutron energy below 270 keV. Low energy neutrons (E_n < 1 MeV) mainly interact with the TEPC wall and gas via the elastic scattering of protons. The energy distribution of recoil protons is a rectangular function of proton energies ranging from *0* to E_n. The energy deposition of these protons in the gas cavity depends upon their stopping power and track length. Among these recoil protons, the protons corresponding to the Bragg peak have the maximum stopping power. The tracks of recoil protons also follow a distribution of tracks in the gas cavity (*0* to *d*). The recoil protons of Bragg peak energy traversing through the diameter (maximum track length) of the gas sphere deposit the maximum energy, ε_{max}. The proton edge (or y_{max}) for neutron energies greater than 270 keV can thus be obtained by $y_{\max} = \frac{\varepsilon_{\max}}{\frac{2}{3}d}$, where $\frac{2}{3}d$ is the mean chord length of a sphere of simulated diameter *d*. This proton edge is independent of the neutron energy above 270 keV showing that the mean track length of the recoil protons does not depend on the neutron energy. This defines the lower limit for a TEPC simulating 2 μm TE diameter to meet the necessary assumptions for correlating lineal energy to LET.

The proton edge shifts to lower values when the range of most of the recoil protons depositing energy in the cavity becomes smaller than the simulated diameter. Below 212 keV (Figure 6(c)), the proton edge is lower than the maximum edge and continues to drop until at 65 keV neutron energy where we observed the maximum drop in proton edge. The recoil protons produced by neutron energies below 212 keV have insufficient ranges to cross the cavity diameter and thus deposit the entire energy in the cavity. The proton edge in those cases may be obtained from the neutron energy divided by the average chord length.[61] In agreement with Schumacher *et al.*,[61] the calculated proton edges for these spectra match within 5-20% those obtained in the measured lineal energy spectra shown in **Figure 6** except at 35 keV neutron energy, where the measured proton edge is twice that of the calculated one. We suspect that the beam was contaminated with thermal neutrons causing the $^{14}N(n, p)^{14}C$ interaction to produce 580 keV protons in the counter wall to shift the lineal energy distribution spectrum to higher lineal energies. This measurement was made

orthogonal to the beam and there was a 5 cm thick copper target backing between the TEPC and target.

The short-range recoil protons produced by low energy primary neutrons (< 270 keV) seriously challenges the necessary Rossi assumptions[22] for correlating lineal energy to LET. Note that the range of 144 keV protons (mean recoil proton energy produced by ~ 290 keV primary neutrons) in unit density material is 1.8 μm and that for 24 keV protons (mean recoil proton energy produced by ~ 48 keV primary neutrons) is 0.5 μm. Thus the extraction of LET spectra from the lineal energy distributions of neutron energies below 270 keV measured by using a TEPC simulating 2 μm site size would involve complicated calculations and rigorous unfolding procedures.

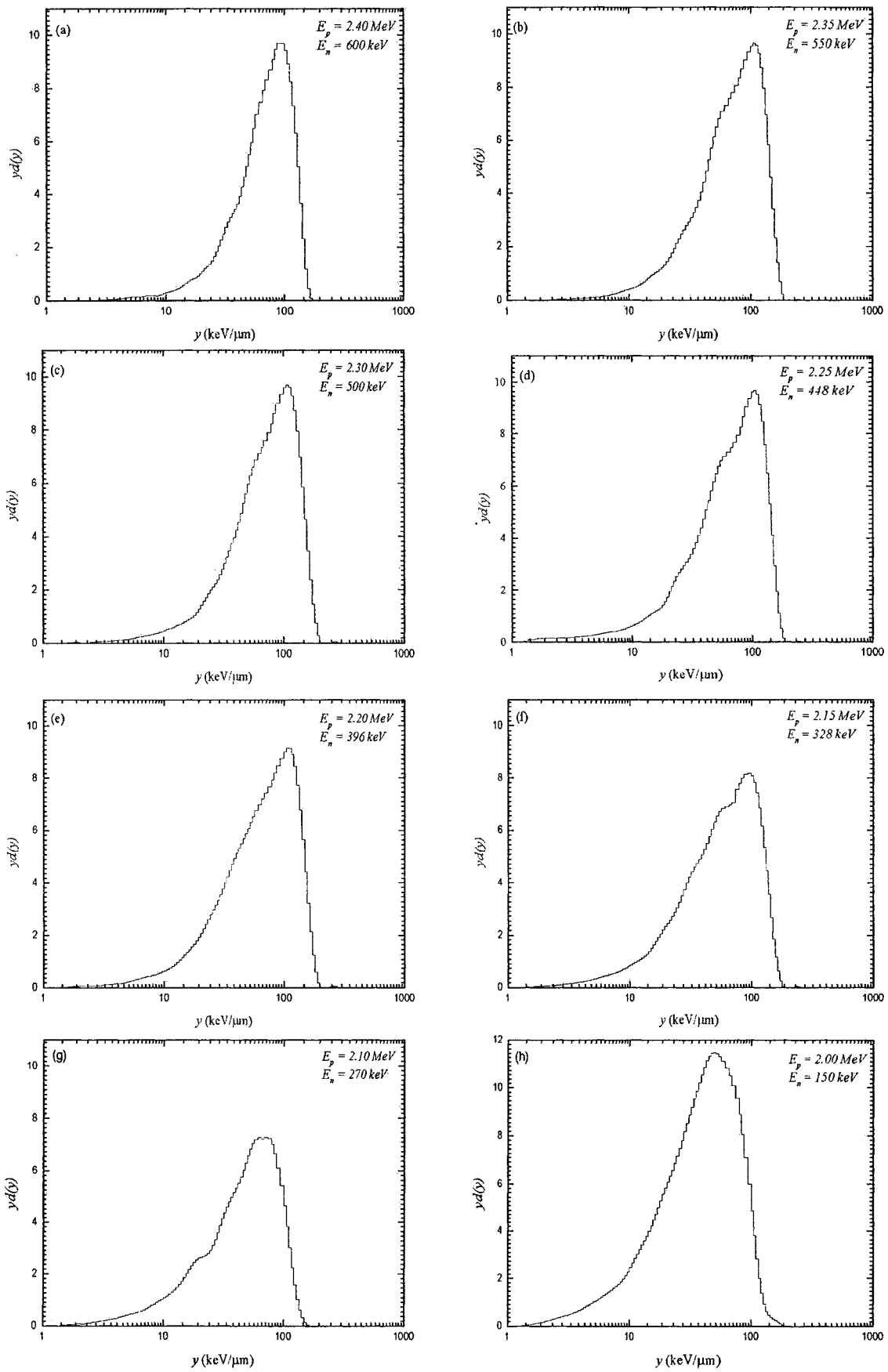

FIG. 5: Measured lineal energy distributions of monoenergetic neutrons (150 – 600 keV) using a 2 μm diameter simulated size for E_p = 2.40, 2.35, 2.30, 2.25, 2.20, 2.15, 2.10, 2.00 MeV.

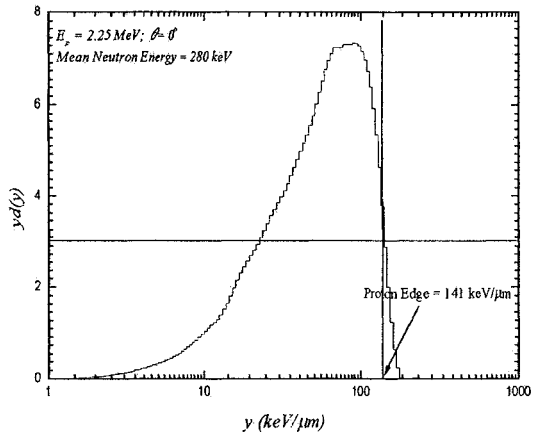
E_p = 2.25 MeV; θ= 0°
Mean Neutron Energy = 280 keV
Proton Edge = 141 keV/μm
yd(y)
y (keV/μm)

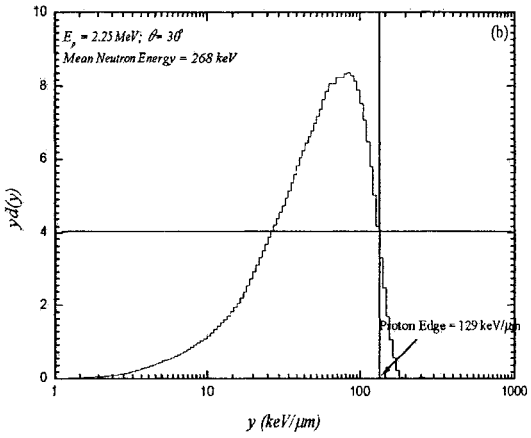
E_p = 2.25 MeV; θ= 30°
Mean Neutron Energy = 268 keV
(b)
Proton Edge = 129 keV/μm
yd(y)
y (keV/μm)

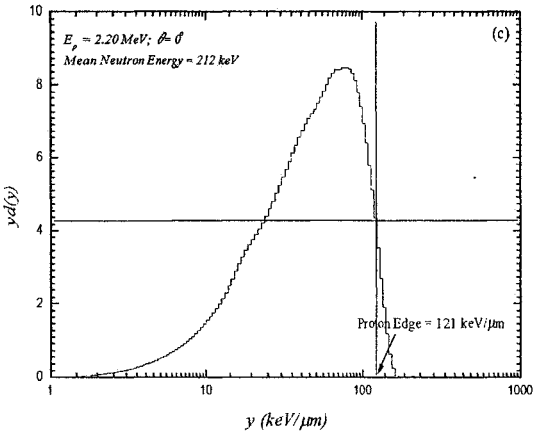
E_p = 2.20 MeV; θ= 0°
Mean Neutron Energy = 212 keV
(c)
Proton Edge = 121 keV/μm
yd(y)
y (keV/μm)

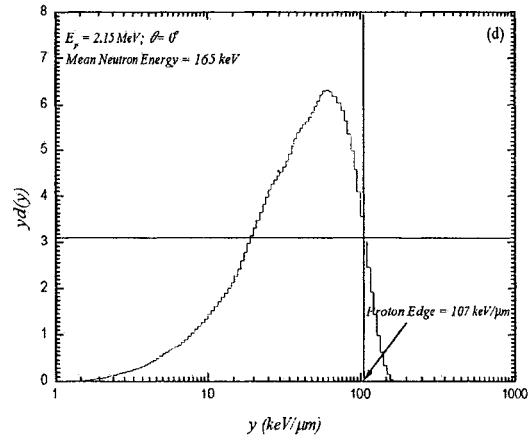
E_p = 2.15 MeV; θ= 0°
Mean Neutron Energy = 165 keV
(d)
Proton Edge = 107 keV/μm
yd(y)
y (keV/μm)

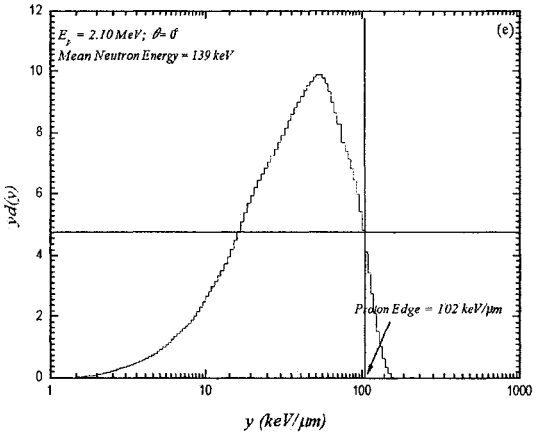
E_p = 2.10 MeV; θ= 0°
Mean Neutron Energy = 139 keV
(e)
Proton Edge = 102 keV/μm
yd(y)
y (keV/μm)

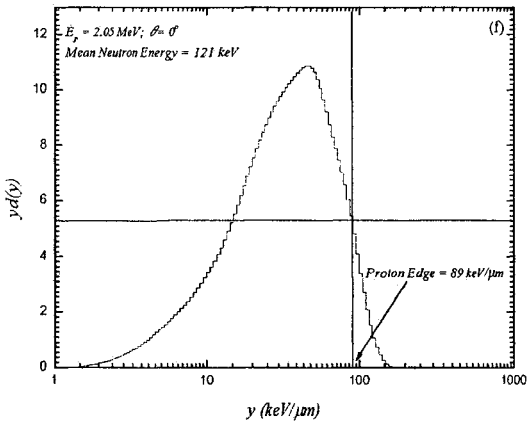
E_p = 2.05 MeV; θ= 0°
Mean Neutron Energy = 121 keV
(f)
Proton Edge = 89 keV/μm
yd(y)
y (keV/μm)

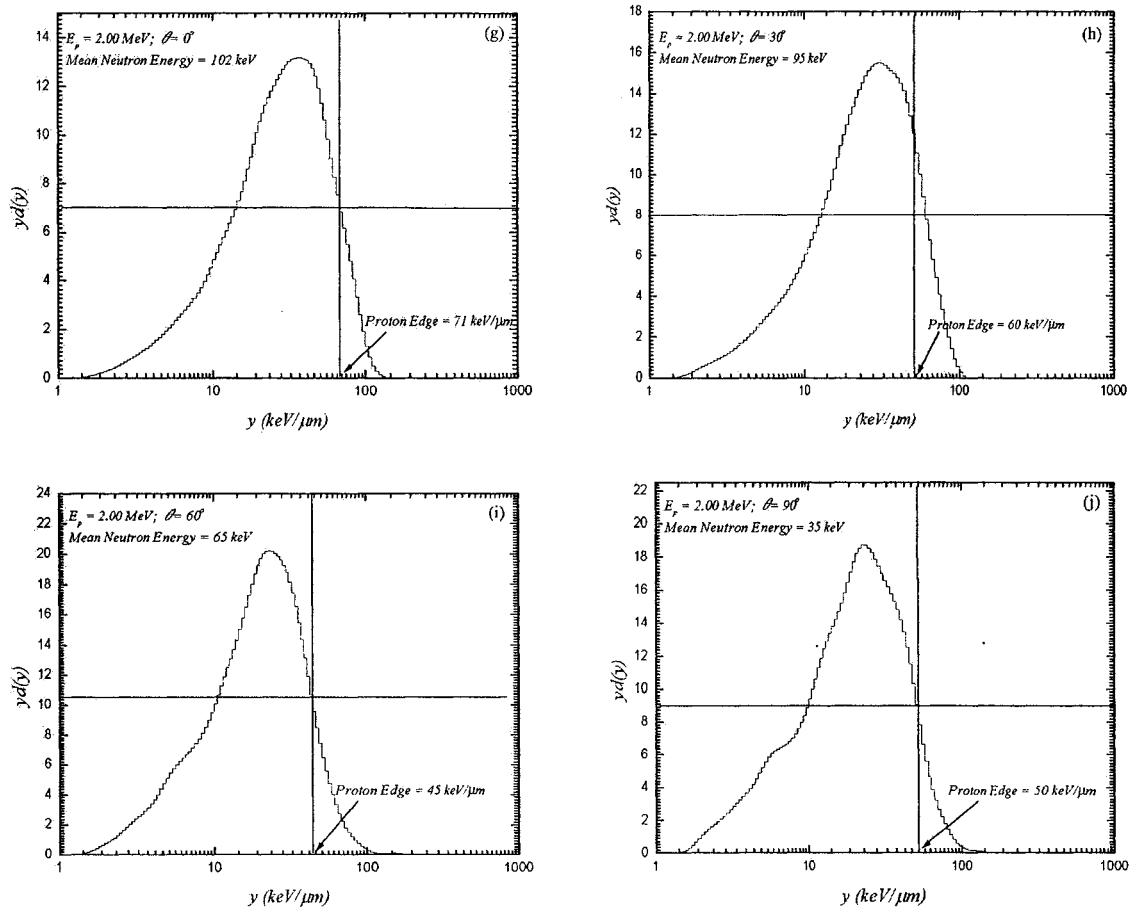

FIG. 6: Lineal energy distributions of continuous energy neutrons (35 – 280 keV) measured in–air using a 2 μm equivalent diameter. Compared to high energy neutrons where proton edge was observed at 136 keV/μm (E_n > 280 keV), a decreasing trend is observed in the proton edge with the decrease in mean neutron energy. This results from the decreasing range and stopping power of recoil protons, thus causing a decrease in the average track length. The short-range recoil protons produced by low energy primary neutrons seriously challenges Rossi's basic assumptions for transforming the lineal energy distributions into LET distribution. Thus the approximation $L = y$ also becomes invalid in this energy range; it seems difficult to extract useful LET information from the measured lineal energy distributions.

B. TEPC Quality Factor Response

The effective quality factor, $\overline{Q}$, was determined by equating L to y and the measured lineal energy dose distributions and the definition of $Q(L)$ given in ICRP 60[13] for the entire range of measured neutron energies. The measured and calculated Q values in the energy range $35 < E_n < 600$ keV is shown in **Figure 7**. The $\overline{Q}$ in the energy range of 150 to 600 keV was calculated using the lineal energy dose distributions measured with monoenergetic neutrons. Below 150 keV neutron energy, the lineal energy dose distributions measured with continuous energy spectra of mean neutron energies were used to evaluate $\overline{Q}$. The calculated values shown in **Figure 7** for the effective quality factors based on ICRP 60[13] in an ICRU tissue sphere at a 10 mm depth have been taken from Dietze *et al.*[64]. The measured quality factor increases slowly and is approximately constant within 15% above 270 keV neutron energy. These values are in good agreement with earlier measured results.[28]

The difference between the measured and calculated values increases with the decrease in neutron energy. These differences arise primarily because of the invalid approximation of LET by y and secondarily because of the differences in the energy spectra of secondary charged particles in the TEPC gas cavity and the ICRU tissue sphere.

The error incurred in the measured effective quality factors due to invalid approximation $L = y$ at low neutron energies, was estimated by calculating the ratio of the measured to that of calculated quality factor[64], Q, in an ICRU tissue sphere at a 10 mm depth. The detector response, R_Q, calculated from the corresponding measured and calculated Q values in the energy range $35 < E_n < 600$ keV is illustrated in **Figure 8**. The detector response deteriorates with decreasing mean neutron energy. The maximum underestimate was observed at 65 keV and the situation improved as the neutron energy increased. The counter response in case of ICRP 60[13] was ~0.65 at 150 keV which dropped to ~0.4 at 65 keV. Comparing this with the counter response based on ICRP 26[12] calculated by assuming $L = y$, is ~0.7 at 150 keV which deteriorates further to ~0.6 at 65 keV.[13, 14] The decline in counter

response in the case of ICRP 60[13] was found to be much sharper than in case of ICRP 26[12]. This underestimation of the quality factor in the low energy region using a TEPC simulating 2 μm TE diameter contributes about a half to the deviation of dose equivalent measurement from the ambient dose equivalent.[13,14]

Measured quality factor values increase with the decrease in sensitive site size at low neutron energies[13, 14, 16, 34, 64] because of the decreasing number of protons starting and stopping in TEPC cavity gas and a relative increase in range.[34] The small physical size of the detector is needed to simulate the small tissue site sizes in order to improve the operational stability.[27] Although the use of the counters simulating the smaller diameters will improve the counter response, it does not present a feasible solution to the problem as the neutron energies in the fields range from 10 – 200 keV. For 10 keV neutron energy, the average initial recoil proton energy is 5 keV which has a range of ~0.2 μm in propane based TE gas.[30] Moreover, the reduced simulated site size with a small physical diameter will also reduce the sensitivity of the counter. Thus the selection of a site diameter is a compromise between optimal counter operation and the smallest possible site size with a reasonable sensitivity. Alternatively, the counter response is improved by physically modifying the counter either by altering the gas composition[15, 16, 18] or changing the detector wall thickness.[16] However, any physical modification of the counter will restrict the experimental conditions under which it can be operated.[18, 19] Thus we have followed an analytical approach discussed in the literature[31] to improve the detector response for quality factor evaluation at low energies.

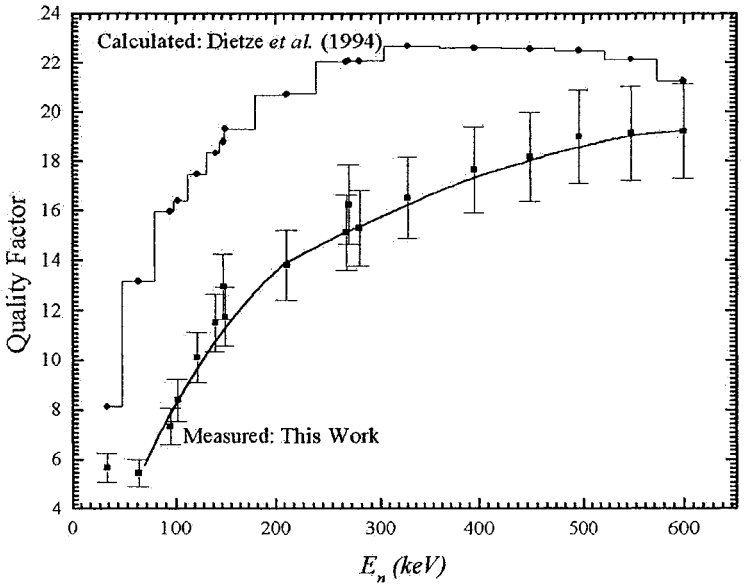

FIG. 7: Comparison of quality factors measured using a TEPC simulating 2 μm TE diameter in the energy range, $35 < E_n < 600$ keV with calculated quality factors[62] in an ICRU tissue sphere at 10 mm depth. Quality factors measured using continuous energy spectra neutrons (35 – 280 keV) are included in this figure as a function of mean neutron energy. A fairly good agreement in measured values using monoenergetic and continuous spectra neutrons can be seen in the overlapping region of 150-280 keV.

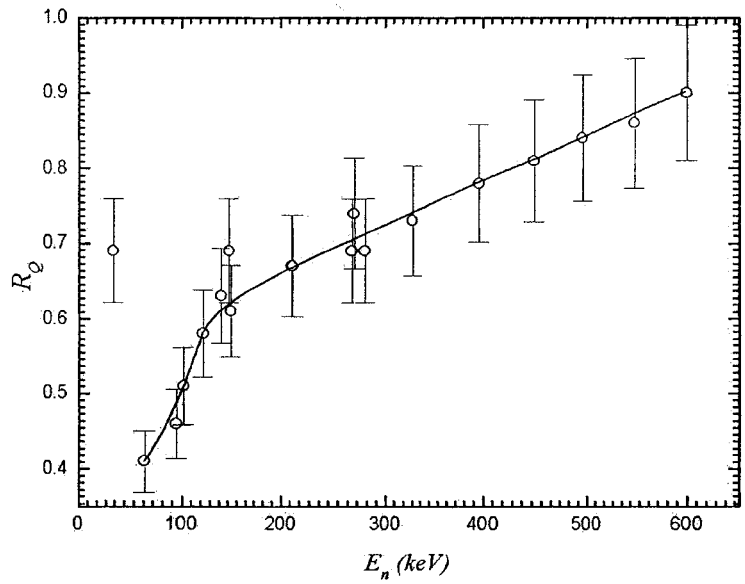

FIG. 8: Neutron quality factor response (R_Q) of a TEPC simulating 2 μm TE diameter defined as the ratio of measured (This Work) to the calculated quality factors in an ICRU tissue sphere at 10 mm depth.[62]

C. Development of Quality Factor Algorithm

This work describes an algorithm which permits a more direct method of measuring neutron quality factor based on ICRP 60[13]. The algorithm developed for the evaluation of effective quality factor is of the form,

$$Q(E_n) = a + b\,\overline{y_D}(E_n) \tag{10}$$

where Q is the calculated quality factor[13, 62] in an ICRU tissue sphere at 10 mm depth, $\overline{y_D}$ is the average of measured lineal energy dose distribution, and a and b are the fitting parameters obtained by fitting a straight line between calculated Q and the measured $\overline{y_D}$ values. This algorithm utilizes the average of the measured lineal energy dose distributions thus eliminates any necessity for transforming the measured lineal energy dose distribution, *d(y)*, into an LET dose distribution, *d(L)*.

1. Average of Measured Lineal Energy Dose Distributions

The average of the lineal energy dose distribution, *d(y)*, is defined as[31]

$$\overline{y_D} = \frac{\int y d(y) dy}{\int d(y) dy}, \tag{11}$$

The $\overline{y_D}$ values were averaged only over the neutron dose. Thus these values were calculated after the subtraction of gamma-ray contribution from the measured lineal energy dose distributions.

The statistical uncertainty estimated in $\overline{y_D}$ using the error propagation formula[63] is given by

$$\frac{\sigma_{\overline{y_D}}}{\overline{y_D}} = \sqrt{\frac{\sum_i y_i^2 d(y_i)}{\left(\sum_i y_i d(y_i)\right)^2} + \frac{\sum_i d(y_i)}{\left(\sum_i d(y_i)\right)^2}} \tag{12}$$

where i is the log bin number.

The $\overline{y_D}$ values of the measured lineal energy dose distributions in the energy range $35 < E_n < 600$ keV using monoenergetic (illustrated in **Figure 5** in the energy range of 150 to 600 keV) and continuous energy (illustrated in **Figure 6** in the mean neutron energy range of 35 to 280 keV) neutron spectra are shown **Figure 9**. This decrease in the average energy deposited in the simulated site with decreasing neutron energy is both because of the decreasing LET for recoil protons with energies below 70 keV and the decreasing range of the recoil protons in general.[27, 31] The $\overline{y_D}$ values are in fairly good agreement within the experimental uncertainty (10%) with those calculated[34] and measured published values.[27] It is noteworthy that the $\overline{y_D}$ values for continuous energy neutron spectra at the corresponding mean neutron energy are also in good agreement within the experimental uncertainty (10%) with those calculated[34] and measured published values[27] using monoenergetic neutron beams.

2. The Algorithm

The expression derived for the quality factor by fitting the calculated Q values (**Figure 7**) and $\overline{y_D}$ values (**Figure 9**) is

$$Q(\overline{y_D}) = 10.02 + 0.20\,\overline{y_D} \tag{13}$$

with $24 \leq \overline{y_D} \leq 63$ keV/μm, or in terms of neutron energy, $35 \leq E_n \leq 600$ keV. The fitting procedure is demonstrated in **Figure 10**.

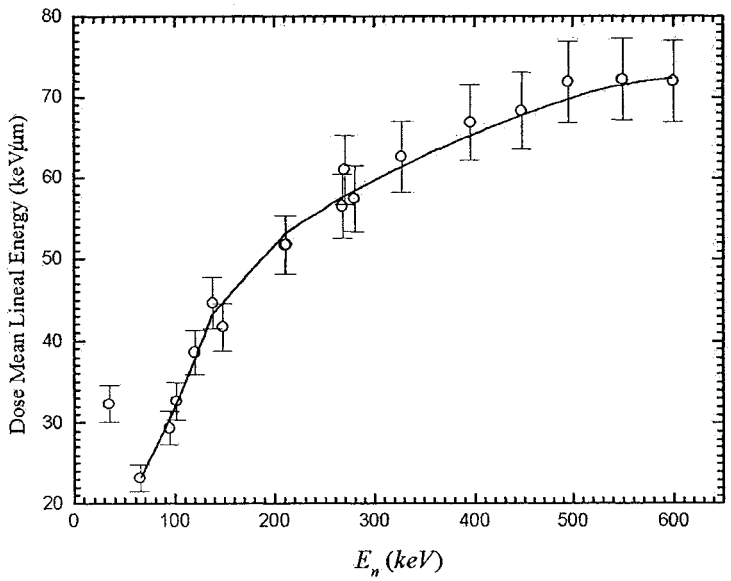

FIG. 9: Measured Dose-mean lineal energy as a function of mean neutron energy using monoenergetic (150 – 600 keV) and continuous spectra neutrons (35 – 280 keV).

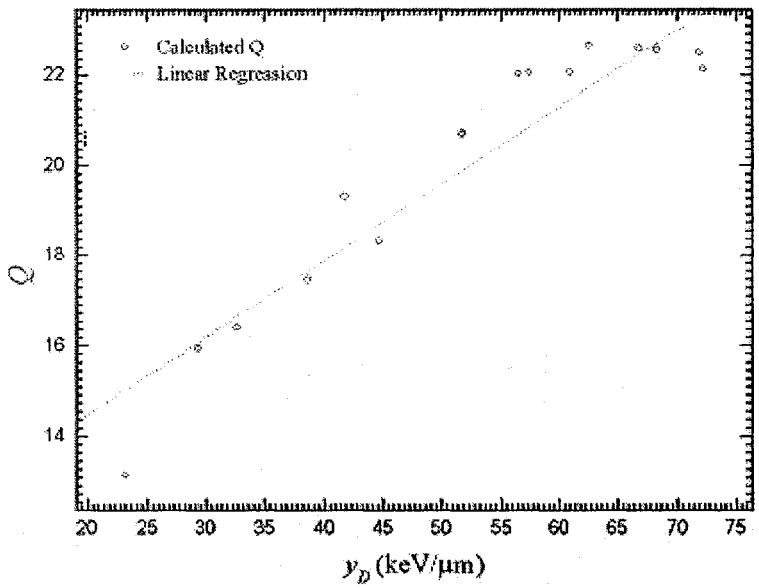

FIG. 10: Development of a neutron quality factor algorithm using monoenergetic and continuous energy spectra neutrons in the energy range 35 $\leq E_n \leq$600 keV.

D. Measurement of Neutron Quality Factors in Hand Irradiation Facility

MDL measurements for Al and Mn in human hand bones have been carried out at beam energies E_p = 2.00 and 2.25 MeV in the hand irradiation facility. The dose equivalent delivered to the patient's irradiated hand is the limiting factor for such measurements. The neutron and gamma doses to the patient's irradiated hand using a TEPC simulating 2 μm TE diameter has been reported earlier.[7, 8, 10, 11] Using the reported measured absorbed doses, the total dose equivalent to the patient's irradiated hand can be estimated if the neutron quality factor is known under the same experimental conditions as those used to measure the neutron and gamma doses. This section describes the use of the algorithm developed in the earlier section to evaluate the neutron quality factors in the center and at horizontal distances of ±7 cm in the irradiation facility for E_p = 2.00 and 2.25 MeV. The neutron quality factors have been determined in the same experimental conditions as described earlier for neutron and gamma dose measurements.[7, 8, 10, 11]

The data for the TEPC measurements in the hand irradiation facility are given in **Table 1**. Each measurement was performed twice, the repeated results were always lying within the estimated experimental uncertainty.

TABLE 1: Estimation of the dose equivalent rates in the hand irradiation facility. The neutron field is non-uniform as the ratio of the maximum (at (0, 0, 0)) to the minimum (at (±7, 0, 0)) dose equivalent rates is greater than 1.30. A conservative total dose equivalent to the patient's irradiated hand is estimated by multiplying the maximum H_T with the proposed hand irradiation time and the selected beam current.

E_p (MeV)	Position (cm)	Reported Dose Rate[7] (mGy/h-μA)		$\overline{y_D}$ (keV/μm)	Q_n	Total Hand Dose Eq Rate (mSv/h-μA)
		D_n	D_γ			$H_T = D_n \times Q_n + D_\gamma$
2.00	(0, 0, 0)	1.02	1.56	37.91	17.60	19.51
	(-7, 0, 0)	0.21	0.88	59.76	21.97	5.49
	(7, 0, 0)	0.21	0.84	55.93	21.21	5.29
2.25	(0, 0, 0)	3.53	1.21	53.47	20.71	74.32
	(-7, 0, 0)	1.19	0.82	54.27	20.87	25.65
	(7, 0, 0)	1.10	0.75	53.62	20.74	23.56

1. *Lineal Energy Measurements in Hand Irradiation Facility at E_p = 2.00 MeV*

The measured lineal energy dose distributions in the center and at horizontal distances of ±7 cm in the irradiation facility using E_p = 2.00 MeV are illustrated in **Figure 11**. The proton edge along beam axis measurement is at 89 keV/μm, whereas in off-axis measurements, the proton edge is observed at 116 keV/μm. The proton edge at the same beam energy and beam axis measurement (see **Figure 6(g)**) without irradiation facility in its place was observed at 71 keV/μm. The mean neutron energy in this case is 102 keV. The irradiation facility, consisting of a moderator and reflectors, decreases the mean neutron energy from 102 keV along the beam axis to some lower value. The difference in the energy ranges of the resulting recoil protons in each case should have resulted in significantly different proton edges. The neutron beams in the hand irradiation facility contains a large fraction of thermal neutrons which cause ^{14}N(n, p) interactions in the counter wall and gas and produce 580 keV protons. These capture protons have a range larger than the simulated diameter while at the same time recoil protons have range smaller than the simulated diameter. Thus instead of observing a drop in the proton edge in case of hand irradiation facility where the neutron energy was much lower than the corresponding beam in-air, an increase in the proton edge was observed.

A similar phenomenon was observed while comparing the proton edges at other positions in the hand irradiation facility with those of in-air measurements i.e., even though the neutron energies in case of hand irradiation facility at the corresponding position are much lower than those of in-air measurements, the proton edges are higher in value than the corresponding edges. The proton edge in off-axis measurements made in the hand irradiation facility is approximately at 115 keV/μm while in case of in-air measurement is little above 45 keV/μm. The shift in proton edge in case of off-axis measurements is because of larger relative contribution of thermal neutrons (causing ^{14}N(n, p) interactions) as compared to in-axis beam.

The shapes of the lineal energy spectra measured off-axis are different than the one measured in the beam axis. The shift in proton edge will further be explored by looking at variation of the contamination of low energy thermal and epithermal

neutrons in the neutron beams at the measurement sites using MCNP. The elastic scattering of these low energy neutrons in the TEPC wall causes moderation and produces thermal neutrons which may be captured via the reactions $^{1}H(n, \gamma)^{2}H$ and $^{14}N(n, p)^{14}C$. For thermal and thermalized neutrons Rossi's assumptions are again satisfied.

2. Average of Lineal Energy Dose Distributions in Hand Irradiation Facility at E_p = 2.00 MeV

The values of $\overline{y_D}$ obtained after the subtraction of the γ-ray contribution are listed in **Table 1.** Because of the reasons discussed earlier for the observed proton edges, a similar trend in the average of the measured lineal energy dose distributions is observed.

3. Measured Neutron Quality Factors in Hand Irradiation Facility at E_p = 2.00 MeV

The effective quality factors calculated employing the algorithm defined in (13) is listed in **Table 1**. The $\overline{y_D}$ values listed in **Table 1** were used for these calculations. The proton edge, $\overline{y_D}$ values and the quality factors show a similar trend i.e., off-axis values are higher than that of beam axis. The comparison of these measured quality factors with those calculated by using MCNP is presented in the next section.

4. Lineal Energy Measurements in Hand Irradiation Facility at E_p = 2.25 MeV

The measured lineal energy dose distributions in the hand irradiation facility for E_p = 2.25 are shown in **Figure 12**. The apparent shapes of the lineal energy spectra were found to be almost the same in all three locations. The proton edges for on axis and off-axis measurements were almost the same as compared to E_p = 2.00 MeV where we observed different proton edges for beam axis and off-axis measurements. The proton edges in the lineal energy spectra at the corresponding position in hand irradiation facility are lower than in-air measurements as expected.

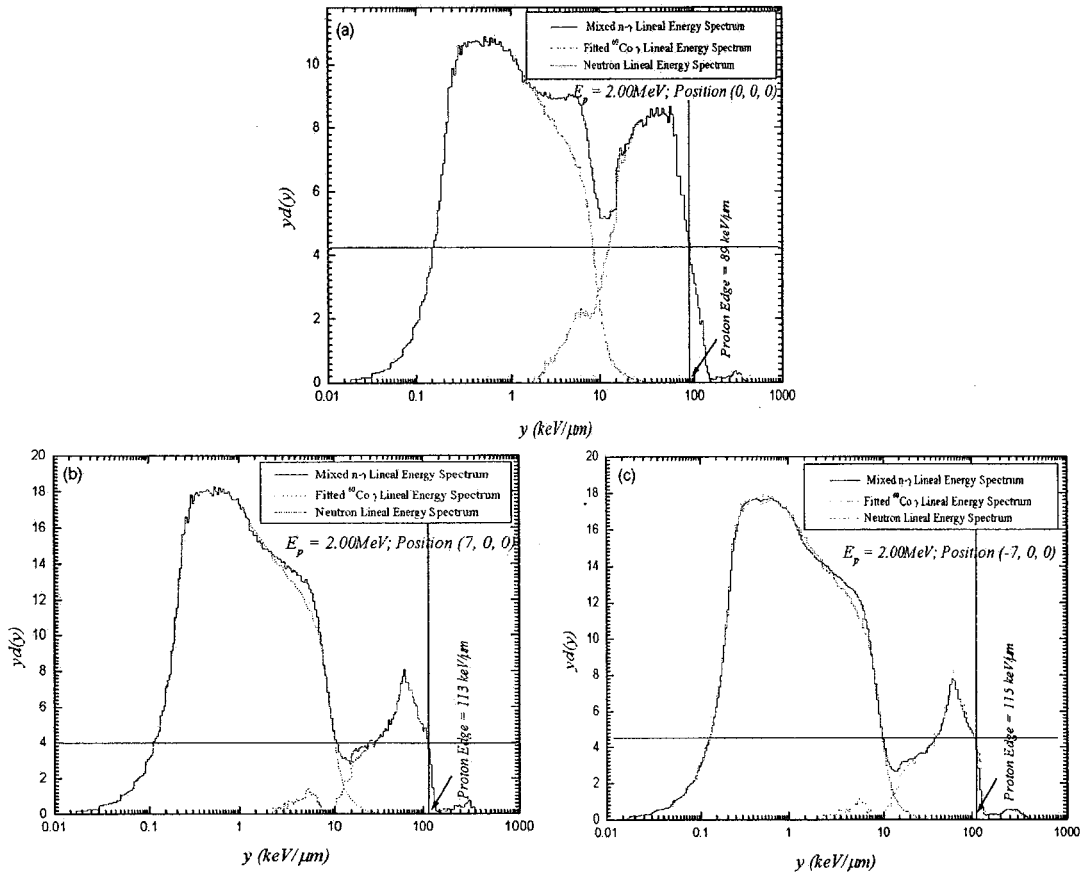

FIG. 11: Measured lineal energy distributions in hand irradiation facility at E_p = 2.00 MeV. Along beam axis, the proton edge is at 82 keV/μm whereas in off-axis measurements, the proton edge is observed at 116 keV/μm. Larger relative low energy neutron contribution (Φ_E/Φ_{tot}) for off-axis measurements producing larger fraction of large range 580 keV protons via $^{14}N(n, p)^{14}C$ interactions shifted the proton edge to larger values. Further the moderation of neutrons in the counter wall may be contributing to this behavior. Gamma contamination (D_γ/D_n) for off-axis measurements is approximately 4.0 which decreases to 1.5 for beam axis measurement.

With E_p = 2.25 MeV measurements in-air, the mean neutron energies at the corresponding positions (θ = 0° and 45°) were 280 and 243 keV. The maximum range of most of the recoil protons produced at these neutron energies was more than the simulated diameter. Thus the proton edges in the measured lineal energy spectra in those beams are observed at around 136 keV/μm (see **Figure 6(a)** and **6(b)**). Because of the lower primary neutron energy in the hand irradiation facility than in-air (280 and 243 keV), we have observed a drop in the proton edge at the corresponding

positions in the hand irradiation facility. The proton edges were still below 136 keV/μm clearly indicating that the range of the protons was smaller than the simulated diameter.

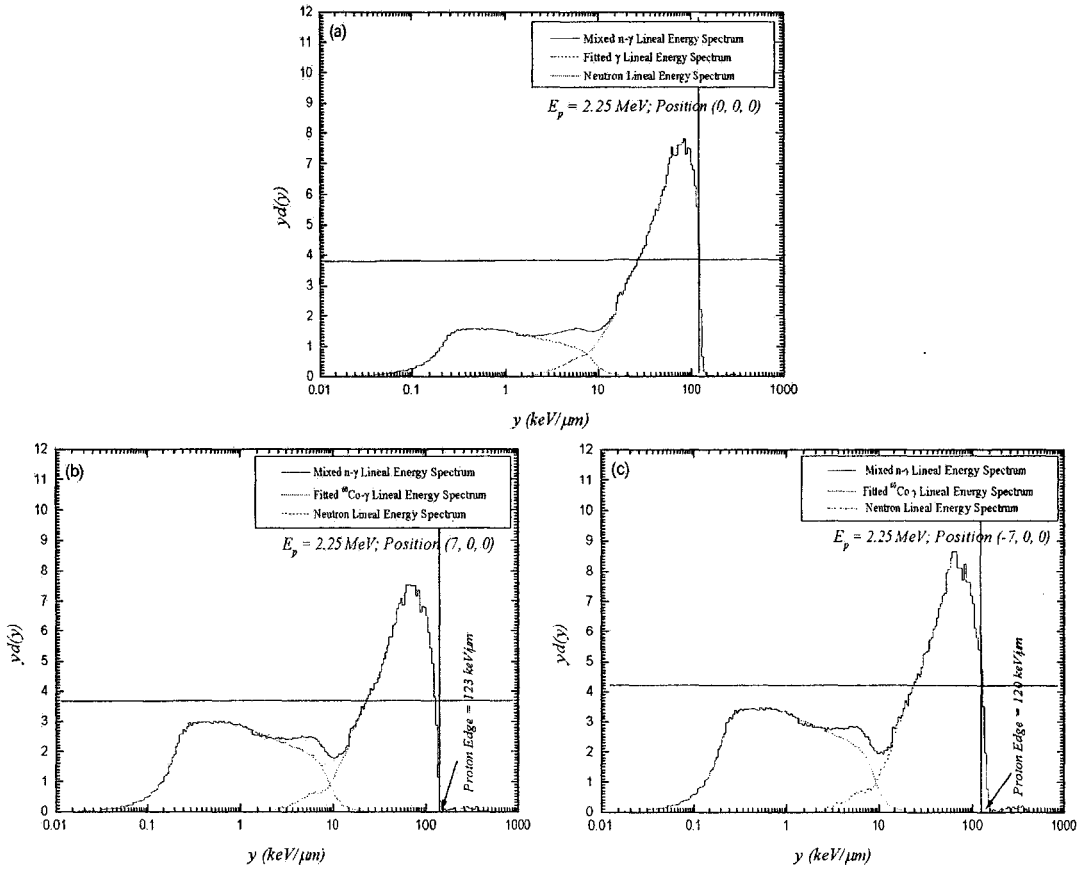

FIG. 12: Measured lineal energy spectra in hand irradiation facility at E_p = 2.25 MeV using a TEPC simulating 2 μm TE diameter. In contrary to beam energy E_p = 2.00 MeV, the proton edge was approximately constant at all measurement sites. Gamma contamination (D_γ/D_n) for off-axis measurements is approximately 0.7 which decreases to 0.3 for beam axis measurements.

5. *Average of Lineal Energy Dose Distributions in Hand Irradiation Facility at E_p = 2.25 MeV*

The $\overline{y_D}$ values calculated after the subtraction of γ-ray contribution are listed in **Table 1**. These values are approximately constant.

6. Measured Neutron Quality Factors in Hand Irradiation Facility at E_p = 2.25 MeV

The $\overline{y_D}$ values listed in **Table 1** were used to calculate the effective quality factors employing the algorithm defined in (13). The values of the effective quality factors at different positions inside the irradiation facility are listed in **Table 1**. The comparison of these measured quality factors with those calculated by using MCNP has been presented in the next section.

E. Simulation of Hand Irradiation Facility for IVNAA

This section describes the calculation of dose averaged quality factors in the center and at horizontal distances of ±7 cm in the irradiation facility for E_p = 2.00 and 2.25 MeV.

1. MCNP Model

To validate the modeling and the Monte Carlo coding of the designed hand irradiation facility, some simple calculations were carried out to make sure the model gives agreeable results under similar exposure conditions. For this purpose, a simple point neutron source with the anisotropic properties, as discussed in the earlier section, was modeled. The angular neutron fluence was calculated at θ_{lab} = 0°, 30°, 60°, and 90° relative to proton beam direction at an arbitrarily chosen distance of 50 cm from the target. The calculated neutron fluences were used to calculate the mean neutron energies in those directions. The mesh sizes for energy and angular distribution of produced neutrons at the target site were chosen to produce the same results as those of analytical calculations matching within 2-3%. Although finer mesh sizes in terms of energy and angular distribution may produce better agreement, the trade off was between better agreement and longer execution time of the model. Experimental validation of the MCNP model of the hand irradiation facility has previously done by others.[7]

2. Fluence Spectrum Calculation

The normalized fluence spectra (per source neutron) calculated at the locations and beam energies in the hand irradiation facility where measurements were carried out

are shown in **Figures 13** and **14**. The number of histories was chosen to calculate the fluence in a reasonable time with sufficient counting precision of 2-3%. The neutron fluence spectra at (-7, 0, 0) and (7, 0, 0) are slightly different at low neutron energies (E_n < 10 eV) because of the presence of reflector towards (-7, 0, 0). The normalized neutron fluence at E_p = 2.00 MeV is higher at all corresponding positions inside the hand irradiation facility than that of 2.25 MeV beam energy. The absolute fluence spectra at a given beam energy can be obtained by multiplying the normalized fluence spectra with the respective total neutron yield at that beam energy.

At all measurement sites where calculations have been carried out, there is a peak in the thermal energy region (<0.5 eV), however, it is evident from **Figures 13** and **14** that the fast neutron component forms a large fraction of the total neutron fluence. The neutron activation (n, γ) cross-sections at neutron energies above thermal energy are very low for the isotopes of interest (Al and Mn). The thermal neutron fluence is expected to decrease with the depth in the hand because of the capture reactions in the hand. This attenuation of thermal neutron fluence may be compensated by the moderation of the epithermal neutrons. The kerma coefficients in tissue equivalent materials, shown in **Figures 13,** increase with the increase in neutron energy (E_n > 30 eV). The non-useful fast neutron group produces an increase of dose equivalent to the patient's hand. This suggests an addition of a fast neutron filter to remove the fast neutrons from the beam. **Figures 16** and **17** show the convolution of fluence spectra shown in **Figures 13** and **14** with the kerma coefficients shown in **Figures 15**. These spectra were finally used to calculate the neutron quality factors.

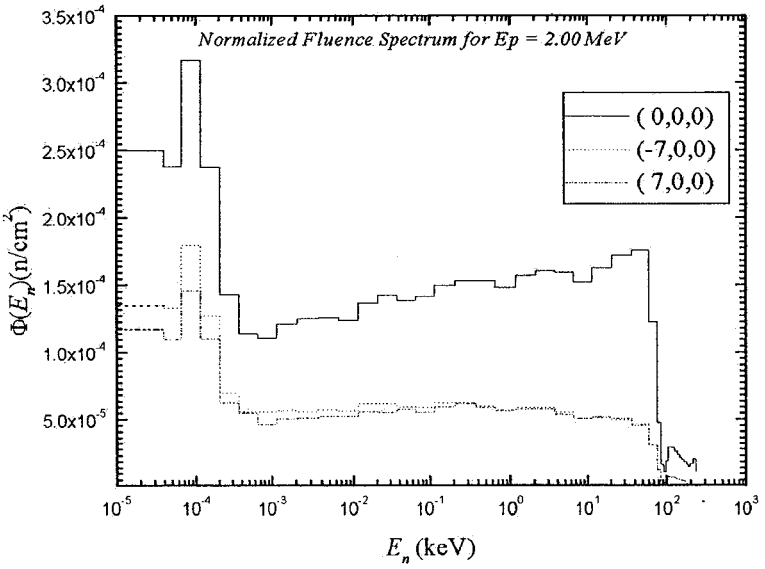

FIG. 13: Calculated normalized neutron fluence spectra per source neutron in the hand irradiation facility at E_p = 2.00 MeV. The neutron fluence spectra at (-7, 0, 0) and (7, 0, 0) are same as expected because of the angular symmetry of the neutrons produced via ^{7}Li(p, n)^{7}Be about the azimuthal angle. However slight differences at low neutron energies (E_n < 10 eV) resulted because of the presence of reflector towards (-7, 0, 0).

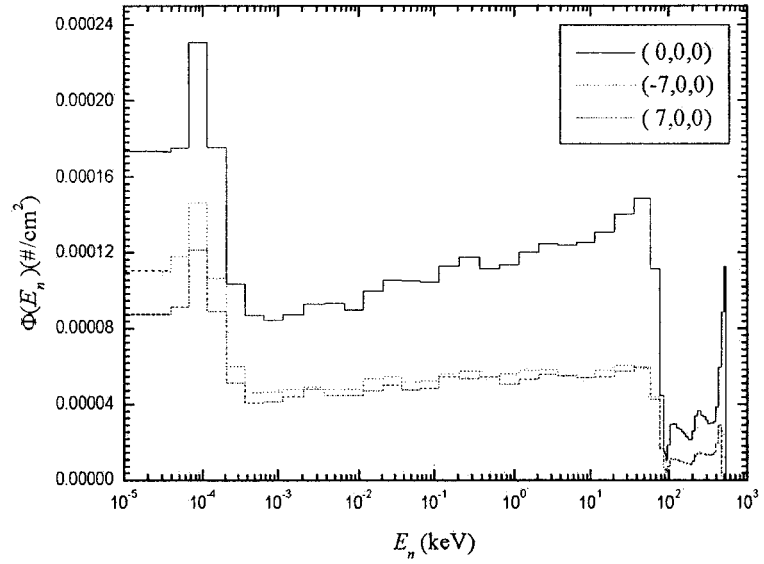

FIG. 14: Calculated normalized neutron fluence spectra per source neutron in the hand irradiation facility at E_p = 2.25 MeV. Again, the neutron fluence spectra at (-7, 0, 0) and (7, 0, 0) are slightly different at low neutron energies (E_n < 10 eV) resulted because of the presence of reflector towards (-7, 0, 0).

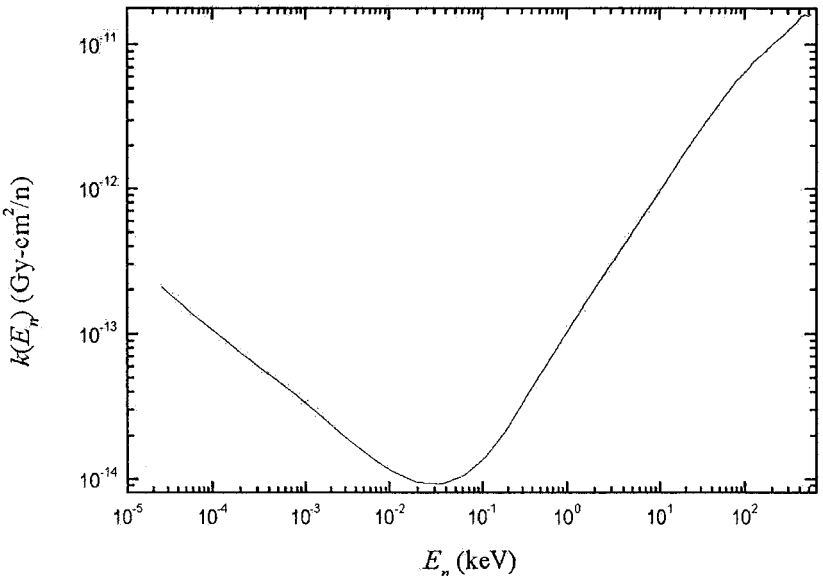

FIG. 15: Kerma coefficient in TE muscle tissue as a function of neutron energy[46].

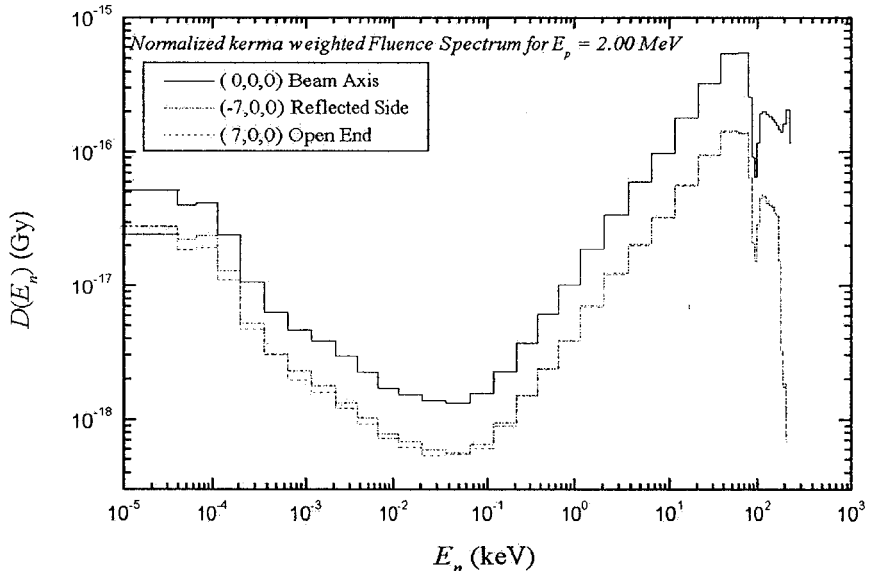

FIG. 16: Calculated normalized kerma weighted neutron fluence spectra per source neutron in the hand irradiation facility at E_p = 2.00 MeV.

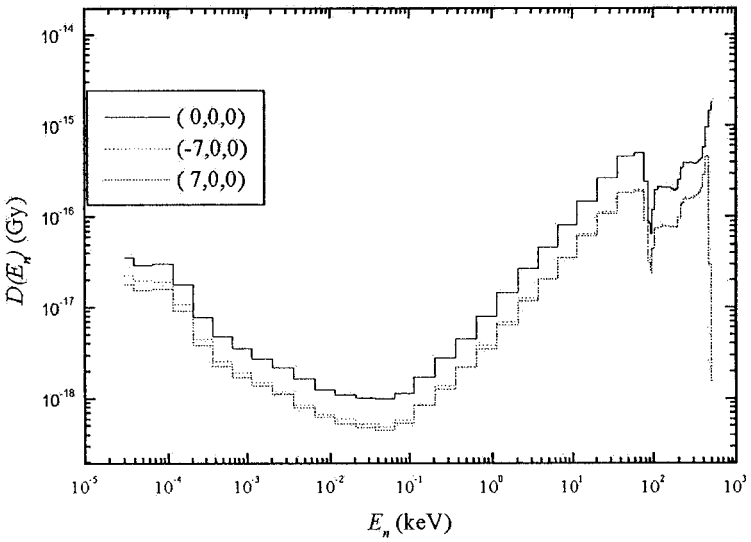

FIG. 17: Calculated normalized kerma weighted neutron fluence spectra per source neutron in the hand irradiation facility at E_p = 2.25 MeV.

3. *Comparison of Measured and Calculated Quality Factors*

Quality factors measured by employing the algorithm developed in this work have been compared with calculations performed using MCNP. The calculated and measured quality factors and their ratio (C/E) are listed in **Table 2**. This table also lists the fraction of low energy thermal and epithermal neutrons in the neutron beams at the measurement sites using MCNP. These values were obtained from the fluence spectra shown in **Figures 13** and **14** by calculating the ratio of the integral of the spectrum below epithermal range to the total fluence spectrum. The deviation (C/E) of calculated quality factors with measured values increases as the fraction of these low energy neutrons in the beam increases. This is explained in the following paragraph.

The neutron beams in the hand irradiation facility are accompanied by a large fraction of low energy (less than 10 keV) and thermal neutrons. The elastic scattering of these neutrons in the TEPC wall causes moderation and produces thermal neutrons which may be captured via the reactions $^{1}H(n, \gamma)^{2}H$ and $^{14}N(n, p)^{14}C$. The capture protons have a larger range than the recoil protons (produced via elastic scattering) which shifts the proton edge towards higher lineal energies and thus

overestimates the $\overline{y_D}$ which in turn overestimates the quality factor. The off-axis neutron beams carry a larger fraction of low energy and thermal neutrons as compared to in-axis beam. This low energy fraction is maximum at E_p = 2.00 MeV compared to 2.25 MeV.

TABLE 2: Comparison of measured and calculated effective quality factors in the hand irradiation facility. The effective quality factor was calculated using Eq. (13). Here C/E stands for the ratio of the calculated to the measured quality factors. The Φ_E/Φ_{tot} is the fraction of neutrons of energy less than 10 keV to the total neutron fluence in the given direction. The maximum fraction is observed in off-axis measurements at E_p = 2.00 MeV where maximum shift in proton edge was observed.

E_p	Position	Q_n		C/E	Φ_E/Φ_{tot}
(MeV)	(cm)	Measured	Calculated		(%)
2.00	(0, 0, 0)	17.50	13.57	0.78	8.0
	(-7, 0, 0)	21.22	11.72	0.55	12.0
	(7, 0, 0)	20.58	11.82	0.57	11.6
2.25	(0, 0, 0)	20.15	18.90	0.94	0.4
	(-7, 0, 0)	20.29	17.97	0.89	5.0
	(7, 0, 0)	20.18	18.05	0.89	4.8

F. Estimation of Dose Equivalent to Patient's Hand During IVNAA Measurement of Toxic Trace Elements at MAL

1. Estimation of Dose to Soft Tissue

The recoil protons produced in the TEPC wall and gas cavity by the neutron energies employed for IVNAA (spectra illustrated in **Figures 11** and **12**) have insufficient ranges to cross the cavity diameter (2 μm) and thus behave as an infinite cavity for almost all the recoil protons. The total absorbed dose to the A-150 wall, D_w, in this situation can be estimated from the measured dose, D_g, as[58, 65]

$$D_w = \left(\overline{K}_n\right)_g^w \times D_g \tag{14}$$

where $\left(\overline{K}_n\right)_g^w$ is the ratio of the neutron spectrum weighted coefficients in the irradiation field for the A-150 TE wall to TE gas. This equation can also be derived by following the Burlin cavity theory for infinite cavity (d = 0).[66] **Figure 18** shows the ratio of the neutron kerma coefficients of the A-150 TE wall to TE gas. The ratio of

the kerma coefficients is almost constant and close to unity in the energy range $1 \leq E_n \leq 300$ keV. The spectrum weighted kerma coefficients for the dose measurements carried out in the irradiation facility at different proton beam energies are given in **Table 3**. The neutron dose absorbed in the counter wall, D_w, estimated by (14) was converted into the absorbed dose in soft tissue by multiplying D_w with the ratio of spectrum weighted kerma coefficients, $\left(\overline{K}_n\right)_w^{tissue}$. A correction factor is also needed for the calibration of lineal energy dose distribution carried out using internal alpha source with the assumption of constant W value for all ionizing events caused by different LET particles. Correction factor for recoil protons was evaluated using a procedure mentioned earlier in the literature.[57, 58] These correction factors and overall correction factor for the dose measurements carried out in the irradiation facility at different proton beam energies are given in **Table 3** and finally applied to the measured neutron doses.

Neutron production using ^{7}Li(p,n)^{7}Be is accompanied mainly by 478 keV inelastic γ-rays resulting from (p, p'γ) with other very low intensity high-energy capture gammas produced by (p, γ) interactions (< 1%). Thermal neutron capture reaction with hydrogen in the moderator-reflector also produces 2.2 MeV gamma rays. It was estimated through Monte Carlo simulations that the more than 90% of the gamma dose was deposited by 478 keV gamma rays. Further, secondary electrons may also be generated by 2.2 MeV gamma rays produced via the thermal neutron capture reaction with hydrogen in the counter wall and gas cavity and their contribution is most likely to be negligible as compared to the external gamma rays. Assuming that the secondary electron fluence produced mostly by 478 keV gamma rays measured in the detector volume arises from the interactions in the counter wall,[57, 58] the gamma dose measured in the cavity can be converted into the dose to counter wall using (d = 1)[66]

$$D_w^{\gamma} = \frac{W_e}{W_\alpha} \times \left(\frac{\overline{L}}{\rho}\right)_g^w \times \left(\frac{\overline{\mu_{en}}}{\rho}\right)_w^{tissue} \times D_g^{\gamma} \qquad (15)$$

A W-value of (W_e) 26.1 eV/ion pair was determined for electrons in propane,[67] which is lower than the assumed value of (W_α) 26.92 eV/ion pair for 5.8 MeV α particles used

for TEPC calibration. Thus the value of W_e/W_α is 0.97. The stopping power ratio for A-150 to TE gas is roughly 0.98 for electron energies below 1 MeV[30, 57] and the mass energy absorption coefficients for soft tissue to A-150 is approximately unity. Thus the overall correction factor for the gamma dose component was calculated as 0.95.

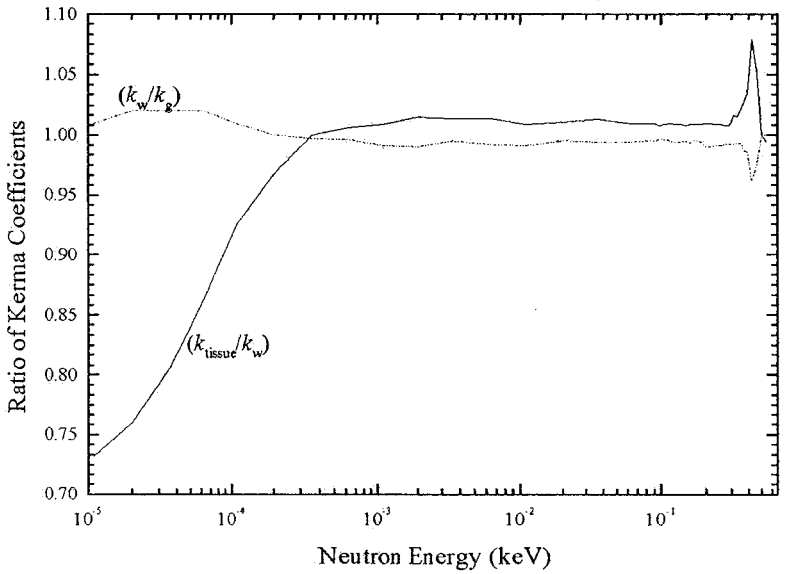

FIG. 18: Ratio of kerma coefficients for the neutron energies employed at IVNAA.

TABLE 3: Correction factors determined for neutron absorbed dose, D_g, measured by TEPC simulating a 2 μm TE diameter.

Beam Energy (MeV)	Position (cm)	$(\overline{K}_n)_g^w$	$(\overline{K}_n)_w^{tissue}$	$\frac{W_p}{W_\alpha}$	Overall Correction Factor
2.00	(0, 0, 0)	0.993	1.010	1.007	1.010
	(-7, 0, 0)	0.993	1.011	1.011	1.015
	(7, 0, 0)	0.993	1.011	1.010	1.014
2.25	(0, 0, 0)	0.988	1.020	1.009	1.017
	(-7, 0, 0)	0.989	1.021	1.009	1.019
	(7, 0, 0)	0.988	1.021	1.009	1.018

2. *Maximum Dose Equivalent Rate*

The maximum dose equivalent rate on the hand phantom surface was observed in the beam axis and the minimum was observed in off-axis measurements. The ratio of the maximum to minimum dose equivalent rate is ~3.5 for E_p = 2.25 MeV compared

to the ratio of the maximum to minimum dose rate is ~5 for E_p = 2.00 MeV. This happens because of the overestimation in measured quality factor values for off-axis measurements. However, for E_p = 2.25 MeV, the ratio of the maximum to minimum dose equivalent rate is almost the same as the ratio of the maximum to minimum dose rate. At this beam energy, the quality factor is almost constant over the phantom surface. The dose heterogeneity for gamma contamination varies only from ~1.5 to ~1.7 for E_p = 2.25 and 2.00 MeV which is much less than the corresponding dose heterogeneity for neutrons.

Thus instead of estimating the radiation dose equivalent received to the patient's irradiated hand either by using the maximum or minimum dose equivalent, a methodology is needed which can take into account this spatial variation of dose equivalent. This is discussed in the following section.

3. *Average Dose Equivalent Rate*

The neutron field inside the irradiation facility in the plane perpendicular to the beam axis is symmetric along the beam axis.[4, 7, 11] Taking the beam axis as the origin of coordinate system represented in cylindrical polar coordinate system because of the symmetry of the neutron field, the doses, $D(r)$, and the quality factors, $Q(r)$, measured at carefully chosen radial distances, r, on the hand phantom surface in the hand irradiation facility can be used to calculate the average quality factor of the neutron beam incident on the phantom surface as

$$\overline{Q} = \frac{\int_0^R \overline{Q}(r) D(r) 2\pi r dr}{\int_0^R D(r) 2\pi r dr} \qquad (16)$$

where R is the equivalent radius of the rectangular hand phantom determined from the area, A, of the hand phantom as $A = \pi R^2$. To evaluate the integrals in (16), measured $Q(r)$ and $D(r)$ values mentioned in **Table 1**, were represented by linear fits. The effects of fitting different interpolating polynomials was studied by using MCNP, however insignificant change less than 2-3% was observed. Thus we conservatively

estimate the total uncertainty in the average neutron quality factor to be less than 12-13%.

The average dose on the phantom surface can be estimated from the measured doses, $D_n(r)$, and the fluence, $\Phi_n(r)$, calculated by using MCNP at radial position r, as

$$\overline{D_n} = \overline{k_n} \times \overline{\Phi_n} = \frac{\int_0^R k_n(r)\,2\pi r dr}{\int_0^R 2\pi r dr} \times \overline{\Phi_n} = \frac{\int_0^R \frac{\int_{E_n} k_n(E_n,r)\Phi(E_n,r)dE_n}{\int_{E_n}\Phi(E_n,r)dE_n} 2\pi r dr}{\int_0^R 2\pi r dr} \times \overline{\Phi_n} = \frac{\int_0^R \frac{D_n(r)}{\Phi_n(r)} r dr}{\int_0^R r dr} \times \overline{\Phi_n} \tag{17}$$

where $\overline{\Phi_n}$ is the incident neutron fluence over the phantom surface calculated by using by using the neutron surface tally **F2**. The $\overline{k_n}$ is the average kerma coefficient of the incident neutron fluence over the phantom surface. We estimate the total uncertainty in dose rates to be less than 15%. The average neutron dose equivalent was calculated from the product of $\overline{D_n}$ and $\overline{Q}$ calculated using (17) and (16) respectively. The gamma dose heterogeneity was not taken into account and the maximum gamma dose rates (observed along beam axis) were used to calculate the total radiation dose equivalent. The total radiation dose equivalents at E_p = 2.25 and 2.00 MeV are presented in **Table 4**. The total uncertainty in dose equivalent rates is estimated to be 20%.

TABLE 4: Estimation of the average dose equivalent rates in the hand irradiation facility. The non-uniformity of the neutron field was taken into account by spatially averaging the quality factors and dose rates. The average dose equivalent to the patient's irradiated hand is estimated by multiplying the average H_T with the proposed hand irradiation time and the selected beam current.

E_p	Average Dose Rate (mGy/h-μA)			Total Average Hand Dose Eq Rate (mSv/h-μA)
(MeV)	$\overline{D_n}$	D_γ	$\overline{Q}$	$\overline{H_T} = \overline{D_n} \times \overline{Q} + D_\gamma$
2.00	0.33	1.48	18.90	7.72
2.25	1.35	1.15	20.20	28.48

4. MDLs of Manganese at MAL Using IVNAA

The MDL for an IVNAA measurement of Mn in the hand with proton beam energy of 2.00 MeV, beam current of 42 μA, irradiation time of 10 min was reported to be (1.0±0.2) μg/g of bone, which corresponds to the normal concentration of Mn in bone. The total dose equivalent received to the patient hand as a result of this proposed diagnostic procedure can be calculated by multiplying the average dose equivalent rate at E_p = 2.00 MeV listed in **Table 4** by the beam current (42 μA) and irradiation time (10 min = 0.17 h) as 54 mSv, this is slightly larger than the maximum allowable local dose equivalent (50 mSv) to the patient's irradiated hand restricted by the McMaster University Human Ethics Board for an *in-vivo* measurement of toxic trace elements. Thus the proposed irradiation procedure for the IVNAA measurement of manganese in human hands with normal (1 ppm) and elevated manganese content can be carried out without violating the prescribed dose limits for such diagnostic procedures. This finding is of significant importance because such low energies and beam currents can be achieved even by small accelerators and the normal manganese concentrations are still measurable.

These dose equivalent rates estimated in this work can be used to calculate the radiation dose equivalent received to patient's hand for IVNAA measurement of aluminum in human hand bones.

5. Shielding of External Gamma Rays

At E_p = 2.00 MeV beam energy, the gamma dose constitutes to about 20% of the total dose equivalent. The gamma dose to the patient can be avoided by providing a gamma shield between the moderator and the patient hand. This irradiation facility has the inner dimensions of 30×30×4.5 cm^3 and placing a lead shield of 30×30×0.5 cm^3 inside the facility after the moderator would reduce the inner dimensions to 30×30×4.0 cm^3. The effect of putting the lead shield inside the facility was studied by calculating the ratio of thermal and epithermal fluence to the total neutron dose equivalent (Φ_{TE}/H_T) with and without the proposed gamma shield using MCNP. The ratio Φ_{TE}/H_T was calculated as 1.10×10^8 ± 1.0% n-cm^{-2}/mSv and 1.15×10^8 ± 0.6% n-cm^{-2}/mSv with and without gamma shield. As a result of gamma shield both the Φ_{TE} and H_T were reduced by 5% and 10% respectively. Consequently this results in an

increase of Φ_{TE}/H_T by approximately 5%. However, the insertion of gamma shield inside the facility is expected to decrease the gamma dose from approximately 20% to 5% of the total dose equivalent.

IV. DISCUSSION AND CONCLUSION

This study describes the development of a method based on TEPC measurements to estimate the radiation dose equivalent received to the patient's hand undergoing the irradiation of hand in the facility developed at the McMaster University 3 MV Van de Graaff accelerator for the IVNAA measurement of toxic elements in human hand bones.

Following conclusions can be drawn from this work:

- LET information required to calculate the quality factors below 300 keV neutron energy can not be retrieved from lineal energy measurements made by a TEPC simulating 2 μm TE diameter either by using the approximation $L = y$, or the Rossi's transformation algorithm. Thus counter fails to provide a flat R_Q response based on the definition of $Q(L)$ provided in ICRP 60[13] and showed a sharp drop below 200 keV neutron energy. This decreasing trend in quality factor with the decreasing neutron energy is much more pronounced than that of similar TEPC measurements reported for ICRP 26[12].

- A neutron quality factor algorithm has been developed which utilizes the average of the measured lineal energy dose distributions to provide a better estimate of the effective quality factors based on ICRP 60[13] for low energy accelerator based *in-vivo* neutron activation measurements. The algorithm does not need any transformation of the measured lineal energy dose distribution, $d(y)$, into an LET dose distribution, $d(L)$.

- The algorithm reported in this work employing the TEPC system was used to determine the effective quality factors in the center and at horizontal distances of ±7 cm in the hand irradiation facility using the beam energies E_p = 2.00 MeV and 2.25 MeV. The measured quality factors were compared with those calculated by using MCNP. The algorithm overestimates the quality factors in the irradiation facility. The overestimation of the measured

neutron quality factors always lies within the estimated experimental uncertainty at a beam energy of E_p = 2.25 MeV. However, the overestimation in the measured value in the center of the irradiation facility at beam energy of E_p = 2.00 MeV was 30% which increased further to approximately 45% for off-axis measurements. The overestimation is shown to be correlated with the presence of low energy neutrons (< 5 keV) at the point of measurement in hand irradiation facility.

- TEPC measurements carried out as a function of position on the phantom surface in the hand irradiation facility were used to calculate the average neutron quality factor of the incident beam on the phantom. The dose heterogeneity was also taken into account to calculate the average absorbed neutron dose on the front phantom surface. The product of the average quality factor and the average dose on the phantom surface was used to calculate the average dose equivalent received to the patient's hand.
- The proposed irradiation procedure for the IVNAA measurement of manganese in human hands with normal (1 ppm) and elevated manganese content can be carried out without violating the prescribed dose limits for such diagnostic procedures. This MDL was achieved with proton beam energy of 2.00 MeV and a beam current of 42 μA. This finding is of significant importance because such low energies and beam currents can be achieved even by small accelerators and the normal manganese concentrations are still measurable.
- The filtration of the non-useful fast energy neutron group from the beam will further decrease the dose equivalent to the patient's hand.

REFERENCES

[1]L. T. Somervaille, D. R. Chettle, M. C. Scott, D. R. Tennant, M. J. McKiernan, A. Skilbeck, W. N. Tethowan, "In-vivo tibia lead measurements as an index of cumulative exposure in occupationally exposed subjects," Br. J. Ind. Med. **45**, 174-181 (1988).

[2]S. Palerme, *Pilot Studies for In-Vivo Bone Aluminum Measurements*, MSc Thesis, McMaster University, Hamilton, ON, Canada (1993).

[3]S. Palerme, D. R. Chettle, T. J. Kennett, W. V. Prestwich, C. E. Webber, "Pilot studies for in-vivo bone aluminum measurements," Basic Life Sci. **60**, 303-306 (1993).

[4]A. Pejović-Milić, *An accelerator based in vivo measurement of aluminum in human bone by neutron activation analysis*, MSc Thesis, McMaster University, Hamilton, ON, Canada (1998).

[5]A. Pejović-Milić, F. E. McNeill, W. V. Prestwich, A. J. Waker, D. R. Chettle, "Development of an accelerator-based determination of aluminum burden in peripheral bone by neutron activation analysis," Appl. Radiat. Isot. **49 No. 5/6**, 717-719 (1998).

[6]M. L. Arnold, F.E. McNeill, D.R. Chettle, "The feasibility of measuring manganese concentrations in human liver using neutron activation analysis," NeuroToxicology **20(2-3),** 407-412 (1999).

[7]M. L. Arnold, *Development of an Accelerator Based System for In-Vivo Neutron Activation Analysis Measurements of Manganese in Humans*, PhD Thesis, McMaster University, Hamilton, ON, Canada (2000).

[8]M. L. Arnold, F. E. McNeill, W. V. Prestwich, D. R. Chettle, "System design for in-vivo neutron activation analysis measurements of manganese in the human brain: based on Monte Carlo modeling," Appl. Radiat. Isot., **53**, 651-656 (2000).

[9]A. Pejović-Milić, M. L. Arnold, F. E. McNeill, D. R. Chettle, "Monte Carlo design study for in vivo bone aluminum measurement using a low energy accelerator beam," Appl. Radiat. Isot. **53**, 657-664 (2000).

[10]A. Pejović-Milić, *In-Vivo Measurement of Some Trace Elements In Human Bone*, PhD Thesis, McMaster University, Hamilton, ON, Canada (2001).

[11]M. L. Arnold, F.E. McNeill, I.M. Stronach, A.J. Waker, A. Pejović-Milić, D.R. Chettle, "An accelerator based system for in vivo neutron activation analysis measurements of manganese in human hand bones," Med. Phys. **29(11),** 2718-2724 (2002).

[12]ICRP. *Recommendation of the ICRP: Annals of ICRP.* ICRP Publication 26 (Pergamon Press, Oxford 1977).

[13]G. Dietze, J. Booz, A. A. Edwards, S. Guldbakke, H. Kluge, J. B. Leroux, L. Lindborg, H. G. Menzel, V. D. Nguyen, Th. Schmitz, H. Schuhmacher,

"Intercomparison of dose equivalent meters based on microdosimetric techniques," Radiat. Prot. Dosim. **23(1/4)**, 227-234 (1988).

[14]W. G. Alberts, E. Dietze, S. Guldbakke, H. Kluge, H. Schuhmacher, "International intercomparison of TEPC systems used for radiation protection," Radiat. Prot. Dosim. **29**, 47-53 (1989).

[15]P. Pihet, H. G. Menzel, W.G. Alberts, H. Kluge, "Response of tissue-equivalent proportional counters to low and intermediate energy neutrons using modified TE-^{3}He gas mixtures," Radiat. Prot. Dosim. **29(1-2)**, 113-118 (1989).

[16]S. Gerdung, R. E. Grillmaier, T. Lim, P. Pihet, H. Schuhmacher, P. Ségur, "Performance of TEPCs at low pressures: some attempts to improve their dose equivalent response in the neutron energy range from 10 keV to 1 MeV," Radiat. Prot. Dosim. **52(1-4)**, 57-59 (1994).

[17]A. J. Waker, "Principles of experimental microdosimetry," Radiat. Prot. Dosim. **61(4)**, 297-308 (1995).

[18]R. Khaloo, A. J. Waker, "An evaluation of hydrogen as a TEPC counting gas in radiation protection microdosimetry," Rad Prot. Dosim. **58(3)**,185-191 (1995).

[19]G. C. Taylor, "An analytical correction for the TEPC dose equivalent response problem," Radiat. Prot. Dosim. **61(1-3)**, 67-70 (1995).

[20]T. Nunomiya, E. Kim, T. Kurosawa, S. Taniguchi, S. Yonai, T. Nakamura, Y. Nakane, Y. Sakamoto, S. Tanaka, "Measurement of lineal-energy distributions for neutrons of 8 keV to 65 MeV by using a tissue-equivalent proportional counter," Radiat. Prot. Dosim. **102(1)**, 49-59 (2002).

[21]ICRP. *Radiation protection recommendation of the international commission on radiological protection*. ICRP Publication 60 (Pergamon Press, Oxford 1991).

[22]H. H. Rossi, *Microscopic energy distribution in irradiated matter*. IN Radiation Dosimetry. Eds F. H. Attix and W. C. Roesch (Academic Press, NewYork, Vol. 1, 70-92, 1968).

[23]Aslam, W.V. Prestwich, F.E. McNeill, "Thin Target ^{7}Li(p,p'γ)^{7}Li Inelastic Gamma Ray Yield Measurements," J. Radioanal. Nucl. Chem. **254(3)**, 533-544 (2002).

[24]Aslam, W.V. Prestwich, F.E. McNeill, "Lithium Target Performance Evaluation for Low Energy Acclerator Based In-vivo Measurements using Gamma Spectroscopy," Appl. Radiat. Isot. **58(3)**, 321-331 (2003).

[25]Aslam, W.V. Prestwich WV, F.E. McNeill, Waker AJ, (2003d) *Spectrometry and Dosimetry for Accelerator Based In-vivo Measurements*, Annual Report McMaster Accelerator Laboratory, McMaster University, Hamilton, ON, Canada (2002).

[26]ICRU. *Photon, electron, proton and neutron interaction data for body tissues,* ICRU Report 46 (ICRU Publications, Bethesda, MD 1986).

[27]D. Srdoc, S. A. Marino, "Microdosimetry of monoenergetic neutrons," Radiat. Res. 146(4), 466-474 (1996).

[28]Aslam, W.V. Prestwich, F.E. McNeill, Waker AJ, "Investigating the TEPC radiation quality response for radiation protection in low energy accelerator based clinical applications," Radiat. Prot. Dosim., **103(4)**, 311-322 (2003).

[29]C. L. Lee, X. L. Zhou, "Thick target neutron yields for the ^{7}li(p, n)^{7}be reaction near threshold," Nucl. Inst. Meth. Phys. Res. B **152,** 1-11 (1999).

[30]ICRU. *Stopping powers and ranges for protons and alpha particles.* ICRU Report 49 (ICRU Publications, Bethesda, MD 1983).

[31]ICRU. *Microdosimetry.* ICRU Report 36 (ICRU Publications, Bethesda, MD 1983).

[32]ICRU. *The quality factor in radiation protection.* ICRU Report 40 (ICRU Publications, Bethesda, MD 1986).

[33]A. Ricourt, F. Posny, R. Soulié, M. Chemtob, V.D. Nguyen, *Possibilitiés d'utilization des techniques microdosimètriques pour la détermination de l'équivalent de dose*, IN Seventh Symposium on Microdosimetry, Oxford, 1981. EUR7147. eds. J. Booz, H. G. Ebert, H. D. Hartfield (Harwood Academic for CEC, London 1981).

[34]T. G. Stinchcomb, T.B. Borak, "Neutron quality parameters versus energy below 4 MeV from microdosimetric calculations," Radiat. Res. **93(1)**, 1-18 (1983).

[35]Y. Eisen, R. J. Brake, D. G. Vasilik, B. H. Erkkila, G. J. Littlejohn, "The performance of low pressure tissue-equivalent chambers and a new method for parameterising the dose equivalent," Radiat. Prot. Dosim. **15(2)**, 117-130 (1986).

[36]C. K. C. Wang, T. E. Blue, R. Gahbauer, R., "A neutronic study of an accelerator-based neutron irradiation facility for boron neutron capture therapy," Nucl. Tech. **84(1),** 93-107 (1985).

[37]J. C. Yanch, X. L. Zhou, R. E. Shefer, R.E., Klinkowstein, "Accelerator-based epithermal neutron beam design for neutron capture therapy," Med. Phys. **19(3),** 709-721 (1992).

[38]D. A. Allen, T. D. Benyon, "A design study for an accelerator-based epithermal neutron beam for BNCT," Phys. Med. Biol. **40,** 807-821 (1995).

[39]X. L. Zhou, C. Lee, "Analysis of epithermal neutron production by near-threshold (p, n) reactions," Appl. Rad Isot. **48,** 1571-1575 (1997).

[40]X. L. Zhou, C. Lee, "Lithium compounds as targets for (p, n) reactions," Appl. Rad Isot. **48,** 1493-1496 (1997).

[41]B. F. Bayanov, V. P. Belov, E. D. Bender, M. V. Bokhovko, G. I. Dimov, V. N. Kononov, O. E. Kononov, N. K. Kuksanov, V. E. Palchikov, V. A. Pivovarov, R. A. Salimov, G. I. Silvestrov, A. N. Skrinsky, N. A. Soloviov,

S. Yu Taskaev, "Accelerator-based neutron source for the neutron-capture and fast neutron therapy at hospital," Nucl. Inst. Meth. Phys. Res. A **413(2-3),** 397-426 (1998).

[42] J. A. Powell, H. Ludewig, M. Todosow, M. Reich, "Target and filter concepts for accelerator-driven boron neutron capture therapy applications," Nucl. Tech. **125,** 104-115 (1999).

[43]J. P. Pignol, P. Cuendet, N. Brassart, G. Fares, F. Colomb, C. M'Bake Diop, R. Sabattier, A. Hachem, G. Prevot, "Combined use of FLUKA and MCNP-4A for Monte Carlo simulation of the dosimetry of ^{10}B neutron capture enhancement of fast neutron irradiations," Med. Phys. **25(60),** 885-891 (1998).

[44]D. P. Gierga, J.C. Yanch, R. E. Shefer, "An Investigation of the feasibility of gadolinium for neutron capture synovectomy," Med. Phys. **27(7)**, 1685-92 (2000).

[45]D. P. Gierga, J. C. Yanch, R. E. Shefer, "Development and construction of a neutron beam line for accelerator-based boron neutron capture synovectomy," Med. Phys. **27(1)**, 203-14 (2000).

[46]S. Endo, M. Hoshi, H. Tauchi, S. Takeoka, K. Kitagawa, S. Suga, N. Meada, K. Komatsu, S. Sawada, E. Iwamoto, S. Sakamoto, K. Takeyama, M. Omura, "Neutron generator at hiroshima university for use in radiobiology study," J. Radiat. Res. **36,** 91-102 (1995).

[47]S. Endo, M. Hoshi, J. Takada, H. Tauchi, S. Matsuura, S. Takeoka, K. Kitagawa, S. Suga, K. Komatsu, "Neutron generator (HIRRAC) and dosimetry study," J. Radiat. Res. (Tokyo). **40** Suppl, 14-20 (1999).

[48]E. Schmid, D. Regulla, S. Guldbakke, D. Schlegel, M. Bauchinger, "The effectiveness of monoenergetic neutrons at 565 keV in producing dicentric chromosomes in human lymphocytes at low doses, Radiat. Res. **154** p307-312 (2000).

[49]E. Schmid, D. Regulla, S. Guldbakke, D. Schlegel, M. Roos, "Relative biological effectiveness of 144 keV neutrons in producing dicentric chromosomes in human lymphocytes compared with ^{60}Co gamma rays under head-to-head conditions," Radiat Res. **157(4)**, 453-460 (2002).

[50]Aslam, W.V. Prestwich, F.E. McNeill, A. J. Waker, "Development of low energy monoenergetic neutron source for applications in low dose radiobiological and radiochemical research," Appl. Radiat. Isot. **58(6)**, 629-641 (2003).

[51]A. I. M. Ritchie, "Neutron yields and energy spectra from thick target Li(p, n) source," J. Phys. D: Appl. Phys. **9,** 15-26 (1976).

[52]J. W. Meadows, *Determination of the Energy Scale for Neutron Cross-section Measurements Employing a Monoenergetic Accelerator*, ANL/TDM-25 (1977).

[53]V. N. Kononov, E. D. Poletaev, B. D. Yurlov, "Absolute yield and spectrum of neutrons from the ^{7}Li(p, n)^{7}Be" At. Energ. **43,** 947-949 (1977).

[54]H. Liskien, A. Paulsen, "Neutron production cross-sections and energies for the reactions ^{7}Li(p, n)^{7}Be and ^{7}Li(p, n)^{7}Be*", At. Data Nucl. Data Tables **15,** 57-84 (1975).

[55]J. F. Janni, "Proton range-energy tables, 1 keV–10 GeV," At. Data Nucl. Data Tables **27**, 147(1982).

[56]J. F. Briesmeister (Ed.), *MCNP: A General Monte Carlo N-Particle Transport Code, Version 4B*, LA-12625-M, Los Alamos, USA, (1997).

[57]J. Burmeister, *Specification of the physical and biologically effective absorbed dose in radiation therapies utilizing the boron neutron capture reaction*, PhD Thesis, Wayne State University, Detroit, MI, USA (1999).

[58]C. Kota, *Microdosimetric considerations in the use of the boron neutron capture reaction in radiation therapy*, PhD Thesis, Wayne State University, Detroit, MI, USA (1996).

[59]T. Cousins, *The application of monochromatic photoneutron spectroscopy in an examination of nuclear levels of ^{180}Ta, ^{202}Tl and ^{204}Tl*, PhD Thesis, McMaster University, Hamilton, ON, Canada (1982).

[60]T. Iguchi, N. Nakayamada, H. Takahshi, M. Nakazawa, "Neutron spectrometry using a ^{3}He ionization chamber," Nucl. Inst. Meth. Phys. Res. A **353**, 152-155 (1994).

[61]H. Schuhmacher, W. G. Alberts, H. G. Menzel, G. Buhler, "Dosimetry of low-energy neutrons using low-pressure proportional counters," Radiat Res. **111(1)**, 1-9 (1987).

[62]G. Dietze, B. R. Siebert, "Photon and neutron dose contributions and mean quality factors phantoms of different size irradiated by monoenergetic neutrons," Radiat. Res. **140(1)**, 130-133 (1994).

[63]G. F. Knoll, *Radiation detection and measurement*. 2nd Ed., (Wiley, New York, USA 1989).

[64]A. Kadachi, A. Waheed, M. Al-Eshaikh, M. Obeid, "Use of photodiode in microdosimetry and evaluation of effective quality factor," Nucl. Inst. Meth. Res. A **404(2-3)**, 400-406 (1998).

[65]S. Pszona and M. Makarewicz "Effect of cavity size on the sensitivity of a TE-walled, TE-gas -filled ionization chamber for fast neutrons," Phys. Med. Biol, **27(8)**, 1015-1022 (1982).

[66]T. E. Burlin "A general theory of cavity ionization," Brit. J. Radiol., **39**, 727-734 (1966).

[67]I. A. Combecher "Measurement of W values of low energy electrons in several gases," Radiat. Res., **84**, 189-218 (1980).

CHAPTER VI

Paper V

This article describes the Monte Carlo simulation of hand irradiation facility developed at the McMaster University 3 MV Van de Graaff accelerator for the IVNAA measurement of potentially toxic elements in human hand bones. Compared to the method presented in our earlier work (*Paper IV*), a simpler method is described in this work to estimate the average radiation dose equivalent delivered to hand employing the dose rate measured using a small volume TEPC in the center of the irradiation facility.

The work presented in this paper was performed by me under the supervision of Drs. Prestwich, McNeill and Waker. This problem was formulated by Dr. McNeill. The manuscript was written by me and edited by Drs. Prestwich, McNeill and Waker.

Monte Carlo Simulation of Neutron Irradiation Facility Developed for Accelerator Based *In-Vivo* Neutron Activation Measurements in Human Hand Bones

Aslam[1], W.V. Prestwich[1], F.E. McNeill[1] and A.J. Waker[2]

[1]Medical Physics and Applied Radiation Sciences Unit, McMaster University, Hamilton, ON, Canada, L8S 4K1.

[2]AECL, Chalk River Laboratories, Chalk River, ON, Canada K0J 1J0

ABSTRACT

The neutron irradiation facility developed at the McMaster University 3 MV Van de Graaff accelerator is employed to assess *in vivo* elemental content of aluminum and manganese in human hands. These measurements are carried out to monitor the long-term exposure of these potentially toxic trace elements through hand bone levels. The dose received to a patient during an irradiation procedure is the limiting factor for IVNAA measurements. This article describes a method to estimate the average radiation dose equivalent delivered to the patient's hand during irradiation. The computational method described in this work augments the dose measurements carried out earlier (Med Phys 29(11) (2002) 2718). This method employs the Monte Carlo simulation of hand irradiation facility using MCNP4B. Based on the estimated doses received to the patient hand, the proposed irradiation procedure for the IVNAA measurement of manganese in human hands (Med Phys 29(11) (2002) 2718) with normal (1 ppm) and elevated manganese content can be carried out with a reasonably low dose of 31 mSv to the hand. 63% of the total dose equivalent is delivered by non-useful fast group (>10 keV), the filtration of this neutron group from the beam will further decrease the dose equivalent to the patient's hand.

1. INTRODUCTION

In vivo neutron activation analysis (IVNAA) is a technique that has been in use for almost four decades for the measurement of various major, minor and trace elements in the human body for medical research, clinical diagnosis and occupational health purposes (for example, Cohn, 1980; Cohn, 1981; Chettle and Fremlin, 1984; Beddoe and Hill, 1985; Cohn and Parr, 1985; Heymsfield *et al.*, 1989; Chettle *et al.*, 1990; Pierson *et al.*, 1990; Hill, 1990; Burkinshaw, 1990; Heymsfield and Waki, 1991; Greenfield, 1992; Heymsfield *et al.*, 1993; Jebb and Elia, 1993; Sutcliffe, 1996; Pichard and Kyle, 1998; Kehayias and Valtuena, 1999; Ellis, 2000; Plank and Hill, 2000; Morgan, 2000; Lee *et al.*, 2001). This technique is based on the measurement of characteristic γ-rays produced in the body by neutron interaction with the element of interest. *In vivo* elemental content of the body is assessed by employing the

fast neutron interaction (for N and P), neutron inelastic scattering (for C and O) and thermal neutron capture reactions (for N, Ca, Cd, Al, Mn). The induced activity is measured either during the irradiation procedure (called prompt IVNAA) or after the irradiation (called delayed IVNAA). In cyclic activation, irradiations and activity measurements are carried out in alternate cycles.

Several research groups around the world have been involved in the development and application of the technique of IVNAA for the measurement of potentially toxic elements found in trace amounts in the human body. IVNAA determination of Cd (Henke *et al.*, 1970; Karlicek *et al.*, 1971; Karlicek and Topolcan, 1974; McLellan *et al.*, 1974; McLellan *et al.*, 1975; Harvey *et al.*, 1975; Vartsky *et al.*, 1977; Sabbioni *et al.*, 1978; Al-Hiti *et al.*, 1979; Thomas *et al.*, 1979; Scott *et al.*, 1980; Scott and Chettle, 1986; Ryde *et al.*, 1987; Morgan *et al.*, 1981; Morgan *et al.*, 1981;Mason *et al.*, 1988; Lindh *et al.*, 1980; Krauel *et al.*, 1980; Greenberg *et al.*, 1986; Gompertz *et al.*, 1983; Gerhardsson *et al.*, 1988; Gerhardsson *et al.*, 1986; Ellis *et al.*, 1985; Ellis *et al.*, 1983; Davison *et al.*, 1988; Cummins *et al.*, 1980; Cohn *et al.*, 1983; Chung *et al.*, 1985; Chettle and Fremlin, 1984; Brune *et al.*, 1980; Baron and Schweinsberg, 1988; Baddeley *et al.*, 1983; Al-Haddad *et al.*, 1981; Ryde *et al.*, 1989; Shaikh *et al.*, 1990; Krishnan *et al.*, 1990; Morgan *et al.*, 1990; Franklin *et al.*, 1990a, b; Chettle *et al.*, 1990; Skerfving and Nilsson, 1992; Gerhardsson and Nordberg, 1993; Fedorowicz *et al.*, 1993; Ralston *et al.*, 1994; McNeill and Chettle, 1998; Perrin *et al.*, 1998; Mason *et al.*, 1999; Landsberger and Wu, 1999), Al (Williams *et al.* 1980; Ellis *et al.* 1988; Green and Chettle 1992; Wyatt *et al.* 1993; Palerme, 1993; Palerme *et al.*, 1993; Green et al. 1993; Lewis *et al.*, 1997; Pejović-Milić, 1998, 2001; Pejović-Milić *et al.*, 1998, 2000), Mn (Arnold, 2000; Arnold *et al.*, 2002), Si (Ettinger *et al.* 1982; Kacperek *et al.* 1993), Be (Ali *et al.*, 1985), and Li (Vartsky *et al.* 1985; Glaros *et al.* 1986) in body has produced a significant volume of knowledge in studying diseases, such as anorexia, renal disorders, encephalopathy, osteodystrophy and anaemia (Lewis *et al.*, 1997).

A neutron irradiation facility at the McMaster University 3 MV Van de Graaff accelerator for *in-vivo* neutron activation measurement of potentially toxic elements aluminum and manganese in human hand bones has also been developed (Palerme, 1993; Palerme *et al.*, 1993; Pejović-Milić, 1998, 2001; Pejović-Milić *et al.*, 1998, 2000; Arnold, 2000; Arnold *et al.*, 2002; Aslam *et al.*, 2002, 2003a, b, c, d). Various issues of system design and evaluation have been addressed with the aim to maximize the activation of the intended isotope with

minimum dose received to the subject. These investigations include the selection of the target material for neutron production, development of lithium targets with appropriate cooling system, selection of proton beam energy above the threshold of the neutron production reaction, determination of moderator and reflector material type and thicknesses, verification of reproducibility of the activation and counting processes, consideration of various shapes and position of the hand phantom, measurement and control of dose equivalent to the patient's hand undergoing irradiation, and lastly the use of the calcium activation signal from the bone to normalize the measurement to the amount of bone.

The reports of the *in-vivo* measurements of aluminum and manganese in human hand bones by activation analysis at McMaster University Accelerator Laboratory (MAL) have demonstrated its clinical feasibility for screening patients with significantly elevated levels of these elements. The sensitivity (minimum detectable limit) of the system was not sufficiently low to detect the lower levels of Mn and Al found in normal subjects or patients in the early stages of diseases. The minimum detectable limits (MDLs) for Mn and Al in the hand bone was reported for a dose equivalent of 50 mSv delivered to the hand phantom, following the maximum permissible dose equivalent limit defined for such clinical diagnostic procedures conducted under the jurisdiction of McMaster University by McMaster University Human Ethics Board. A major limitation of the reported system (Pejović-Milić, 1998, 2001; Arnold, 2000; Arnold *et al.*, 2002) was the high contamination of the neutron beam with non-useful fast neutron group delivering unacceptably high dose and therefore low thermal neutron fluence per unit dose equivalent was available for the activation of the element of interest.

To improve the MDL for a given dose to the hand, there are various important issues regarding the neutron source and the radiation dosimetry which need to be addressed for example, (a) estimation of the neutron quality factors for the neutron beams used for IVNAA of hand to augment the dose measurements carried out earlier (Arnold *et al.*, 2002) for the calculation of dose equivalent received to the patient's hand, (b) development of a method to estimate the average dose equivalent received to the patient's hand undergoing irradiation because of the heterogeneous dose distribution over the hand surface, (c) gamma shield design from those photons produced either in the target due to $^{7}Li(p, p'\gamma)^{7}Li$ (E_γ = 478 keV) or in the neutron moderating assembly due to $^{1}H(n, \gamma)$ interaction (E_γ = 2.2 MeV), (d) non-uniformity of activation and its measurement along the transverse (phantom surface) and longitudinal (phantom depth) directions in the hand phantom due to non-uniform distribution of the useful neutron fluence, (e) estimation of the contamination of the non-

useful fast neutron component of the total fluence at the beam energies of 2.00 and 2.25 MeV and its filtration to increase the useful neutron fluence (thermal and epithermal) per unit dose equivalent available for activation. These issues have been investigated by simulating the hand irradiation facility developed at MAL using the radiation (neutron, photon, and electron) transport code MCNP4B (Briesmeister, 1997). A series of Monte Carlo computer simulations have been performed for this purpose. Further, this report would provide a comparison of the efficacy of different proton beam energies used for IVNAA at MAL.

2. MATERIALS AND METHODS

2.1. Neutron Source

The 3 MV Van de Graaff accelerator at the McMaster University Accelerator Laboratory (MAL) is used to produce low energy fast neutrons of mean neutron energy less than 500 keV for *in-vivo* neutron activation (IVNAA) measurement of trace elements in human hand bones. These neutrons are produced using thick lithium metal targets via the $^{7}Li(p, n)^{7}Be$ interaction. These targets are mounted at the end of a beam duct and cooled with water to prevent heating by proton beam currents. The target holder used for experimentation has a copper backing of 10 mm between the water channel and the target. This facility is operated at proton beam currents as low as a few nA (Aslam *et al.*, 2002) up to 100 μA (Pejović-Milić, 1998; 2001). The total neutron yield (n/μC) of a thick lithium target increases with increase in the incident proton beam energy (Lee and Zhou, 1999; Aslam *et al.*, 2001, 2003c). This increase in total neutron yield of a thick lithium target with increase in beam energy is accompanied by an increase in mean neutron energy (80 and 225 keV at E_p = 2.00 and 2.25 MeV respectively averaged in the forward direction) (Lee and Zhou, 1999; Aslam *et al.*, 2001, 2003b, c). Kerma coefficient in tissue equivalent materials also increases with increase in neutron energy (E_n > 30 eV) (ICRU, 1986). To reduce the patient dose, lower beam energies (E_p = 2.00 MeV) are preferred for IVNAA using higher beam currents to compensate for lower neutron yield at these beam energies. The neutron activation (n, γ) cross-sections at these neutron energies are very low for the isotopes of interest (Al and Mn). Thus in order to maximize the activation of the isotope in question and also to minimize the dose at the same time, the direct neutron beams are moderated in a manner dependent upon the application. Higher beam energies would require extensive neutron moderation because of the higher neutron energies at these beam energies to produce the same useful neutron fluence per unit dose equivalent. The beam current and the irradiation time depending upon the half-life of

the radioisotope produced as a result of activation are chosen to be optimal (Palerme, 1993; Pejović-Milić, 1998; Arnold *et al.*, 1999; Arnold, 2000; Pejović-Milić, 2001; Arnold *et al.*, 2002).

2.2. Patient Hand Dose

The dose received to a patient during an irradiation procedure is the limiting factor for IVNAA measurements. To use this technique in clinical medicine, it is desirable to keep the radiation dose as small as possible consistent with the statistical precision requirements of the procedure. The absorbed dose includes contributions from both neutrons and accompanying external and internal γ rays. The total dose equivalent to the patient's irradiated hand is estimated by multiplying the measured neutron and gamma doses with appropriate quality factors. A quality factor ranging from 5 to 20 depending upon the neutron spectrum is normally taken for neutrons (ICRU, 1986; ICRP, 1991; Aslam *et al.*, 2003b) and that for γ-rays is 1 (ICRU, 1986; ICRP, 1991). Thus neutrons dose equivalent dominates over the gamma dose equivalent. The neutron dose equivalent accounts for about 70-90% of the total dose equivalent for the neutron sources used for IVNAA.

The McMaster University Human Ethics Board restricts the maximum local dose equivalent to the irradiated hand to less than 50 mSv for an *in-vivo* measurement of toxic trace elements (Arnold, 2000; Pejović-Milić, 2001; Arnold *et al.*, 2002). Neutron sources that have been in use in IVNAA produce energy spectra, which are continuous and have a wide range. The neutron dose is thus calculated as the convolution of the incident neutron fluence spectrum and the kerma coefficients. Kerma coefficients in tissue equivalent materials increase with increase in neutron energy (E_n>30 eV) (ICRU, 1986). Thus considering the radiation dose, neutrons with relatively low energies are most desirable for IVNAA.

2.3. Neutron Fluence Spectrum

Aluminum and manganese are measured in hand bones by the (n, γ) reaction. For this reaction, the activation cross-section is maximum at thermal neutron energies and decreases very rapidly with increase in neutron energy for the isotopes of interest. The thermal neutron fluence declines exponentially in tissue. The mean free path of thermal neutrons equals the average thickness of the palm of a hand (Palmer *et al.*, 1968). Thus the direct use of an incident beam of thermal neutrons for IVNAA measurements in a hand will introduce a fairly non-uniform thermal fluence distribution and hence will result in non-uniform activation of the element of interest. Therefore, the ideal neutron source is an epithermal beam having an incident energy spectrum on the order of a few keV, which is partially

moderated in the hand itself. However, the composite sensitivity at any location within the hand phantom is determined from the product of the thermal neutron fluence and efficiency of the detector used to measure the induced gamma activity.

2.4. Hand Irradiation Facility for IVNAA

The hand irradiation facility designed for IVNAA of aluminum (Palerme, 1993; Palerme *et al.*, 1993; Pejović-Milić, 1998; Pejović-Milić *et al.*, 1998; Pejović-Milić *et al.*, 2000; Pejović-Milić, 2001) and manganese (Arnold, 2000; Arnold *et al.*, 2002) is illustrated in **Figure 1**. This irradiation facility has the inner dimensions of 30×30×4.5 cm^3 and consists of 2.4 cm thick polyethylene walls on five of the six sides. These walls are used to moderate and reflect the neutrons entering the irradiation facility. The open side of the irradiation facility is used to insert hand phantom inside the facility for IVNAA.

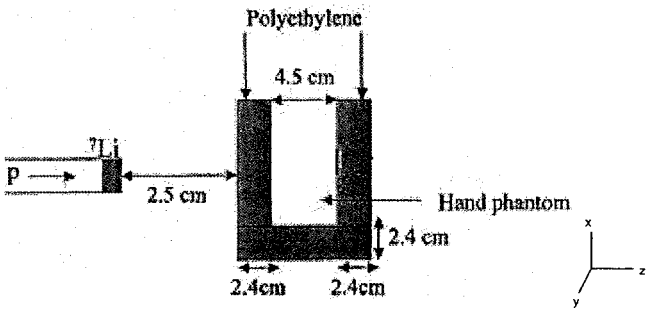

FIG. 1: Schematic diagram of the hand irradiation facility used for IVNAA of hand at MAL.

2.5. MCNP Modeling of Hand Irradiation Facility

The Monte Carlo simulation of the neutron irradiation facility was carried out using MCNP4B (Briesmeister, 1997). A computer model of the existing IVNAA facility at MAL was produced to simulate the transport of neutrons and associated photons. Time independent simulation was used as the accelerator is normally run under constant operating conditions for any given measurement. The target cooling systems and other aspects of the beam line were not included in the modeling. The target backing was made of high Z material (Cu) to minimize neutron scattering.

2.5.1. Thick Target Energy Spectrum and Angular Distribution of Neutrons Produced via ^{7}Li(p, n)^{7}Be Reaction

Low energy neutrons for many clinical applications are produced by low energy charged particle induced reactions with low mass number targets using charged-particle accelerators. Lithium targets using the ^{7}Li(p, n)^{7}Be reaction are widely used as a low energy neutron

source for clinical applications in BNCT (Wang *et al.*, 1985; Yanch *et al.*, 1992; Allen and Benyon, 1995; Zhou and Lee, 1997 a, b; Bayanov *et al.*, 1998; Powell *et al.*, 1999; Lee and Zhou, 1999) BNCEFNT (Pignol *et al.*, 1998), BNCS (Gierga *et al.*, 2000a, b), *in-vivo* neutron activation measurements (Palerme, 1993; Pejović-Milić, 1998; Arnold, 2000; Arnold *et al.*, 1999, 2000; Pejović-Milić *et al.*, 1998, 2000) and in radiobiological experiments (Endo *et al.*, 1995; Schmid *et al.*, 2000, 2002). The neutron energy spectrum and angular distribution of the neutrons in the near threshold region of 1.88 – 1.93 MeV were calculated using the Breit-Wigner approximation for the differential cross-sections to avoid singularities (Ritchie, 1976; Meadows, 1977; Kononov *et al.*, 1977; Lee and Zhou, 1999) and the reported measured (p, n) differential cross-section data for ^{7}Li (Liskien and Paulsen, 1975) were employed above this region. Our calculations are briefly summarized here.

The number of neutrons produced from an element of target of thickness dx (corresponding to an energy loss of dE_p in thickness dx) emitted at angle θ into an element of solid angle dΩ per unit incident proton charge is given by

$$\frac{d^2Y(E_n,\theta)}{d\Omega dE_n} = \frac{n_T}{e}\frac{d\sigma}{d\Omega'}\frac{d\Omega'}{d\Omega}\frac{1}{S(E_p)}\frac{dE_p}{dE_n} \qquad (1)$$

where n_T is the lithium target atomic density, dE_n refers to the width of the neutron spectrum because of the thickness dx (or dE_p), and dE_p/dE_n was calculated from the Q-value equation (Ritchie, 1976; Lee and Zhou, 1999; Arnold, 2000). The term dσ/dΩ′ representing the differential cross-sections in the c.m. and the stopping powers, $S(E_p)$, for ^{7}Li were taken from Janni (1982).

The spectrum of the neutrons produced as a result of bombardment of a unidirectional proton beam on a thick lithium target was calculated by assuming the thick target to consist of several thin targets each of thickness dx, with decreasing incident proton energies, ranging from the incident beam energy, E_p, down to the E_{th}. The generated spectrum was used to define the energy and angular distributions of neutrons for Monte Carlo simulation of the hand irradiation facility.

2.5.2. MCNP Source Card

The energy and angular distributions of neutrons produced via the ^{7}Li(p, n)^{7}Be were used to characterize the neutron source using the MCNP4B (Briesmeister, 1997) source cards. A realistic model of thick target ^{7}Li(p, n)^{7}Be interaction was provided to quantify the energy,

angular, and positional, distributions of neutrons entering the irradiation facility. The lithium target source was represented by point source geometry. The angular and energy distribution of the neutrons produced as a result of (p, n) interaction with thick lithium target depend upon the incident proton beam energy. The probability density functions (PDFs) for the resulting neutron energy spectrum as a function of cosine of angle, μ ($=\cos\theta$), corresponding to a particular proton beam energy were provided in the MCNP input file. The lab angle, θ, was defined relative to the proton beam axis.

Step 1: The PDF for initial direction cosines, $p(\mu)$, was calculated using the angular neutron yield. This PDF was used by MCNP to assign randomly the initial direction cosine, μ, to each source neutron. The azimuth angle, φ, was selected uniformly between 0° and 360° to produce a neutron beam symmetric along the beam axis. The differential angular neutron yield, $\frac{dY(\theta)}{d\Omega}$, was calculated by using the double differential neutron energy spectrum, $\frac{d^2Y(E_n,\theta)}{d\Omega dE_n}$, as

$$\frac{dY(\theta)}{d\Omega} = \int \frac{d^2Y(E_n,\theta)}{d\Omega dE_n} dE_n \tag{2}$$

The PDF, $p(\mu)$, for the initial direction cosines was calculated using the relationship

$$\frac{dY(\theta)}{d\mu} = \frac{dY(\theta)}{d\Omega}\left|\frac{d\Omega}{d\mu}\right| = 2\pi\frac{dY(\theta)}{d\Omega} \tag{3}$$

as

$$p(\mu) = \frac{\dfrac{dY(\theta)}{d\mu}}{\displaystyle\int_{\mu=0}^{\mu=1}\frac{dY}{d\mu}d\mu} = \frac{\dfrac{dY}{d\Omega}}{\displaystyle\int_{\theta=0}^{\theta=\pi/2}\frac{dY}{d\Omega}d\Omega}. \tag{4}$$

The denominator in (4) represents the total neutron yield at a given proton beam energy. The PDF $p(\mu)$ was defined as a 19 bin histogram in the forward direction only ($0 \le \mu \le 1$). The PDFs $p(\mu)$ for beam energies of 2.00 and 2.25 MeV are illustrated in **Figure 2**. This figure demonstrates that the neutron field is more forward directed for lower beam energies and broadens as the proton beam energy is increased.

Step 2: The PDF for the initial neutron energy, $p(E_n|\mu)$, corresponding to a pre-selected direction μ was calculated using the double differential neutron energy spectrum, $\frac{d^2Y(E_n,\theta)}{d\Omega dE_n}$, as

$$p(E_n|\mu) = \frac{\left|\frac{d^2Y}{d\mu dE_n}\right|}{\int\left|\frac{d^2Y}{d\mu dE_n}\right|dE_n} = \frac{\frac{d^2Y}{d\Omega dE_n}\left|\frac{d\Omega}{d\mu}\right|}{\int\frac{d^2Y}{d\Omega dE_n}\left|\frac{d\Omega}{d\mu}\right|dE_n} = \frac{\frac{d^2Y}{d\Omega dE_n}}{\int\frac{d^2Y}{d\Omega dE_n}dE_n} \quad (5)$$

For each bin in the histogram of μ, a corresponding histogram for neutron energy distribution calculated by using the PDF $p(E_n|\mu)$ was provided in the MCNP input file. Each energy distribution was represented by a 40 bin histogram. The PDFs $p(E_n|\mu)$ for beam energies of 2.00 and 2.25 MeV are illustrated in **Figure 3** and **4**. These figures demonstrate that with increase in beam energy, the spectrum hardens and the mean neutron energy increases in the given direction. At any particular beam energy, the maximum mean neutron energy is obtained on the beam axis and the minimum in the direction orthogonal to the beam. These spectra contain very small fractions of thermal and epithermal neutrons. The neutron activation (n, γ) cross-sections above these neutron energies are very low for the isotopes of interest (Al and Mn). This fraction of neutron energies decreases with increase in beam energy. The direct neutron beams are thus moderated to increase the fraction of thermal and epithermal neutrons.

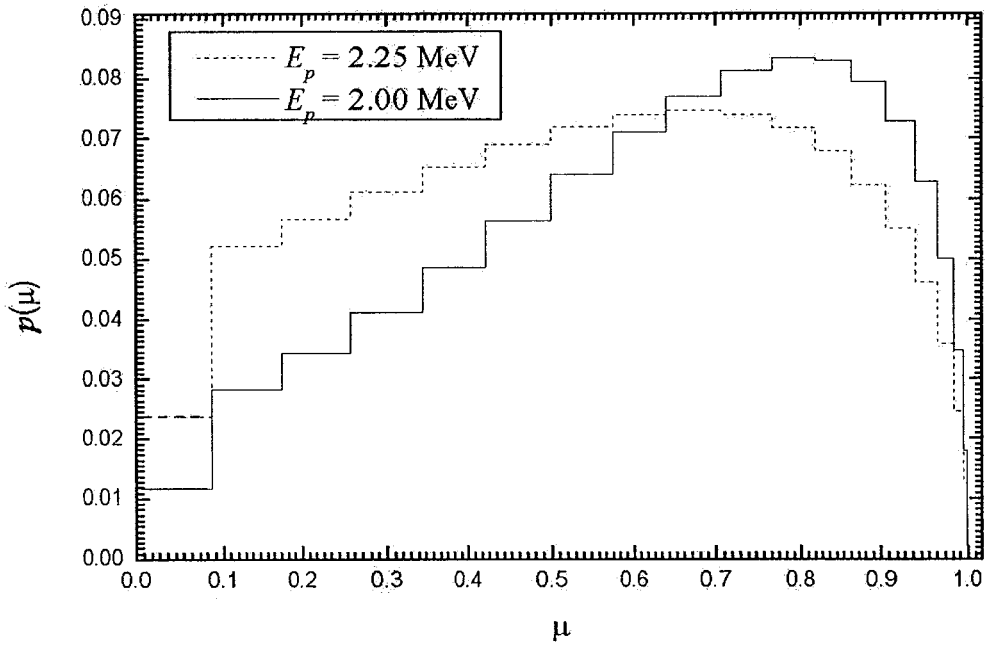

FIG. 2: PDFs for the angular distribution of the neutrons produced as a result of (p, n) interaction with thick lithium target for proton beam energies E_p = 2.00 and 2.25 MeV.

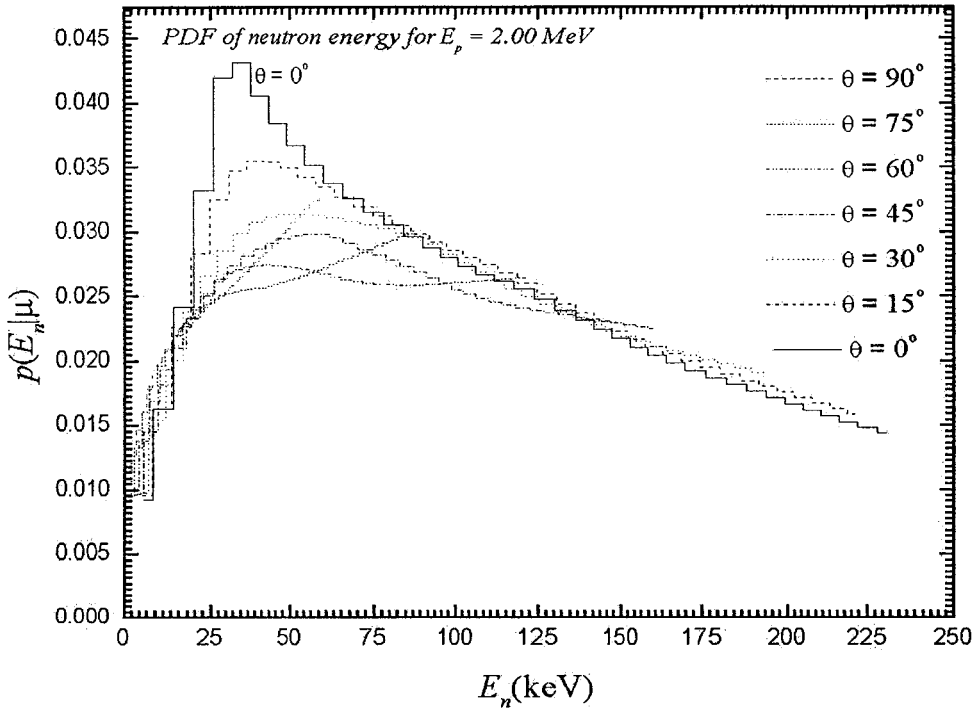

FIG. 3: PDFs for the direction-dependent energy distribution of the neutrons produced as a result of (p, n) interaction with thick lithium target for proton beam energy E_p = 2.00 MeV.

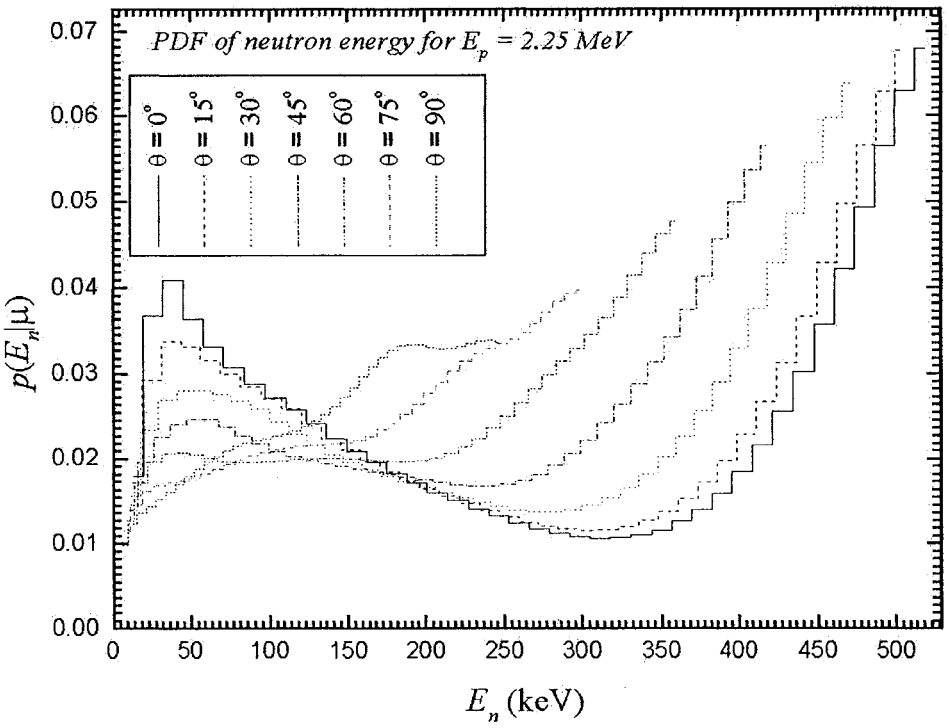

FIG. 4: PDFs for the direction-dependent energy distribution of the neutrons produced as a result of (p, n) interaction with thick lithium target for proton beam energy E_p = 2.25 MeV.

2.5.3. Average absorbed dose and dose equivalent Rates

As we discussed earlier, changing the proton energy from E_p = 2.00 MeV to 2.25 MeV also extends the neutron spectrum to higher neutron energies. The dose equivalent rate delivered to the patient's hand undergoing neutron irradiation at a given beam energy, E_p, due to the neutron fluence, $\Phi(E)$, incident on the phantom front face inside the hand irradiation facility was calculated by using

$$\dot{D}(E_p) = \int_0^{E_{n\max}} k(E_n)\Phi(E_n)dE_n \qquad (6)$$

where $k(E_n)$ is the fluence to kerma conversion coefficient for neutrons in soft tissue taken from ICRU (1986), and E_{nmax} is the maximum neutron energy corresponding to the proton energy E_p. The neutron fluence, $\Phi(E_n)$, incident on the phantom front face was calculated by using surface fluence tally F2 and point detector fluence tally F5 defined in MCNP. The tally F2 was used to calculate the average fluence while F5 was used to estimate the fluence at a point on phantom surface. These tallies also provide the integral over energy bins defined using the tally E2.

Similarly using the calculated neutron fluence rate spectrum, $\Phi(E_n)$, the neutron dose equivalent rate was calculated as follows

$$\dot{H}(E_p) = \int_0^{E_n \max} Q(E_n)k(E_n)\Phi(E_n)dE_n \tag{7}$$

The values of neutron quality factors, *Q(E)*, in an ICRU tissue sphere phantom at a depth of 10 mm based on most recent ICRP recommendations were taken from literature (ICRP, 1991).

2.5.4. Neutron Quality Factor

The neutron and gamma doses to the patient's irradiated hand are estimated using a tissue equivalent proportional counter (TEPC) simulating a 2 μm tissue equivalent (TE) diameter filled with propane based TE gas (Pejović-Milić *et al.*, 2000; Arnold, 2000; Pejović-Milić, 2001; Arnold *et al.*, 2002). The lineal energy dose distributions measured by the TEPC are not only used to estimate the neutron and gamma doses but are also used to estimate the neutron quality factors. However, the TEPC underestimates the neutron quality factors by a factor of 2-3 for the neutron energies employed for IVNAA of the hand at MAL (Arnold *et al.*, 2002; Aslam *et al.*, 2001, 2003b). Therefore, instead of using the quality factor measured by employing a TEPC, a maximum neutron quality factor of 20 was arbitrarily assigned to estimate the dose equivalent to the irradiated hand. Thus a computational or experimental method is needed to estimate the neutron quality factors to augment the measured doses for the calculation of dose equivalent. This section describes a computational procedure to calculate the neutron quality factors in the hand irradiation facility.

Dose averaged quality factors (Stinchcomb and Borak, 1983) at a given beam energy, E_p, producing a neutron fluence, $\Phi(E_n)$, incident on phantom front face inside the hand irradiation facility was calculated as follows

$$\overline{Q} = \frac{\dot{H}(E_p)}{\dot{D}(E_p)} = \frac{\int_0^{E_n} Q(E_n)D(E_n)dE_n}{\int_0^{E_n} D(E_n)dE_n} = \frac{\int Q(E_n)k(E_n)\Phi(E_n)dE_n}{\int k(E_n)\Phi(E_n)dE_n} \tag{8}$$

Here the numerator represents the dose equivalent calculated in (7) and the denominator represents the absorbed dose calculated in (6). The fluence spectrum calculated either by using the neutron tallies F2 and F5 were modified using the dose function DF2 and DF5

defined in MCNP4B. The function DF2 and DF5 in case of numerator in (8) was defined as fluence-to-dose equivalent conversion factors while in case of denominator it was defined as fluence-to-dose conversion factors as a function of energy. This modified tally also provides the integral over energy bins defined using the tallies E2 and E5. An appropriate number of energy bins was used in MCNP to get the integrals used in the denominator and the numerator of (8). The quality factors were averaged only over the neutron dose. No account was taken of the contribution to quality factor from any external or internal γ radiations which were present (Stinchcomb and Borak, 1983).

3. RESULTS AND DISCUSSION

3.1. Simulation of Hand Irradiation Facility for IVNAA

This section describes the calculation of fluence, dose and dose averaged quality factors in the center (0, 0, 0) and at horizontal distances of ±7 cm ((±7, 0, 0)) in the irradiation facility for E_p = 2.00 and 2.25 MeV to compare and augment the calculations with the measurements carried out earlier (Arnold *et al.*, 2002, Aslam *et al.*, 2003d).

3.1.1. MCNP Model

To validate the modeling and the Monte Carlo coding of the designed hand irradiation facility, some simple calculations were carried out to make sure the model gives agreeable results under similar exposure conditions. For this purpose, a simple point neutron source with the anisotropic properties as discussed in the earlier section was modeled. The angular neutron fluence was calculated at θ_{lab} = 0°, 30°, 60°, and 90° relative to proton beam direction at an arbitrarily chosen distance of 50 cm from the target. The calculated neutron fluence spectra were used to evaluate the mean neutron energies in those directions. The mesh sizes for energy and angular distribution of produced neutrons at the target site were chosen to produce the same results as those of analytical calculations matching within 2-3%. Although finer mesh sizes in terms of energy and angular distribution may produce better agreement, the trade off was the selection of better agreement and longer execution time of the model. Experimental validation of MCNP model of the hand irradiation facility has previously done by others (Arnold, 2000).

3.1.2. Fluence Spectrum Calculation

The normalized fluence spectra (per source neutron simulated) calculated at the locations and beam energies in the hand irradiation facility where measurements were carried out are

shown in **Figures 5** and **6**. The number of histories was chosen to calculate the fluence in a reasonable time with sufficient counting precision (2-3%). The neutron fluence spectra at (-7, 0, 0) and (7, 0, 0) are slightly different at low neutron energies (E_n < 10 eV) because of the presence of reflector towards (-7, 0, 0). The normalized neutron fluence at E_p = 2.00 MeV is higher at all corresponding positions inside the hand irradiation facility than that of 2.25 MeV beam energy. The neutron fluence spectra at (-7, 0, 0) and (7, 0, 0) are same as expected because of the angular symmetry of the neutrons produced via ^{7}Li(p, n)^{7}Be about the azimuthal angle. However slight differences at low neutron energies (E_n < 10 eV) resulted because of the presence of reflector towards (-7, 0, 0).

At all measurement sites where calculations have been carried out, there is peak in the thermal energy region (<0.5 eV), however, it is evident from **Figures 5** and **6** that the fast neutron component forms a large fraction of the total neutron fluence. The neutron activation (n, γ) cross-sections at the neutron energies above thermal energy are very low for the isotopes of interest (Al and Mn). The thermal neutron fluence is expected to decrease with the depth in the hand because of the capture reactions in the hand. This attenuation of thermal neutron fluence may be compensated by the moderation of the epithermal neutrons. **Figures 5** and **6** illustrate that the useful neutron fluence, Φ_{TE} (E_n < 10 keV), which is available for activation of the element of interest is maximum in the center and decreases in the radial direction on the phantom surface. This introduces a non-uniform activation of the element of interest both in the radial and axial directions. The uniformity of activation defined as the ratio of Φ_{TE} in the beam direction (0, 0, 0) to that of extreme edges (±7, 0, 0) was improved for E_p = 2.25 MeV compared to E_p = 2.00 MeV. However, the contamination of the neutron beam with non-useful fast group inferred from the ratio of useful fluence, Φ_{TE}, to the total fluence, Φ_t, is higher than that of E_p = 2.00 MeV delivering a higher neutron dose to the phantom.

The neutron fluence averaged over the phantom surface at the beam energies 2.00 and 2.25 MeV is illustrated in **Figure 7(a)** and **(b)**. The neutron beam at E_p = 2.00 MeV is predominately epithermal with an average energy of 8.58 keV compared to E_p = 2.25 MeV where the fluence is predominately fast (>10 keV) with an average energy of 44.69 keV and a fast neutron contamination of more than 25% at this energy. The fast neutron contamination is approximately 14% at E_p = 2.00 MeV which is lower than at E_p = 2.25 MeV. Despite the high contamination of the beam, the absolute Φ_{TE} (n-cm^{-2}/μC) calculated by multiplying the

normalized neutron fluence spectra (n-cm^{-2}/neutron) with the total neutron yields (n/μC) at E_p = 2.25 MeV, is 3.74 times higher than that of E_p = 2.00 MeV.

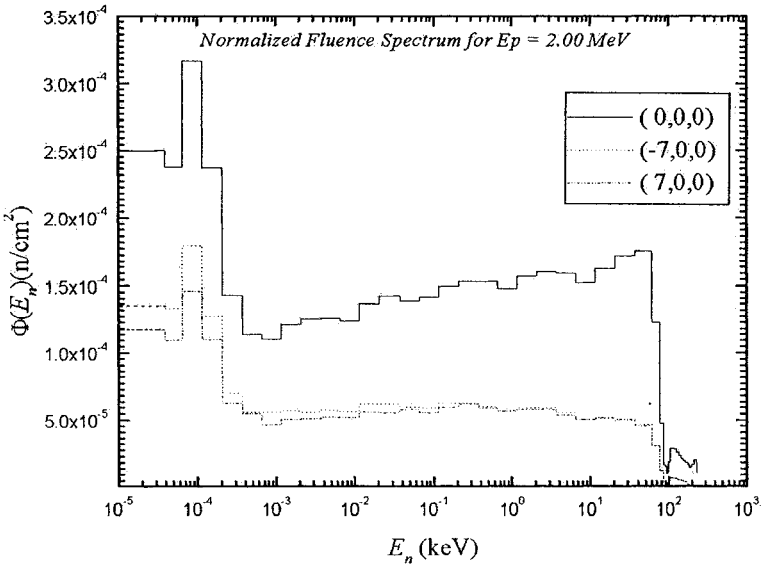

FIG. 5: Calculated normalized neutron fluence spectra per source neutron incident on the hand phantom in the hand irradiation facility at E_p = 2.00 MeV. The neutron fluence spectra at (-7, 0, 0) and (7, 0, 0) are the same as was expected because of the angular symmetry of the neutrons produced via ^{7}Li(p, n)^{7}Be about the azimuthal angle. However slight differences at low neutron energies (E_n < 10 eV) resulted because of the presence of reflector towards (-7, 0, 0). The useful neutron fluence, Φ_{TE} (E_n < 10 keV), which is available for activation of the element of interest is maximum in the center and decreases in the radial direction on the phantom surface. This introduces a non-uniform activation of the element of interest both in the radial and axial directions. Further, the ratio of useful fluence, Φ_{TE}, to the total fluence, Φ_t, indicating the contamination of the neutron beam with non-useful fast group can also be inferred from the calculated fluences. This ratio is minimum (0.8) in the center and maximum (0.9) at edges of the phantom.

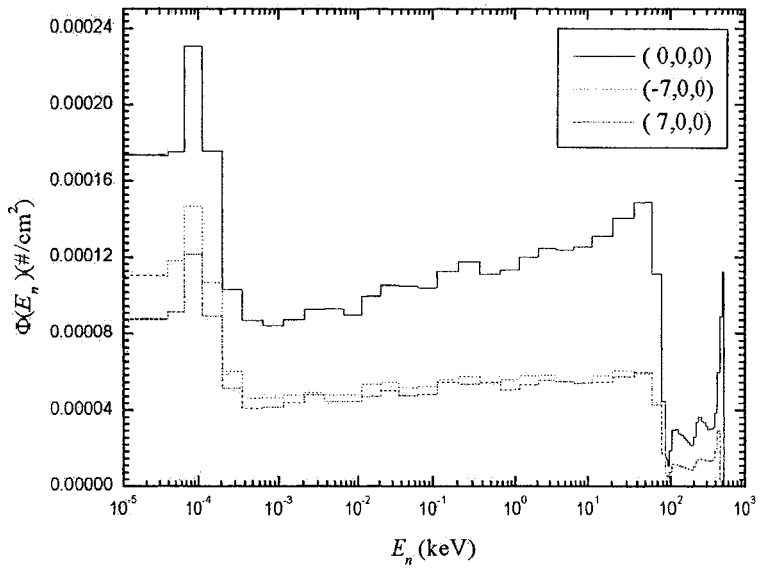

FIG. 6: Calculated normalized neutron fluence spectra per source neutron incident on the hand phantom in the hand irradiation facility at E_p = 2.25 MeV. Again, the neutron fluence spectra at (-7, 0, 0) and (7, 0, 0) are slightly different at low neutron energies (E_n < 10 eV) resulted because of the presence of reflector towards (-7, 0, 0). A similar decreasing trend of Φ_{TE} was observed in the radial direction on the phantom surface as in case of E_p = 2.00 MeV. However, the uniformity of activation defined as the ratio of Φ_{TE} in the beam direction (0, 0, 0) to that of extreme edges was improved compared to E_p = 2.00 MeV. The contamination of beam with non-useful fast group is higher than that of E_p = 2.00 MeV delivering higher neutron dose to the phantom. The contamination is maximum (1 - 0.7 = 0.3) in the beam direction and minimum (1 - 0.8 = 0.2) at edges of the phantom. Despite of high contamination of beam, the absolute Φ_{TE} (n-cm^{-2}/μC) calculated by multiplying the normalized neutron fluence spectra (n-cm^{-2}/neutron) with the total neutron yields (n/μC) is higher at all positions at E_p = 2.25 MeV than those at E_p = 2.00 MeV.

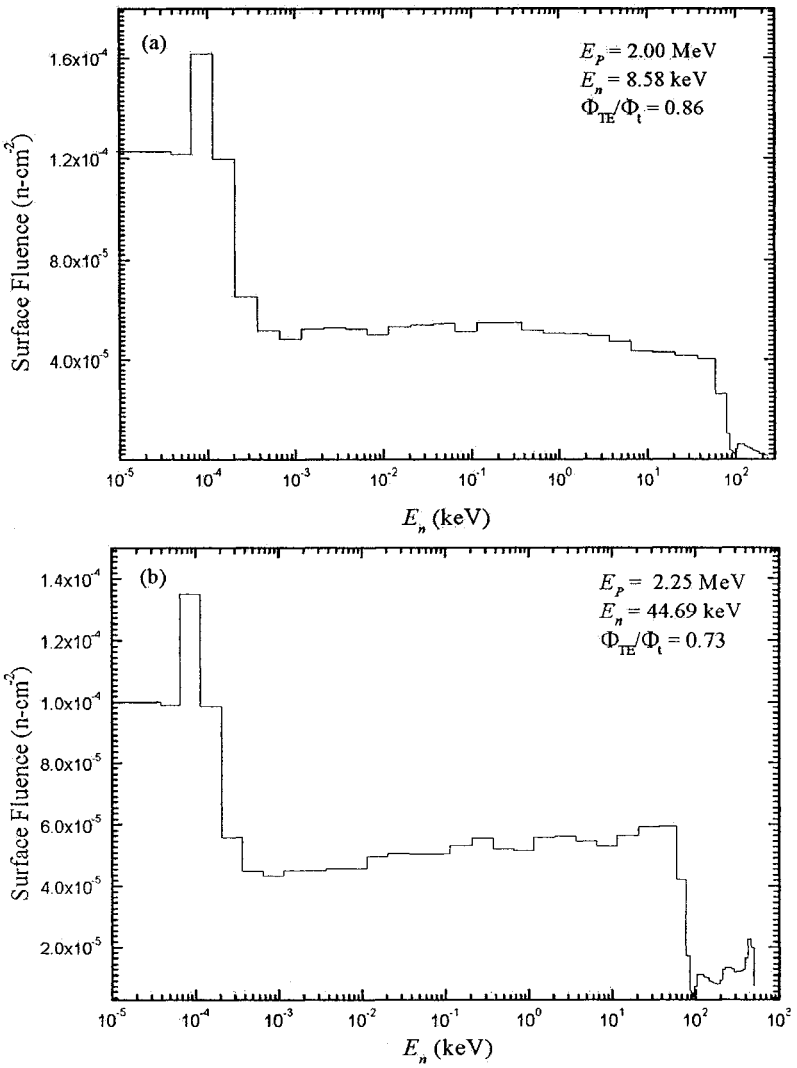

FIG. 7: Calculated normalized surface neutron fluence spectra per source neutron incident on the hand phantom in the hand irradiation facility at (a) E_p = 2.00 MeV, (b) E_p = 2.25 MeV.

3.1.3. Dose Calculations

The kerma coefficient in tissue equivalent materials illustrated in **Figure 8** (ICRU, 1986) increases with increase in neutron energy (E_n > 30 eV). **Figures 9** and **10** show the convolution of fluence spectra shown in **Figures 5** and **6** with the kerma coefficients shown in **Figures 8**. The dose distribution on the phantom surface is heterogeneous as illustrated in **Figures 9** and **10**. Maximum dose was delivered in the center and minimum was delivered on the edges of the phantom. The dose heterogeneity defined as D_{max}/D_{min} was 4.6 for

E_p = 2.00 MeV and 3.1 for E_p = 2.25 MeV. These dose heterogeneity factors can be compared with the dose measurement carried out earlier in the hand irradiation facility at MAL at E_p = 2.00 and 2.25 MeV (Arnold, 2000; Arnold *et al.*, 2002; Aslam *et al.*, 2003d). The neutron and gamma dose measurements were carried out by Arnold (2000) using a 1.27 cm (½″) diameter TEPC filled with a TE gas simulating a 2 μm TE diameter. The measured and calculated dose heterogeneity values provide a fairly good agreement (6% and 9% at E_p = 2.00 and 2.25 MeV respectively) within the experimental uncertainty and a validation to the Monte Carlo modeling of hand irradiation facility developed at MAL. To account for the heterogeneous dose distribution, doses measured by small volume dosimeters like ionization chambers, bubble detectors, or TEPCs, a method must be employed to estimate average dose to the hand.

The kerma weighted neutron fluences averaged over the phantom surface at the beam energies 2.00 and 2.25 MeV are illustrated in **Figure 11(a)** and **(b)**. For E_p = 2.00 MeV, 84% of the total neutron dose was delivered by the non-useful fast neutron group (14% of total fluence) which became even more severe at E_p = 2.00 MeV where these fast neutrons (27% of the total fluence) delivered 96% of the total dose to the hand phantom. The non-useful fast neutron group produces a high increase of dose to the patient's hands. This emphasizes an addition of a fast neutron filter to remove the fast neutrons from the beam.

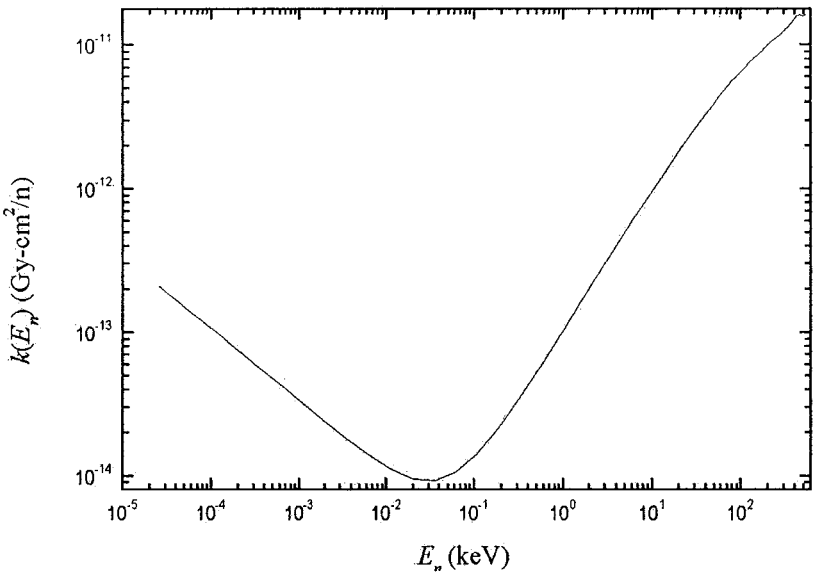

FIG. 8: Kerma coefficient in TE muscle tissue as a function of neutron energy (ICRU, 1986).

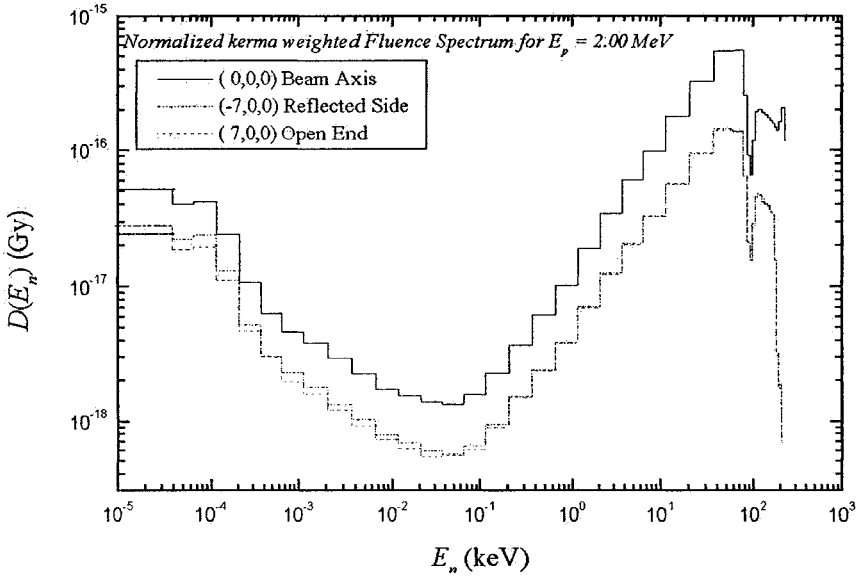

FIG. 9: Calculated normalized kerma weighted neutron fluence spectra per source neutron incident on the hand phantom in the hand irradiation facility at E_p = 2.00 MeV. The dose distribution on the phantom surface is heterogeneous. Maximum dose was delivered in the beam axis and decreased radially. The dose heterogeneity defined as D_{max}/D_{min} is 4.6 for E_p = 2.00 MeV on the phantom surface. This calculated dose heterogeneity is fairly agreement (6%) with the one estimated from measured dose rates at E_p = 2.00 MeV in the hand irradiation facility (Arnold, 2000, Arnold *et al.*, 2002; Aslam *et al.*, 2003d) as 4.9. Thus it is essential to estimate the average radiation dose received to the patient's hand to account for the heterogeneous dose distribution.

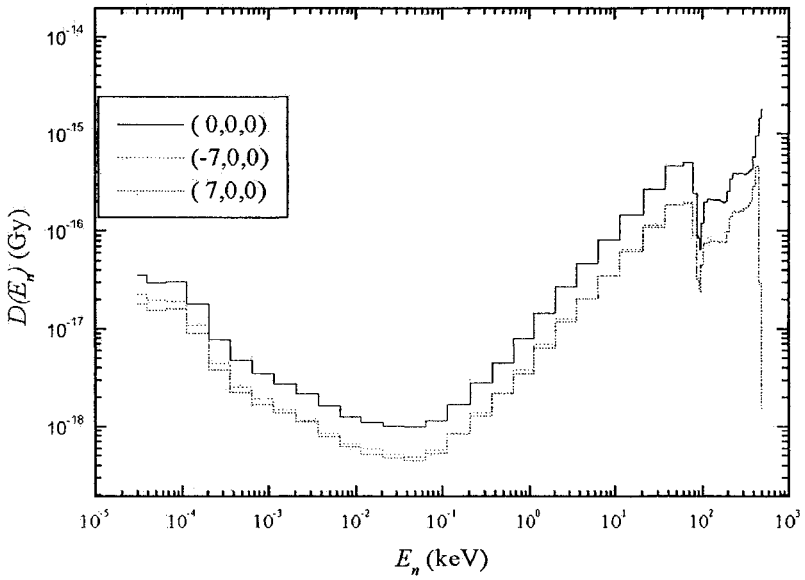

FIG. 10: Calculated normalized kerma weighted neutron fluence spectra per source neutron incident on the hand phantom in the hand irradiation facility at E_p = 2.25 MeV. Again, maximum dose was delivered in the beam axis and decreased radially. The dose heterogeneity observed at E_p = 2.25 MeV was improved compared to E_p = 2.00 MeV. The dose heterogeneity is 3.1 for E_p = 2.25 MeV. The dose heterogeneity estimated from the measured dose rates at E_p = 2.25 MeV in the hand irradiation facility (Arnold, 2000, Arnold *et al.*, 2002; Aslam *et al.*, 2003d) is 3.0. The measured and calculated dose heterogeneity values provide a fairly good agreement (6%) within the experimental uncertainty. Thus to account for the heterogeneous dose distribution, doses measured by small volume dosimeters like ionization chambers, bubble detectors, or TEPCs, a method must be employed to estimate average dose to the hand, otherwise a large volume dosimeter must be employed which can average the dose over the volume.

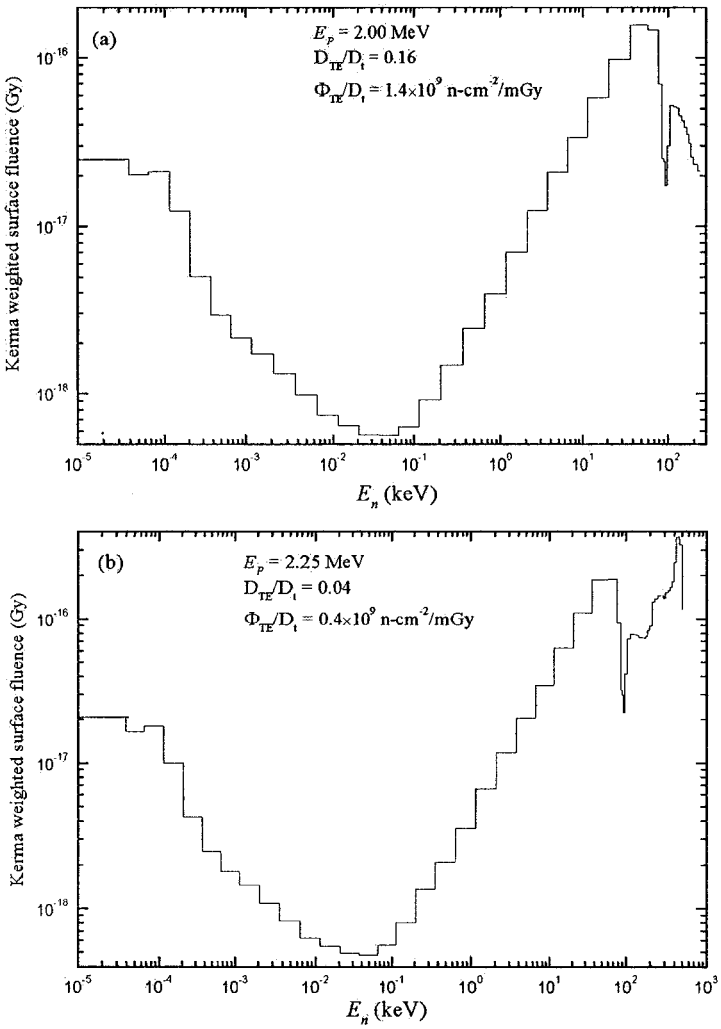

FIG. 11: Calculated normalized kerma weighted surface neutron fluence spectra per source neutron incident on the hand phantom in the hand irradiation facility at (a) E_p = 2.00 MeV, (b) E_p = 2.25 MeV. The neutron beam used at E_p = 2.00 MeV for IVNAA of hand at MAL is 3.5 times more efficient at delivering useful fluence per unit dose delivered than the beam produced at E_p = 2.25 MeV. By taking into account the neutron quality factors, the neutron beam produced at E_p = 2.00 MeV is 4.9 times more efficient for delivering useful fluence per unit dose equivalent delivered than the beam produced at E_p = 2.25 MeV. More than 84% of the dose is delivered by the non-useful fast neutron group at E_p = 2.00 MeV, filtration of this group would help to improve the MDL of the elements of interest.

3.1.4. Quality Factor Calculations

The neutron quality factors calculated using a procedure as discussed in the section 2.5.4 are presented in **Tables 1** and **2**. The quality factors vary as a function of position as expected. These factors are lower at E_p = 2.00 MeV compared to E_p = 2.25 MeV. Employing these calculated quality factors instead of the maximum quality factor of 20 for E_p = 2.00 MeV, and the measured neutron and gamma dose rates in the center (Arnold *et al.*, 2002, Aslam *et al.*, 2003d), the dose equivalent rate is estimated as 15.22 mSv/μA h which is 1.3 times lower than that reported (Arnold *et al.*, 2002). The MDL varies as the square root of the dose equivalent (Lewis *et al.*, 1997; Arnold *et al.*, 2002), this would result in a lower MDL of (1.5±0.3) μg Mn/g of bone compared to that estimated MDL of (1.8±0.4) μg Mn/g of bone with the assumption of Q = 20. Dose heterogeneity corrections which if applied would further improve the MDL, are considered in the next section.

Table 1: Quality factor as a function of position on the phantom surface at E_p = 2.00 MeV. The quality factor Q represents the quality factor averaged over the total dose (D_t = D_{TE} + D_F). The quality factor does not vary as rapidly with position as neutron dose. The quality factor used for the estimation of dose equivalent to hand (Arnold *et al.*, 2002) was 20. Dose measured in the center of the hand irradiation facility was used to make such estimation. The quality factor calculated in the center is 1.5 times lower than the maximum quality factor used. Using the measured neutron and gamma dose rates in the center of facility (Arnold *et al.*, 2002; Aslam *et al.*, 2003d) and the quality factor calculated in this work, the dose equivalent rate is estimated as 15.22 mSv/μA h which is 1.3 times lower than that reported (Arnold *et al.*, 2002). The MDL varies as the square root of the dose (Lewis *et al.*, 1997; Arnold *et al.*, 2002), this would result in a lower MDL of (1.5±0.3) μg Mn/g of bone compared to that estimated MDL of (1.8±0.4) μg Mn/g of bone with the assumption of Q = 20. These calculations assume homogenous dose distribution over the phantom surface in contrary to the measurements (Arnold *et al.*, 2002) and the calculations carried out in this work.

Position (cm)	D_{TE} (mGy/n)×10^{-13}	D_F (mGy/n)×10^{-13}	H_{TE} (mSv/n)×10^{-13}	H_F (mSv/n)×10^{-13}	Q_{TE}	Q_F	Q
(-7,0,0)	1.78	6.61	8.92	86.0	5.0	13.0	11.3
(0,0,0)	4.43	34.98	22.13	494.0	5.0	14.5	13.4
(7,0,0)	1.63	6.63	8.13	86.8	5.0	13.1	11.5

Table 2: Quality factor as a function of position on the phantom surface at E_p = 2.25 MeV. The quality factor Q represents the quality factor averaged over the total dose (D_t = D_{TE} + D_F). Quality factors calculated for E_p = 2.25 MeV are higher than those calculated for E_p = 2.00 MeV (Table 1). The quality factor used for the estimation of dose equivalent to hand (Arnold *et al.*, 2002) was 20 which is in agreement (1.1 times higher than calculated) with that calculated in this work. Although higher useful fluence per unit beam current is available for activation of the element of interest at E_p = 2.25 MeV, the useful fluence per unit dose equivalent is lower compared to E_p = 2.00 MeV. Therefore IVNAA measurements of Mn are carried out at E_p = 2.00 MeV using higher beam current to produce the same useful fluence per unit incident proton charge on target as at E_p = 2.25 MeV.

Position	D_{TE}	D_F	H_{TE}	H_F	Q_{TE}	Q_F	Q
(cm)	(mGy/n)×10^{-13}		(mSv/n)×10^{-13}				
(-7,0,0)	1.85	38.5	9.37	683.	5.1	17.7	17.2
(0,0,0)	3.56	123.2	18.0	2270.	5.0	18.4	18.0
(7,0,0)	1.66	38.2	8.15	689.	4.9	18.0	17.5

3.2. Average Neutron Dose Equivalent

Isodose distribution curves in the hand irradiation facility at E_p = 2.00 and 2.25 MeV in the plane perpendicular to the proton beam direction (along the phantom surface) are illustrated in **Figure 12**. The dose heterogeneity as determined earlier is larger at E_p = 2.00 MeV compared to 2.25 MeV. The neutron fields inside the irradiation facility in the plane perpendicular to the beam axis are symmetric along the beam axis. Taking the center of the phantom as the origin of coordinate system represented in cylindrical polar coordinate system because of the symmetry of the neutron field (independent of polar angle, θ_c), the neutron dose rate, $D(r)$, normalized to maximum dose rate (D_{max} in the center) on the hand phantom surface can be used to calculate the average neutron dose rate of the neutron beam incident on the phantom surface as

$$\overline{D} = \frac{\int_0^R D(r) 2\pi r dr}{\int_0^R 2\pi r dr} D_{max} \qquad (9)$$

where R is the equivalent radius of the rectangular hand phantom determined from the area, A, of the hand phantom as $A = \pi R^2$. To evaluate the integrals in (9), calculated $D(r)$ values illustrated in **Figure 12** were represented by linear fits with $R^2 \geq 0.97$. Higher order interpolating polynomials provided better fits with $R^2 = 0.99$, insignificant change less than 2-3% was observed. Thus this linear fit resulted in

$$\overline{D} = \frac{\int_0^R D(r)2\pi r dr}{\int_0^R 2\pi r dr} D_{max} = \frac{\int_0^R (a+br) r dr}{\int_0^R r dr} D_{max} = \frac{\frac{a}{2}R^2 + \frac{b}{3}R^3}{\frac{1}{2}R^2} D_{max} = (a + \frac{2}{3}bR) D_{max} \quad (10)$$

The parameters a and b were obtained using the Microsoft Excel® as a = 1.02 and b = -0.10 cm^{-1} for E_p = 2.00 MeV and a = 1.03 and b = -0.09 cm^{-1} for E_p = 2.00 MeV. The averaging factor for different equivalent radii is presented in **Table 3**. The averaging factor as expected decreases as the phantom (phantom center coinciding with the proton beam direction) equivalent radius increases.

Table 3: Dose averaging factor for different equivalent radii of the phantom. Averaging factor is lower for E_p = 2.00 MeV compared to E_p = 2.25 MeV for same equivalent radius. Measured neutron dose rates in the center of the hand irradiation facility would be multiplied with the averaging factor corresponding to the equivalent radius. The MDL measurements of Mn were carried out using a phantom of equivalent radius of 10 cm at a beam energy of E_p = 2.00 MeV (Arnold *et al*, 2002).

R	$a + \frac{2}{3}bR$	
(cm)	E_p = 2.00 MeV	E_p = 2.25 MeV
1	0.95	0.97
2	0.88	0.90
3	0.81	0.83
4	0.74	0.78
6	0.60	0.65
8	0.47	0.52
10	0.34	0.40

Similarly the average quality factor of the neutron beam incident on the phantom surface as

$$\overline{Q} = \frac{\int_0^R \overline{Q}(r) D(r) 2\pi r dr}{\int_0^R D(r) 2\pi r dr} \quad (11)$$

To evaluate the integrals in (11), calculated $Q(r)$ was represented by linear fits with $R^2 \geq 0.96$. The parameters a and b were obtained using the Microsoft Excel® as a = 14.0 and b = -0.32 cm^{-1} for E_p = 2.00 MeV and a = 18.16 and b = -0.11 cm^{-1} for E_p = 2.00 MeV.

Table 4: Average quality factor for different equivalent radii of the phantom. The statistical precision the calculated values is approximately 5%. The variation in quality factor at E_p = 2.00 MeV as a function of equivalent radius is less than 10%. The average quality factor is almost constant within 3% (less than the statistical precision of calculated values) for all equivalent radii at E_p = 2.25 MeV.

R	$\overline{Q}$	
(cm)	E_p = 2.00 MeV	E_p = 2.25 MeV
1	13.7	18.1
2	13.6	18.0
3	13.4	17.9
4	13.2	17.8
6	12.8	17.7
8	12.5	17.6
10	12.4	17.5

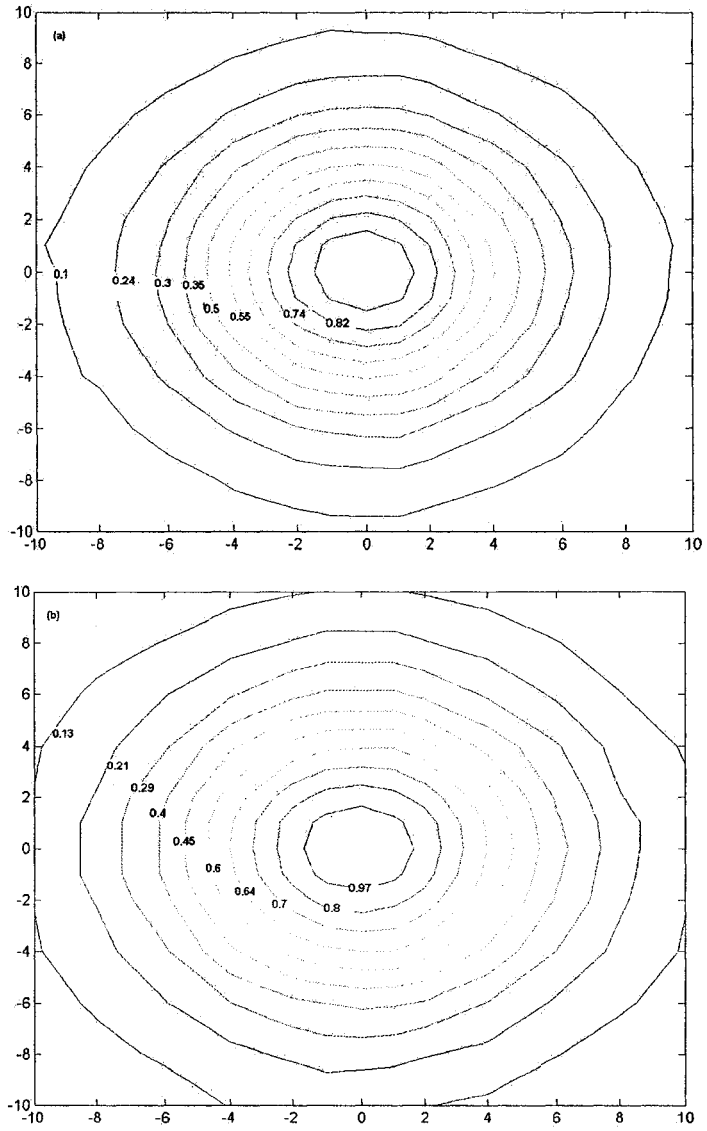

FIG. 12: Isodose distribution curves normalized to maximum dose (in the center) in the hand irradiation facility at (a) E_p = 2.00 MeV, (b) E_p = 2.00 MeV in the plane perpendicular to the proton beam direction (along the phantom surface). The neutron field inside the irradiation facility in the plane perpendicular to the beam axis is symmetric along the beam axis. The dose decreases rapidly in the radial direction. This decreasing trend in dose is much sharper for E_p = 2.00 MeV than E_p = 2.00 MeV. The symmetry of the radiation fields suggest the average neutron dose measured by small volume dosimeters in a plane can be estimated as $D=\int_0^R D(r)2\pi r dr \Big/ \int_0^R 2\pi r dr$, where R is the equivalent radius of the rectangular hand phantom determined from the area, A, of the hand phantom as $A = \pi R^2$.

3.3. MDLs of Manganese at MAL Using IVNAA

The MDL for an IVNAA measurement of Mn in the hand with proton beam energy of 2.00 MeV, beam current of 42 μA, irradiation time of 10 min was reported to be (1.0±0.2) μg/g of bone, which corresponds to the normal concentration of Mn in bone. The MDL measurements of Mn were carried out using a phantom of equivalent radius of 10 cm at a beam energy of E_p = 2.00 MeV (Arnold *et al*, 2002). The neutron and gamma dose rates in the center of the irradiation facility were reported as 1.02 and 1.56 mGy/μA h respectively. Employing the dose averaging factors (listed in **Table 3**) and the average quality factors (listed in **Table 4**), these dose rates can be used to calculate the average dose equivalent delivered to hand phantom by using

$$\overline{H_t} = \overline{D} \times \overline{Q} + D_\gamma = (a + \tfrac{2}{3} bR) D_{\max} \times \overline{Q} + D_\gamma \qquad (12)$$

as 5.9 mSv/μA h. The total dose received to the patient hand as a result of this proposed diagnostic procedure can be calculated by multiplying the average dose rate at E_p = 2.00 MeV by the beam current (42 μA) and the irradiation time (10 min = 0.17 h) as 41 mSv, this is smaller than the maximum allowable local dose (50 mSv) to the patient's irradiated hand restricted by the McMaster University Human Ethics Board for an *in-vivo* measurement of toxic trace elements. The gamma dose heterogeneity was not taken into account and the maximum gamma dose rates (observed along beam axis) were used to calculate the total radiation dose equivalent. Thus the proposed irradiation procedure for the IVNAA measurement of manganese in human hands with normal (1 ppm) and elevated manganese content can be carried out without violating the prescribed dose limits for such diagnostic procedures. This finding is of significant importance because such low energies and beam currents can be achieved even by small accelerators and the normal manganese concentrations are still measurable.

These dose rates estimated in this work can be used to calculate the radiation dose received to patient's hand for IVNAA measurement of aluminum in human hand bones.

3.4. Gamma Shielding

At E_p = 2.00 MeV beam energy, the gamma dose constitutes more than 25% of the total dose equivalent. The gamma dose is contributed by 478 keV inelastic gamma rays produced via the ^{7}Li($p, p'\gamma$)^{7}Li interactions taking place in the target, residual activity of ^{7}Be in the target produced as a result of ^{7}Li(p, n)^{7}Be which also produces 478 keV gamma rays and the capture

gamma rays in hydrogen producing 2.2 MeV gamma rays in the moderator-reflector assembly. The yield of proton capture reaction occurring in the target is almost negligible (< 1%) compared to $^{7}Li(p, p'\gamma)^{7}Li$ at low proton beam energies (Lee *et al.*, 2000). A gamma shield placed between the moderator and the patient hand will not only reduce the gamma flux arising from the target but also those coming from the moderator assembly. It was estimated through Monte Carlo simulations that the more than 90% of the gamma dose was deposited by 478 keV gamma rays from the target.

This irradiation facility has the inner dimensions of 30×30×4.5 cm^3 and placing a lead shield of 30×30×0.5 cm^3 inside the facility after the moderator would reduce the inner dimensions to 30×30×4.0 cm^3 which is still more than the phantom thickness (2.4 cm).

The effect of putting the lead shield inside the facility was studied by calculating the ratio of thermal and epithermal fluence to the total neutron dose equivalent (Φ_{TE}/H_t) with and without the proposed gamma shield using MCNP. The ratio Φ_{TE}/H_t was calculated as 1.10×10^{8} ± 1.0% n-cm^{-2}/mSv and 1.15×10^{8} ± 0.6% n-cm^{-2}/mSv with and without gamma shield. As a result of gamma shield both the Φ_{TE} and H_t were reduced by 5% and 10% respectively. Consequently this results in an increase of Φ_{TE}/H_t by approximately 5%. However, the insertion of gamma shield inside the facility is expected to decrease the gamma dose from approximately 25% to 5% of the total dose equivalent. The 5% loss in thermal neutron fluence can be compensated either by increasing the beam current or the irradiation time by 5%. By taking into account the 10% neutron dose reduction, 80% gamma dose reduction, 5% increase in beam current due to decrease in thermal fluence and the averaging factors mentioned in Tables 3 and 4, the total dose equivalent delivered to the patient as a result of irradiation will be reduced to 30.7 mSv. Fast neutron component of the beam delivers most of this dose equivalent.

3.5. Uniformity of Sensitivity

The system sensitivity at any location in the phantom is defined as the product of the thermal neutron fluence and the efficiency of the detector employed for activity measurements (Dilmanian *et al.*, 1998). MCNP was used to map the thermal neutron fluence in the horizontal (along the phantom surface) and vertical planes (along the phantom width). The space dependent absolute detector efficiency, which accounts for the detector solid angle as a function of the position at which (n, γ) reaction occurs, was also determined using

MCNP. The photon attenuation in the phantom material was neglected because of their larger mean free paths in TE materials.

Figure 13 depicts the distribution of thermal neutron fluence on the phantom surface at E_p = 2.00 MeV beam energy. The distribution was generated with the assumption of unilateral irradiation of the phantom. The precision of the calculated thermal fluences is approximately 5%. This figure demonstrates that the thermal neutron field will be non-uniform on the phantom surface and the central region of the phantom will be activated more relative to outer edges of the phantom. Quantitatively, the variation of the differential thermal neutron activation sensitivity is approximately 30-40% on the phantom surface. This non-uniformity of thermal fluence is caused by the incident neutron energy spectrum. The sensitivity improves as the distance between the neutron producing target and the moderator-reflector assembly is increased, however, it will reduce the thermal neutron fluence rate (Arnold, 2000) which will require higher beam current to produce the same fluence as at closer distances for the same irradiation time.

The composite sensitivity, which is the product of the thermal neutron activation sensitivity (illustrated in Figure 13) and the γ-detection sensitivity, is shown in **Figure 14**. The space dependent absolute efficiency of a single large cylindrical NaI(Tl) detector of radius of 10 cm and thickness of 5 cm placed at 1 cm away from the phantom as a function of the phantom surface position at which (n, γ) reaction occurs emitting 847 keV γ-rays (γ-ray energy emitted following the beta decay of activated ^{56}Mn) was calculated at different locations using MCNP. **Figure 14** demonstrates that the non-uniformity of the differential composite sensitivity of the system was caused predominately by the differential thermal neutron activation sensitivity. A single large detector will sample the central region of the phantom more efficiently than those at the edges of the phantom. The variation of the differential composite sensitivity is approximately 70-80% on the phantom surface.

This problem of non-uniform sensitivity of the system can be improved by using a set of small detectors instead of single large detector for γ-detection, for example using a detector to sample the points at phantom edges more efficiently than the detector used at the center of the phantom to compensate for lower activation at the edges. The uniformity of composite sensitivity can be carried by placing the detectors tilted towards the edges of phantom (by optimally selecting the polar angle, θ_c, and the azimuthal angle, φ). MCNP can be used to assess the optimal arrangement of γ-detectors (delayed counting mode) around the irradiated

phantom for a given radiation dose equivalent without compromising on the integral sensitivity of the system.

Figure 15 depicts the distribution of composite sensitivity in a cross-section of the hand phantom at E_p = 2.00 MeV beam energy. Again the distribution was generated with the assumption of unilateral irradiation of the phantom and a single large NaI detector placed in front of irradiated surface of phantom. This distribution is consistent with attenuation of the thermal neutron fluence as it penetrates the phantom. However, the variation of the differential composite sensitivity along the width (vertical direction) of phantom is smaller than on the phantom surface (horizontal direction). The general decrease of the thermal neutron flux with increasing penetration in the hand phantom can largely be compensated by irradiating the hand bilaterally. Moreover, to increase the integral sensitivity of the system instead of using a single large detector, two detectors are used on opposite sides. In first half of the hand width (1.2 cm), the variation in differential composite sensitivity is less than 10% and then decreases rapidly with increasing thickness. Thus bilateral irradiation will result in minimum variations of composite sensitivity (~10%) along the phantom width because of the improved uniformity of the thermal fluence due to opposing irradiations and also because of an initial build-up of thermal flux in first few mm (~0.6 cm) of hand phantom surface. For bilateral irradiation, the positioning of the γ-detectors will be determined by the thermal neutron activation sensitivity on the phantom surface.

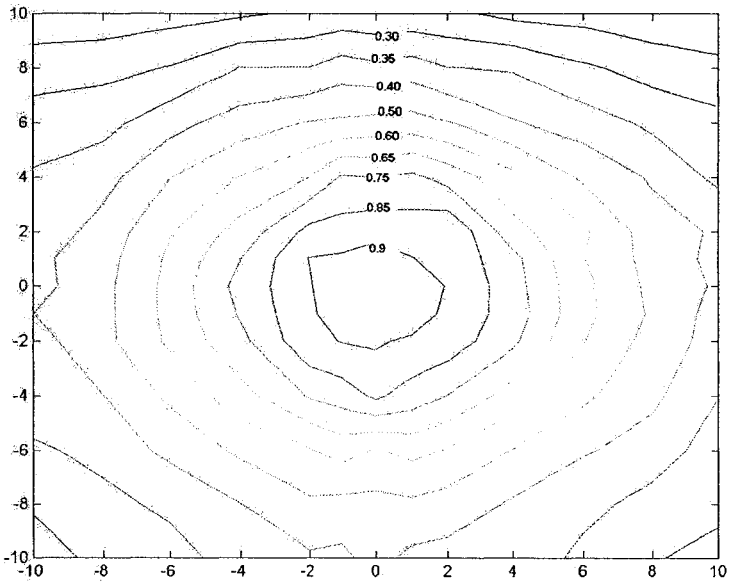

FIG. 13: Isofluence (thermal) showing the thermal distribution of thermal neutron fluence, Φ_{th}, on the in the plane parallel to the phantom surface in the hand irradiation facility at E_p = 2.00 MeV. The values were normalized to maximum thermal fluence in the center. This non-uniformity of thermal fluence caused by the incident neutron energy spectrum would contribute towards the non-uniformity in the composite sensitivity. The central region of the phantom will be activated more relative to the outer edges.

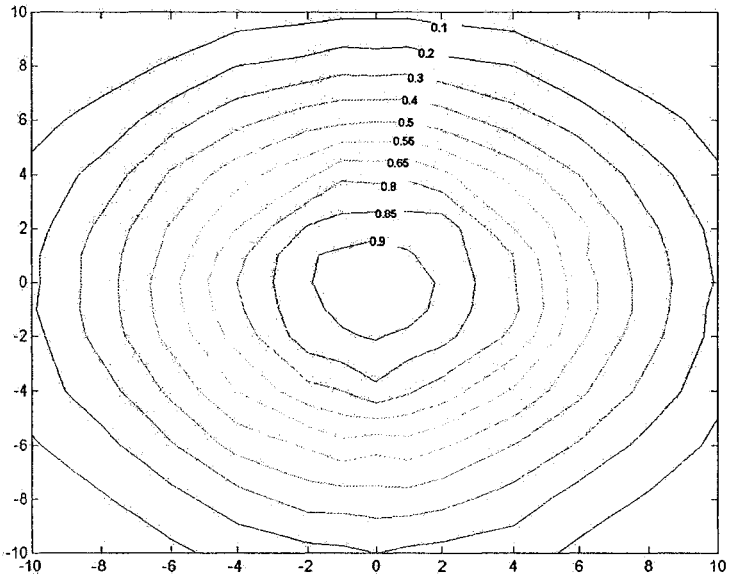

FIG. 14: Isoefficiency contours depicting the distribution of composite sensitivity in the plane parallel to the phantom surface (front) at E_p = 2.00 MeV. The values were normalized to unity maximum efficiency in the center. This non-uniformity of thermal fluence caused mainly by the incident neutron energy spectrum contributed towards the non-uniformity in the composite sensitivity. The space dependent absolute efficiency of a single large cylindrical NaI(Tl) detector of radius of 10 cm and thickness of 5 cm placed at 1 cm away from the phantom as a function of the phantom surface position at which (n, γ) reaction occurs emitting 847 keV γ-rays (γ-ray energy emitted following the beta decay of activated ^{56}Mn) was calculated at different locations using MCNP. This non-uniformity of composite sensitivity is caused mainly by the incident neutron energy spectrum. The central region of the phantom will be sampled more efficiently relative to the outer edges using a single large detector. In this geometry, the decrease in thermal neutron flux by increasing the radial distance from the centre of the phantom is deteriorated further by the decrease in γ-detection efficiency as the observation point approaches the edges of the detector. This problem needs investigation using a set of small detectors instead of single large detector for γ-detection by considering the tradeoff between dose and integral sensitivity.

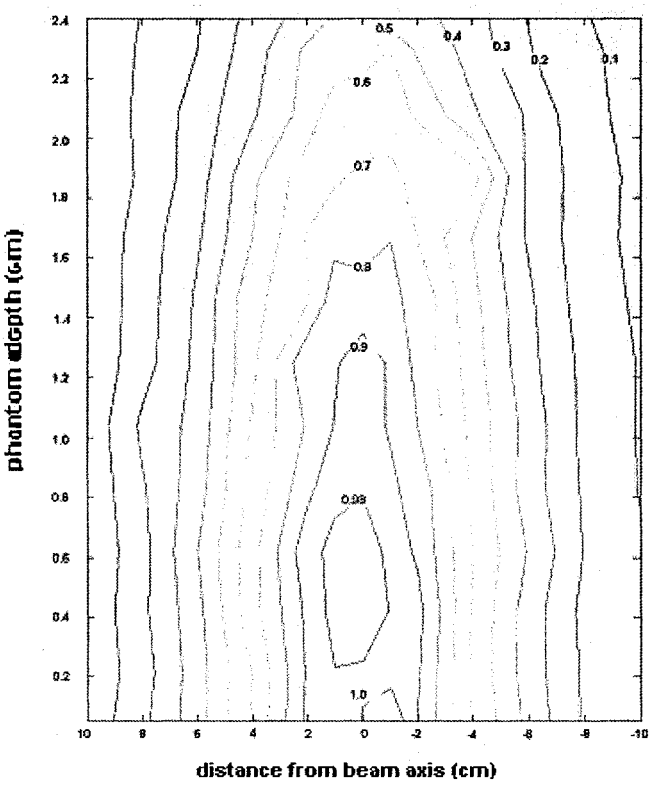

FIG. 15: Isoefficiency contours depicting the distribution of composite sensitivity along the width of the phantom at E_p = 2.00 MeV. The values were normalized to unity maximum efficiency in the center. The minimum composite sensitivity was obtained on the opposite side of the irradiated side. This is consistent with attenuation of the thermal neutron flux as it penetrates the sample. From this figure, it is clear that the side opposite to the irradiated side of the phantom is under-sampled relative to the irradiated side. In first half of the hand width (1.2 cm), the variation in differential composite sensitivity is less than 10% and then decreases rapidly with increasing thickness. Thus bilateral irradiation will result in minimum variations of composite sensitivity along the phantom width because of the improved uniformity of the thermal fluence due to opposing irradiations and also because of an initial build-up of thermal flux in first few mm (~0.6 cm) of hand phantom surface. Moreover, to increase the integral sensitivity of the system instead of using a single large detector, two detectors are used on opposite sides.

The non-uniformity depicted in **Figure 14** indicates that such measurements will be sensitive to the dimensions of the hand, amount of bone in the hand, beam energy and the irradiation and counting geometries. As a result of the neutron activation of other elements such as ^{48}Ca, an isotope of one of the major constituent elements of bone, deposit gamma energy in the γ-detector. This may be used to assess the amount of bone in the hand. To cope with the problem of achieving uniform composite sensitivity, use is made of some internal standard like the amount of bone in hand (Palerme, 1993, Pejović-Milić, 1998; Arnold, 2000;

Arnold *et al.*, 2002; Pejović-Milić, 2000). As the measurement of Ca is also dependent upon the same factors as that of Mn, the measurement of Mn concentration per unit bone mass will be independent of the exact geometry and experimental conditions (Arnold *et al.*, 2002). The measured ratio of Mn to bone mass in a patient's hand can be then converted to an absolute amount of Mn in hand by comparison with the Mn/Ca ratio of the appropriate size phantom.

4. SUMMARY AND CONCLUSIONS

The work describes the Monte Carlo simulation of the hand irradiation facility developed at the McMaster University 3 MV Van De Graaff accelerator. Important results and conclusions of this work are as follows:

- The Monte Carlo modeling of the designed hand irradiation facility was validated by comparing the measured and calculated thermal fluence non-uniformity. The calculated dose heterogeneity was also in fairly good agreement (~10%) with the measured dose heterogeneity at all the beam energies employed for hand irradiation at MAL (Arnold, 2000; Arnold *et al.*, 2002; Aslam *et al.*, 2003d).

- The difference between the dose equivalent measured by small volume TEPCs employing the appropriate quality factor algorithm (Aslam *et al.* 2003b) and the large volume neutron dose equivalent counters at the same distance (~<100 cm) exist mainly because of the highly non-uniform neutron field. This difference increases with decreasing beam energy and also with decreasing distance between the neutron producing target and the detector. Because of the difference in cross-sectional areas of two detectors, the solid angle must be kept same in two measurements using large and small volume detector by placing the large volume detector at a distance from the neutron producing target larger than that of small volume detector. Inverse square variation of neutron fluence should be taken into account to estimate the dose equivalent at the point of measurement of small volume detector.

- Because of the heterogeneous dose distribution over the hand surface, this paper describes the development of a method employing the TEPC (1.27 cm diameter counter) measured dose rates and the dose averaging factors calculated using MCNP to estimate the average dose equivalent delivered to the patient's hand (equivalent diameter ~ 9 cm) undergoing irradiation. This method is different from the one reported earlier (Aslam *et al.*, 2003d). Contrary to our earlier method, the method

described in this work employs only one measured dose rate in the center of the irradiation facility.

- A method is also described in this paper to estimate the neutron quality factors for the neutron beams used for IVNAA of hand to augment the dose measurements carried out earlier (Arnold *et al.*, 2002) for the calculation of dose equivalent delivered to the patient's hand.

- At E_p = 2.00 MeV beam energy, the gamma dose constitutes more than 25% of the total dose equivalent. This paper also discusses gamma shield design from those photons produced either in the target due to ^{7}Li(p, $p'\gamma$)^{7}Li (E_γ = 478 keV) or in the neutron moderating assembly due to ^{1}H(n, γ) interaction (E_γ = 2.2 MeV) to reduce the gamma dose equivalent to less than 5% of the total dose equivalent. The total dose equivalent delivered to the patient as a result of gamma shield will be reduced from 41 mSv to 31 mSv. The fast neutron component of the beam delivers (63%) most of this dose equivalent.

- Thus the proposed irradiation procedure for the IVNAA measurement of manganese in human hands with normal (1 ppm) and elevated manganese content can be carried out without violating the prescribed dose limits for such diagnostic procedures. This finding is of significant importance because such low energies and beam currents can be achieved even by small accelerators and the normal manganese concentrations are still measurable. These dose rates estimated in this work can be used to calculate the radiation dose received to patient's hand for IVNAA measurement of aluminum in human hand bones.

- The non-useful fast neutron component of the beam delivers 63% of the total dose equivalent. Its filtration will increase the useful neutron fluence (thermal and epithermal) per unit dose equivalent available for activation.

- This paper also discusses a method to calculate the differential composite sensitivity along the phantom surface and along the depth of the phantom. For bilateral irradiation of hand, the differential composite sensitivity along the phantom depth will be minimum (~10%) because of the improved uniformity of the thermal fluence due to opposing irradiations and also because of an initial build-up of thermal flux in first few mm from hand surface. The variation of the differential composite sensitivity on the phantom surface is approximately 70-80%. This problem of non-

uniform sensitivity of the system can be improved by using an arrangement of a set of small detectors instead of single large detector for γ-detection, however, it will reduce the integral sensitivity of the system. This problem of achieving uniform composite sensitivity is dealt by the use of the calcium activation signal from the bone to normalize the measurement to the amount of bone.

REFERENCES

Al-Haddad IK, Chettle DR, Fletcher JG, Fremlin JH. 1981. A transportable system for measurement of kidney cadmium *in vivo*. Int J Appl Radiat Isot. **32(2)**, 109-112.

Al-Hiti K, Slaibi S, Al-Kayat T. 1979. Portable system for detecting cadmium in the human liver. Int J Appl Radiat Isot. **30(1)**, 55-60.

Ali, P.A., Dutton, J., Evans, C.J., Morgan, W.D., Sivyer, A., 1985. A feasibility study for the in vivo measurement of beryllium by photonuclear activation. Phys Med Biol. **30(12)**, 1277-87.

Allen, D.A., Benyon, T.D., 1995. A design study for an accelerator-based epithermal neutron beam for BNCT, Phys. Med. Biol. **40,** 807-821.

Arnold, M.L., McNeill, F.E., Chettle, D.R., 1999. The feasibility of measuring manganese concentrations in human liver using neutron activation analysis, NeuroToxicology **20(2-3),** 407-412.

Arnold, M.L., 2000. *Development of an accelerator based system for in-vivo neutron activation analysis measurements of manganese in humans*, PhD Thesis, McMaster University, Hamilton, ON, Canada.

Arnold, M.L., McNeill, F.E., Prestwich, W.V., Chettle, D.R., 2000. System design for in-vivo neutron activation analysis measurements of manganese in the human brain: based on Monte Carlo modeling, Appl. Radiat. Isot., **53**, 651-656.

Arnold, M.L., McNeill, F.E., Stronach, I.M., Waker, A.J., Pejović-Milić, A., Chettle, D.R., 2002. An accelerator based system for in vivo neutron activation analysis measurements of manganese in human hand bones, Med. Phys. **29(11),** 2718-2724.

Aslam, Prestwich, W.V., McNeill, F.E., Waker A.J., 2001. *Spectrometry and Dosimetry for Accelerator Based In-vivo Measurements*, Annual Report McMaster Accelerator Laboratory, McMaster University, Hamilton, ON, Canada.

Aslam, Prestwich, W.V., McNeill, F.E., 2002. Thin target ^{7}Li(p,$p'\gamma$)^{7}Li inelastic gamma ray yield measurements, J. Radioanal. Nucl. Chem. **254(3),** 533-544 (2002).

Aslam, Prestwich, W.V., McNeill, F.E., 2003a. Lithium target performance evaluation for low energy acclerator based in-vivo measurements using gamma spectroscopy, Appl. Radiat. Isot. **58(3),** 321-331.

Aslam, Prestwich, W.V., McNeill, F.E., Waker, A.J., 2003b. Investigating the TEPC radiation quality response for radiation protection in low energy accelerator based clinical applications, Radiat. Prot. Dosim. **103(4),**311-322.

Aslam, Prestwich, W.V., McNeill, F.E., Waker, A.J., 2003c. Development of a low-energy monoenergetic neutron source for applications in low-dose radiobiological and radiochemical research, Appl. Radiat. Isot. **58(6),** 629-642.

Aslam, Prestwich, W.V., McNeill, F.E., Waker, A.J., 2003d. Estimation of dose equivalent to patients undergoing hand irradiation at the facility developed for accelerator based *in-vivo* neutron activation measurements in human hand bones, submitted to Medical Physics.

Baddeley H, Thomas BJ, Thomas BW, Summers V., 1983. Liver cadmium concentrations in metal industry workers. Br J Radiol. **56(667)**, 449-451.

Baron P, Schweinsberg F. 1988. A study of the literature on the concentrations of arsenic, lead, cadmium and mercury in body fluids and tissues to define normal values and detection of overload. 1. Description of analytical methods and arsenic, Zentralbl Bakteriol Mikrobiol Hyg [B]. **186(4)**, 289-310.

Bayanov, B.F., Belov, V.P., Bender, E.D., Bokhovko, M.V., Dimov, G.I., Kononov, V.N., Kononov, O.E., Kuksanov, N.K., Palchikov, V.E., Pivovarov, V.A., Salimov, R.A., Silvestrov, G.I., Skrinsky, A.N., Soloviov, N.A., Taskaev, S. Yu, 1998. Accelerator-based neutron source for the neutron-capture and fast neutron therapy at hospital, Nucl. Inst. Meth. Phys. Res. A **413(2-3),** 397-426.

Beddoe AH, Hill GL., 1985. Clinical measurement of body composition using in vivo neutron activation analysis. JPEN J Parenter Enteral Nutr. 9(4), 504-520.

Boddy, K., 1967. *In vivo* activation analysis of iodine in the thyroid gland-a preliminary study, Strahlentherapie (Sonderb). **65**, 377-83.

Briesmeister, J.F., (Ed.), 1997. *MCNP: A general Monte Carlo N-Particle transport code, Version 4B*, LA-12625-M, Los Alamos, USA.

Brune D, Nordberg G, Wester PO., 1980. Distribution of 23 elements in the kidney, liver and lungs of workers from a smeltery and refinery in North Sweden exposed to a number of elements and of a control group. Sci Total Environ. **16(1)**, 13-35.

Burkinshaw L., 1990. Some aspects of body composition in cancer. Infusionstherapie. **17 Suppl 3**, 57-58.

Chettle DR, Armstrong R, Todd AC, Franklin DM, Scott MC, Somervaille LJ. 1990. Measurements of trace elements *in vivo*. Basic Life Sci. **55**, 247-257.

Chettle DR, Fremlin JH., 1984. Techniques of *in vivo* neutron activation analysis. Phys Med Biol. **29(9)**, 1011-1043.

Chung C, Yuan LJ, Chen KB, Weng PS, Chang PS, Ho YH. 1985. A feasibility study of the *in vivo* prompt gamma activation analysis using a mobile nuclear reactor. Int J Appl Radiat Isot. **36(5)**, 357-367.

Cohn SH., 1981. In vivo neutron activation analysis: state of the art and future prospects. Med Phys. **8(2)**, 145-154.

Cohn SH., 1980. The present state of in vivo neutron activation analysis in clinical diagnosis and therapy. At Energy Rev. **18(3)**, 599-660.

Cohn SH, Ellis KJ, Vartsky D, Wielopolski L., 1983. Applications of nuclear technologies for *in vivo* elemental analysis. Neurotoxicology. **4(3)**, 34-47.

Cohn SH, Parr RM., 1985. Nuclear-based techniques for the in vivo study of human body composition. Report of an Advisory Group of the International Atomic Energy Agency. Clin Phys Physiol Meas. **6(4)**, 275-301.

Cummins PE, Dutton J, Evans CJ, Morgan WD, Sivyer A, Elwood PC. 1980. An in-vivo study of renal cadmium and hypertension. Eur J Clin Invest. **10(6)**, 459-461.

Davison AG, Fayers PM, Taylor AJ, Venables KM, Darbyshire J, Pickering CA, Chettle DR, Franklin D, Guthrie CJ, Scott MC, et al. 1988. Cadmium fume inhalation and emphysema. Lancet. **26;1(8587)**, 663-667.

Dilmanian, F.A., Lidofsky, L.J., Stamatelatos, I., Kamen, Y., Yasumura, S., Vartsky, D., Pierson, R.N. Jr., Weber, D.A., Moore, R.I., Ma R., 1998. Improvement of the prompt-gamma neutron activation facility at Brookhaven National Laboratory. Phys Med Biol. **43(2)**, 339-49.

Ellis, K.J., Kelleher, S., Raciti, A., Savory, J., Wills, M., 1988. *In vivo* monitoring of skeletal aluminium burden in patients with renal failure J. Radioanal. Nucl. Chem. **124**, 85–95.

Ellis KJ, Cohn SH, Smith TJ., 1985. Cadmium inhalation exposure estimates: their significance with respect to kidney and liver cadmium burden. J Toxicol Environ Health. **15(1)**, 173-187.

Ellis KJ, Vartsky D, Cohn SH., 1983. *In vivo* monitoring of heavy metals in man: cadmium and mercury. Neurotoxicology. **4(3)**, 164-168.

Ellis KJ., 2000. Human body composition: in vivo methods. Physiol Rev. **80(2)** 649-80.

Endo, S., Hoshi, M., Tauchi, H., Takeoka, S., Kitagawa, K., Suga, S., Meada, N., Komatsu, K., Sawada, S., Iwamoto, E., Sakamoto, S., Takeyama, K., Omura, M., 1995. Neutron generator at Hiroshima University for use in radiobiology study, J. Radiat. Res. **36,** 91-102.

Endo, S., Hoshi, M., Takada, J., Tauchi, H., Matsuura, S., Takeoka, S., Kitagawa, K., Suga, S., Komatsu, K., 1999. Neutron generator (HIRRAC) and dosimetry study, J. Radiat. Res. (Tokyo). **40 Suppl**, 14-20.

Ettinger, K.V., Morgan, W.D., Miola, U.J., Vartsky, D., Ellis, K.J., Wielopolski, L., Cohn, S.H., 1982. Silicon measurement in a lung phantom by neutron inelastic scattering. Med Phys. **9(4)**, 550-558.

Fedorowicz RP, Chettle DR, Kennett TJ, Prestwich WV, Webber CE., 1993. A ^{238}Pu/Be facility for *in vivo* cadmium measurements. Basic Life Sci. **60**, 323-324.

Franklin DM, Armstrong R, Chettle DR, Scott MC., 1990a. An improved *in vivo* neutron activation system for measuring kidney cadmium. Phys Med Biol. **35(10)**, 1397-1408.

Franklin DM, Guthrie CJ, Chettle DR, Scott MC, Mason HJ, Davison AG, Newman Taylor AJ, 1990b. *In vivo* neutron activation analysis of organ cadmium burdens. Referent levels in liver and kidney and the impact of smoking. Biol Trace Elem Res. **26-27**, 401-406.

Gerhardsson L, Nordberg GF., 1993. Lung cancer in smelter workers-interactions of metals as indicated by tissue levels. Scand J Work Environ Health. **19 Suppl 1**, 90-94.

Gerhardsson L, Brune D, Nordberg GF, Wester PO., 1986. Distribution of cadmium, lead and zinc in lung, liver and kidney in long-term exposed smelter workers. Sci Total Environ. **50**, 65-85.

Gerhardsson L, Brune D, Nordberg GF, Wester PO. 1988. Multielemental assay of tissues of deceased smelter workers and controls. Sci Total Environ. **74**, 97-110.

Gierga, D.P., Yanch, J.C., Shefer, R.E., 2000. An Investigation of the feasibility of gadolinium for neutron capture synovectomy, Med. Phys. **27(7)**, 1685-92.

Gierga, D.P., Yanch, J.C., Shefer, R.E., 2000. Development and construction of a neutron beam line for accelerator-based boron neutron capture synovectomy, Med. Phys. **27(1)**, 203-14.

Glaros, D., LoMonte, A.F., Ellis, K.J., Yasumura, S., Stoenner, R.W., Cohn, S.H., 1986. In vivo measurement of lithium in the body by a neutron activation analysis technique. Med Phys. **13(1)**, 45-49.

Gompertz D, Chettle DR, Fletcher JG, Mason H, Perkins J, Scott MC, Smith NJ, Topping MD, Blindt M., 1983. Renal dysfunction in cadmium smelters: relation to in-vivo liver and kidney cadmium concentrations. Lancet. **1(8335)**, 1185-1187.

Green S., Bradley D.A., Mountford P.J., Morgan W.D., Chettle D.R., Weaver D.R., 1993. Characteristics of an accelerator based system for in vivo aluminium measurement in peripheral bone. Basic Life Sci. **60**, 289-93.

Green S, Chettle DR., 1992. A feasibility study of the in vivo measurement of aluminium in peripheral bone. Phys Med Biol. **37(12)**, 2287-96

Greenberg A, Parkinson DK, Fetterolf DE, Puschett JB, Ellis KJ, Wielopolski L, Vaswani AN, Cohn SH, Landrigan PJ., 1986. Effects of elevated lead and cadmium burdens on renal function and calcium metabolism. Arch Environ Health. **41(2)**, 69-76.

Greenfield MA., 1992. Current status of physical measurements of the skeleton. Med Phys. **19(6)**, 1349-57.

Harvey TC, Thomas BJ, McLellan JS, Fremlin JH., 1975. Measurement of liver-cadmium concentrations in patients and industrial workers by neutron-activation analysis. Lancet. **1(7919)**, 1269-72.

Henke G, Sachs HW, Bohn G., 1970. Cadmium determination in the liver and kidneys of children and juveniles by means of neutron activation analysis. Arch Toxikol. **26(1)**, 8-16.

Heymsfield SB, Wang J, Lichtman S, Kamen Y, Kehayias J, Pierson RN Jr., 1989. Body composition in elderly subjects: a critical appraisal of clinical methodology. Am J Clin Nutr. **50(5 Suppl)**, 1167-75; discussion 1231-1235.

Heymsfield SB, Waki M., 1991. Body composition in humans: advances in the development of multicompartment chemical models. Nutr Rev. **49(4)**, 97-108.

Heymsfield SB, Wang Z, Baumgartner RN, Dilmanian FA, Ma R, Yasumura S., 1993. Body composition and aging: a study by in vivo neutron activation analysis. J Nutr. **123(2 Suppl)**, 432-7.

Hill GL., 1990. Clinical body composition using in vivo neutron activation analysis. Infusionstherapie. **17 Suppl 3**, 18-20.

ICRP, 1991. International Commission on Radiation Protection, Radiation Protection. Recommendation of the International Commission on Radiation Protection (ICRP: Report 60), Pergamon, Oxford.

ICRU, 1986. *Photon, electron, proton and neutron interaction data for body tissues,* ICRU Report 46 (ICRU Publications, Bethesda, MD 1986).

Janni, J.F., 1982. Proton range-energy tables, 1 keV–10 GeV, At. Data Nucl. Data Tables **27**, 147.

Jebb SA, Elia M., 1993. Techniques for the measurement of body composition: a practical guide. Int J Obes Relat Metab Disord. **17(11)**, 611-21.

Kacperek, A., Ryde, S.J., Evans, C.J., Dutton, J., Morgan, W.D., Sivyer, A., 1993. The measurement of silicon in a lung phantom--a comparison of two nuclear reactions for in vivo activation analysis. Phys Med Biol. **38(6)**, 689-98.

Kehayias JJ, Valtuena S., 1999. Neutron activation analysis determination of body composition. Curr Opin Clin Nutr Metab Care. **2(6)**, 453-63.

Kononov, V.N., Poletaev, E.D., Yurlov, B.D., 1977. Absolute yield and spectrum of neutrons from the ^{7}Li(p, n)^{7}Be. At. Energ. **43,** 947-949.

Krishnan SS, Lui SM, Jervis RE, Harrison JE., 1990. Studies of cadmium uptake in bone and its environmental distribution. Biol Trace Elem Res. **26-27**, 257-261.

Krauel JB, Speed MA, Thomas BW, Baddeley H, Thomas BJ., 1980. The *in vivo* measurement of organ tissue levels of cadmium. Int J Appl Radiat Isot. **31(2)**, 101-106.

Karlicek V, Topolcan O., 1974. Cadmium in kidneys of patients with essential hypertension and renal hypertension. Cas Lek Cesk. **113(2)**, 41-43.

Karlicek V, Topolcan O, Bilkova L, Kott J, Sova J., 1971. Concentration of trace-elements in kidneys of hypertensive patients determined by neutron activation analysis. Cas Lek Cesk. **110(32)**, 756-761.

Landsberger S., Wu D., 1999. An evaluation of thermal and epithermal neutron activation analysis Compton suppression methods for biological reference materials. Biol Trace Elem Res. **71-72**, 453-461.

Lee, C.L., Zhou, X.L., 1999. Thick target neutron yields for the ^{7}Li(p, n)^{7}Be reaction near threshold, Nucl. Inst. Meth. Phys. Res. B **152,** 1-11.

Lee, C.L., Zhou, X.L., Kudchadker, R.J., Harmon, F., 2000. Harker, Y.D., A Monte Carlo dosimetry-based evaluation of the ^{7}Li(p, n)^{7}Be reaction near threshold for accelerator boron neutron capture therapy, Med. Phys. **27(1)**, 192-202.

Lee RC, Wang ZM, Heymsfield SB., 2001. Skeletal muscle mass and aging: regional and whole-body measurement methods. Can J Appl Physiol. **26(1)**, 102-22.

Lewis, D.G., Natto, S.S.A., Ryde S.J.S., Evans, C.J., 1997. Monte Carlo design study of a moderated ^{252}Cf source for in vivo neutron activation analysis of aluminium, Phys. Med. Biol. **42(4)**, 625–636.

Lindh U, Brune D, Nordberg G, Wester PO., 1980. Levels of antimony, arsenic, cadmium, copper, lead, mercury, selenium, silver, tin and zinc in bone tissue of industrially exposed workers. Sci Total Environ. **16(2)**, 109-116.

Liskien, H., Paulsen, A., 1975. Neutron production cross-sections and energies for the reactions ^{7}Li(p, n)^{7}Be and ^{7}Li(p, n)^{7}Be*, At. Data Nucl. Data Tables **15,** 57-84.

Mason HJ, Davison AG, Wright AL, Guthrie CJ, Fayers PM, Venables KM, Smith, NJ, Chettle DR, Franklin DM, Scott MC, et al. 1988. Relations between liver cadmium, cumulative exposure, and renal function in cadmium alloy workers. Br J Ind Med. **45(12)**, 793-802.

Mason HJ, Williams N, Armitage S, Morgan M, Green S, Perrin B, Morgan WD., 1999. Follow up of workers previously exposed to silver solder containing cadmium. Occup Environ Med. **56(8),** 553-558.

McLellan JS, Thomas BJ, Fremlin JH, Harvey TC., 1975. Cadmium-its *in vivo* detection in man. Phys Med Biol. **20(1)**, 88-95.

McLellan J, Thomas BJ, Fremlin JH, Harvey TC., 1974. Proceedings: Measurement of cadmium in the human liver by *in vivo* neutron activation analysis. Clin Sci Mol Med. **47(5)**, 21.

McNeill FE, Chettle DR., 1998. Improvements to the *in vivo* measurement of cadmium in the kidney by neutron activation analysis. Appl Radiat Isot. **49(5-6)**, 699-700.

Meadows, J.W., 1977. *Determination of the energy scale for neutron cross-section measurements employing a monoenergetic accelerator*, ANL/TDM-25.

Morgan WD, Ellis KJ, Vartsky D, Yasumura S, Cohn SH., 1981. Calibration of a ^{238}Pu,Be facility for partial-body measurements of organ cadmium. Phys Med Biol. **26(4)**, 577-590.

Morgan WD, Vartsky D, Ellis KJ, Cohn SH. 1981. A comparison of ^{252}Cf and ^{238}Pu, Be neutron sources for partial-body *in vivo* activation analysis. Phys Med Biol. **26(3)**, 413-424.

Morgan WD, Ryde SJ, Jones SJ, Wyatt RM, Hainsworth IR, Cobbold SS, Evans CJ, Braithwaite RA. 1990. *In vivo* measurements of cadmium and lead in occupationally-exposed workers and an urban population. Biol Trace Elem Res. **26-27**, 407-414.

Morgan WD., 2000. Of mermaids and mountains. Three decades of prompt activation in vivo. Ann N Y Acad Sci. **904**, 128-33.

Palerme, S. 1993. *Pilot studies for in-vivo bone aluminum measurements*, MSc Thesis, McMaster University, Hamilton, ON, Canada.

Palerme, S., Chettle, D.R., Kennett, T.J., Prestwich, W.V., Webber, C.E., 1993. Pilot studies for in-vivo bone aluminum measurements, Basic Life Sci. **60**, 303-306.

Pejović-Milić, A., 1998. *An accelerator based in vivo measurement of aluminum in human bone by neutron activation analysis*, MSc Thesis, McMaster University.

Pejović-Milić, A., McNeill, F.E., Prestwich, W.V., Waker, A.J., Chettle, D. R., 1998. Development of an accelerator-based determination of aluminum burden in peripheral bone by neutron activation analysis, Appl. Radiat. Isot. **49 No. 5/6**, 717-719.

Pejović-Milić, A., Arnold, M.L., McNeill, F.E., Chettle, D.R., 2000. Monte Carlo design study for in vivo bone aluminum measurement using a low energy accelerator beam, Appl. Radiat. Isot. **53**, 657-664.

Pejović-Milić, A., 2001. *In-vivo measurement of some trace elements in human bone*, PhD Thesis, McMaster University.

Perrin B, Green S, Morgan WD., 1998. Longitudinal measurements of the cadmium burden of 'jig solderers' using IVNAA. Appl Radiat Isot. **49(5-6)**, 701-702.

Pichard C, Kyle UG., 1998. Body composition measurements during wasting diseases. Curr Opin Clin Nutr Metab Care. **1(4)**, 357-61.

Pierson RN Jr, Wang J, Heymsfield SB, Dilmanian FA, Weber DA. 1990. High precision in-vivo neutron activation analysis: a new era for compartmental analysis in body composition. Basic Life Sci. **55**, 317-325.

Pignol, J.P., Cuendet, P., Brassart, N., Fares, G., Colomb, F., M'Bake Diop, C., Sabattier, A., Hachem, A., Prevot, G., Combined use of FLUKA and MCNP-4A for Monte Carlo simulation of the dosimetry of ^{10}B neutron capture enhancement of fast neutron irradiations, 1998. Med. Phys. **25(60)**, 885-891.

Plank LD, Hill GL., 2000. Sequential metabolic changes following induction of systemic inflammatory response in patients with severe sepsis or major blunt trauma. World J Surg. **24(6)**, 630-8.

Powell, J.A., Ludewig, H., Todosow, M., Reich, M., 1999. Target and filter concepts for accelerator-driven boron neutron capture therapy applications, Nucl. Tech. **125**, 104-115.

Ralston A, Utteridge T, Paix D, Beddoe A. 1994. Calibration of a cadmium IVNAA system. Australas Phys Eng Sci Med. **17(1)**, 34-42.

Ritchie, A.I.M., 1976. Neutron yields and energy spectra from thick target Li(p, n) source, J. Phys. D: Appl. Phys. **9**, 15-26.

Ryde SJ, Morgan WD, Sivyer A, Evans CJ, Dutton J., 1987. A clinical instrument for multi-element *in vivo* analysis by prompt, delayed and cyclic neutron activation using ^{252}Cf. Phys Med Biol. **32(10)**, 1257-1271.

Ryde SJ, Morgan WD, Evans CJ, Sivyer A, Dutton J. 1989. Calibration and evaluation of a ^{252}Cf-based neutron activation analysis instrument for the determination of nitrogen *in vivo*. Phys Med Biol. **34(10)**, 1429-1441.

Sabbioni E, Marafante E, Amantini L, Ubertalli L, Pietra R., 1978. Cadmium toxicity studies under long term-low level exposure (LLE) conditions. I. Metabolic patterns in rats exposed to present environmental dietary levels of Cd for two years. Sci Total Environ. **10(2)**, 131-61.

Schmid, E., Regulla, D., Guldbakke, S., Schlegel, D., Bauchinger, M., 2000. The effectiveness of monoenergetic neutrons at 565 keV in producing dicentric chromosomes in human lymphocytes at low doses, Radiat. Res. **154**, 307-312.

Schmid, E., Regulla, D., Guldbakke, S., Schlegel, D., Roos, M., 2002. Relative biological effectiveness of 144 keV neutrons in producing dicentric chromosomes in human lymphocytes compared with ^{60}Co gamma rays under head-to-head conditions, Radiat Res. **157(4)**, 453-460.

Scott MC, Chettle DR., 1986. *In vivo* elemental analysis in occupational medicine. Scand J Work Environ Health. **12(2)**, 81-96.

Scott R, Haywood JK, Boddy K, Williams ED, Harvey I, Paterson PJ., 1980. Whole body calcium deficit in cadmium-exposed workers with hypercalciuria. Urology. **15(4),** 356-359.

Shaikh ZA, Ellis KJ, Subramanian KS, Greenberg A., 1990. Biological monitoring for occupational cadmium exposure: the urinary metallothionein. Toxicology. **63(1),** 53-62.

Skerfving S, Nilsson U., 1992. Assessment of accumulated body burden of metals. Toxicol Lett. **64-65 Spec No**, 17-24.

Stinchcomb, T.G., Borak, T.B., (1983). Neutron quality parameters versus energy below 4 MeV from microdosimetric calculations, Radiat. Res. **93(1)**, 1-18.

Sutcliffe JF., 1996. A review of in vivo experimental methods to determine the composition of the human body. Phys Med Biol. **41(5)**, 791-833.

Thomas BJ, Harvey TC, Chettle DR, McLellan JS, Fremlin JH., 1979. A transportable system for the measurement of liver cadmium *in vivo*. Phys Med Biol. **24(2)**, 432-437.

Vartsky, D., LoMonte, A., Ellis, K.J., Yasumura, S., Cohn, S.H., 1985. A proposed method for in vivo determination of lithium in human brain. Phys Med Biol. **30(11)**, 1225-36.

Vartsky D, Ellis KJ, Chen NS, Cohn SH., 1977. A facility for *in vivo* measurement of kidney and liver cadmium by neutron capture prompt gamma ray analysis. Phys Med Biol. **22(6)**, 1085-1096.

Wang, C.K.C., Blue, T.E., Gahbauer, R., 1985. A neutronic study of an accelerator-based neutron irradiation facility for boron neutron capture therapy, Nucl. Tech. **84(1),** 93-107.

Williams, E.D., Elliott, H.L., Boddy, K., Haywood, J.K., Henderson, I.S., Harvey, I., Kennedy, A.C., 1980. Whole body aluminium in chronic renal failure and dialysis encephalopathy, Clin. Nephrol. **14**, 198–200.

Wyatt, R.M., Ryde, S.J.S., Morgan, W.D., McNeil, E.A., Hainsworth, I.R., Williams, A.J., 1993. The development of a technique to measure bone aluminium content using neutron activation analysis, Physiol. Meas. **14**, 327–35.

Yanch, J.C., Zhou, X.L., Shefer, R.E., Klinkowstein, R.E., 1992. Accelerator-based epithermal neutron beam design for neutron capture therapy, Med. Phys. **19(3),** 709-721.

Zhou, X.L., Lee, C., 1997a. Analysis of epithermal neutron production by near-threshold (p, n) reactions, Appl. Rad Isot. **48,** 1571-1575.

Zhou, X.L., Lee, C. 1997b, Lithium compounds as targets for (p, n) reactions, Appl. Rad Isot. **48,** 1493-1496.

CHAPTER VII

Paper VI

The following paper examines the feasibility of producing monoenergetic neutron beams of energy less than 1 MeV at the McMaster University 3 MV KN Van de Graff accelerator. This will extend the use of facility for those applications in radiobiological and radiochemical research where moderate neutron dose rates of monoenergetic neutrons are needed. A tissue equivalent proportional counter (TEPC) filled with propane based tissue equivalent (TE) gas simulating a 2 μm diameter was employed to determine the neutron and gamma dose rates of the monenergetic neutron fields as a function of proton beam energy.

The work presented in this paper was performed by me under the supervision of Drs. Prestwich and McNeill. The TEPC based microdosimetric system and the computer programs employed for data acquisition and analysis of the raw data that was used in the experiments at MAL had been previously developed and characterized at AECL, Chalk River, Canada by Dr. Waker. Dr. Waker acted as a consultant and collaborator for the research presented in this paper. The manuscript was written by me and edited by Drs. Prestwich, McNeill and Waker.

(Reprinted from Appl. Radiat. Isot., 58(6), Aslam, W. V. Prestwich, F. E. McNeill, A. J. Waker, Development of a low-energy monoenergetic neutron source for applications in low-dose radiobiological and radiochemical research, 629-641, Copyright (2003), with permission from Elsevier)

PERGAMON

Applied Radiation and Isotopes 58 (2003) 629–642

Applied Radiation and Isotopes

www.elsevier.com/locate/apradiso

Development of a low-energy monoenergetic neutron source for applications in low-dose radiobiological and radiochemical research

Aslam[a,*], W.V. Prestwich[a], F.E. McNeill[a], A.J. Waker[b]

[a] *Medical Physics and Applied Radiation Sciences Unit, McMaster University, Nuclear Research Building, Hamilton, Ont., Canada L8S 4K1*

[b] *AECL, Chalk River Laboratories, Chalk River, Ont., Canada K0J 1J0*

Received 16 January 2003; received in revised form 3 February 2003; accepted 14 February 2003

Abstract

The McMaster University 3 MV KN Van de Graff accelerator facility primarily dedicated to in vivo neutron activation measurements has been used to produce moderate dose rates of monoenergetic fast neutrons of energy ranging from 150 to 600 keV with a small energy spread of about 25 keV (1σ width of Gaussian) by bombarding thin lithium targets with 2.00–2.40 MeV protons. The calculated dose rate of the monoenergetic neutrons produced using thin lithium targets as functions of beam energy, target thickness, lab angle relative to beam direction, and the solid angle subtended by the sample with the target has also been reported.

Keywords: Monoenergetic Neutrons; Low-energy; Beam quality; Energy distribution; Dose distribution

1. Introduction

This paper describes the characterization of monoenergetic neutron fields of energy less than 600 keV developed at the McMaster University 3 MV Van de Graaff accelerator using thin lithium targets for use in radiobiological and radiochemical studies. Section 2 describes the materials and methods used for the development and characterization of monoenergetic neutron fields. Measurement techniques for neutron energy distributions and lineal energy distributions are also discussed in this section. The computational procedure to produce the low-energy monoenergetic neutron fields of required dose rates is also outlined in this section. Section 3 describes the energy distributions, dose rates, γ-ray contaminations, beam quality of the neutron fields measured as a function of proton beam energy ranging from 2.00 to 2.40 MeV. Computational procedure described in the last section is validated by comparing calculations with those of experimental measurements. The potential of the developed neutron fields are also discussed for those radiobiological and radiochemical studies where high-dose rates of monoenergetic neutron fields are needed.

2. Materials and methods

2.1. The neutron source

Thin ^{7}Li and ^{7}LiF targets were designed to produce monoenergetic neutrons of energy ranging from 150 to 600 keV using the ^{7}Li(p,n)^{7}Be reaction at the McMaster University 3 MV KN Van De Graaff Accelerator. The thickness of the targets was controlled by the evaporated weight of each target material onto 1-mm-thick tantalum disks. The tantalum disks were mounted on the end

of a beam duct and cooled with water to prevent heating by proton beam currents. This Van De Graaff Accelerator can be operated at proton beam currents as low as a few nA (Aslam et al., 2002) up to 100 μA (Arnold, 2000; Pejović-Milić, 2001).

2.2. Neutron energy measurements

Energy of the monoenergetic neutrons was measured by a ^{3}He-filled gridded ionization chamber (FNS-1, Seforad Applied Radiation Ltd. of Emek Hayarden, Israel). The dimensions of the active volume of the chamber filled with a gas containing ^{3}He gas at a pressure of 10 atm, exceeded the range of the low-energy charged particles produced by the ^{3}He(n,p)T reaction in the active volume of the counter at the energies employed here. Thus, the neutron energy measured was proportional to the energy deposited inside the active volume. All the energy measurements were performed in such a way that the detector axis always coincided with the beam axis. The counter was also used to monitor the time-dependent variations in neutron fluence rate.

2.2.1. Measurement technique

The anode of the ^{3}He ionization chamber was maintained at a constant +3000 V by the Power Designs AEC1000 power supply. A voltage divider within the preamp (SR-101) kept the grid at +850 V. Output signal amplified by an amplifier module (ORTEC, 572) was analyzed using a commercial data acquisition system APTEC. A 3 μs shaping time constant was chosen for optimum resolution. The detector provided an energy resolution of 20 keV for thermal neutrons and 27 keV for 600 keV neutrons. The neutron energy was determined by establishing a linear relationship between the pulse heights and the known pulser amplitudes and the thermal neutron energy.

2.3. Microdosimetric measurements

A Rossi-type spherical proportional counter (model LET $\frac{1}{2}''$, Far West Technology, Goleta, USA), with 2.5-mm thick walls made of A-150 tissue-equivalent plastic (TEPC), filled with propane-based tissue equivalent (TE) gas at a pressure of 8.8 kPa to simulate a tissue sphere of 2 μm diameter was used to characterize the monoenergetic neutron fields.

2.3.1. Measurement technique

The experimental technique generally followed has been described in detail elsewhere (Arnold, 2000; Waker, 1995; Khaloo and Waker, 1995). The counter gas gain was kept constant by adjusting the voltage difference between the helix and the central wire in such a way that the calibration peak matched a predetermined position at a specified amplifier setting (Arnold, 2000).

The pulse height spectra of single energy-deposition events due to secondary charged particles produced in the cavity wall and the gas of Tissue Equivalent Proportional Counter (TEPC) were measured using a low-noise preamplifier connected directly to the anode of the counter. Analog pulses from the preamplifier were fed through dual SPEC amplifier with high and low gain settings into two 16 k analog-to-digital converters (ADCs) and stored in an ORTEC HM 413 HISTO memory unit. The processing of the raw data was carried out employing the computer programs written in **KMAX** version 4.1 developed at AECL, Chalk River, Canada (Waker, 1995; Khaloo and Waker, 1995).

The measured pulse height spectra were converted into the lineal energy distributions $f(y)$ and $d(y)$ to evaluate the beam quality and the dose rates of mixed radiation fields by applying the appropriate calibration factors using an internal alpha source, ^{244}Cm, and taking into account the mean chord length of the sensitive volume simulated. The mean lineal energy, y_α, of the α particles emitted by ^{244}Cm was calculated as the quotient the energy deposited in the cavity to the mean chord length in the cavity. The ^{244}Cm emits α particles with an average energy of 5.80 MeV (Srdoc and Marino, 1996), which deposit an energy of 170 keV (ICRU, 1983b) in a 2 μm diameter TE gas and correspond to a lineal energy of $y_\alpha = 127$ keV/μm. The mean pulse height, h_α, corresponding to the mean energy imparted at an amplifier setting, A_α, in the cavity was evaluated by fitting a Gaussian curve to the measured peak. Using y_α and h_α, the calibration factors were calculated to convert the pulse height measurements conducted with two overlapping blocks of amplifier settings (A_1 and A_2) into a single spectrum of lineal energy as (Arnold, 2000; Waker, 1995; Khaloo and Waker, 1995)

$$y = \frac{y_\alpha}{h_\alpha} G \times h, \tag{1}$$

where $G(A_\alpha/A_1$ and $A_\alpha/A_2)$ is the gain ratio for the two different amplifiers. Sources of uncertainties associated with this method of calibration have been discussed elsewhere (ICRU, 1983a).

2.3.2. Total uncertainty in microdosimetric measurements

The total uncertainty in the measured lineal energy distributions arises from: the counting statistics (±3%), drift in the gain of the counter during the measurements (±2–3%) (Arnold, 2000; Waker, 1995; Khaloo and Waker, 1995), uncertainty in calibration using internal α particles (±4%) (Srdoc and Marino, 1996), and the merging of two spectra collected at two different amplifier gains (3–4%) (Arnold, 2000; Waker, 1995, Khaloo and Waker, 1995). We estimate the experimental uncertainty conservatively in measured dose-mean lineal energies around ±7–10% as recommended (ICRU,

1983a) and ±9–11% in dose rates per unit of accumulated proton charge.

2.4. Thin target dose calculations

The smallest value of bombarding proton energy at which the (p,n) reaction can take place is called the threshold energy, E_{th}. As the beam passes through the target material, the mean beam energy decreases and leaves a thin target with mean beam energy $E_{p\,exit}$ ($< E_{th}$). Thin targets may be used to produce monoenergetic neutrons (Endo et al., 1995, 1999; Schmid et al., 2000). The energy spread and angular neutron fluence spectrum, $\Phi(E,r,\theta)$ of the monoenergetic neutrons produced depends upon the energy of incident protons and the target thickness. The thickness of the target material is controlled by the evaporated weight of target material. Computational procedure to calculate angular fluence spectrum for thin targets is discussed in the next section.

2.4.1. Mean neutron energies

The 3 MV Van de Graaff accelerator at McMaster University Accelerator Laboratory uses thin lithium target to produce monoenergetic fast neutrons. For the purpose of calculations, the neutron production target was assumed at the origin of the coordinate system, r as the radial distance between the target and the biological sample to be irradiated and θ as the lab angle relative to beam direction. The neutron field is uniform with respect to the azimuthal angle, φ, with the beam axis. Thus, knowing the angular neutron fluence spectrum, $\Phi(E,r,\theta)$, calculated from kinematic calculations based on the neutron production (p, n) cross-sections, the fluence spectrum weighted mean neutron energy at position (r,θ) in the neutron field, was calculated as

$$\bar{E}_n(r,\theta) = \frac{\int_{En\,\min}^{En\,\max} E_n \Phi(E_n,r,\theta)\,\mathrm{d}E_n}{\int_{En\,\min}^{En\,\max} \Phi(E_n,r,\theta)\,\mathrm{d}E_n}. \quad (2)$$

Here $E_{n\,\max}$ and $E_{n\,\min}$ are the neutron energy spectrum boundaries corresponding to the incident beam energy E_{po} and the exit beam energy $E_{p\,exit}$. Calculation of $E_{p\,exit}$ has been discussed in Section 2.4.3. However, in practical situations, the exposed biological sample will be subtending a solid angle with the target (neutron source), in such case the average neutron energy may be calculated as

$$\bar{E}_n(r,\Omega(\theta)) = \frac{\int_{En\,\min}^{En\,\max}\int_{\theta\,\min}^{\theta\,\max} E_n \Phi(E_n,r,\theta)\sin\theta\,\mathrm{d}\theta\,\mathrm{d}E_n}{\int\int \Phi(E_n,r,\theta)\sin\theta\,\mathrm{d}\theta\,\mathrm{d}E_n}. \quad (3)$$

2.4.2. Neutron absorbed dose

The neutron dose rate at any location (r,θ) in the radiation field was calculated as follows:

$$D(r,\theta) = \int_{E_{n\,\min}}^{E_{n\,\max}} k(E)\Phi(E,r,\theta)\,\mathrm{d}E, \quad (4)$$

where $k(E)$ is the fluence to kerma conversion coefficients for ICRU tissue sphere calculated from the function provided in literature (Wagner et al., 1985). The integral in (4) have been evaluated using the cubic spline integrations (Press et al., 1992).

However, in practical situations, the exposed biological sample will be subtending a solid angle, Ω, with the target (neutron source), in such case the absorbed dose rate in units of Gy cm^2/μC, may be calculated using

$$D(r,\Omega(\theta))A = A\int_{\theta_{\min}}^{\theta_{\max}}\int_{E_{n\,\min}}^{E_{n\,\max}} k(E)\Phi(E,r,\theta)\,\mathrm{d}\Omega\,\mathrm{d}E, \quad (5)$$

$$D(r,\Omega(\theta))A = \int_{\theta_{\min}}^{\theta_{\max}}\int_{E_{n\,\min}}^{E_{n\,\max}} k(E)\frac{\mathrm{d}^2 Y(E,\theta)}{\mathrm{d}\Omega\,\mathrm{d}E} \times (E,\theta)2\pi\sin\theta\,\mathrm{d}\theta\,\mathrm{d}E. \quad (6)$$

The dose averaged over the sample can be obtained by dividing the dose D calculated above by the area of the exposed sample.

2.4.3. Neutron fluence spectrum

Lithium targets using ^{7}Li(p,n)^{7}Be reaction are widely used as a neutron source for applications in BNCT (Wang et al., 1985; Yanch et al., 1992; Allen and Benyon, 1995; Zhou and Lee, 1997a, b; Magagula and Watterson, 1998; Bayanov et al., 1998; Powell et al., 1999; Lee and Zhou, 1999), BNCEFNT (Pignol et al., 1998), BNCS (Gierga et al., 2000a, b), in vivo neutron activation measurements (Palerme, 1993; Pejović-Milić, 2001, 1998; Arnold, 2000; Arnold et al., 2000, 1999; Pejović-Milić et al., 1998, 2000) and in radiobiological experiments (Endo et al., 1995; Schmid et al., 2000, 2002). The differential neutron yields in the near threshold region of 1.88–1.93 MeV is calculated by using the Breit–Wigner approximation (Ritchie, 1976; Kononov et al., 1977; Meadows, 1977; Lee and Zhou, 1999) and measured cross-sections are employed for the above threshold region (Ritchie, 1976; Meadows, 1977; Lee and Zhou, 1999). We have summarized our calculations briefly here.

The ^{7}Li(p,n)^{7}Be nuclear reaction has been modeled by following an analytical approach to calculate the neutron angular fluence spectrum as a function of the proton beam energy. The number of neutrons produced from an element of target of thickness dx (corresponding to an energy loss of dE_p in thickness dx) emitted at angle θ into an element of solid angle dΩ per incident proton is given by

$$\frac{\mathrm{d}^2 Y(E_n,\theta)}{\mathrm{d}\Omega\,\mathrm{d}E_n} = n_T \frac{\mathrm{d}\sigma}{\mathrm{d}\Omega'}\frac{\mathrm{d}\Omega'}{\mathrm{d}\Omega}\frac{1}{S(E_p)}\frac{\mathrm{d}E_p}{\mathrm{d}E_n}, \quad (7)$$

where n_T is the lithium target atomic density and dE_n refers to the width of the neutron spectrum because of the thickness dx (or dE_p), dE_p/dE_n was calculated from the Q-value equation (Ritchie, 1976; Lee and Zhou,

1999; Arnold, 2000). The differential cross-section, $d\sigma/d\Omega'$, in cm was taken from the compilations of (p,n) cross-section for ^{7}Li (Liskien and Paulsen, 1975) and the stopping powers, $S(E_p)$, for lithium metal was calculated by using the Bethe stopping power as (Attix, 1986)

$$\frac{1}{\rho}S(E) = 4\pi N_a\left(\frac{Z}{A}\right)\frac{m_e c^2}{\beta^2}r_0^2 \ln\left(\frac{2m_e v^2}{I}\right), \tag{8}$$

where N_a is Avogadro's number, $\beta = v/c$, and r_0 is the classical electron radius with $Z = 3$, $A = 6$, and $I = 57.20$ eV (Janni, 1982).

When a proton beam impinges on a lithium target, the initial neutron yield is determined from the incident proton energy. As the proton beam penetrates further into the target, energy is lost in the thickness, dx, and the neutron yield is determined from decreasing proton energy, until either the beam energy drops below the threshold energy or beam leaves the target material. Since the proton beam leaves a thin target before reaching energies below E_{th}, the differential neutron yield for proton energies below this is zero. Neutrons will only be produced in the region bounded by $E_{p\,exit} \leqslant E_p \leqslant E_{po}$. The exit proton energy, $E_{p\,exit}$, can be determined using the range–energy relationship and the target thickness.

The range of protons of incident energy E_p in lithium metal target can be expressed as an exponential function of the form defined as

$$R(E) = CE_p^n, \tag{9}$$

where C and n are fitted parameters. The parameters, C and n, were obtained using Microsoft Excel® as 122.17 and -0.7685, respectively, with $R^2 = 1$ in the proton energy range $1.75 \leqslant E_p \leqslant 3.0$ MeV. After passing through a target of thickness, $\Delta x < R(E_p)$, the proton range is reduced to $R(E_{po}) - \Delta x$ and the exit energy can be determined using the range–energy relationship as

$$E_{p\,exit} = R^{-1}(R(E_{po}) - \Delta x), \tag{10}$$

where $R^{-1}(x)$ is the proton energy with range x in the target material. Using (9) and (10), the exit beam energy can be determined as

$$E_{p\,exit} = \left(E_{po} - \frac{\Delta x}{C}\right)^{1/n}, \tag{11}$$

where $E_{p\,exit}$ is in MeV and Δx is in μm.

The generated neutron spectrum at any location (r, θ) in the monoenergetic neutron fields was used to calculate the fluence weighted mean neutron energies and doses as functions of beam energy, target thickness and the solid angle subtended by the sample with the target.

3. Results and discussion

3.1. Neutron energy measurements

The neutron energy spectra at proton beam energies of 2.00–2.40 MeV in steps of 50 keV using a thin ^{7}Li target were measured by the ^{3}He gas filled ionization chamber shown in Figs. 1(a) and (b). The results have also been summarized in Table 1. The full energy peaks are clearly seen in all spectra; however, below 150 keV neutron energy the spectrometer does not resolve the peak and merges in the thermal neutron peak. In the energy region from 150 to 600 keV, the FWHM in the energy range was almost energy independent and its

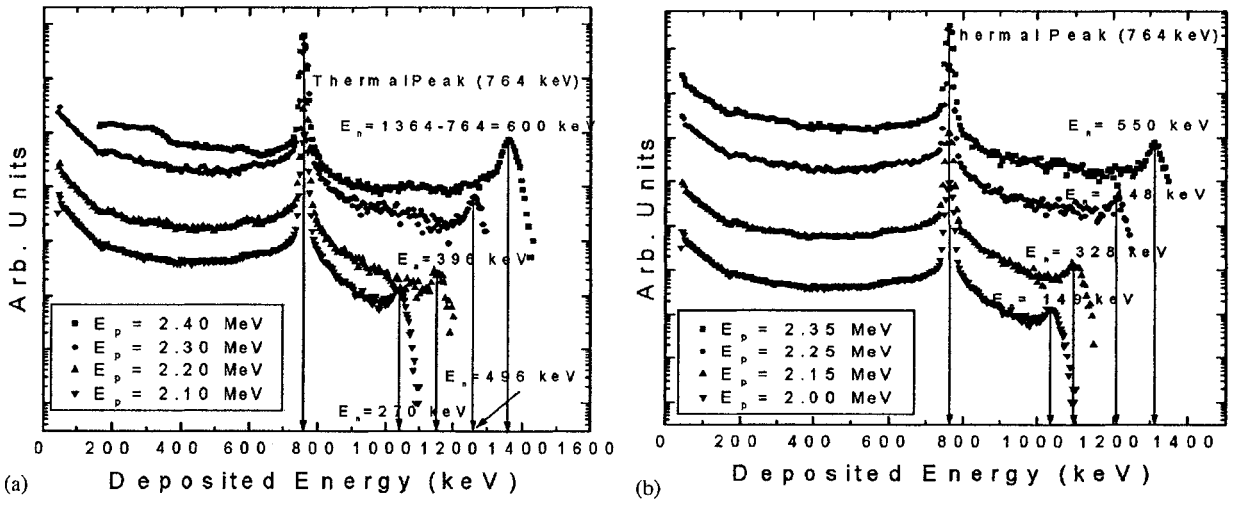

Fig. 1. Measured neutron energy spectra (150–600 keV) using ^{3}He ionization chamber for: (a) $E_p = 2.40$, 2.30, 2.20, 2.10 MeV, (b) $E_p = 2.35$, 2.25, 2.15, 2.00 MeV.

spread was about 25 keV. As demonstrated through our calculations of fluence weighted mean neutron energies summarized in Tables 3–8, the mean neutron energy depends upon the incident proton beam energy, E_p, target thickness, τ, relative lab angle between target–sample and the beam direction, θ_{lab}, and the solid angle subtended by the biological sample with the target, Ω.

Table 1
Measured neutron energies in beam direction using ^{3}He ionization chamber

Proton energy (MeV)	Neutron energy (keV)	
	This work	Endo et al.
2.00	149	110
2.05	214	—
2.10	270	—
2.15	328	—
2.20	396	370
2.25	448	—
2.30	496	—
2.35	550	—
2.40	600	570

—, No measurements have been reported at those proton energies.

The mean neutron energy shows a decreasing trend with the increase in target thickness at the same incident proton energy and target–sample geometry. This happens because the neutron energy spectrum broadens and softens with the increase in target thickness. However, increases in target thickness also result in the increase in neutron yield and hence the higher dose rate.

The unavailability of target thickness in this work made it impossible to compare our measured dose rates with either those of calculated or those reported measurements (Endo et al., 1995, 1999). However, in an earlier study for beam characterization of monoenergetic neutron fields produced at HIRRAC using a 10 μm thick ^{7}Li target, Endo et al. (1995, 1999) reported the neutron energies as 110, 370, 570 and 990 keV corresponding to incident proton beam energies of 2.0, 2.2, 2.4 and 2.8 MeV, respectively, measured at a distance of 10 cm from the target with ^{3}He gas proportional counter of same physical dimensions as used in this work. Using the provided information, the ^{3}He counter subtended an angle of $\sim 15°$ with the target. The calculated values at these proton energies except at 2.8 MeV are listed in Table 8(b). The comparison of these measured neutron energies with our calculations is presented in Table 2(b). The difference in calculated and measured mean neutron energy at $E_p = 2.00$ MeV is

Table 2

(a) Dose rates and γ-ray contaminations at 35 cm distance from the target are summarized as a function of the neutron energy. Neutron energy spread was obtained from Gaussian fitting after the subtraction of background assuming a linear function from the spectrum of ^{3}He ionization chamber. Percentage of γ-ray contaminations for thin ^{7}Li metal target at proton energies ranging from 2.0 to 2.4 MeV

E_p (MeV)	E_n (keV)	Energy spread, FWHM/E_n (%)	$\overline{yD}$ (keV/μm)	Absorbed dose (μGy/mC)			D_γ/D_n (%)
				Mixed field	Neutron dose		
					(This work)	Endo et al.	
2.40	600	4.5	71.97±1.92	82.05	80.50	7433.3	1.92
2.35	550	4.9	72.19±1.68	84.32	82.55	—	2.15
2.30	500	5.0	71.84±1.63	71.40	69.83	—	2.24
2.25	448	5.6	68.28±1.83	41.16	39.78	—	3.48
2.20	396	6.3	66.86±2.22			1501.6	
2.15	328	7.6	62.62±1.80	14.02	14.62	—	6.47
2.10	270	9.3	60.97±1.90	13.02	11.33	—	6.93
2.00	149	16.8	41.73±0.84	12.65	11.35	725	11.45

(b) Comparison of our calculated mean neutron energies and dose rates with those reported (Endo et al., 1995). C/E refers to ratio of calculated to that of experimental results

E_p (MeV)	E_n(keV)			Dose rate (μGy/min.μA)		
	Calculated	Endo et al.	C/E ratio	Calculated	Endo et al.	C/E ratio
2.8	1059	990	1.07	350	309	1.13
2.4	638	570	1.11	404	446	0.91
2.2	425	370	1.15	157	90	1.75
2.0	174	110	1.58	84	44	1.93

significantly higher than those at higher beam energies 2.2, 2.4 and 2.8 MeV. Endo et al. (1995) explicitly mentioned that the fast neutron peak at $E_p = 2.00$ MeV could not be observed in the neutron spectrum collected by using ^{3}He counter and was hidden in the thermal neutron peak. However, the authors did mention that the peak should have been observed at 0.11 MeV; the procedure for extraction of mean neutron energy from the thermal peak has not been specified clearly. The other factor, which may contribute to the difference in calculated and measured neutron energies, is the presence of an oxide layer on the lithium metal target (Aslam et al., 2003). This may be justified, as the agreement between the calculations and experiment improves with the increase in incident proton energy.

3.2. Microdosimetric measurements

Lineal energies in this study were measured in the range of 0.2–1000 keV/μm. The γ-ray contribution extending below 10 keV/μm was eliminated from the n–γ overlapping region between 1 and 10 keV/μm by subtracting a measured and scaled ^{60}Co gamma spectrum using the same simulated tissue site size (Arnold, 2000; Waker, 1995; Khaloo and Waker, 1995). The complete set of measured lineal energy spectra ranging in neutron energies from 150 to 600 keV corresponding to $E_p = 2.00$–2.40 MeV, has been presented in Fig. 2. The first six spectra ranging in neutron energies $320 < E_n < 600$ keV, have a sharp proton edge at approximately 136 keV/μm which drops to lower values. A maximum shift in the proton edge is observed in case of 150 keV neutron energy where the proton edge moved down from 136 keV/μm to about 110 keV/μm. This happened because at these neutron energies, the range of the recoil protons becomes less than 2 μm.

3.2.1. Beam quality

The *dose-mean lineal energy*, $\overline{y_D}$, estimated from lineal energy measurements can be used to compare the efficacy of neutron beams used in radiotherapy (Pignol and Slabbert, 2001; Pignol et al., 2001) and in radiobiological studies (Endo et al., 1999). The $\overline{Y_D}$ is defined

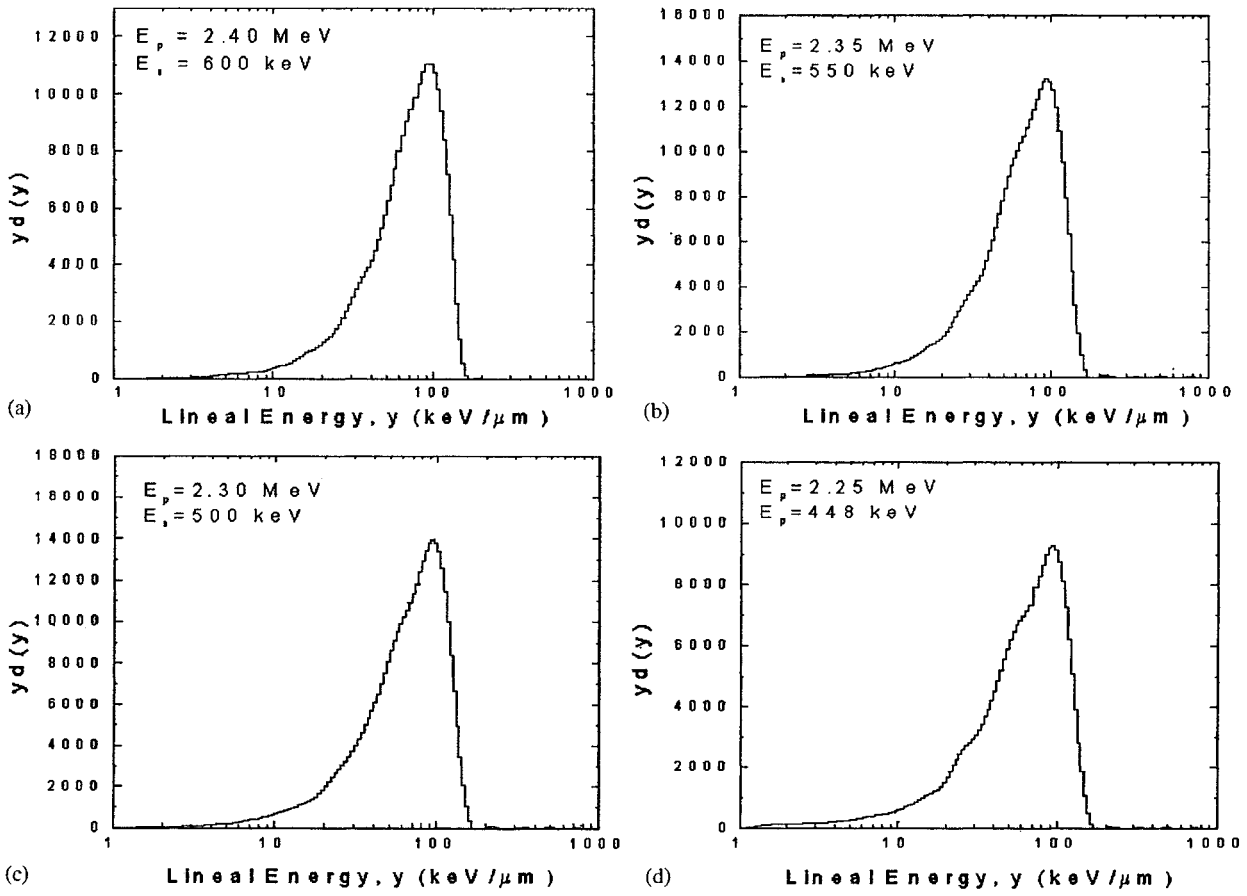

Fig. 2. Measured lineal energy distributions of monoenergetic neutrons (150–600 keV) using a 2 μm diameter simulated size for $E_p = 2.40$, 2.35, 2.30, 2.25, 2.20, 2.15, 2.10, 2.00 MeV.

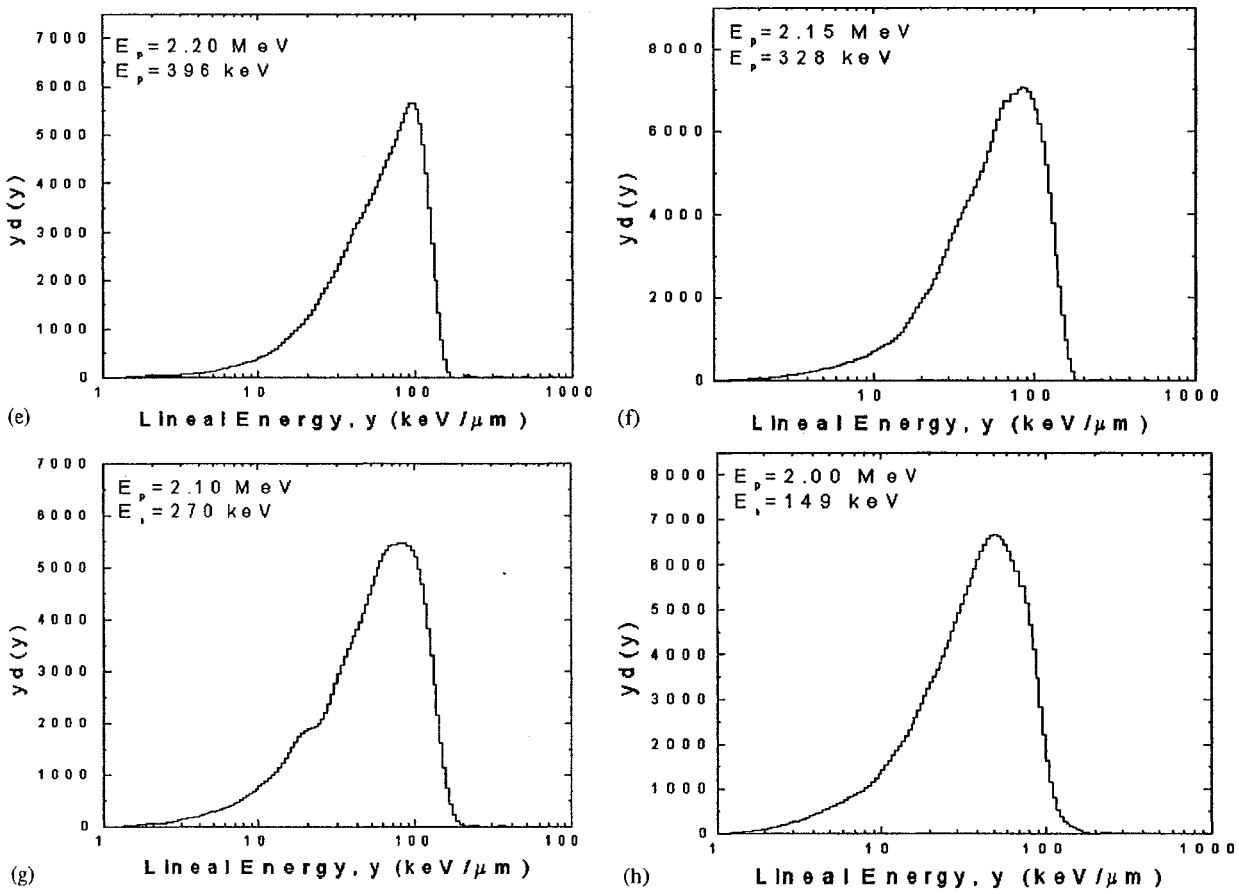

Fig. 2 (*continued*).

as (ICRU, 1983a)

$$\overline{y_D} = \frac{\int_0^\infty y d(y)\,\mathrm{d}y}{\int_0^\infty d(y)\mathrm{d}y}. \tag{12}$$

Table 2(a) gives the values of $\overline{y_D}$ obtained after the subtraction of γ-rays contribution. In agreement with other studies (Srdoc and Marino, 1996), the $\overline{y_D}$ values show no appreciable change in the energy range of 450–600 keV and a decreasing trend below this region. The decrease in the average energy deposited in the simulated site with the decreasing neutron energy is both because of the decreasing LET (the maximum proton LET is at a proton energy of about 100 keV) and the decreasing range of the recoil protons (ICRU, 1983b; Srdoc and Marino, 1996). Quantitatively, the ratio of our measured $\overline{y_D}$ value to that of Srdoc and Marino (1996) at 440 keV neutron energy is 1.065, the values agree fairly well within the experimental uncertainty.

3.2.2. Neutron dose measurements

Neutron production using ^{7}Li(p,n)^{7}Be is accompanied mainly by 478 keV inelastic γ-rays resulting from $(p,p'\gamma)$ with other low and high-energy gammas namely $(p,n'\gamma)$ and (p,γ) interactions (Aslam et al., 2002a). Measured lineal energy distributions of the mixed n – γ radiation fields at different proton beam energies were used to estimate the neutron and gamma dose rates for thin lithium targets.

The absorbed dose in the gas cavity was calculated by using the lineal energy distribution and the mean chord length for 2 μm simulated diameter as

$$D = 1.25 \times 10^{-3} \sum_i y_i f(y_i). \tag{13}$$

The results of the neutron dose rate measurements for neutron energies ranging from approximately 150–600 keV with corresponding beam energies are listed in Table 2(a). The dose rates per unit of accumulated proton charge increase with the increasing proton beam energy. However, the increase is less pronounced below 2.20 MeV beam energy and it increases sharply beyond 2.2 MeV. Above 2.35 MeV beam energy that corresponds to neutron energies of 550 and 600 keV neutron energies, the dose rates saturate. This increase in neutron dose rates with the proton beam energy is partly because of the increase in ^{7}Li(p,n)^{7}Be reaction cross-section with proton energy and it shows a resonance at around

2.25 MeV (Liskien and Paulsen, 1975). Another factor, which contributes to the increase in dose rate with the increase in proton energy, is the kerma coefficients. As the incident proton energy increases, the energy of the neutrons produced also increases. The same increasing trend is also evident in case of kerma coefficient (Wagner et al., 1985). Endo et al. has also observed an increasing trend in measured dose rates with the increase in beam energy. The maximum dose rate was reported at $E_p = 2.3$ MeV. This result is in agreement with our calculations for the target thicknesses ranging from 1 to 10 μm as shown in Tables 3–8. It is noteworthy that this maximum in neutron dose rates above 8 μm is observed in all the directions $0° \leqslant \theta \leqslant 90°$. More importantly, for proton energies ranging from 1.95 to 2.5 MeV, the maximum neutron yield and also the dose rate is obtained in the angle bin 30–45°. The yield in this bin for all proton energies we investigated is 2.5–3.5 times higher than that of 0–15° angle bin. Lee and Zhou (1999) pointed out the similar trend for thick lithium targets in neutron yields in case of proton energies in the energy range 1.89–2.00 MeV. However, this is not the case for mean neutron energies, the maximum neutron energy was observed in the case of 0–15° and a decreasing trend was observed in the range $0° \leqslant \theta \leqslant 90°$. We have also observed a linear increase in yield and dose with the increase in target thickness.

In order to validate the adopted computational procedure, we have compared the calculated dose rates with those measured ones reported in the literature (Endo et al., 1995). The paired ionization chambers 1C-17 (TE-TE chamber) and IC-17G (C–CO_2 chamber) were used to measure the neutron dose rates from HIRRAC. These measurements were performed in the beam direction at a distance of 10 cm from the target. The dimensions of the ionization chambers have not been specified there in the report. These dimensions were then directly obtained from the manufacturer's website (Far West Technology, Inc). Using the provided information, the chambers subtended an angle of $\ll 1°$ with the target. Thus, no integration was performed over the dose integrals and calculated directly using (4) with the fluence calculated as

$$\Phi(E_n, r, \theta) = \frac{1}{r^2} \frac{\mathrm{d}^2 Y(E_n, \theta)}{\mathrm{d}\Omega \, \mathrm{d}E_n}. \tag{14}$$

The results of these calculations have been summarized in Table 2(b). The calculated dose rates at 2.8 and 2.4 MeV agree fairly well with those of measured within the expected overall uncertainty involved in such experiments. However, at 2.2 and 2.0 MeV, the calculated dose rates deviate from the experimental results by approximately a factor of 2. Interestingly, the deviation is approximately of the same order as reported in literature for thick lithium targets (Yu et al., 1998;

Table 3

Angle (deg)	Proton energy (MeV)											
	1.95	2.00	2.05	2.10	2.15	2.20	2.25	2.30	2.35	2.40	2.45	2.50
(a) Integrated angular neutron yield (15 degrees step) ($\times 10^5$ n/μC); target thickness = 1 μm												
0–15	3.46	2.22	1.60	1.55	2.43	4.72	7.86	8.20	6.90	5.78	4.94	4.35
15–30	9.73	6.53	4.92	4.77	7.10	12.80	20.70	21.30	17.90	15.00	12.80	11.40
30–45	14.00	10.20	8.27	8.05	11.10	17.70	26.80	26.70	22.40	18.80	16.20	14.50
45–60	15.20	12.30	10.90	10.80	14.00	19.10	26.30	24.80	20.80	17.30	15.10	13.90
60–75	13.00	12.20	11.90	12.10	15.20	18.10	22.00	19.10	15.90	13.10	11.80	11.10
75–90	8.72	10.20	11.00	11.70	14.60	15.60	16.80	13.00	10.70	8.73	8.13	8.00
(b) Fluence weighted mean neutron energy $\overline{E_n}$(keV); target thickness = 1 μm												
0–15	156	222	282	342	399	453	509	563	616	671	723	777
15–30	140	204	264	321	377	431	483	540	592	643	698	746
30–45	113	174	231	286	340	390	444	494	545	590	642	697
45–60	80	137	190	240	290	339	388	435	481	530	578	623
60–75	51	102	148	194	239	283	328	374	416	461	502	548
75–90	29	71	112	152	191	233	271	314	351	392	431	471
(c) Integrated kerma weighted angular neutron yield (μGy cm^2/μC); target thickness = 1 μm												
0–15	3.2	2.5	2.1	2.3	4.0	8.3	14.9	16.5	14.6	12.9	11.5	10.6
15–30	8.3	7.0	6.2	6.8	11.2	21.9	38.0	41.7	37.1	32.7	29.2	27.1
30–45	10.5	9.9	9.6	10.6	16.4	28.4	46.4	49.5	44.2	38.9	35.2	33.1
45–60	9.5	10.4	11.2	12.8	18.7	28.2	42.1	42.7	38.0	33.5	30.9	29.7
60–75	6.4	8.6	10.5	12.6	17.9	23.8	31.7	29.9	26.6	23.3	22.1	22.0
75–90	3.4	5.9	8.2	10.5	15.0	18.1	21.5	18.2	16.1	14.1	13.9	14.4

Table 4

Angle (deg)	Proton energy (MeV)											
	1.95	2.00	2.05	2.10	2.15	2.20	2.25	2.30	2.35	2.40	2.45	2.50
(a) Integrated angular neutron yield (15 degrees step) ($\times 10^5$ n/μC); target thickness = 2 μm												
0–15	7.22	4.57	3.25	3.07	4.67	9.03	15.40	16.50	14.00	11.70	9.97	8.75
15–30	20.30	13.40	10.00	9.44	13.70	24.60	40.60	42.90	36.30	30.30	25.90	22.90
30–45	29.20	20.70	16.70	16.00	21.60	34.20	52.60	53.90	45.50	37.90	32.60	29.20
45–60	31.50	24.80	22.00	21.40	27.40	37.40	51.80	50.10	42.10	35.00	30.50	27.90
60–75	26.60	24.40	23.90	24.10	29.90	35.80	43.60	38.80	32.20	26.50	23.60	22.30
75–90	17.30	20.10	22.10	23.30	28.70	31.30	33.50	26.70	21.60	17.70	16.30	16.00
(b) Fluence weighted mean neutron energy $\overline{E_n}$(keV); target thickness = 2 μm												
0–15	151	217	279	336	394	451	505	560	612	667	719	773
15–30	135	199	260	317	374	427	483	534	587	640	691	742
30–45	108	170	228	281	336	389	439	490	541	591	641	692
45–60	76	133	186	237	286	337	386	433	480	526	574	620
60–75	47	98	145	190	235	279	326	371	413	457	500	543
75–90	26	68	108	148	189	229	270	309	350	388	428	469
(c) Integrated kerma weighted angular neutron yield (μGy cm^2/μC); target thickness = 2 μm												
0–15	6.4	5.1	4.2	4.5	7.6	15.8	29.0	33.1	29.6	26.0	23.2	21.2
15–30	16.9	14.2	12.4	13.3	21.4	41.9	74.3	83.6	74.8	65.8	58.8	54.3
30–45	21.3	19.8	19.1	20.9	31.6	54.7	91.0	99.6	89.2	78.5	70.9	66.3
45–60	19.0	20.5	22.2	25.1	36.3	54.7	82.6	86.0	76.8	67.5	62.0	59.4
60–75	12.6	16.9	20.8	24.7	35.0	46.8	62.6	60.4	53.6	47.0	44.2	44.0
75–90	6.4	11.4	16.2	20.6	29.3	36.0	42.7	37.1	32.4	28.3	27.7	28.8

Table 5

Angle (deg)	Proton energy (MeV)											
	1.95	2.00	2.05	2.10	2.15	2.20	2.25	2.30	2.35	2.40	2.45	2.50
(a) Integrated angular neutron yield (15 degrees step) ($\times 10^5$ n/μC); target thickness = 4 μm												
0–15	15.90	9.71	6.78	6.04	8.67	16.60	29.40	33.30	28.60	23.90	20.30	17.70
15–30	44.70	28.10	20.70	18.60	25.60	45.50	77.40	86.60	74.30	61.90	52.80	46.40
30–45	64.10	43.00	34.50	31.60	41.00	64.30	101.00	109.00	93.10	77.40	66.40	59.10
45–60	68.60	50.60	44.70	42.40	52.50	71.80	100.00	102.00	86.30	71.50	61.80	56.30
60–75	56.00	48.70	48.20	47.60	57.70	70.20	85.50	79.90	65.80	54.30	47.70	44.90
75–90	32.80	39.20	43.90	45.90	55.60	62.50	66.50	55.60	44.10	36.20	32.60	32.10
(b) Fluence weighted mean neutron energy $\overline{E_n}$(keV); target thickness = 4 μm												
0–15	138	207	270	329	388	442	497	553	608	661	714	768
15–30	123	191	251	310	367	422	475	529	581	633	686	737
30–45	97	161	218	274	327	381	433	484	535	585	634	685
45–60	65	125	179	230	280	330	380	428	474	522	570	615
60–75	38	91	138	184	231	275	320	364	409	451	495	539
75–90	19	62	103	143	183	224	265	304	345	384	423	464
(c) Integrated kerma weighted angular neutron yield (μGy cm^2/μC); target thickness = 4 μm												
0–15	13.5	10.5	8.6	8.7	13.9	28.8	54.8	66.2	60.3	52.8	47.0	42.8
15–30	35.3	28.9	25.2	25.9	39.6	76.7	140.0	168.0	152.0	134.0	119.0	109.0
30–45	44.0	39.8	38.4	40.7	59.1	102.0	173.0	200.0	182.0	159.0	143.0	133.0
45–60	38.3	40.4	44.1	48.9	68.5	104.0	158.0	174.0	156.0	137.0	125.0	119.0
60–75	24.1	32.4	40.7	47.9	66.6	90.6	121.0	123.0	109.0	95.5	88.8	87.9
75–90	11.0	21.3	31.2	39.6	55.9	70.9	83.8	76.5	65.6	57.5	55.3	57.5

Table 6

Angle (deg)	Proton energy (MeV)											
	1.95	2.00	2.05	2.10	2.15	2.20	2.25	2.30	2.35	2.40	2.45	2.50
(a) Integrated angular neutron yield (15 degrees step) ($\times 10^6$ n/μC); target thickness = 6 μm												
0–15	6.83	1.56	1.07	0.90	1.22	2.28	4.15	5.01	4.41	3.67	3.11	2.70
15–30	16.40	4.48	3.24	2.79	3.63	6.33	11.00	13.00	11.40	9.50	8.07	7.06
30–45	17.00	6.73	5.31	4.74	5.86	9.09	14.40	16.50	14.30	11.90	10.10	8.97
45–60	13.40	7.77	6.83	6.36	7.57	10.30	14.50	15.60	13.30	11.00	9.43	8.53
60–75	7.69	7.32	7.26	7.11	8.37	10.30	12.50	12.30	10.10	8.34	7.24	6.78
75–90	3.49	5.74	6.52	6.81	8.09	9.34	9.86	8.70	6.78	5.58	4.93	4.83
(b) Fluence weighted mean neutron energy $\overline{E_n}$(keV); target thickness = 6 μm												
0–15	80	196	260	321	380	438	492	545	599	651	707	759
15–30	74	180	242	302	358	415	468	523	575	626	679	731
30–45	66	152	211	266	321	374	427	477	529	577	631	679
45–60	47	117	171	222	273	325	372	419	466	515	562	608
60–75	31	83	131	177	223	270	314	359	403	446	490	532
75–90	18	56	97	138	178	218	260	299	339	378	420	460
(c) Integrated kerma weighted angular neutron yield (μGy cm^2/μC); target thickness = 6 μm												
0–15	41.3	16.3	13.3	12.9	19.3	39.4	76.8	98.7	92.0	80.4	71.5	64.8
15–30	95.7	44.4	38.5	38.2	55.3	106.0	198.0	250.0	233.0	204.0	182.0	166.0
30–45	95.4	60.1	58.0	59.9	83.4	142.0	245.0	300.0	277.0	243.0	218.0	202.0
45–60	63.2	59.5	65.6	71.8	97.4	148.0	226.0	262.0	238.0	209.0	189.0	180.0
60–75	30.5	46.4	59.6	70.0	95.0	131.0	175.0	187.0	165.0	146.0	134.0	132.0
75–90	11.5	29.6	44.9	57.4	79.8	104.0	123.0	118.0	99.7	87.9	82.7	85.7

Table 7

Angle (deg)	Proton energy (MeV)											
	1.95	2.00	2.05	2.10	2.15	2.20	2.25	2.30	2.35	2.40	2.45	2.50
(a) Integrated angular neutron yield (15 degrees step) ($\times 10^6$ n/μC); target thickness = 8 μm												
0–15	6.84	2.23	1.5	1.22	1.54	2.81	5.18	6.63	6.02	4.99	4.23	3.66
15–30	16.3	6.37	4.52	3.76	4.61	7.85	13.8	17.3	15.6	13	11	9.55
30–45	17.7	9.47	7.32	6.36	7.5	11.4	18.2	22	19.5	16.2	13.8	12.1
45–60	13.4	10.7	9.26	8.51	9.76	13.3	18.5	20.9	18.1	15	12.8	11.5
60–75	7.69	9.89	9.69	9.48	10.8	13.4	16.2	16.7	13.8	11.4	9.79	9.1
75–90	3.49	7.49	8.58	9.02	10.5	12.3	13	12	9.27	7.64	6.63	6.45
(b) Fluence weighted mean neutron energy $\overline{E_n}$(keV); target thickness = 8 μm												
0–15	81	186	250	311	373	431	486	538	591	647	700	751
15–30	75	170	232	293	351	409	462	514	567	618	671	725
30–45	63	141	201	259	315	369	420	468	523	572	621	674
45–60	47	108	163	215	267	317	366	414	461	509	555	603
60–75	31	76	125	172	219	264	309	352	396	441	484	527
75–90	18	50	91	132	173	213	254	293	334	373	413	454
(c) Integrated kerma weighted angular neutron yield (μGy cm^2/μC); target thickness = 8 μm												
0–15	42.0	22.5	18.2	17.0	24.0	48.0	95.2	130.0	125.0	109.0	96.8	87.4
15–30	96.1	60.9	52.4	50.5	69.3	130.0	245.0	330.0	314.0	276.0	245.0	223.0
30–45	95.6	80.9	77.7	79.1	105.0	177.0	306.0	396.0	375.0	329.0	294.0	271.0
45–60	63.2	78.4	86.5	94.3	124.0	187.0	285.0	348.0	322.0	284.0	255.0	241.0
60–75	30.5	59.3	77.0	91.3	121.0	169.0	225.0	252.0	224.0	198.0	180.0	176.0
75–90	11.5	36.7	57.2	74.2	101.0	135.0	160.0	161.0	135.0	119.0	110.0	114.0

Table 8

Angle (deg)	Proton energy (MeV)											
	1.95	2.00	2.05	2.100	2.15	2.20	2.25	2.30	2.35	2.40	2.45	2.50
(a) Integrated angular neutron yield (15 degrees step) ($\times 10^6$ n/μC); target thickness = 10 μm												
0–15	7.03	3.02	1.98	1.55	1.84	3.25	6.04	8.15	7.66	6.40	5.40	4.66
15–30	16.40	8.61	5.92	4.79	5.54	9.16	16.10	21.30	19.90	16.60	14.00	12.10
30–45	17.70	12.70	9.47	8.08	9.08	13.50	21.50	27.20	24.90	20.80	17.60	15.40
45–60	13.40	14.20	11.80	10.70	11.90	15.90	22.10	26.00	23.10	19.20	16.30	14.50
60–75	7.69	12.70	12.10	11.90	13.20	16.40	19.70	21.00	17.70	14.60	12.50	11.50
75–90	3.49	9.16	10.50	11.20	12.80	15.10	16.10	15.40	12.00	9.80	8.40	8.08
(b) Fluence weighted mean neutron energy $\overline{E_n}$(keV); target thickness = 10 μm												
0–15	79	174	240	305	366	425	480	531	585	638	693	745
15–30	74	158	223	284	345	403	458	507	558	614	666	720
30–45	63	130	192	250	308	363	415	463	514	563	614	662
45–60	47	97	155	208	261	312	362	408	455	503	550	599
60–75	31	67	118	165	213	257	304	347	391	436	477	521
75–90	18	44	86	127	168	208	249	286	328	368	408	449
(c) Integrated kerma weighted angular neutron yield (μGy cm^2/μC); target thickness = 10 μm												
0–15	42.7	29.3	23.5	21.3	28.4	55.1	110.0	158.0	158.0	139.0	123.0	110.0
15–30	96.3	78.5	66.8	63.1	82.4	150.0	286.0	402.0	399.0	351.0	311.0	282.0
30–45	95.6	103.0	97.6	98.3	126.0	207.0	359.0	485.0	474.0	419.0	373.0	342.0
45–60	63.2	97.5	107.0	116.0	148.0	222.0	339.0	430.0	408.0	361.0	322.0	303.0
60–75	30.5	71.4	93.2	112.0	145.0	203.0	270.0	314.0	284.0	251.0	227.0	220.0
75–90	11.5	42.2	67.8	90.0	121.0	164.0	195.0	204.0	172.0	152.0	139.0	141.0

Bleuel et al., 1999; Aslam et al., 2003). Possible reasons of such deviations may be the presence of oxides on lithium target, detector calibration or the detector response at low neutron energies (Aslam et al., 2003).

In order to compare the dose rates of the monoenergetic neutron fields described in this work with those of Endo et al. (1995, 1999) under similar experimental conditions, the dose rates were corrected for the difference in distance from the target by utilizing the inverse square variation of fluence rate with the distance. Endo et al. measured dose rates at a distance of 10 cm from the target while we performed our measurements at 35 cm away from the target in the beam direction. The maximum neutron dose rate achieved in this work is about 0.5 mGy/min at proton energy of 2.35 MeV with a beam current of 100 μA. Dose rates up to 6 mGy/min can be achieved by decreasing the distance of detector from 35 to 10 cm. Dose rates may further be improved by approximately a factor 3 when irradiated in the direction $30° \leqslant \theta \leqslant 45°$. Use of thicker target than the one used in this work will also increase the dose rates. Increasing the target thickness by factor of ~10, and exposing the samples in the direction $30° \leqslant \theta \leqslant 45°$ instead of beam direction by using 100 μA beam current, dose rates up to ~200 mGy/min may be achieved. This maximum dose rate is smaller by a factor 2 than that of Endo et al. achieved at 2.3 MeV using 1 mA. By decreasing the neutron source and sample distance (SSD), a further increase in the dose rate at the same beam current can be obtained. However, the selection of SSD in a particular situation depends upon the required dose uniformity conditions.

3.2.3. *Gamma dose measurements*

The measured values of γ-ray contamination for lithium metal target for proton energies ranging from 2.00 to 2.40 MeV are listed in Table 2(a). Contamination of the γ-rays decrease with the increase in proton energy, 12% at 2.00 MeV and reduced to 2% at 2.4 MeV proton energies. Endo et al. have mentioned the γ-ray contamination below 2.4 MeV proton energy. At 2.4 MeV proton energy, the γ-ray contamination was found to be about half of what has been reported in literature (Endo et al., 1995). One of the possible reasons of this decrease in γ-ray contamination comes from the difference in target holder (High Z material chosen to minimize neutron scattering) construction material because it attenuates the gamma flux resulting from the target while passing through the target backing and target holder. In our case, there was a target backing made of copper of around 1 cm thickness. The gamma dose is mainly contributed by the 478 keV inelastic γ-rays resulting from $(p,p'\gamma)$ with other low and high-energy gammas namely $(p,n'\gamma)$ and (p,γ) interactions. By taking into account the attenuation of 478 keV γ-rays in target backing, the gamma contamination comes out to

be around 4.5%. However, Endo et al. has not mentioned the target backing thickness. A second possible reason for the difference in γ-ray contamination is because of the difference in target thickness itself. We have not quantified such a difference resulting from the difference in target thickness because of the unavailability of differential cross-section for $(p,p'\gamma)$.

The ^{7}LiF target is easier to handle as compared to the ^{7}Li target because of its stable nature as compared to ^{7}Li which upon exposure to air quickly oxidizes and forms oxides on the surface of target (Aslam et al., 2003). The γ-ray contaminations for the ^{7}LiF target are high. These γ-rays mainly are induced by the $^{19}F(p,\alpha\gamma)^{16}O$ reaction, of which γ-ray energies are 6.14, 6.92 and 7.12 MeV (Fessler et al., 2000). Contamination of the γ-ray was about 64% when using ^{7}LiF as a target at proton energy of 2.00 MeV in comparison to lithium metal target where the contamination was around 12% at the same beam energy (both targets of approximately of same thickness). In radiobiological or radiochemical experiments, where a condition of low γ-ray contamination of about 5% or less is required, ^{7}Li is used (Endo et al., 1995). The ^{7}LiF is used when γ-ray contamination is not effective in radiobiological studies. However, for same energy thickness of ^{7}Li and ^{7}LiF targets, the dose rates of ^{7}LiF targets will be lower by approximately a factor of 4 because of lower neutron yeild (Aslam et al., 2003).

3.3. Thin target dose calculations

In order to facilitate the research activities in future keeping in view the demands of doses and dose rates of varying neutron energies, the lengthy calculations are being summarized in Tables 3–8. The selection of neutron energy and dose rate depends upon the phenomenon to be studied. These tables provide the facility of optimal selection of neutron energy and dose rate using the proper choice of beam energy, target thickness, target–sample distance, and direction relative to the beam. The use of these tables has been demonstrated through a practical example in the following paragraph.

Dytlewski et al. (1990) reported the development of a charged particle accelerator based monoenergetic neutron source for radiobiological studies using $D(d,n)^{3}$He reaction in the deuteron beam energy range $1 \leqslant E_d \leqslant 10$ MeV. A circular sample of 1 cm diameter at a distance of 1 cm from the target received the maximum dose rate of 1600 mGy/min using $E_d = 2.5$ MeV ($E_n = 5.4$ MeV) with a beam current of 30 μA. A similar dose rate can be achieved using thin lithium targets under similar conditions. For instance, a circular sample of 1 cm diameter at a distance of 1 cm from a 10-μm thick lithium metal target, subtending an angle of $\sim 26°$, the dose rates inferred from Table 8 can be achieved as 1711 mGy/min using $E_p = 2.30$ MeV ($E_n = 514$ keV) for a beam current of 40 μA while irradiating in the beam direction ($0° \leqslant \theta_{lab} \leqslant 30°$). Approximately, the same dose rate in the same target–sample geometry can be achieved while moving the sample in the direction of $15° \leqslant \theta_{lab} \leqslant 45°$ relative to beam using $E_p = 2.30$ MeV($E_n = 482$ keV) with a beam current of 25 μA.

4. Conclusions

We found that the McMaster University 3 MV Van De Graaff Accelerator can produce small energy spread neutrons and at sufficient dose rates for use in radiobiology studies with moderate beam current. We have constructed the neutron irradiation system with small neutron energy spread, $\Delta E/E < 5\%$ in the energy region from 150 to 600 keV system at a moderate-dose rate up to 20 mGy/min. In order to increase the use of the facility besides from low-dose irradiations, high-dose rates up to 200 mGy/min may be achieved by constructing thicker targets within 10% resolution.

References

Allen, D.A., Benyon, T.D., 1995. A design study for an accelerator-based epithermal neutron beam for BNCT. Phys. Med. Biol. 40, 807–821.

Arnold, M., 2000. Development of an accelerator based system for in vivo neutron activation analysis measurements of manganese in humans. Ph.D. Thesis, McMaster University, Hamilton, ON, Canada.

Arnold, M.L., McNeill, F.E., Prestwich, W.V., Chettle, D.R., 2000. System design for in-vivo neutron activation analysis measurements of manganese in the human brain: based on Monte Carlo modeling. Appl. Radiat. Isot. 53, 651–656.

Aslam, Prestwich, W.V., McNeill, F.E., 2002. Thin target ^{7}Li(p, p'γ)^{7}Li inelastic gamma ray yield measurements. J. Radioanal. Nucl. Chem. 254(3), 533–544.

Aslam, Prestwich, W.V., McNeill, F.E., 2003. Lithium target performance evaluation using gamma spectroscopy. Appl. Radiat. Isot. 58(3), 321–331.

Attix, F.H., 1986. Introduction to Radiological Physics and Radiation Dosimetry. Wiley-Interscience Publication, New York.

Bayanov, B.F., Belov, V.P., Bender, E.D., Bokhovko, M.V., Dimov, G.I., Kononov, V.N., Kononov, O.E., Kuksanov, N.K., Palchikov, V.E., Pivovarov, V.A., Salimov, R.A., Silvestrov, G.I., Skrinsky, A.N., Soloviov, N.A., Taskaev, S.Yu., 1998. Accelerator-based neutron source for the neutron-capture and fast neutron therapy at hospital. Nucl. Instrum. Methods Phys. Res. A 413 (2–3), 397–426.

Bleuel, D.L., Chu, W.T., Donahue, R.J., Ludewigt, B.A., McDonald, R.J., Smith, A.R., Stone, N.A., Vujic, J., 1999. Initial experimental verification of the neutron beam modeling for the LBNL BNCT facility, in application of accelerators in research and industry. Proceedings of the

Fifteenth International Conference, Denton, TX, November 4–7, 1998; AIP Conf. Proc. 475 (Part Two), 1050–1055.

Dytlewski, N., Croal, A., Cohen, D., Katsaros, A., Lavin, M., Singh, S., 1990. A monoenergetic neutron facility for biological irradiations. Nucl. Instrum. Methods Phys. Res. A 288, 641–648.

Endo, S., Hoshi, M., Tauchi, H., Takeoka, S., Kitagawa, K., Suga, S., Maeda, N., Komatsu, K., Sawada, S., Iwamoto, E., Sakamoto, S., Takeyama, K., Omura, M., 1995. Neutron generator at Hiroshima University for use in radiobiology study. J. Radiat. Res. (Tokyo) 36 (2), 94–102.

Endo, S., Hoshi, M., Takada, J., Tauchi, H., Matsuura, S., Takeoka, S., Kitagawa, K., Suga, S., Komatsu, K., 1999. Neutron generator (HIRRAC) and dosimetry study. J. Radiat. Res. (Tokyo) 40 (Suppl), 14–20.

Fessler, A., Massey, T.N., Micklich, B.J., Smith, D.L., 2000. Thick target photon yields and angular distribution for the $^{19}F(p, \alpha\gamma)^{16}O$ source reaction at the incident proton energies between 1.5 and 4.0 MeV. Nucl. Instrum. Methods Phys. Res. A 450, 353–359.

Gierga, D.P., Yanch, J.C., Shefer, R.E., 2000a. An investigation of the feasibility of gadolinium for neutron capture synovectomy. Med. Phys. 27 (7), 1685–1692.

Gierga, D.P., Yanch, J.C., Shefer, R.E., 2000b. Development and construction of a neutron beam line for accelerator-based boron neutron capture synovectomy. Med. Phys. 27 (1), 203–214.

ICRU, 1983a. International Commission on Radiation Units and Measurements Microdosimetry. ICRU: Report 36, Bethesda, MD.

ICRU, 1983b. International Commission on Radiation Units and Measurements Stopping Powers and Ranges for Protons and Alpha Particles. ICRU: Report 49, Bethesda, MD.

Janni, J.F., 1982. Proton range-energy Tables, 1 keV–10 GeV. At. Data Nucl. Data Tables 27, 147.

Khaloo, R., Waker, A.J., 1995. An evaluation of hydrogen as a TEPC counting gas in radiation protection microdosimetry. Radiat. Prot. Dosim. 58 (3), 185–191.

Kononov, V.N., Poletaev, E.D., Yurlov, B.D., 1977. Absoulte yield and spectrum of neutrons from the $^{7}Li(p, n)^{7}Be$. At. Energ. 43, 947–949.

Lee, C.L., Zhou, X.L., 1999. Thick target neutron yields for the $^{7}Li(p,n)^{7}Be$ reaction near threshold. Nucl. Instrum. Methods Phys. Res. B 152, 1–11.

Liskien, H., Paulsen, A., 1975. Neutron production cross-sections and energies for the reactions $^{7}Li(p,n)^{7}Be$ and $^{7}Li(p,n)^{7}Be^{*}$. At. Data Nucl. Data Tables 15, 57.

Magagula, T.K., Watterson, J.W., 1998. The excitation of isomeric states by accelerator neutrons from the $^{7}Li(p,n)^{7}Be$ reaction and their application in selective activation analysis. Nucl. Instrum. Methods Phys. Res. B 139, 293–297.

Meadows, J.W., 1977. Determination of the Energy Scale for Neutron Cross-section Measurements Employing a Monoenergetic Accelerator, ANL/TDM-25.

Palerme, S., 1993. Pilot Studies for In-Vivo Bone Aluminum Measurements. MSc Thesis, McMaster University, Hamilton, ON, Canada.

Pejović-Milić, A., 1998. An accelerator-based in-vivo measurement of aluminum in human bone by neutron activation analysis, MSc Thesis, McMaster University, Hamilton, ON, Canada.

Pejović-Milić, A., McNeill, F.E., Prestwitch, W.V., Waker, A.J., Chettle, D.R., 1998. Development of an accelerator-based determination of aluminum burden in peripheral bone by neutron activation analysis. Appl. Radiat. Isot. 49 No. 5/6, 717–719.

Pejović-Milić, A., Arnold, M.L., McNeill, F.E., Chettle, D.R., 2000. Monte Carlo design study for in-vivo bone aluminum measurement using a low energy accelerator beam. Appl. Radiat. Isot. 53, 657–664.

Pejović-Milić, A., 2001. In-vivo measurement of some trace elements in human bone. Ph.D. Thesis, McMaster University, Hamilton, ON, Canada.

Pignol, J.P., Slabbert, J., 2001. Recoil proton, alpha particle, and heavy ion impacts on microdosimetry and RBE of fast neutrons: analysis of kerma spectra calculated by Monte Carlo simulation. Can. J. Physiol. Pharmacol. 79 (2), 189–195.

Pignol, J.P., Cuendet, P., Brassart, N., Fares, G., Colomb, F., M'Bake Diop, C., Sabattier, R., Hachem, A., Prevot, G., 1998. Combined use of FLUKA and MCNP-4A for Monte Carlo simulation of the dosimetry of ^{10}B neutron capture enhancement of fast neutron irradiations. Med. Phys. 25 (60), 885–891.

Pignol, J.P., Slabbert, J., Binns, P., 2001. Monte Carlo simulation of fast neutron spectra: mean lineal energy estimation with an effectiveness function and correlation to RBE. Int. J. Radiat. Oncol. Biol. Phys. 49 (1), 251–260.

Powell, J.A., Ludewig, H., Todosow, M., Reich, M., 1999. Target and filter concepts for accelerator-driven boron neutron capture therapy applications. Nucl. Tech. 125, 104–115.

Press, W.H., Teukolsky, S.A., Vetterling, W.T., Flannery, B.P., 1992. Numerical Recipes in Fortran 77: The Art of Scientific Computing, 2nd Edition, Vol. 1 of Fortran Numerical Recipes. Cambridge University Press, Cambridge.

Ritchie, A.I.M., 1976. Neutron yields and energy spectra from thick target Li(p, n) source. J Phys. D: Appl. Phys. 9, 15–26.

Schmid, E., Regulla, D., Guldbakke, S., Schlegel, D., Bauchinger, M., 2000. The effectiveness of monoenergetic neutrons at 565 keV in producing dicentric chromosomes in human lymphocytes at low doses. Radiat. Res. 154, 307–312.

Schmid, E., Regulla, D., Guldbakke, S., Schlegel, D., Roos, M., 2002. Relative biological effectiveness of 144 KeV neutrons in producing dicentric chromosomes in human lymphocytes compared with ^{60}Co gamma rays under head-to-head conditions. Radiat. Res. 157 (4), 453–460.

Srdoc, D., Marino, S.A., 1996. Microdosimetry of monoenergetic neutrons. Radiat. Res. 146 (4), 466–474.

Wagner, S.R., Grosswendt, B., Harvey, J.R., Mill, A.J., Selbach, H.J., Siebert, B.R.L., 1985. Unified conversion functions for the ICRU operational radiation protection quantities. Radiat. Prot. Dosim. 12 (2), 231–235.

Waker, A.J., 1995. Principles of experimental microdosimetry. Radiat. Prot. Dosim. 61 (4), 297–308.

Wang, C.K.C., Blue, T.E., Gahbauer, R., 1985. A neutronic study of an accelerator-based neutron irradiation facility

for boron neutron capture therapy. Nucl. Tech. 84 (1), 93–107.

Yanch, J.C., Zhou, X.L., Shefer, R.E., Klinkowstein, R.E., 1992. Accelerator-based epithermal neutron beam design for neutron capture therapy. Med. Phys. 19 (3), 709–721.

Yu, W., Yue, G., Han, X., Chen, J., Tian, B., 1998,. Measurement of the neutron yields from $^{7}Li(p,n)^{7}Be$ reaction (Thick Target) with incident energies from 1.885 to 2.0 MeV. Med. Phys. 25 (7), 1222–1224.

Zhou, X.L., Lee, C., 1997a. Analysis of epithermal neutron production by near-threshold (p,n) reactions. Appl. Radiat. Isot. 48, 1571–1575.

Zhou, X.L., Lee, C., 1997b. Lithium compounds as targets for (p,n) reactions. Appl. Radiat. Isot. 48, 1493–1496.

Chapter VIII

Summary and Concluding Remarks

The most important results of this work are summarized in this chapter. This work consists of three main parts. The first part is related to the optimization of operating conditions at the 3 MV KN Van de Graaff accelerator at McMaster University Accelerator Laboratory to produce neutrons via $^{7}Li(p, n)^{7}Be$ reaction for *in-vivo* neutron activation analysis (IVNAA). The second part relates to the use of a TEPC for investigation of the neutron quality factor and neutron and gamma dose measurements in the hand irradiation facility for IVNAA measurement of potentially toxic trace elements. The last part of the report describes the feasibility of the use of the facility for applications in radiobiological and radiochemical research.

8.1 Development of Neutron Source for Low Energy Accelerator Based *In-vivo* Measurements

This portion of the work is discussed in chapters II and III. This section describes the optimization of operating conditions at the McMaster University 3 MV KN Van de Graaf accelerator to produce neutrons via the $^{7}Li(p, n)^{7}Be$ reaction for IVNAA. It was observed that inefficient target cooling and the presence of oxides layer on the target surface resulted in lower measured yields than calculated yields. The improvement in target cooling was achieved by using the reduced target thickness, reduction in target backing thickness and wider coolant channel widths. The oxides layers formed on the target surface due to exposure of target to air was avoided by preparing targets either in a completely inert environment or by vapor deposition.

Although the performance of a lithium target for neutron production had been optimized by measuring the ^{7}Be activity produced as a result of (p, n) interaction, the online measurement of inelastic γ ray yields resulting from $^{7}Li(p, p'\gamma)^{7}Li$ interaction below the (p, n) threshold could provide a much simpler way for such optimization. However, despite its importance, relatively few measurements either for differential cross section or thick target yields are available, and these are largely inconsistent. Thus thin target angular distributions of

inelastic gamma ray yields resulting from $^{7}Li(p, p'\gamma)^{7}Li$ interaction have been measured for incident proton energies between 1.0 and 1.8 MeV. The results for angular distribution provide evidence for an anisotropic nature of the radiation as compared to the presumed isotropic nature. Interestingly, not only did our measured total cross-section closely match the reported measurements based on the assumption of the isotropic nature of radiation but also the differential cross-section at 90° relative to beam direction also matches the reported measurements. Although neither the reported absolute nor normalized thick target yields (at θ_{lab}=55° and 90°) agree with each other (assuming isotropic distribution), our normalized thick target yields calculated by using thin target yields agree to the respective yields.

8.2 Dosimetry for Low Energy Accelerator Based *In-Vivo* Measurements

The second part of thesis is composed of three chapters namely IV, V, and VI. The use of a tissue equivalent proportional counter (TEPC) filled with propane based tissue equivalent gas simulating 2 μm diameter tissue sphere has been investigated to estimate the neutron quality factors, neutron and gamma absorbed doses and dose equivalents of the neutron fields used in *in-vivo* neutron activation measurements at 3 MV Van de Graaff accelerator.

The LET information required to calculate the quality factors below 300 keV neutron energy can not be retrieved from lineal energy measurements made by a TEPC simulating 2 μm TE diameter either by using the approximation $L = y$, or the Rossi's transformation algorithm. Thus the counter fails to provide a flat R_Q response based on the definition of *Q(L)* provided in ICRP 60 and shows a sharp drop below 200 keV neutron energy. This decreasing trend in quality factor with decreasing neutron energy is much more pronounced than that of similar TEPC measurements reported using the definition of *Q(L)* for ICRP 26. A neutron quality factor algorithm has been developed which utilizes the average of the measured lineal energy dose distributions to provide a better estimate of the effective quality factors based on ICRP 60 for low energy accelerator based *in-vivo* neutron activation measurements. The algorithm does not need any transformation of the measured lineal energy dose distribution, *d(y)*, into an LET dose distribution, *d(L)*.

The algorithm overestimates the quality factors in the irradiation facility. The overestimation of the measured neutron quality factors always lies within the estimated experimental uncertainty at a beam energy of E_p = 2.25 MeV. However, the overestimation in the measured value in the center of the irradiation facility at beam energy of E_p = 2.00 MeV was 30% which increased further to approximately 45% for off-axis measurements. The

overestimation is shown to be correlated with the relative fluence (to total fluence) of low energy neutrons (< 5 keV) at the point of measurement in hand irradiation facility.

Using the calculated angular and neutrons energy distribution for different incident proton energies for $^{7}Li(p, n)^{7}Be$, experimental conditions used for *in-vivo* measurement of aluminum and manganese in the hand have been simulated using the Monte Carlo radiation transport code MCNP4B. The Monte Carlo modeling of the designed hand irradiation facility was validated by comparing the measured and calculated thermal fluence non-uniformity. The calculated dose heterogeneity defined as D_{max}/D_{min} was also in fairly good agreement (~10%) with the measured dose heterogeneity at all the beam energies employed for hand irradiation at MAL (Arnold, 2000; Arnold *et al.*, 2002; Aslam *et al.*, 2003d). A method based on the Monte Carlo simulation of the irradiation facility was described to calculate the quality factors of the neutron beams encountered in IVNAA of the hand at MAL.

The non-uniformity of the incident neutron spectrum on the phantom surface resulted in a non-uniformity of activation in the transverse and longitudinal directions as well as the dose to the hand. It was deemed essential to determine the average radiation dose received to the patient's hand because the dose heterogeneity defined as D_{max}/D_{min} is 3 for E_p = 2.25 MeV and 5 for E_p = 2.00 MeV on the phantom surface. The computational method described in this work augments the dose measurements carried out using ½" diameter TEPC (Arnold *et al.*, 2002) for the calculation of average dose equivalent received to the patient's hand. Employing the neutron and gamma doses measured along the center of the hand phantom and using the dose averaging factor and the neutron quality factor calculated for the appropriate size phantom, the average dose equivalent delivered to the hand phantom can be determined. This method which is the modified form of the method presented in Paper IV employs the Monte Carlo simulation of hand irradiation facility using MCNP4B to calculate the dose averaging factors. Based on the estimated doses delivered to the patient hand, the proposed irradiation procedure for the IVNAA measurement of manganese in human hands (Med Phys 29(11) (2002) 2718) with normal (1 ppm) and elevated manganese content can be carried out with a reasonably low dose of 31 mSv to the hand. 63% of the total dose equivalent is delivered by non-useful fast group (>10 keV), the filtration of this neutron group from the beam will further reduce the dose equivalent to the patient's hand. This finding is of significant importance because such low energies and beam currents can be achieved even by small accelerators and the normal manganese concentrations are still

measurable. These dose rates estimated in this work can be used to calculate the radiation dose received to patient's hand for IVNAA measurement of aluminum in human hand bones.

At E_p = 2.00 MeV beam energy, the gamma dose constituted more than 25% of the total dose equivalent. *Paper VI* also discusses gamma shield design from those photons produced either in the target due to ^{7}Li($p, p'\gamma$)^{7}Li (E_γ = 478 keV) or in the neutron moderating assembly due to ^{1}H(n, γ) interaction (E_γ = 2.2 MeV) to reduce the gamma dose equivalent to less than 5% of the total dose equivalent. The total dose equivalent delivered to the patient as a result of gamma shield will be reduced from 41 mSv to 31 mSv. The fast neutron component of the beam delivers (63%) most of this dose equivalent.

This paper also discusses a method to calculate the differential composite sensitivity along the phantom surface and also along the depth of the phantom. For bilateral irradiation of hand, the differential composite sensitivity along the phantom depth will be minimum (~10%) because of the improved uniformity of the thermal fluence due to opposing irradiations and also because of an initial build-up of thermal flux in first few mm from the hand surface. The variation of the differential composite sensitivity on the phantom surface is approximately 70-80%. This problem of non-uniform sensitivity of the system can be improved by using an arrangement of a set of small detectors instead of single large detector for γ-detection, however, it will reduce the integral sensitivity of the system. This problem of achieving uniform composite sensitivity is dealt by the use of the calcium activation signal from the bone to normalize the measurement to the amount of bone.

8.3 Development of Neutron Source for Low Energy Accelerator Based *In-vitro* Measurements

The third part is composed of one chapter. This chapter describes the development of monoenergetic neutron fields of energy less than 600 keV for radiobiological and radiochemical studies at McMaster 3 MV KN Van de Graff accelerator facility primarily dedicated to *in-vivo* neutron activation measurements. This will extend the use of the facility for those applications in radiobiological and radiochemical research where moderate neutron dose rates of monoenergetic neutrons are needed. A tissue equivalent proportional counter (TEPC) filled with propane based tissue equivalent (TE) gas simulating a 2 μm diameter was employed to determine the neutron and gamma dose rates of the monenergetic neutron fields as a function of proton beam energy. The dose rates of the monoenergetic neutrons produced using thin lithium metal targets via the ^{7}Li(p, n)^{7}Be calculated as functions of beam energy, target thickness, lab angle, and the solid angle subtended by the sample with the target are

also reported. These tabulated data provide the facility of optimal selection of neutron energy and dose rate using the proper choice of beam energy, target thickness, target–sample distance, and direction relative to the beam.

8.4 Future Research for Low Energy Accelerator Based *In-vivo* Measurements

The non-useful fast neutron component of the beam delivers 63% the total dose equivalent. Its filtration will increase the useful neutron fluence (thermal and epithermal) per unit dose equivalent available for activation. The filtration of the non-useful fast energy neutron group from the beam will further reduce the dose equivalent to the patient's hand.

Filtration of the beam will reduce the thermal neutron fluence because of the larger distance involved between the target and the phantom. However, the distance that exists between the target and moderator assembly (2.5 cm) can be used to adjust the moderator and fast neutron filter. This will require a higher beam current or longer irradiation time (where $t_{irr} << T_{½}$) to produce the same activation as with existing 2.4 cm thick polyethylene moderator. A fast neutron filter has a low absorption cross-section for thermal neutrons but a high absorption and elastic scattering cross-section for fast neutrons. The elastic scattering resonances of ^{7}Li, fluorine, iron, aluminum, sulphur etc, can be combined and their cross-section matched in such a way that the useful neutron fluence dominates the incident neutron spectrum over the phantom surface.

Other viable neutron sources for accelerator based *in-vivo* measurements could be ^{9}Be(p, n)^{9}B, ^{9}Be(d, n)^{10}B, ^{13}C(d, n)^{13}N. Although the neutron yields for ^{9}Be(p, n)^{9}B are relatively low as compared to ^{7}Li(p, n)^{7}Be, the neutron spectrum below E_p = 3.0 MeV, is also softer relative to ^{7}Li(p, n)^{7}Be. Thus lower neutron yield may be compensated by smaller moderator thickness to obtain a pre-dominantly thermal-epithermal neutron fluence. Moreover, it is much more feasible to construct high current ^{9}Be targets because of its high melting point compared to ^{7}Li. Despite its importance for low energy accelerator based clinical applications in BNCT, BNCS, BNEFNT, and *in-vivo* measurements, differential cross-sections are not available below E_p = 2.5 MeV. The techniques developed to construct thin targets (Chapter IV, V, VII) in conjunction with a calibrated ^{3}He spectrometer may be employed to make such measurements available. Colonna *et al.* (1999) have recently carried out few such measurements for ^{9}Be(d, n)^{10}B and ^{13}C(d, n)^{13}N for E_d = 1.5 MeV. The uncertainty involved in the measurements using a plastic scintillator was around 30% and the lower limit for neutron detection was ~100 keV. Much better accuracy in the measurements could be

achieved with a ^{3}He spectrometer while keeping the lower limit of detection the same as mentioned earlier. Measurement of differential cross-sections in the low energy range for ^{9}Be(p, n)^{9}B, ^{9}Be(d, n)^{10}B, ^{13}C(d, n)^{13}N using a ^{3}He spectrometer is not only useful for applications in *in-vivo* measurement but is also needed for other clinical applications such as BNCT, BNCEFNT, neutron brachytherapy. Development of targets for high current applications in *in-vivo* and *in-vitro* measurements would pave the way for extensive use of the facility for many other clinical applications.

Looking at the neutron producing reactions ^{7}Li(p, n)^{7}Be, ^{9}Be(p, n)^{10}B, and T(p, n)^{3}He, the relationship between the produced neutron energy and the angle of emission related by kinematic relations reveal that the neutron energy decreases as we move away from the beam direction. Thus the neutron spectrum softens as one moves away from the beam direction, however, this is also accompanied by a decrease in neutron yield. The decrease in yield may partially be compensated by using a smaller moderator thickness because of lower energy spectrum as compared to that of beam direction. Thus instead of constructing the *in-vivo* measurement facility in the beam direction, investigations may be carried out by constructing facilities in other directions for example, orthogonal to beam. Such investigations have already been carried out by the BNCT group at Birmingham University (Allen *et al.* 1999).

Alternative low energy charged particle induced neutron-producing reactions with high neutron yields are needed to increase the portability as in case of radioisotope based neutron sources. The development of high current compact neutron generators using DD and DT reactions for BNCT and BNCS has paved the way for other clinical applications like *in-vivo* measurements making the portability of a generator more feasible than other accelerator based neutron sources. The neutron fluxes obtainable from commercial generators are 4×10^{9} n/s for the D-D and 4×10^{11} n/s for D-T reactions (Yanch *et al.,* 1999). The energy of the neutrons produced by the D-D reaction is similar to the average energy of the neutrons emitted by ^{252}Cf and the neutron flux is ~2 times higher than the 1 mg ^{252}Cf source used in IVNAA applications. Thus there is a possibility to construct a similar compact moderator and reflector assembly as optimized for ^{252}Cf (Lewis *et al.,* 1997). Such a system will have the added benefits of compactness; it will be safer to use because the target does not use radioactive tritium, it will be simpler to transport, and a less costly irradiation facility, which is easier to install, easier to operate, and able to operate in pulsed mode compared with the large accelerator facilities. Moreover, D-D neutron generators have a constant neutron

output over the lifetime of the tube which suggests the reproducibility obtained with D-D generators will be as good as obtained with other sources.

Absolute measurement of $(p, p'\gamma)$ above the (p, n) threshold for $^{7}Li(p, p'\gamma)^{7}Li$ are needed for other clinical applications such as BNCT, BNCEFNT, neutron brachytherapy and also in *in-vivo* measurements.

References

Al-Hiti, K., Slaibi, S., Al-Kayat, T., 1979. Portable system for detecting cadmium in the human liver. Int J Appl Radiat Isot. **30(1)** 55-60.

Allen, D.A., Beynon, T.D., Green, S., 1999. Design for an accelerator-based orthogonal epithermal neutron beam for boron neutron capture therapy. Med Phys. **26(1)** 71-76.

Arnold, M.L., 2000. *Development of an accelerator based system for in-vivo neutron activation analysis measurements of manganese in humans, PhD Thesis, McMaster University*, Hamilton, ON, Canada.

Arnold, M.L., McNeill, F.E., Stronach, I.M., Waker, A.J., Pejović-Milić, A., Chettle, D.R., 2002. An accelerator based system for *in vivo* neutron activation analysis measurements of manganese in human hand bones, Med. Phys. **29(11)** 2718-2724.

Aslam, Prestwich, W.V., McNeill, F.E., Waker, A.J., 2003. Estimation of dose equivalent to patients undergoing hand irradiation at the facility developed for accelerator based *in-vivo* neutron activation measurements in human hand bones, submitted to Medical Physics.

Beddoe, A.H., Zuidmeer, H., Hill, G.L., 1984. A prompt gamma *in vivo* neutron activation analysis facility for measurement of total body nitrogen in the critically ill. Phys Med Biol. **29(4)** 371-383.

Bush, D., 1972. Measurement and control of dose equivalent to patients undergoing whole-body neutron irradiation for *in vivo* activation analysis. Phys Med Biol. **17(1)** 32-41.

Chamberlain, M.J., Fremlin, J.H., Peters, D.K., Philip, H., 1968. Total body calcium by whole body neutron activation: new technique for study of bone disease. Br Med J. **2(605)** 581-583.

Chamberlain, M.J., Fremlin, J.H., Peters, D.K., Philip, H., 1970. Applications of the whole-body counter in total-body neutron activation analysis. Br J Radiol. **43(508)** 287-288.

Cohn, S.H., Dombrowski, C.S., 1971. Measurement of total-body calcium, sodium, chlorine, nitrogen, and phosphorus in man by *in vivo* neutron activation analysis. J Nucl Med. **12(7)** 499-505.

Cohn, S.H., Dombrowski, C.S., Fairchild, R.G., 1970. *In-vivo* neutron activation analysis of calcium in man. Int J Appl Radiat Isot. **21(3)** 127-37.

Cohn, S.H., 1980. The present state of *in vivo* neutron activation analysis in clinical diagnosis and therapy. At Energy Rev. **18(3)** 599-660.

Chettle, D.R., Fremlin, J.H., 1984. Techniques of *in vivo* neutron activation analysis. Phys Med Biol. **29(9)** 1011-43.

Colonna, N., Beaulieu, L., Phair, L., Wozniak, G.J., Moretto, L.G., Chu, W.T., Ludewigt, B.A., 1999. Measurements of low-energy (d,n) reactions for BNCT. Boron Neutron Capture Therapy. Med Phys. **26(5)** 793-8.

Cummins, P.E., Dutton, J., Evans, C.J., Morgan, W.D., Sivyer, A., Elwood, P.C., 1980. An *in-vivo* study of renal cadmium and hypertension. Eur J Clin Invest. **10(6)** 459-61.

Dietze, G., Booz, J., Edwards, A.A., Guldbakke, S., Kluge, H., Leroux, J.B., Lindborg, L., Menzel, H.G., Nguyen, V.D., Schmitz, Th., Schuhmacher, H., 1988. Intercomparison of dose equivalent meters based on microdosimetric techniques. Radiat. Prot. Dosim. **23(1/4)** 227-234.

Eisen, Y., Brake, R.J., Vasilik, D.G., Erkkila, B.H., Littlejohn, G.J., 1986. The performance of low pressure tissue-equivalent chambers and a new method for parameterising the dose equivalent. Radiat. Prot. Dosim. **15(2)** 117-130.

Ellis, K.J., 2000. Human body composition: *in vivo* methods. Physiol Rev. **80(2)** 649-80.

Ellis, K.J., Lee, P.D., Pivarnik, J.M., Bukar, J.G., Gesundheit, N., 1996. Changes in body composition of human immunodeficiency virus-infected males receiving insulin-like growth factor I and growth hormone. J Clin Endocrinol Metab. 81(8):3033-3038.

Evans, H.J., Leblanc, A.D., Johnson, P.C., 1979. Facility for regional *in vivo* neutron activation analysis of skeletal calcium. Phys Med Biol. **24(1)** 181-187.

Gerdung, S., Grillmaier, R.E., Lim, T., Pihet, P., Schuhmacher, H., Ségur, P., 1994. Performance of TEPCs at low pressures: some attempts to improve their dose equivalent response in the neutron energy range from 10 keV to 1 MeV. Radiat. Prot. Dosim. **52(1-4)** 57-59.

ICRP. 1977. *Recommendation of the ICRP.* Ann. ICRP **1(3)**. ICRP Publication 26 (Pergamon Press, Oxford).

ICRP. 1991. *Radiation protection recommendation of the international commission on radiological protection*. ICRP Publication 60 (Pergamon Press, Oxford).

ICRU. 1983. *Microdosimetry*. ICRU Report 36 (ICRU Publications, Bethesda, MD).

Kehayias, J.J., Valtuena, S., Waitekus, A.B., Sheahan, C.A., O'Neill, M. 2000. *In vivo* elemental partition analysis using fast neutrons. A tool for testing the efficacy of new clinical interventions. Ann N Y Acad Sci. **904** 140-7.

Khaloo, R., Waker, A.J., 1995. An evaluation of hydrogen as a TEPC counting gas in radiation protection microdosimetry, Rad Prot. Dosim. **58(3)** 185-191.

Krauel, J.B., Speed, M.A., Thomas, B.W., Baddeley, H., Thomas, B.J., 1980. The *in vivo* measurement of organ tissue levels of cadmium. Int J Appl Radiat Isot. **31(2)** 101-6.

Leach, M.O., Thomas, B.J., Vartsky, D., 1977. Total body nitrogen measured by the $^{14}N(n, 2n)^{13}N$ method: a study of the interfering reactions and the variation of spatial sensitivity with depth. Int J Appl Radiat Isot. **28(3)** 263-269.

Lewis, D.G., Natto, S.S., Ryde, S.J., Evans, C.J., 1997. Monte Carlo design study of a moderated 252Cf source for *in vivo* neutron activation analysis of aluminium. Phys Med Biol. **42(4)** 625-36.

Mernagh, J.R., Harrison, J.E., McNeill, K.G., 1977. *In vivo* determination of nitrogen using Pu-Be sources. Phys Med Biol. **22(5)** 831-835.

Morgan, W.D., Vartsky, D., Ellis, K.J., Cohn, S.H., 1981. A comparison of ^{252}Cf and ^{238}Pu, Be neutron sources for partial-body *in vivo* activation analysis. Phys Med Biol. **26(3)** 413-24.

Nelp, W.B., Palmer, H.E., Murano, R., Pailthorp, K., Hinn, G.M., Rich, C., Williams, J.L., Rudd, T.G., Denney, J.D., 1970. Measurement of total body calcium (bone mass) *in vivo* with the use of total body neutron activation analysis. J Lab Clin Med. **76(1)** 151-162.

Nunomiya, T., Kim, E., Kurosawa, T., Taniguchi, S., Yonai, S., Nakamura, T., Nakane, Y., Sakamoto, Y., Tanaka, S., 2002. Measurement of lineal-energy distributions for neutrons of 8 keV to 65 MeV by using a tissue-equivalent proportional counter. Radiat. Prot. Dosim. **102(1)** 49-59.

O'Meara, J.M., Blackburn, B.W., Chichester, D.L., Gierga, D.P., Yanch, J.C., 2001. The feasibility of accelerator-based in vivo neutron activation analysis of nitrogen. Appl Radiat Isot. **55(6)** 767-74.

Palmer, H.E., Nelp, W.B., Murano, R., Rich, C., 1968. The feasibility of *in vivo* neutron activation analysis of total body calcium and other elements of body composition. Phys Med Biol. **13(2)** 269-279.

Pejović-Milić, A., 1998. *An accelerator based in vivo measurement of aluminum in human bone by neutron activation analysis*, MSc Thesis, McMaster University.

Pejović-Milić, A., 2001. *In-vivo measurement of some trace elements in human bone*, PhD Thesis, McMaster University.

Pihet, P., Menzel, H.G., Alberts, W.G., Kluge, H., 1989. Response of tissue-equivalent proportional counters to low and intermediate energy neutrons using modified TE-^{3}He gas mixtures. Radiat. Prot. Dosim. **29(1-2)** 113-118.

Pszona S., Makarewicz, M., 1982. Effect of cavity size on the sensitivity of a TE-walled, TE-gas -filled ionization chamber for fast neutrons. Phys. Med. Biol, **27(8)** 1015-1022.

Ricourt, A., Posny, F., Soulié, R., Chemtob, M., Nguyen, V.D., 1981. *Possibilitiés d'utilization des techniques microdosimètriques pour la détermination de l'équivalent de dose,* IN Seventh Symposium on Microdosimetry, Oxford, 1981. EUR7147. eds. J. Booz, H. G. Ebert, H. D. Hartfield (Harwood Academic for CEC, London).

Rossi, H.H., 1968. *Microscopic energy distribution in irradiated matter.* IN Radiation Dosimetry. Eds F. H. Attix and W. C. Roesch (Academic Press, New York, Vol. 1, 70-92).

Ryde, S.J., Morgan, W.D., Sivyer, A., Evans, C.J., Dutton, J., 1987. A clinical instrument for multi-element *in vivo* analysis by prompt, delayed and cyclic neutron activation using ^{252}Cf. Phys Med Biol. **32(10)** 1257-1271.

Scott, M.C., Chettle, D.R., 1986. *In vivo* elemental analysis in occupational medicine. Scand J Work Environ Health. **12(2)** 81-96.

Srdoc, D., Marino, S.A., 1996. Microdosimetry of monoenergetic neutrons. Radiat. Res. **146(4)** 466-474.

Stinchcomb, T.G., Borak, T.B., 1983. Neutron quality parameters versus energy below 4 MeV from microdosimetric calculations. Radiat. Res. **93(1)** 1-18.

Sutcliffe, J.F., 1996. A review of *in vivo* experimental methods to determine the composition of the human body. Phys Med Biol. **41(5)** 791-833.

Taylor, G.C., 1995. An analytical correction for the TEPC dose equivalent response problem. Radiat. Prot. Dosim. **61(1-3)** 67-70 (1995).

Thomas, B.J., Harvey, T.C., Chettle, D.R., McLellan, J.S., Fremlin, J.H., 1979. A transportable system for the measurement of liver cadmium *in vivo*. Phys Med Biol. 24(2) 432-437.

Vartsky, D., Ellis, K.J., Chen, N.S., Cohn, S.H., 1977. A facility for *in vivo* measurement of kidney and liver cadmium by neutron capture prompt gamma ray analysis. Phys Med Biol. **22(6)** 1085-1096.

Vartsky, D., Ellis, K.J., Cohn, S.H., 1979. *In vivo* measurement of body nitrogen by analysis of prompt gammas from neutron capture. J Nucl Med. **20(11)** 1158-1165.

Waker, A.J., 1995. Principles of experimental microdosimetry. Radiat. Prot. Dosim. **61(4)** 297-308.

Williams, E.D., Boddy, K., Harvey, I., Haywood, J.K., 1978. Calibration and evaluation of a system of total body *in vivo* activation analysis using 14 MeV neutrons. Phys Med Biol. **23(3)** 405-415.

Wyatt, R.M., Ryde, S.J., Morgan, W.D., McNeil, E.A., Hainsworth, I.R., Williams, A.J., 1993. The development of a technique to measure bone aluminium content using neutron activation analysis. Physiol Meas. **14(3)** 327-335.

Yanch, J.C., Shortkroff, S., Shefer, R.E., Johnson, S., Binello, E., Gierga, D., Jones, A.G., Young, G., Vivieros, C., Davison, A. and Sledge, C., 1999. Boron neutron capture synovectomy: treatment of rheumatoid arthritis based on the ^{10}B(n,)^{7}Li nuclear reaction. Med. Phys. **26(3)** 364–375.

Glossary of Terms

Absorbed dose. The energy imparted to matter by ionizing radiation per unit mass of the irradiated material at the point of interest. The unit is gray (Gy), defined to be an energy deposition of 1 J/kg.

Differential composite sensitivity. This is defined as the product of thermal neutron activation sensitivity and the gamma detection sensitivity. It expresses the uniformity of IVNAA measurement of a particular element along a plane.

Detector efficiency. The ratio of measured counting rate to the source emission rate.

Dose equivalent. A quantity used for radiation-protection purposes that takes into account the different probability of effects that occur with the same absorbed dose delivered by ionizing radiations. It is defined as the product of the absorbed dose and the quality factor. The unit of equivalent dose is sievert (Sv).

Dosimetry. The theory and application of the principles and techniques involved in the measurement of ionizing radiation doses.

Dose-mean lineal energy. An average of the lineal energy dose distribution which depends upon the energy of the incident radiation and the simulated diameter.

***In-vivo* neutron activation analysis (IVNAA)**. A non-invasive technique which provides a measure of an element of interest in a living subject by measuring the activity induced in the body with that particular element from neutron interactions.

Linear energy transfer (LET). An indicator of the quality of ionizing radiations which is defined as $L=dE/dx$ where dE is the mean energy lost by a charged particle in collisions along an element of dx of its trajectory. It has units of keV/μm.

Lineal Energy. The ratio of the energy imparted to the matter in a volume by a single energy-deposition event to the mean chord length in that volume. It is expressed in units of keV/μm.

Microdosimetry. The study of the microscopic nature of ionizing radiation and its method of interaction and energy deposition.

MDL. It is an important indicator of the sensitivity of an analytical technique like NAA for the element in question. The MDL of an element using IVNAA is determined by following the dose equivalent limit.

Monte Carlo radiation transport simulation. The Monte Carlo method is a special numerical method which uses random numbers to simulate the transport of particle by sampling various probability distributions. The desired statistical uncertainty in the average result of simulation is achieved by taking the average of a very large number of particles.

Neutron yield. The total number of neutrons emitted in a certain direction. Yield in 4π directions is referred as the total neutron yield.

Quality factor. A factor used for radiation-protection purposes that accounts for differences in biological effectiveness between different radiations.

Neutron Spectrometry. The theory and application of the principles and techniques involved in the measurement of neutron energy distributions.

Tissue Equivalent Proportional Counter (TEPC). A tissue equivalent walled proportional counter filled with tissue equivalent gas most commonly used to measure the lineal energy distributions, absorbed dose, quality factors and dose equivalent.

Threshold energy. This defines the lowest energy for an interaction at which reaction can take place.